



HAL
open science

Actionneurs piézoélectriques ultrasoniques miniatures pour la réalisation de moteurs sphériques compacts

Edouard Leroy

► **To cite this version:**

Edouard Leroy. Actionneurs piézoélectriques ultrasoniques miniatures pour la réalisation de moteurs sphériques compacts. Vibrations [physics.class-ph]. Ecole Polytechnique X, 2013. English. NNT : . pastel-00927417

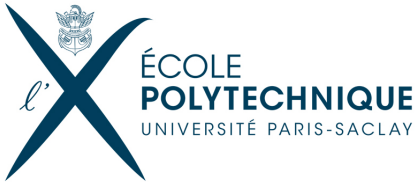
HAL Id: pastel-00927417

<https://pastel.hal.science/pastel-00927417v1>

Submitted on 13 Jan 2014

HAL is a multi-disciplinary open access archive for the deposit and dissemination of scientific research documents, whether they are published or not. The documents may come from teaching and research institutions in France or abroad, or from public or private research centers.

L'archive ouverte pluridisciplinaire **HAL**, est destinée au dépôt et à la diffusion de documents scientifiques de niveau recherche, publiés ou non, émanant des établissements d'enseignement et de recherche français ou étrangers, des laboratoires publics ou privés.



PhD THESIS
OF
ÉCOLE POLYTECHNIQUE

Submitted by:

Edouard LEROY

in Partial Fulfillment of the Requirements for the Degree of
DOCTOR OF PHILOSOPHY

SPECIALTY: Mechanics

**MINIATURE ULTRASONIC PIEZOELECTRIC ACTUATORS
FOR COMPACT SPHERICAL MOTORS**

Prepared at the
Sensorial and Ambient Interfaces Laboratory, CEA LIST

Defended on the 6th of December 2013

Before the committee:

Betty LEMAIRE-SEMAIL	Professor	Polytech'Lille	Reader
Philippe LUTZ	Professor	Femto-st Besançon	Reader
Stéphane REGNIER	Professor	Université Pierre et Marie Curie	Examiner
Jean-Marc BREGUET	Scientific group leader	EMPA, Thun, Suisse	Examiner
Moustapha HAFEZ	Head of research	CEA LIST	Advisor
José LOZADA	Senior Expert	CEA LIST	Co-Advisor

Remerciements

Je tiens à remercier l'ensemble des personnes ayant participé directement ou indirectement à la réalisation de ce travail de thèse. D'abord Moustapha Hafez, mon directeur, qui m'a permis de réaliser ce doctorat dans les meilleures conditions au sein du laboratoire interfaces sensorielles et ambiantes du CEA. Merci de m'avoir guidé durant mon projet tout en m'accordant une grande confiance et en me laissant une importante liberté dans mon travail. Je souhaite également remercier José Lozada dont les conseils aussi bien dans la réalisation du projet que dans la rédaction de mes idées ont été précieux.

Je remercie mon jury de thèse, Betty Lemaire-Semail et Philippe Lutz pour avoir accepté de rapporter cette thèse ainsi que Jean-Marc Breguet et Stéphane Reigner en tant qu'examineurs de mon travail.

Je souhaite remercier toute l'équipe du Laboratoire Interfaces Sensorielles et Ambiantes du CEA. Avec en particulier Laurent Eck pour son aide précieuse en électronique. Christian Boltzmacher pour nos échanges sur les piezo. Annick Latare pour son support administratif sans faille et dans la bonne humeur. Merci également à Carlos Rossa, pour m'avoir supporté dans le même bureau pendant ces trois années, et ce malgré les nombreux débats houleux et parfois sans grand intérêt que nous avons pu avoir. Je remercie Florent Altché pour l'aide qu'il m'a apporté à la production des résultats expérimentaux durant son stage. Je remercie la team thésard du LISA avec plus particulièrement Lucie Brunet et Charles Hudin à qui je souhaite une grande réussite dans la finalisation de leur travail de thèse. Je remercie Gwénaél Changeon, Mehdi Boukallel, Steven Strachan, Harald Zophoniasson, Nicolas Guenard et tous les autres membres du laboratoire qui participent à maintenir une ambiance de travail agréable et sympathique.

Je tiens à remercier également ma famille, mes parents, mon frère et ma sœur qui ont été d'un grand support durant ces trois années et mes amis, en particulier mes colocataires, Antoine et Salim avec qui j'ai vécu durant toute ma thèse. Enfin merci à Cécile, pour sa continuelle présence et ses encouragements sans lesquels la fin de la thèse aurait sans doute été beaucoup plus difficile.

Contents

Remerciements	i
Contents	ii
List of Figures	vi
List of Tables	x
Introduction	1
1 State-of-the-art of spherical motors: a critical review	3
1.1 Introduction	4
1.2 Multi-degree-of-freedom actuation systems	4
1.2.1 Multi-rotor association	5
1.2.2 Single-rotor (spherical) system	6
1.3 Electromagnetic actuators	7
1.3.1 Stepping spherical motors	7
1.3.2 Synchronous spherical motor	8
1.3.3 Induction spherical motors	8
1.3.4 Direct drive spherical motors	8
1.4 Friction-driven actuators: Working principles	9
1.4.1 Traveling wave ultrasonic motors	9
1.4.2 Standing wave ultrasonic motors	12
1.4.3 Inertia motors	13
1.5 Friction-driven actuators: Single-stator ultrasonic motors	13
1.5.1 Standing wave single-stator actuators	13
1.5.2 Traveling wave single stator	20
1.6 Friction-driven actuators: Multi-stator ultrasonic motors	21
1.6.1 Standing wave	21
1.6.2 Traveling wave	22
1.7 Friction-driven actuators: Inertia motors	23
1.8 Discussion	24
1.8.1 Electromagnetic systems	26
1.8.2 Single-stator ultrasonic technologies	27
1.8.3 Multi stator-ultrasonic technologies	28
1.9 Target application of this work	29

1.10	Proposed design method	32
1.11	Conclusion	33
2	Modal Analysis: Design of the resonant mechanical structure	35
2.1	Introduction	36
2.2	Vibrations theory	36
2.2.1	Mass-spring resonator	36
2.2.2	Vibration modes	40
2.2.3	Finite-element method	41
2.3	Modal analysis	44
2.3.1	Generic geometry	44
2.3.2	Finite element model	44
2.3.3	Tracking modes through geometric variations	45
2.3.4	Modes selection	48
2.3.5	Mode symmetry	51
2.3.6	Mode degeneration	52
2.3.7	Angle between movements at contact surface	52
2.3.8	Geometric variations	55
2.3.9	Geometry selection	59
2.4	Modal sensitivity	59
2.4.1	Geometric tolerances	60
2.4.2	Soldering points	61
2.4.3	Influence of contact layer	64
2.4.4	Experimental result of vibration modes tuning	64
2.5	Conclusion	66
3	Contact analysis: From vibration to motor mechanical output	67
3.1	Introduction	68
3.2	Tribology of ultrasonic motors	68
3.2.1	Friction model	68
3.2.2	Ultrasonic motor contact modeling	70
3.2.3	Friction material for ultrasonic motors	75
3.3	Coordinates change for the proposed actuator	76
3.4	Mode displacement amplitudes	77
3.4.1	Contact time	78
3.4.2	Motor output characteristics	78
3.5	Preloading force	81
3.5.1	Contact time	81
3.5.2	Motor output characteristics	81
3.5.3	Torque versus speed characteristics	82
3.6	Contact layer stiffness	83
3.6.1	Contact time	83
3.6.2	Motor output characteristics	84
3.7	Contact length	85
3.7.1	Contact time	86
3.7.2	Motor output characteristics	87
3.8	Frequency response of the actuator	89
3.8.1	Modes frequency response	89

CONTENTS

3.8.2	Motor frequency response	90
3.8.3	Maximum output power	92
3.9	Conclusion	92
4	Electrodes pattern: Electrical energy to mechanical energy conversion	95
4.1	Introduction	96
4.2	Electromechanical model of a piezoelectric resonant actuator	96
4.2.1	Admittance circle	97
4.2.2	Mechanical quality factor	100
4.2.3	Electromechanical coupling factor	101
4.3	General discussion on electrode design and efficiency	102
4.4	Effective electromechanical coupling factor computation	104
4.5	Experimental verification	105
4.5.1	Geometry and mode selection	105
4.5.2	Experimental set-up	107
4.5.3	Experimental measurements	108
4.5.4	Influence of electrode pattern on quality factor	108
4.6	Optimization of the actuator	110
4.6.1	Electrodes for longitudinal-bending actuators	110
4.6.2	Single mode optimization	111
4.6.3	Two mode optimization problem	114
4.6.4	Relation between mode amplitude and equivalent circuit parameters	115
4.6.5	Ultrasonic motor complete modeling	117
4.7	Summary of the ultrasonic motor modeling method	119
4.8	Conclusion	120
5	Ultrasonic motor experimental characterization	123
5.1	Introduction	124
5.2	Actuator implementation	124
5.2.1	Actuator fabrication	124
5.2.2	Holding mechanism	125
5.2.3	Contact wires	127
5.2.4	Contact layer deposition	128
5.3	Experimental set-up	129
5.3.1	Mechanical set-up	129
5.3.2	Measurement set-up	130
5.3.3	Measurement procedure	133
5.3.4	Model comparison	134
5.4	Voltage dependance	134
5.4.1	Admittance response	135
5.4.2	Mechanical response of the actuator	136
5.5	Phase shift influence	139
5.5.1	Speed and torque	139
5.5.2	Power and efficiency	140
5.6	Preloading force dependance	141
5.6.1	Effect of preload on resonance characteristics	141
5.6.2	Preloading force and frequency response of the actuator	142
5.6.3	Torque and speed as a function of preloading force	143

5.6.4	Preloading and efficiency of the actuator	144
5.7	Contact length	145
5.7.1	Influence of contact pattern on resonance characteristics	145
5.7.2	Influence of contact length on speed-torque characteristics	146
5.8	Resonance tracking of the actuator	147
5.8.1	Phase-based resonance tracking	149
5.8.2	Phase tracking for highly damped vibrations	150
5.9	Conclusion	152
6	Conclusion and perspectives	155
6.1	Design methodology	155
6.2	Motor fabrication	157
6.3	Perspectives	159
	Appendices	161
A	Piezoelectric materials	163
A.1	Definition and History	163
A.2	Applications	163
A.3	Ferroelectric materials	165
A.4	Piezoelectric mathematical formalism	170
A.4.1	Piezoelectric effect in ceramics	170
A.4.2	State equations	170
B	Electromechanical coupling factor computation	173
	Bibliography	181

List of Figures

1.1	Classification of multi-degree-of-freedom actuators.	5
1.2	Examples of multidegree-of-freedom angular systems using several rotors associated in parallel.	6
1.3	Spherical stepping motor proposed by Week et al. [1].	7
1.4	Friction-driven actuators working principles.	10
1.5	Degenerating out-of-plane modes of a PZT disc of 50 mm in diameter.	11
1.6	Working principle and assembly of a rod-type single stator spherical motor.	14
1.7	Miniaturized Longitudinal-bending spherical motor proposed by Rogers et al. [2].	15
1.8	Spherical single stator prototype proposed by Zhang et al. [3].	16
1.9	Hybrid Spherical Ultrasonic motor proposed in [4].	17
1.10	Tip-based spherical actuator.	17
1.11	Sandwich-type spherical ultrasonic motor.	18
1.12	Spherical ultrasonic motor based on out-of-plane modes of a planar stator.	19
1.13	Traveling wave spherical motor.	20
1.14	Spherical SAW motor proposed in [5].	21
1.15	Spherical multi-stator ultrasonic motor based on linear actuators [6].	21
1.16	Traveling wave multi-stator ultrasonic spherical motor [7].	22
1.17	Inertia spherical motor based on Gafenol magnetostrictive alloy [8].	23
1.18	Torque as a function of rotor diameter for spherical single rotor MDOF motors.	26
1.19	Qualitative comparison of electromagnetic spherical systems regarding the proposed criteria.	26
1.20	Qualitative comparison of single-stator spherical systems regarding the proposed criteria.	27
1.21	Qualitative comparison of multi-stator spherical systems regarding the proposed criteria.	28
1.22	Target application of this work.	29
1.23	Expected improvements using an extended contact area for the ultrasonic actuator	31
1.24	Overview of the two steps energy conversion of an ultrasonic motor.	32
2.1	Mass-spring-damper mechanical model.	37
2.2	Forced response of a mass-spring-damper system.	38
2.3	Simply-supported beam.	40
2.4	Generic geometry proposed for the design of the actuator.	44
2.5	Set of points used for the application of the modal accordance criterion.	46
2.6	AutoMAC for a set of nine representative modes of a typical actuator geometry.	47

2.7	MAC of a specific mode as a function of the variation of the portion angle θ with or without continuity.	49
2.8	First order in-plane modes found for a typical actuator geometry.	50
2.9	Differences in elliptic paths in function of modes combination symmetry	51
2.10	Evolution of the frequency of the modes as a function of the portion angle θ . . .	52
2.11	Trajectories of the points along the contact area for different mode combinations.	54
2.12	Average angle between mode movements as a function of R_o/R_i	56
2.13	Study of portion angle θ evolution as a function of geometry.	57
2.14	Evolution of the mode frequency as a function of the actuator area.	58
2.15	Geometric tolerances effect on mode degeneracy.	60
2.16	Soldering points are modeled as half spheres of Tin/Lead alloy.	61
2.17	Effect of soldering deposit on modal frequencies and degeneration portion angle.	62
2.18	Solder points modeling for location influence study	62
2.19	Modal frequencies changes as a function of the position of four hemispheric solder points of 0.3 mm in radius disposed symmetrically onto the actuator. . .	63
2.20	Modeled contact layer in finite element analysis.	64
2.21	Influence of contact layer on mode frequencies and mechanical quality factor. .	65
2.22	Mode frequency tuning using soldering points on the actuator.	65
3.1	Two different friction models that can be used to compute friction forces.	69
3.2	Local coordinates system used to define the contact model.	70
3.3	Friction layer is considered as an elastic layer.	71
3.4	Normal displacement as a function of movement phase.	72
3.5	Evolution of torque transmission with respect to rotor velocity.	74
3.6	Classification of some materials used in traveling wave ultrasonic motors	75
3.7	Change in coordinates from global (\vec{x}, \vec{y}) to local (\vec{n}, \vec{t}) coordinate system. . . .	76
3.8	Normalized modes displacements at the contact interface.	77
3.9	Evolution of mean contact time along the contact area with respect to both modes amplitude at $P_0 = 1N$	78
3.10	Evolution of speed and torque characteristics as a function of the two mode displacement amplitudes.	79
3.11	Evolution of output power and contact efficiency as a function of the two modes amplitudes.	80
3.12	Mean contact phase angle φ_c along the contact surface vs preloading force for a given amplitude of $1\mu\text{m}$ on both modes.	81
3.13	Motor output characteristics as a function of preloading force	82
3.14	Evolution of speed vs torque actuator response as a function of preloading. . . .	83
3.15	Contact phase angle φ_c as a function of the layer thickness and the preloading force P_0	84
3.16	Evolution of speed and torque characteristics as a function of the layer thickness and preloading force.	85
3.17	Evolution of power and contact efficiency as a function of the layer thickness and preloading force.	86
3.18	Definition of the parameters used for the change in contact length	86
3.19	Mean contact time φ_c as a function of the length of contact w and preloading force P_0	87
3.20	Evolution of speed and torque as a function of contact length and preloading force.	88

List of Figures

3.21	Evolution of output power and contact efficiency as a function of contact length and preloading force.	89
3.22	Example of two modes amplitude frequency responses.	90
3.23	Effect of mode non-degeneracy on motor speed as a function of frequency. . . .	91
3.24	Effect of mode non-degeneracy on motor torque as a function of frequency. . . .	91
3.25	Evolution of maximum output power as a function of frequency shift between the two modes.	92
4.1	Equivalent Butterworth van Dyke circuit	96
4.2	Typical Admittance circle around resonance.	97
4.3	Modal shape and electrode disposition of the sample used for experimental verification.	105
4.4	Four degenerating non-rotational invariant in-plane modes with the same modal shape. An infinity of modes with this same mode shape exist by rotation along the disc axis.	106
4.5	Strain S_3 distribution of the first radial mode of a piezoelectric disk as a function of the radius from the center of the disk.	106
4.6	Theoretical total strain squared density versus electrode area for all possible electrode patterns.	107
4.7	Experimental setup for admittance measurement.	107
4.8	Fit of experimental data.	108
4.9	Experimental electromechanical coupling factor vs computed $(\int S_3)^2$ density. . .	109
4.10	Quality factor Q_m as a function of excitation parameters for constant voltage harmonic excitation.	109
4.11	Resonator properties comparison for a constant $C_1 U^2$ factor and a constant excitation voltage U	110
4.12	Modal shapes and possible electrodes configuration for a longitudinal-bending actuator.	111
4.13	S_3 strain distribution for the considered actuator modes.	112
4.14	Parametric electrode pattern.	112
4.15	Relation between the total strain squared density $\frac{(\int_{V_e} S_3 dV)^2}{A_e}$ and the electromechanical coupling factor k_{eff}^2 for the two considered modes.	113
4.16	Best electromechanical coupling factor as a function of area using parametric electrodes. Both longitudinal and bending mode presents an optimal electromechanical coupling factor.	114
4.17	Mode amplitudes as a function of dynamic branch energy for both longitudinal and bending modes.	116
4.18	Motor parameters for full motor modeling.	117
4.19	Electrode area optimization for maximum output power.	118
4.20	Electrode area optimization for maximum motor efficiency.	118
4.21	Summary of the proposed ultrasonic modeling method.	119
5.1	A picture of the laser-cut actuator.	125
5.2	Modal shapes of the two modes. Zero displacement points (nodes) are shown as red dots.	126
5.3	Two different possible holding mechanisms.	127
5.4	Contact layer deposition process.	128

5.5	Drying effect of the contact layer	129
5.6	Mechanical set-up used for actuator characterization.	129
5.7	Validated ultrasonic motor prototypes. A single degree-of-freedom actuator using a spherical rotor has been validated. A cylindrical rotor is used for characterization allowing for a simplified measurement of the actuator characteristics.	131
5.8	Measurement set-up for actuator characterization	132
5.9	Impedance measurement of a 1.5mH inductor with and without calibration.	132
5.10	Example of a transient speed response of the actuator.	134
5.11	Evolution of admittance response as a function of the voltage	135
5.12	Evolution of series resonance frequency and dynamic resistor as a function of the voltage applied to the electrodes.	136
5.13	Motor frequency response with respect to excitation voltage.	137
5.14	Motor characteristics with respect to excitation voltage.	138
5.15	Power and efficiency as a function of the excitation voltage.	138
5.16	Evolution of elliptical trajectories as a function of phase shift.	139
5.17	Motor properties as a function of the phase shift between the two signals.	140
5.18	Output power and efficiency of the actuator as a function of the phase shift between the two signals.	141
5.19	Evolution of resonance characteristics as a function of preloading force.	141
5.20	Evolution of resonance characteristics as a function of preloading force.	142
5.21	Frequency response of the actuator as a function of the preloading force.	143
5.22	Evolution of resonance characteristics as a function of preloading force.	143
5.23	Efficiency as a function of preloading force.	144
5.24	Contact layer length change.	145
5.25	Q_m as a function of contact extent for a preloading force of 1N.	146
5.26	Speed versus contact length for various preloading force.	146
5.27	Torque versus layer length for various preloading forces.	147
5.28	Admittance circle of a piezoelectric actuator around resonance.	148
5.29	Control for zero phase tracking implemented in Labview.	149
5.30	Influence of a resonance tracking system on the performance of the actuator.	150
5.31	Admittance circle shift caused by a parallel inductor.	151
5.32	Influence of two modes excitation on admittance phase for both considered modes.	152
6.1	Actuator perspectives.	159
A.1	Direct and inverse piezoelectric effects	164
A.2	Perovskite structure (ABO_3) of Lead Zirconate Titanate (PZT) exhibiting ferroelectric properties	166
A.3	Poling of a ferroelectric ceramic	166
A.4	Hysteresis loop in ferroelectric material	167
A.5	Typical piezoelectric deformation modes used with PZT ceramics	170
B.1	Piezoelectric plate considered	174

List of Tables

1.1	Quantitative data for different single-rotor spherical actuators (when data is available)	25
2.1	PZ26 material properties.	45
4.1	Example of an electrode configuration designation.	105
5.1	Quality factor for both modes in function of the holding mechanism used	127
5.2	Comparison of quality factors with respect to wire diameter.	128
A.1	Examples of applications that use piezoelectric effects	164
A.2	Differences between soft and hard ceramics	169
A.3	Comparison of different materials (piezoelectric and dielectric properties) . . .	169
A.4	Relations between the different piezoelectric properties.	172

Introduction

In the last decade, the miniaturization of electronic components allowed for the development of new mechatronic applications in numerous areas such as automotive, aeronautics or consumer electronics. In this perspective of miniaturization, the development of new actuators, adapted to the realization of miniature mechatronic systems is required.

Electromagnetic motors are widely used in industry. However, they have limited performance as their size decreases. Numerous parts are required for their fabrication and their generated torque is limited. Piezoelectric materials, on the other hand, are an interesting alternative because of their high force density and their adaptation to the microscale. Although they have limited deformation, their high bandwidth allows for ultrasonic vibration generation which can be transformed into continuous linear or rotary motion. Ultrasonic piezoelectric motors use a resonant mechanical structure to generate small movements at high frequency in order to move a rotor placed in contact. Their actuation principle is based on friction forces. Their geometry can be tailored to fit a large variety of applications.

The use of a spherical rotor is interesting for robotic and mechatronic applications such as robot articulations and optical component stabilization. In this work, we focus on the application of ultrasonic motors for micro-cameras stabilization. This application has an important potential for the video capture in mobility especially with the integration of micro-cameras in most existing mobile phones. The association of these devices with a high dynamic actuation system for object tracking or image stabilization has numerous potential applications in image processing, security or sports.

Although they have been developed for more than 30 years, ultrasonic actuators have limited industrial applications. The high number of interdependent design parameters limits their optimization and robustness. This thesis proposes a complete design method for the realization of multimode ultrasonic actuators. The main objective is to provide general design guidelines and study the effect of the different parameters on their performance. A multimode curved actuator used for actuating a spherical rotor is studied. The use of a large contact area allows for a complete rotor guidance while limiting the stresses and wear of the actuator. This thesis is organized in five chapters:

INTRODUCTION

- Chapter 1 describes the state of the art of multi-degree-of-freedom motors based on a spherical rotor. It presents the different technologies of ultrasonic actuation and proposes a classification of existing prototypes. A set of criteria is discussed for comparison and evaluation. This chapter highlights the difficulties of ultrasonic spherical motor design. The result of this analysis leads to an innovative actuator concept for micro-camera stabilization. The design methodology is presented.
- Chapter 2 is dedicated to the mechanical design of the resonant structure. A general introduction to vibration theory and resonance concept is proposed. Actuator geometry is defined and analyzed using finite element modal analysis. Vibration modes are studied as a function of the geometric parameters. A suitable geometry is then proposed. The sensitivity of the structure to geometrical tolerances and added masses is studied.
- Chapter 3 focuses on contact analysis. A contact model is proposed to describe the conversion from stator vibration to rotor rotation. Modal analysis results discussed in chapter 2 are used in order to estimate motor performance as a function of multiple parameters. Different parameters such as mode amplitude, preloading force and contact layer properties are studied. Guidelines for optimal contact conditions are proposed.
- Chapter 4 addresses the electromechanical conversion in the actuator. An electromechanical model of piezoelectric resonators is proposed. A focus on the electrode pattern and its effect on actuation efficiency is presented. Finally, an optimization of the electrodes size based on the complete motor model is proposed.
- Chapter 5 presents the experimental validation. The fabrication of the actuator is described. An experimental set-up for motor performance measurement is proposed. The mechanical properties of the motor are studied as a function of voltage, preloading force and contact layer. These results are compared to the actuator model.
- Chapter 6 proposes a conclusion of the work. A summary of the main achievements of this thesis is presented. It highlights the performance of the model and how it can be adapted to other designs. The limitations of the model are also discussed and a perspective work to improve the robustness and the model is proposed.

State-of-the-art of spherical motors: a critical review



Contents

1.1	Introduction	4
1.2	Multi-degree-of-freedom actuation systems	4
1.2.1	Multi-rotor association	5
1.2.2	Single-rotor (spherical) system	6
1.3	Electromagnetic actuators	7
1.3.1	Stepping spherical motors	7
1.3.2	Synchronous spherical motor	8
1.3.3	Induction spherical motors	8
1.3.4	Direct drive spherical motors	8
1.4	Friction-driven actuators: Working principles	9
1.4.1	Traveling wave ultrasonic motors	9
1.4.2	Standing wave ultrasonic motors	12
1.4.3	Inertia motors	13
1.5	Friction-driven actuators: Single-stator ultrasonic motors	13
1.5.1	Standing wave single-stator actuators	13
1.5.2	Traveling wave single stator	20
1.6	Friction-driven actuators: Multi-stator ultrasonic motors	21
1.6.1	Standing wave	21
1.6.2	Traveling wave	22
1.7	Friction-driven actuators: Inertia motors	23
1.8	Discussion	24
1.8.1	Electromagnetic systems	26
1.8.2	Single-stator ultrasonic technologies	27
1.8.3	Multi stator-ultrasonic technologies	28
1.9	Target application of this work	29
1.10	Proposed design method	32
1.11	Conclusion	33

1.1 Introduction

Multiple degree-of-freedom (MDOF) angular actuation systems are used in numerous technological areas. Typical applications are found in robotics in order to build omnidirectional robots [9], robot limbs or eyes articulations [4]. They are also found in other mechatronic areas such as haptic joysticks [10], security systems and in general inertially stabilized platforms [11] that are used in astronomy [12], defense, cinema, photography and other industrial areas for stabilizing optical components or tracking objects [13]. The conventional method used in order to build such actuators is based on multiple single degree-of-freedom motors associated in series or parallel through a set of gimbals. Although this method is well adapted for most applications, mechatronic systems tend to scale down and there is a need for smaller MDOF angular actuators that can provide high-amplitude and high-dynamic motion in a compact design. Gimbals and conventional electromagnetic motors are difficult to miniaturize and often result in poor compactness of the MDOF platforms. Motors that use a spherical rotor could be a good alternative in order to obtain highly compact, low inertia miniaturizable MDOF actuators.

In this chapter, a critical review of the existing possible solutions to obtain multiple angular degree-of-freedom actuators is proposed. The focus is especially given to the specific case where highly compact and dynamic systems are required. In a first section, the different possibilities to obtain MDOF platforms are presented and classified. The second section introduces electromagnetic technologies. Working principles are not thoroughly explained since they stand on widely known technologies. Friction-driven actuators are presented in four different sections because of the large variety of existing systems: one is introducing the working principles, a second one focuses on single-stator ultrasonic actuators, the third one on multi-stator ultrasonic motors and the last one discusses inertia motors. A qualitative and quantitative summary of single rotor spherical motor technology is proposed with the identification of important design criteria. These criteria are used for the proposition of a new actuator concept, adapted to a specific application.

1.2 Multi-degree-of-freedom actuation systems

It exists various ways to build MDOF actuation systems. Depending on the application and the characteristics that have to be emphasized (precision, bandwidth, compactness...) different solutions may be adapted. A typical classification of MDOF actuators is proposed in figure 1.1. Focus in this review is given to single rotor systems.

Electromagnetic actuators are classified according to the different actuation technologies that are adaptations of well-known electromagnetic single-DOF actuators, whereas friction-based actuators are classified according to both stator geometry and actuation principles.

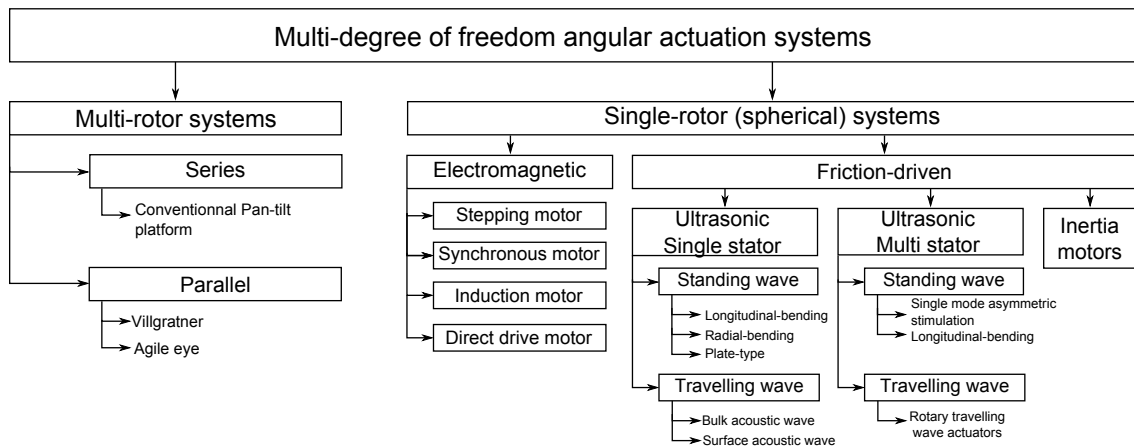


Figure 1.1: Classification of multi-degree-of-freedom actuators. The review focuses on the study of electromagnetic and friction-based single rotor spherical systems. The classification of electromagnetic actuators is based on driving principles while friction-based actuators are classified as a function of both geometry and driving principles.

Throughout this chapter, different characteristics of the systems will be analyzed. We want to emphasize the difference between *compactness* and *miniaturization* since they are often considered as synonyms. The miniaturization is considered as the ability to scale a system down to small sizes, while the compactness is considered as the way the different pieces are packed together. In the case of a spherical motor, a system is considered as compact when its stator-to-rotor volume ratio is low (i.e. the volume of the stator is small as compared to the rotor).

1.2.1 Multi-rotor association

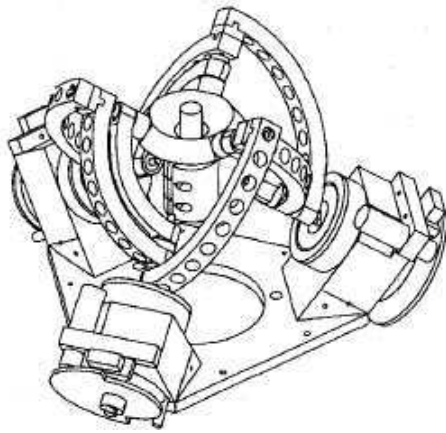
Rotary motor series association

A widely used solution in industry in order to obtain two or three angular degree-of-freedom is the use of multiple rotary motors mounted in series via a set of gimbals. Those platforms are simply designed using commercially available electromagnetic motors and offer simple control with a straightforward dynamic model.

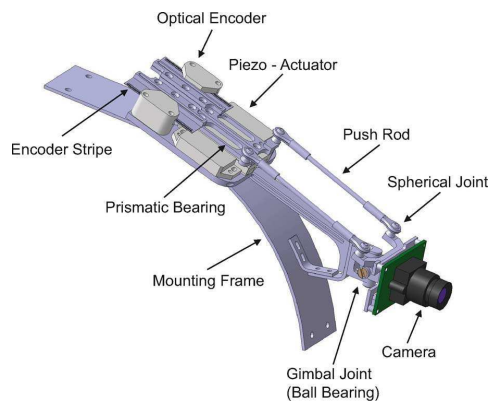
The main limitation of this type of assembly is associated with an extra load and inertia on one of the degree-of-freedom that lead to different dynamic responses on each axis. Moreover, gimbals systems and reduction gears are required to obtain MDOF motion and sufficient torque. These additional parts limit the miniaturization and compactness of the platform. Gimbals systems increase inertia which limits the dynamic response of the platform. Examples of commercial pan-tilt platforms are proposed by FLIR¹.

¹<http://www.flir.com/mcs/view/?id=53484>

Parallel associations



(a) The Agile eye: Parallel 3-DOF rotary actuator based on three rotary actuators and an associated set of gimbals. Reproduced from [14], © 1996 IEEE.



(b) Parallel 2-DOF rotary actuator based on two linear ultrasonic actuators. Reproduced from [15], © 2011 IEEE.

Figure 1.2: Examples of multidegree-of-freedom angular systems using several rotors associated in parallel.

Spherical parallel mechanisms are widely documented in the literature. They are based on the use of single-DOF rotary or linear actuators and offer a large variety of possible designs that can be tuned to the required characteristics of the platform. An example of such mechanisms is the agile eye ([14], figure 1.2a). It is based on the use of three rotary electromagnetic motors mounted in parallel using a mechanism associating three rotary joints (3-RRR). In this design, the same load is applied to each actuator with an equivalent dynamic response on each axis.

Another example of parallel mechanism uses two linear ultrasonic actuators in order to rotate a camera on a pan-tilt platform ([15], figure 1.2b). The system shows high dynamic response with accelerations up to 25000 deg.s^{-2} . However, it presents a complex control method and a reduced displacement amplitude. As a summary, a large number of parallel design can be proposed in order to obtain MDOF angular actuation [16], those parallel mechanisms provide high dynamic response in a limited range of displacements but the use of complex mechanical design induces difficulties in terms of miniaturization and compactness.

1.2.2 Single-rotor (spherical) system

Another design for obtaining MDOF angular movement is the use of a single spherical rotor. Using a spherical rotor actuated by tangential forces at its outer boundary, allows for compact MDOF systems with a large workspace and no need for complex gimbals mechanisms.

Developing an actuator with sufficient torque and reduced number of mechanical parts could lead to new perspectives in terms of integrated robotics and miniaturization of mechatronic systems.

This review focuses on the different single-rotor spherical systems that can be found in literature. Several electromagnetic and friction-based (piezoelectric and magnetostrictive) actuators are studied, they represent the great majority of single rotor spherical actuators that can be found in literature. Some other examples such as pneumatic [17] or shape memory alloy [18] actuators are found in literature but their development is at an early stage and data are hard to find as compared to widely spread electromagnetic and piezoelectric actuators.

1.3 Electromagnetic actuators

Electromagnetic actuators use the interaction between electromagnetic fields produced by coils or magnets. Although single degree-of-freedom motors are well known and commercialized, single-rotor MDOF actuators are still at the prototype stage and have not found commercial applications to our knowledge. Spherical electromagnetic actuators found in literature are based on four major principles: stepping spherical motor, synchronous spherical motor, induction spherical motor and direct drive spherical motor.

1.3.1 Stepping spherical motors

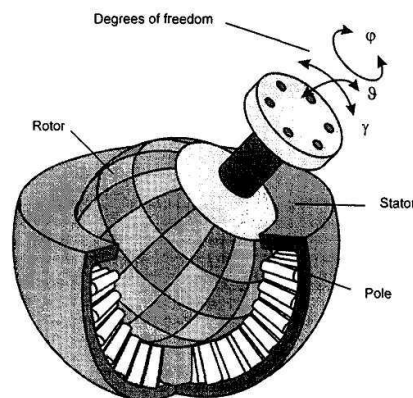


Figure 1.3: Spherical stepping motor proposed by Week et al. [1]. This spherical electromagnetic MDOF actuator consists of 112 magnets placed on a spherical rotor ($\text{\O} 275\text{mm}$) and associated with 96 cylindrical coils. The coils are driven alternatively to move the rotor similarly to a conventional stepper motor. Reprinted from [1], Copyright 2000, with permission from Elsevier.

Stepping spherical motors are based on the use of multiple magnets placed on the rotor and associated with multiple coils (poles) in the stator. Similarly to single-DOF stepping

motors, the goal is to be able to place the rotor in any spherical position using alternative activation of the poles. Existing stepping spherical motors are in general very large machines. The system proposed by Week et al. [1] (figure 1.3) is based on a 275 mm diameter hollow sphere rotor with 112 magnets placed on it. The associated stator is formed of 96 cylindrical coils. The system is expected to produce torque up to 40 N.m with a speed up to 720°/s. The smallest stepping spherical motor that has been found in literature has a diameter of 110mm [19] with numerous parts (8 magnets and 25 coils) and reaches a maximum torque of 13 mN.m and 300 °/s (50 rpm) maximum speed. Rossini et al. [20] propose a spherical stepping motor adapted to the realization of spherical reaction wheels and which is based on a magnetically levitating spherical rotor (89mm radius). In this specific application magnets and coils are both used for rotor guidance and actuation.

Stepping spherical motors are well adapted to large mechanical systems requiring high precision. They present reasonable compactness (stator-to-rotor volume ratio is about 0.67 for [1]) but are not suitable for miniaturization because of a high number of mechanical parts.

1.3.2 Synchronous spherical motor

An example of synchronous spherical motor is given by Yano et al. [21]. The rotor is a 130 mm diameter sphere with 260 magnets placed on it. Output torque is 0.49 N.m for a maximum speed of 90°/s. This type of motors is based on a stator similar to a stepping spherical motor but four electromagnetic actuators are used instead of numerous coils. The system is more compact than stepping motors but still not suitable for miniaturization.

1.3.3 Induction spherical motors

Induction spherical motors are based on the creation of Foucault currents in a conductor in which a varying field is imposed. The current interacts with the magnetic field and causes the rotor to move. Kumagai and Hollis [22] propose an induction spherical motor based on linear induction motor designs. The rotor is a two layers shell composed of an inner iron layer and a outer copper layer. Although the resulting system is quite large with a rotor of 246 mm in diameter, the system could easily be scaled down because of the simple rotor design (no magnet). The stator-to-rotor ratio (0.13) is better than the previously presented prototypes, what is also an indication of the compactness of these systems.

1.3.4 Direct drive spherical motors

The last type of spherical electromagnetic motors is direct drive spherical motors. In this case, the rotor contains a single magnet that orients in the direction of a magnetic field

generated by three or more coils. Wang et al. [23] propose a motor whose stator is 88 mm in diameter associated with a permanent magnet spherical rotor of 48 mm in diameter. The maximum torque is 400 mN.m. A slightly larger 3-DOF prototype is also proposed based on a four-pole spherical rotor and four sets of windings. The motor although slightly larger (60 mm stator for a 30mm rotor) offers a 600 mN.m torque.

Bederson and Wallace [24, 25] propose a similar concept with a non-spherical rotor. A magnet is attached to the rotor which is guided using a spherical joint. The actuator measures 40x50x60 mm, produces a 8 mN.m torque and is the smallest electromagnetic spherical single-rotor actuator that has been found in the literature. The large inertia of the rotor is the main problem of this actuator and causes control problems. Although they are well adapted to pointing actuator systems, these actuators are not suitable for applications where the rotor should be able to realize multiple turns over itself (e.g. omnidirectional wheels).

1.4 Friction-driven actuators: Working principles

Another technology which has great potential for spherical single-rotor actuators is friction-driven actuation used for example in ultrasonic motors. These actuators are based on the formation of small highly repeated movements at a contact interface with a rotor. Most of them use piezoelectric materials in order to produce these vibrations. In this review, focus is given on three main types of friction-based actuators:

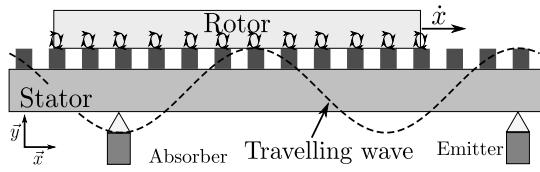
- Traveling (or progressive) wave ultrasonic motors
- Standing wave ultrasonic motors
- Inertia (stick-slip) motors

1.4.1 Traveling wave ultrasonic motors

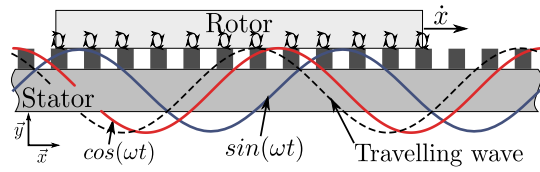
Traveling wave ultrasonic actuators create motion by generating traveling acoustic waves in a stator. The rotor, in contact with the stator, is subjected to a tangential force in the opposite direction to the propagating wave. The traveling wave can be generated using two different solutions: a non-resonant solution using an emitter/absorber configuration or a resonant configuration using degenerating modes of a symmetric structure.

Emitter/absorber configuration

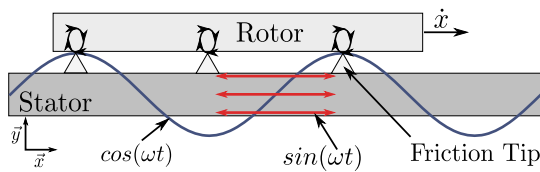
An actuator excites a specific propagating mode of the structure while an absorber on the other end ensures that there is no reflexion that would result in the formation of a standing



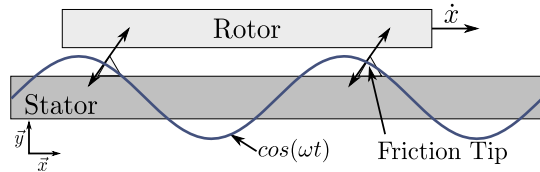
(a) Traveling wave non-resonant actuator. An emitter produces an acoustic wave that propagates from one end of the stator to the other where it is absorbed in order to avoid reflexion and creation of a standing wave. Because there is no standing wave, resonance effect cannot be used.



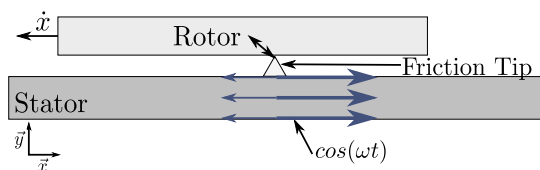
(b) Traveling wave resonant actuator. Two degenerating modes with the same mode shape and a 90° spatial phase shift are excited with a 90° temporal phase difference causing the formation of a travelling wave that set the rotor in motion. A brush-like contact interface is usually adopted to optimize the contact. Because standing waves are generated, resonance effect can be used.



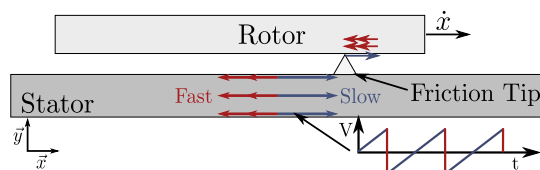
(c) Multi-modes standing wave actuator. Two vibration modes that produces non-collinear movement at the interface are excited with a phase difference causing the formation of elliptical motions that drive a rotor in contact. The direction of the motion can be changed by inverting the sign of the phase difference.



(d) Single-mode standing wave actuator. Friction tips are placed so as to obtain oblique impact on the rotor. This type of actuator cannot reverse its direction of motion and the location of the friction tips determines the driving direction.



(e) Asymmetric excitation single-mode standing wave actuator. A symmetric mode is excited using an asymmetric signal (e.g. the excitation of only one half of a longitudinal mode). An oblique motion is produced at the location of the axis of symmetry of the mode resulting in rotor displacement. Inverting the asymmetry of the excitation results in a inversion of the driving direction.



(f) Inertia motor. Sawtooth driving waveforms are used in order to obtain slow forward motion and fast backward motion. Because of the inertia of the rotor, the stator slides during the fast return. The slow forward motion drives the rotor without sliding resulting in a net displacement.

Figure 1.4: Friction-driven actuators working principles.

wave in the structure (see figure 1.4a). Linear actuators have been designed based on this principle but low amplitude due to non-resonating stator results in poor efficiency.

Emitter/absorber configurations are also used in order to build surface wave acoustic motors. In these motors propagating surface modes are excited at high frequency (>5 MHz) using interdigital transducers (comb-like electrodes deposited onto the active material). Because they are non-resonant actuators, they usually require high voltage but the use of multiple active and passive pairs of transducers allows to create an electric energy re-circulation which improves greatly the system efficiency and reduces the required voltage [26].

Association of degenerating vibration modes

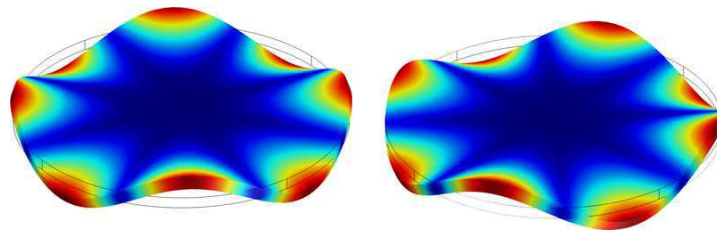


Figure 1.5: Degenerating out-of-plane modes of a PZT disc of 50 mm in diameter. Finite element analysis shows that there exists two vibrations modes at the same frequency (computation gives 30.862 kHz and 30.902 kHz due to meshing approximations). These two modes have the same mode shape with a spatial phase-shift of $\frac{\pi}{2}$.

Two vibration modes with the same modal shape and with a 90° spatial phase shift exist at the same frequency in stators with a circular symmetry (such as presented for a disc in figure 1.5). They can be used in order to generate a pure traveling wave (see figure 1.4b). Assuming these modes can be described as sine functions in space and are excited with a 90° temporal phase shift:

$$\begin{aligned} u_1(r, \theta) &= A(r) \sin(k\theta) \sin(\omega t) \\ u_2(r, \theta) &= A(r) \cos(k\theta) \cos(\omega t) \end{aligned}$$

The sum of both waves results in the traveling wave:

$$u(r, \theta) = A(r) \cos(k\theta + \omega t)$$

Using this principle, energy is stored in the structure during each period because of the resonance effect. Thus, the amplitude of the traveling wave is significantly increased as compared to emitter/absorber traveling wave actuators leading to better performance of the actuator. This kind of actuator has known great developments and is one of the only type of rotary ultrasonic actuator that is commercialized².

²<http://www.shinsei-motor.com>

In some cases, two modes of different order in a non circular symmetric structure (bending modes of a beam for example) can have very similar mode shape and locally be phase shifted because of the change in wavelength. If the modes are close enough in frequency they can be excited at the same time leading to the formation of a traveling wave locally on the bar, even though mode shapes are not exactly the same [27].

1.4.2 Standing wave ultrasonic motors

Standing wave actuators are based on the excitation of one or several vibration modes of a structure which do not result in the formation of a pure traveling wave but of local elliptical or oblique motions that are used to drive a rotor.

Multi-modes standing wave actuators

For some geometries of a given structure, it is possible to find two modes at the same frequency with different mode shapes. The simultaneous excitation of those modes with a temporal phase difference results in elliptic motions at some points of the stator (figure 1.4c). Because the mode shapes are not the same, the elliptic motions are not the same along the stator and friction tips are placed wherever the vibration is the most important. These actuators are widely used in linear actuators based typically on longitudinal and bending mode of a bar [28].

Some actuators, such as the “hybrid actuator” proposed by Kurosawa and Ueha [29], do not use *two* resonant modes but only *one* resonance to produce the elliptical motions. The second displacement is produced using high amplitude actuators such as multi-layered transducers. The advantage is an increased flexibility in terms of design since there is no need for two degenerating modes. A greater variety of motions (Lissajous figures) can be produced at the interface since the non-resonant motion can be generated at any frequency.

Single mode standing wave actuators

With adequate placement of friction tips on a resonating structure, it is possible to generate oblique motion and drive a rotor (figure 1.4d). This kind of actuator is not reversible and the placement of the friction tips governs which direction of thrust is going to be favored. Another way to build single mode standing wave actuators is to use a symmetric mode associated to an asymmetric excitation (figure 1.4e). PI Line motors [30] use this principle in which an oblique motion transmits torque to the rotor via a friction tip placed on the stator. It is possible to reverse the direction of thrust by changing the excitation area of the piezoelement.

As compared to multi-modes actuators, single mode actuators are simpler to implement with only one resonant mode. Multi-modes and asymmetric single mode actuators have the

advantage to be reversible. Although multi-modes is the most complex architecture, it allows for better control of the driving motions especially when low speed control is required [31].

1.4.3 Inertia motors

Inertia motors are quasi-static friction-based motors that use inertia effect in order to drive a rotor. Since they are not resonant they can be operated in a large span of frequencies. Their working principle uses sawtooth driving signals which result in a two steps movement: first, slow motion causes the stator to stick to the rotor and move it forward while a second fast motion results in a sliding of the stator against the rotor causing a total net displacement of the rotor (figure 1.4f). Because of this working principle, inertia motors are often referred as stick-slip actuators.

1.5 Friction-driven actuators: Single-stator ultrasonic motors

The first type of friction based spherical motors that is studied uses a single part as the stator of the motor. Several vibrations are excited in the stator to drive the rotor in the desired direction.

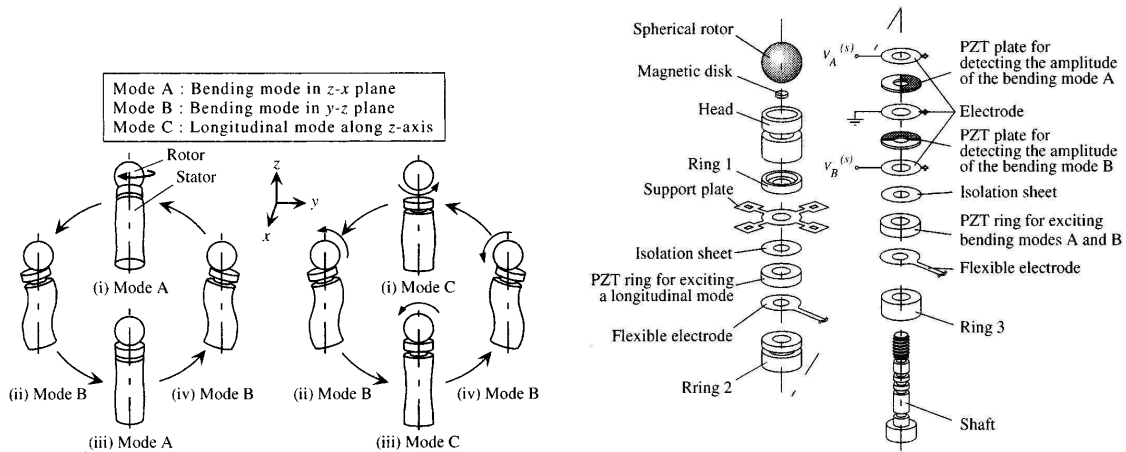
1.5.1 Standing wave single-stator actuators

Longitudinal-bending standing wave actuators

The large majority of ultrasonic spherical motors examples found in literature are based on the use of bending and longitudinal vibrations of cylinders or prismatic beams.

Cylinder-based The first type of single-stator actuator that is studied is based on the vibration modes of a cylinder. A cylinder is designed in order to have one longitudinal mode and a bending mode at the same frequency. Because of the symmetry, there exists two degenerating bending modes at the same frequency along two orthogonal axis. By using a combination of either the longitudinal mode and one bending mode or the two bending modes, three degree-of-freedom motion can be obtained (see figure 1.6).

Cylinder-based ultrasonic spherical motors are among the most popular single-stator motors found in literature. Amano et al. [33] propose one of the first motor based on this principle. They find that it is possible to find a geometry for which both first longitudinal and third bending modes of a hollow cylinder are at the same frequency. The designed motor has an outer diameter of 20 mm and a length of 118 mm. Maximum torque is 30 mN.m and



(a) Working principle of a rod-type MDOF actuator. Two bending modes are used in order to produce a rotation along the z-axis while the longitudinal mode is associated to one bending mode in order to produce a rotation along the y- and x-axes.

(b) Typical assembly. The rod-type MDOF motor is based on cylindrical elements that are assembled together. Three groups of PZT elements are used in order to excite the three modes independently.

Figure 1.6: Working principle and assembly of a rod-type single stator spherical motor. Reproduced from [32], © 2001 IEEE.

maximum speed is 40 rpm at 300 Vpp on longitudinal mode and 360 Vpp on bending mode excitation.

Takemura et al. [32, 34] (figure 1.6) design a similar stator that uses both first longitudinal and second bending modes of a cylinder. Using the second bending mode instead of the third results in a shorter height of the cylinder (the height to length ratio is 3.1 instead of 5.9 for [33]). The obtained mechanical characteristics are a 5 mN.m stall torque and 180 rpm at 20 Vpp (longitudinal) and 40 Vpp (bending). Modal excitation is ensured using d_{33} effect of piezoelectric rings similarly to [33], three groups of piezoelements are used: one causing a symmetric excitation for the longitudinal mode, and two others causing an anti-symmetric excitation along the x- and y- bending axes (see figure 1.6b).

Li et al. [35] discuss key issues when designing cylindrical stators. They show that slots along the cylinder can effectively improve amplitude of the vibration in the stator and be used to tune resonance frequencies of the modes. They also discuss the location of the piezoelectric elements that should be at the maximum strain of each mode. The contact angle between stator and rotor significantly changes the performance of the actuator with an optimum around 55° for x- and y- driving directions.

Although they show quite large stator-to-rotor volume ratio (4.2 to 8.85 when assuming an equal diameter between outer surface of stator and rotor), these motors are well adapted to miniaturization and have been miniaturized. Gouda et al. ([36]) show a miniaturization of a cylinder-type longitudinal-bending actuator, the cylinder is 15mm high for a diameter of

1.5. FRICTION-DRIVEN ACTUATORS: SINGLE-STATOR ULTRASONIC MOTORS

1.7mm. In their design, the vibration modes are no longer excited by independent elements but using a disc with four independent quarter electrodes on which combination of symmetric and anti-symmetric excitations are applied. A 6mm rotor led to a 1 $\mu\text{N}\cdot\text{m}$ torque with a no-load speed of 10 rps (600 rpm) at an excitation voltage of 100 Vpp.

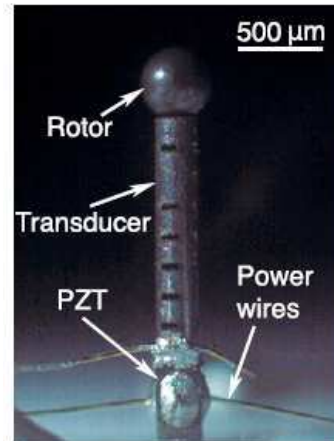


Figure 1.7: Miniaturized Longitudinal-bending spherical motor proposed by Rogers et al. [2]. Rotor is 350 μm in diameter. Modes are excited using shear (d_{15}) piezoelectric effect. © IOP Publishing. Reproduced by permission of IOP Publishing. All rights reserved.

Rogers [2] (figure 1.7) proposes a tiny spherical motor (350 μm diameter rotor) based on the excitation of the vibration modes of a cylinder. Rotation about the z-axis is ensured by exciting the two degenerating first order bending modes while the x- and y-axis rotations use an association of the first longitudinal and second bending modes. The author proposes to reduce bending mode frequency by inserting slots inside the stator, effectively reducing the length needed for 1st longitudinal and 2nd bending mode degeneration. Slots are also used to break symmetry and have better selection of the excited mode. Using this technique, the two bending modes are no longer at the same frequency, therefore simplifying their independent excitation.

The miniaturization of the motor causes problems in terms of excitation of the modes since it is difficult to include three piezoelectric separated groups to excite the different modes. In [2], the modes are excited using a single piezoelectric element with several electrodes. The novelty in the excitation is that the d_{15} effect is used by grounding the bottom electrode while the side electrodes of the element are excited. A symmetric excitation is applied for longitudinal mode excitation while an anti-symmetric signal excites the bending modes. The motor achieves 5000 rpm with a maximum torque of 2 nN.m at 21.2 VRms ($\sim 60\text{Vpp}$). In [37], Yun et al. discuss the difficulty to control the vibration direction of the motor and propose to improve the controllability by tilting the cylinder, therefore causing an increase in non-degeneracy of the bending modes of the cylinder.

These actuators show simple design with great potential of miniaturization and good rotor guidance. However their compactness is limited with a minimum stator to rotor volume of about 2.1 found in literature (when the rotor is slightly larger than the outer diameter of the stator). In addition, the single-stator structure is subjected to interferences between modes which cause difficulties in the control of the rotation direction.

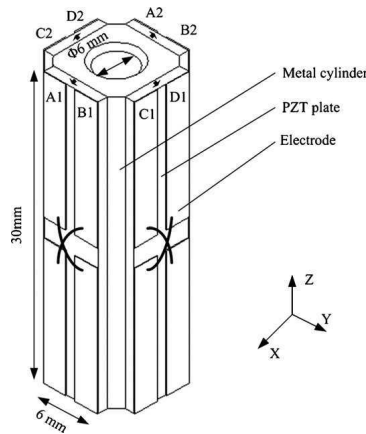


Figure 1.8: Spherical single stator prototype proposed by Zhang et al. [3]. The bending and longitudinal modes are excited using d_{31} effect of piezoelectric elements that are along the outer surface of the stator. Reprinted from [3], Copyright 2008, with permission from Elsevier.

Prismatic rod Zhang et al. [3] (figure 1.8) propose a similar concept of longitudinal-bending actuator associated with a novel way to excite both modes. Plane surfaces are drilled on the cylinder in order to place piezoelectric elements. The structure is designed in order to have the two second order bending modes and first order longitudinal mode at the same frequency. Unlike designs presented previously, the in-plane deformation of the piezoelectric elements is used in order to excite the vibration modes of the stator (d_{31} effect is used instead of d_{33} observed in the previous configurations). The motor shows a maximum torque of 0.85 mN.m with a rotor of 10 mm at 180 V. A very low preloading force (40 mN, weight of the rotor) explains the low torque of the motor.

Resonant and non resonant combination Some ultrasonic motors use only one resonant vibration associated with another non-resonant displacement (usually obtained using multi-layered actuators because of their high deformation). Therefore, they do not require two vibration modes to be degenerating. Zhang et al. [4] propose a “hybrid” actuator based on a multi-layered element in order to produce a large longitudinal displacement at low voltage (4V) without need for a resonance effect (figure 1.9). This displacement is associated with the resonant excitation of one of the degenerating bending modes, depending on the required direction of the movement. Because there is no need for mode degeneration, the stator structure can be smaller and the stator-to-rotor volume ratio is around 1.25 with a

1.5. FRICTION-DRIVEN ACTUATORS: SINGLE-STATOR ULTRASONIC MOTORS

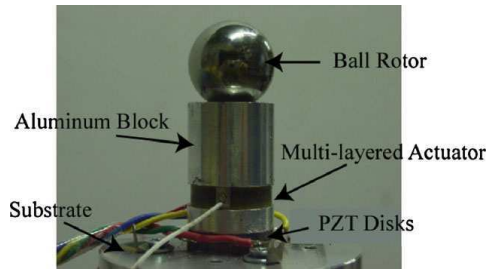


Figure 1.9: Hybrid Spherical Ultrasonic motor proposed in [4]. This longitudinal-bending actuator uses resonant motion in order to produce the bending vibration while the longitudinal vibration is a non-resonant displacement that is performed using multi-layered piezoelectric actuator. Reprinted from [4], Copyright 2011, with permission from Elsevier.

rotor of 25 mm (2.5 with a rotor with the same outer diameter of the stator: 20mm). The obtained stall torque and maximum speed are 23.5 mN.m and 200 rpm.

This kind of actuator have several advantages as compared to longitudinal-bending resonant actuators: There is no need for mode tuning of the stator since only one mode is used and the compactness of the motor can be improved. On the other hand, multilayered actuators are expensive and have high loss as compared to bulk piezoelectric elements [38], they require a power source that can deliver enough current to drive the highly capacitive element and are also less adapted to miniaturization.

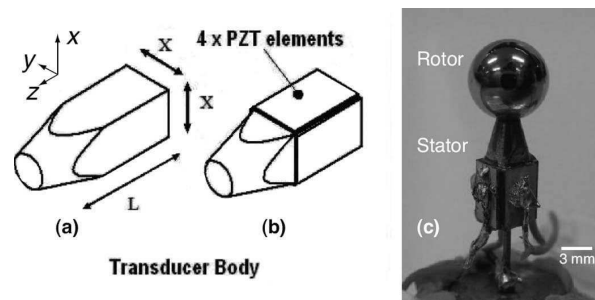


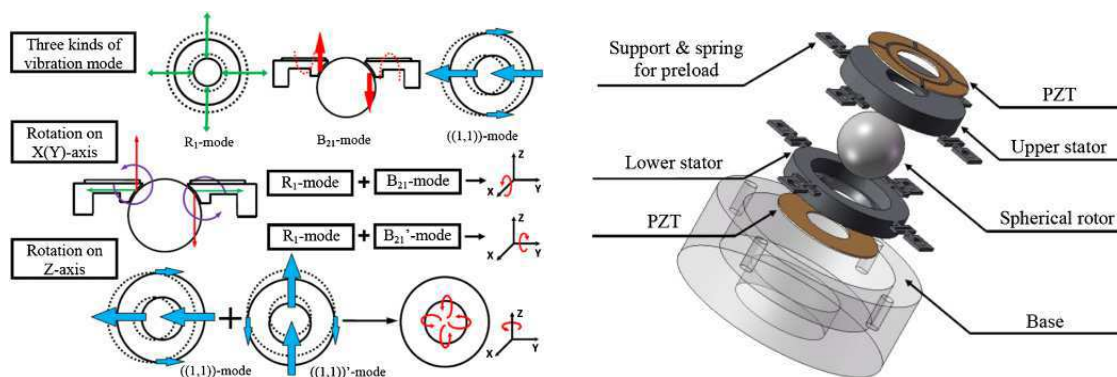
Figure 1.10: Tip-based spherical actuator. A small stator shaped as a tip is used to drive a spherical rotor, bending and longitudinal modes are associated in order to obtain elliptical motions at the contact area with the rotor. Reproduced from [39], © 2009 IEEE.

Tip actuators Tip-based rod-type spherical actuators use elliptical motions generated at a tip by exciting standing waves in a cylindrical or prismatic rod. The tip is placed in contact with the rotor to generate motion of the sphere. Several designs are found in literature, one notable design is the one proposed in [39] (figure 1.10). The stator is a small rod which has its second bending modes and first longitudinal mode at the same frequency. Modes are excited using d_{31} effect of piezoelectric elements. The rod is shaped as a 1.8 mm diameter tip in which a V-notch is machined in order to hold the spherical rotor in place.

In [40], Hu et al. propose a similar tip-based actuator where the semi-spherical stator is static and the actuator is part of the rotor. Although the excitation method is slightly different from [39] and uses d_{33} deformation of a PZT element, the actuator still uses a combination of bending and longitudinal mode of a tip. The advantage of the tip-based actuator is their size that can be very small and can lead to very low stator to rotor ratio. They are also easily miniaturized because of their monolithic structure. However, the contact afforded by a tip is less reliable than a cylinder based actuator and do not offer good guidance of the rotor. The solution of a moving actuator proposed in [40] improves guidance but reduces the workspace and ability of the motor to be miniaturized.

Radial-bending standing wave actuators

Radial-bending single stator spherical motors are based on a similar principle as longitudinal-bending actuators. A radial mode of a ring-like structure is used instead of the longitudinal mode. The resulting geometries are flat as compared to longitudinal-bending actuators but their outside diameter is larger.



(a) Working principle of a ring-type MDOF motor. Three different vibrations are used, radial and bending vibration are combined in order to produce rotation along the three axes.

(b) Assembly of a two disc radial-bending actuators. Two active parts are associated and provide complete guidance of the rotor.

Figure 1.11: Sandwich-type spherical ultrasonic motor. Figures are reproduced from [41]. Copyright 2010 The Japan Society of Applied Physics.

Aoyagi et al. [42] propose an example of a disc shaped spherical actuator. Radial and bending vibrations are combined in order to obtain movement along the x- and y- axis while two degenerating bending modes are used in order to rotate the sphere about the z- axis. Their prototype has a stall torque of 70 mN.m but the outer diameter is more than twice the diameter of the rotor so that, in spite of its flat structure, the motor shows a stator-to-rotor volume ratio of 12. A similar configuration, with a two disc stator, is proposed in [41] (see figure 1.11). In this case, the stator is scaled down with a stator to rotor volume ratio of 5.8 and

1.5. FRICTION-DRIVEN ACTUATORS: SINGLE-STATOR ULTRASONIC MOTORS

the z-axis rotation is not ensured by bending modes but using combined degenerate in-plane modes of the disc (see figure 1.11a). The system shows a maximum torque of 58 mN.m and offers complete guidance of the rotor. Lu and Aoyagi [43] propose also an outer-rotor design based on a similar structure. Although the structure is less suitable for miniaturization, better preloading homogeneity is obtained along with overall easier fabrication.

In [44], Lu et al. propose an interesting concept of rotor embedded ultrasonic spherical motor structure. The stator of the motor is a monolithic structure that act as a cage for the rotor. The spherical rotor is completely constrained and no additional guiding system is required. Working prototype has only be demonstrated for z-axis because of the difficulty to produce a monolithic stator with an embedded rotor.

Plate-type ultrasonic stator

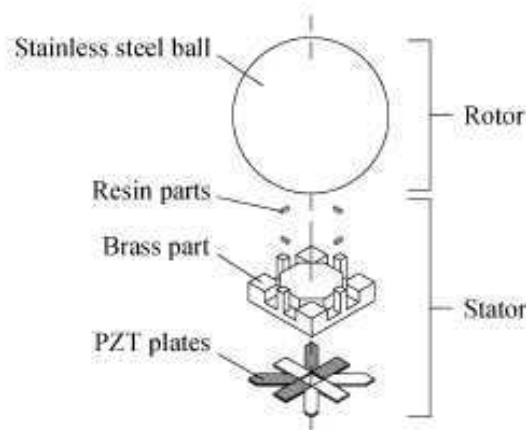


Figure 1.12: Spherical ultrasonic motor based on out-of-plane modes of a planar stator. Several out-of-planes modes of the plate are combined using independent PZT elements. Phase-shifted excitations of two modes result in the formation of elliptical motions that drive the rotor. Reproduced from [45], © 2004 IEEE.

Single stator spherical ultrasonic motors based on the excitation of standing bending waves in a plate have also been reported. In general one or several protrusions are placed on a plate which is excited in order to produce elliptical motions at the tip of the protrusions. Takemura et al. [45] propose a design based on a symmetric and two antisymmetric out-of plane modes which are at the same frequency so that combination of two modes causes displacement about any of x-, y- or z-axis. The stator is built from a mono-block of brass under which several piezoelectric elements are placed (see figure 1.12). No information about transmitted torque is given but the rotor achieves a maximum speed of 50 rpm at 20V amplitude.

Instead of the small tips, Goda et al. [46] propose another design based on the bending modes of a PZT disk on which a cylinder is mounted. A symmetric mode is associated with two anti-symmetric modes of a plate, causing elliptical motions at the top of the cylinder

placed in the middle of the piezoelectric disk. Similar design is proposed in [47] with a stator made of bronze associated with a PZT disk. Another similar design proposed in [48] is based on the out of plane modes of a square plate. The 3 mm diameter motor reaches the maximum speed of 190 rpm at 200 Vpp. No information about the torque of the motor is given.

Spherical motors based on the bending modes of a plate can provide high compactness with reasonable guidance of the rotor. The low number of parts required for their design make them suitable for miniaturization. However, mode coupling due to fabrication defaults is expected and can induce difficulties in the direction control of the motor.

1.5.2 Traveling wave single stator

Bulk acoustic wave

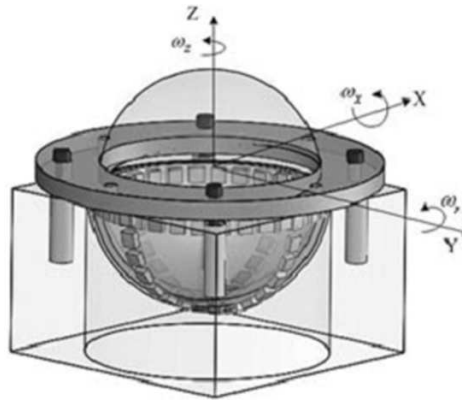


Figure 1.13: Traveling wave spherical motor. A traveling wave is generated using curved piezoelectric elements that are placed over a hemispherical stator. Reproduced from [49] © 2010 IEEE

Ting et al. ([50, 49], figure 1.13) propose to cover a hemispherical stator with curved piezoelectric element placed strategically in order to generate a traveling wave. The elements are half a wavelength long and spaced of a quarter wavelength. The resulting system is expected to show a 0.51 N.m maximum torque and 56 rpm maximum speed. In practice the motor exhibited performance below one third of the estimated values. The motor is compact but the small piezoelectric pieces placed on the stator are difficult to manufacture and limit the miniaturization potential of the concept (in figure 1.13, a 60 mm diameter sphere is used as a rotor).

Surface acoustic wave

Other traveling wave motor designs have been reported using surface acoustic waves (SAW). In this kind of motors surface propagation modes are used to generate traveling waves. Bar-Cohen et al. propose a spherical SAW actuator concept [51] based on a curved SAW actuator.

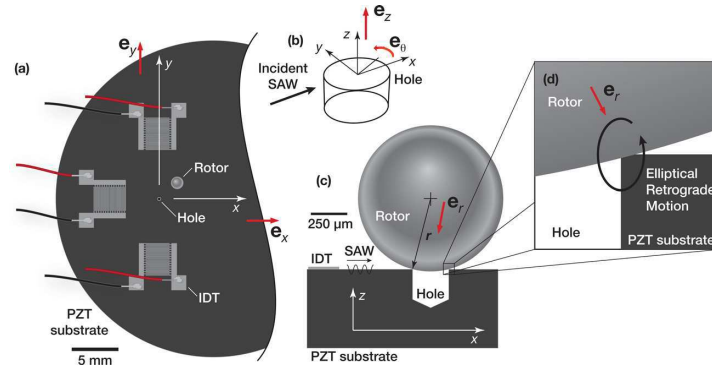


Figure 1.14: Spherical SAW motor proposed in [5]. Surface acoustic waves are excited using comb-like electrodes deposited on a PZT substrate. The traveling wave causes the formation of elliptical motions at the edges of a hole on which a spherical rotor ($\varnothing 1\text{mm}$) is placed. Reprinted with permission from [5]. Copyright 2011, AIP Publishing LLC.

Although the experimental validation is not reported in this work, the concept should allow to design highly compact single stator spherical motors. In [5] (figure 1.14), Tjeung et al. proposed a small spherical motor based on a spherical rotor of 1mm in diameter. They obtained a maximum speed of 1900 rpm and a maximum torque of 5.37 nN.m at 110 Vpp. As force measurement is difficult at this scale, performance is estimated from transient speed response of the motor [52]. Surface acoustic wave motors usually require high surface roughness control since the amplitudes are very small (\sim nanometer) [26]. The system proposed in [5] uses a hole to improve the contact and reduce roughness influence.

1.6 Friction-driven actuators: Multi-stator ultrasonic motors

1.6.1 Standing wave

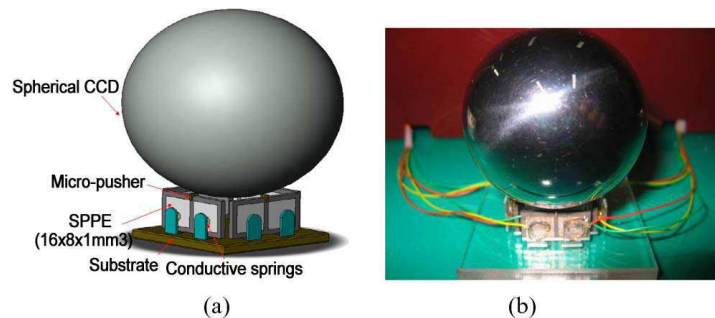


Figure 1.15: Spherical multi-stator ultrasonic motor based on linear actuators [6]. Multiple asymmetric single-mode actuators are placed in parallel in order to actuate a spherical rotor ($\varnothing 44.5\text{mm}$) in the three angular directions. © 2010 IEEE.

Multiple standing wave linear stators can be adapted to a spherical rotor in order to obtain multidegree-of-freedom. Numerous linear designs can be considered and lead to a large versatility of the spherical motor geometry. One example of the adaptation of a linear piezoelectric motor to a spherical motor is presented in [6] (figure 1.15). The proposed motor uses four different asymmetric excitation standing wave linear stators (figure 1.4e) that operate using a principle similar to commercially available Physik Instrumente piezomotors [30]. The actuators are mounted in parallel in order to provide multidegree-of-freedom and their simple operation allows the system to have a very low stator-to-rotor volume ratio of 0.04. The motor shows a maximum speed of 50 rpm along x- and y- axis and 180 rpm along the z-axis for an excitation voltage of 30Vpp.

Another design is proposed by Otokawa and Maeno [53], their motor is based on the use of single vibration modes of different plates. They combine four identical plates for which three different modes can be excited. Combining those modes, they achieve multi-DOF displacement. However, the use of different modes for each motion leads to different characteristics on each axis (5mN.m and 80 rpm on z-axis, 15 mN.m and 45 rpm on x-axis, 4mN.m and 13 rpm on y-axis).

1.6.2 Traveling wave

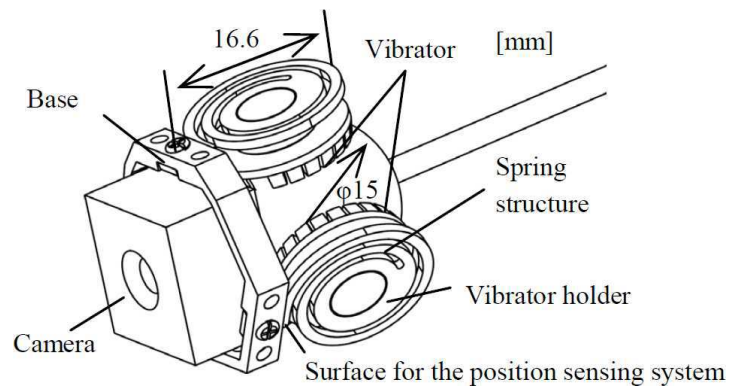


Figure 1.16: Traveling wave multi-stator ultrasonic spherical motor [7]. Three conventional traveling wave actuators are placed in parallel and provide 3-DOF angular motion. © 2009 IEEE.

Traveling wave stators are well known ultrasonic actuators. Since their development by Sashida [54], they have known commercial success and are mature technologies. The use of multiple traveling wave motors on a sphere offers three rotations that can be used to orient the sphere in any direction. One of the first concepts of a spherical motor based on the use of four traveling wave stators, has been proposed by Toyama et al. [55, 56]. It is based on a 60mm rotor and shows a maximum speed of 160 rpm and 290 mN.m at 150 V.

Hoshina et al. [7, 57] proposed a spherical motor based on the use of three traveling wave motors. First, they chose to use a moving spherical rotor in which the payload (a camera) was

placed, but because of the interaction between the camera inside the sphere and the stators, the workspace of the motor was limited to around 60° . An outer stator configuration (see figure 1.16) where the stator is moving while the sphere is fixed was chosen to improve the workspace of the actuator to 270° . The actuator shows a torque of $4\text{mN}\cdot\text{m}$ with a maximum speed of 80 rpm. A closed loop position control using potentiometers shows a good accuracy of 1° .

Traveling wave multi-stator spherical motors offer simple design, with the use of well known actuators that are commercially available. Compactness and miniaturization of these systems is however limited because of the large size of the traveling wave actuators.

1.7 Friction-driven actuators: Inertia motors

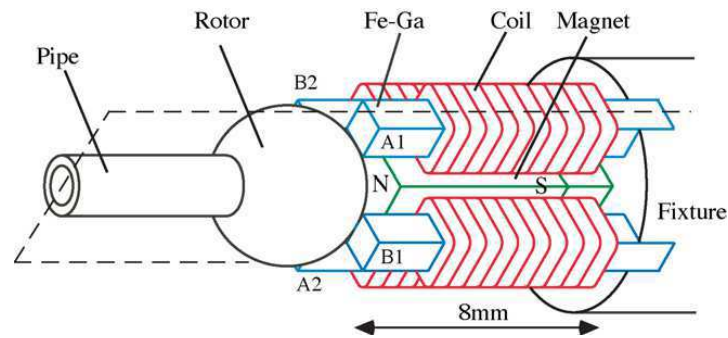


Figure 1.17: Inertia spherical motor based on Gafenol magnetostrictive alloy [8]. Saw-tooth current signals are applied to the coils, resulting in a stick-slip motion that actuate the rotor. Reprinted from [8], Copyright 2009, with permission from Elsevier.

Inertia motors are non-resonant friction-based motors that use a two steps movement of the actuator based on first, a slow sticking movement, followed by a fast sliding movement resulting in a net displacement of the rotor in contact with the actuator. The two motions are generated using saw-tooth driving signals (see figure 1.4f). In [58], several designs for spherical inertial stepping motors are proposed. In general three piezoelements are put in contact with a sphere. Driving the elements with a voltage of 15V_{pp} or more leads to tangential displacement of a few nanometers along the edge of a 4 mm rotor, leading to high precision of about 1 arcsec ($4.8\ \mu\text{rad}$). An interesting example of an application of an inertia spherical motor is the MINIMAN ([59]), a miniature manipulation platform which uses a spherical motor to move a gripper in the three angular directions.

Another inertia motor is proposed in [8] (shown in figure 1.17). This motor is based on four rod of gafenol magnetostrictive alloy which are placed around a spherical rotor. Stick-slip actuation of the alloy lead to a maximum torque of $0.2\ \text{mN}\cdot\text{m}$ and maximum speed of $50^\circ/\text{s}$ for a 4 mm sphere at 1kHz. Higher frequency leads to higher speed (up to $350^\circ/\text{s}$), but controllability is greatly affected above 2 kHz due to limitations in the material bandwidth.

Inertia motors have interesting properties because of their non-resonant nature and simple design but their working principle limits the speed that can be reached. They are interesting actuators when high-precision is required.

1.8 Discussion

Based on the references presented in this review, it is proposed to compare the different spherical actuators principles. Table 1.1 sums up the characteristics of the compared systems when data are available. The first characteristics that are interesting to compare are the output mechanical characteristics (i.e. torque and speed). Nevertheless, although lot of data is found in the literature, it is difficult to offer a fair and objective comparison. Friction-driven technologies have numerous parameters (preloading, ceramics, friction materials, voltage...) that make the comparison difficult. Moreover, because of the low number of prototypes, all with different sizes, it is hard to be definitive about, for example, which technology offer the best torque capability. In figure 1.18, torque of the different systems are represented as a function of the rotor size. As discussed earlier, systems are very different in terms of size and torque capability. Even electromagnetic spherical systems show big discrepancies in performance for systems of about the same size. As expected, the global tendency is a lower torque as the size of the rotor decreases. A fit of the data by a power law gives an average idea of this evolution ($T \propto D^{1.65}$). Although no definitive conclusion can be given in terms of torque, the figure is useful for confronting new systems to the state of the art.

Despite of this lack of information about performances of the presented concepts, a qualitative discussion is proposed. This discussion is based on five important criteria for spherical motor design:

- Miniaturization which is defined as the ability of a system to be scaled down. This criterion measures the ability of a motor concept to be used for the realization of small systems.
- Compactness represents how much the different parts of the system can be packed together. It is measured by the stator-to-rotor ratio.
- Rotor guidance indicates how much the actuation system provides for a guidance of the spherical rotor. This is particularly important as systems are scaled down.
- Implementation simplicity discusses how simple the system is to manufacture and control.
- Driving electronics defines what kind of electronics are required and how complex they are.

TABLE 1.1: QUANTITATIVE DATA FOR DIFFERENT SINGLE-ROTOR SPHERICAL ACTUATORS (WHEN DATA IS AVAILABLE)

Type	Reference	Year	Volume (cm ³)	Rotor diameter (mm)	Stator to rotor ratio	Torque (mN.m)	Speed (rpm)
Longitudinal-Bending	Amano et al [33]	1998	37.07	25	4.5	30	40
	Li et al.[35]	2007	17.69	25	2.2	90	90
	Takemura et al. [32]	2001	2.50	10	4.8	7	250
	Gouda et al. [36]	2006	0.56	6	4.9	1	600
	Rogers et al. [2]	2010	0.00	0.397	2.2	2E-6	5000
	Zhang et al. [3]	2008	3.00	10	5.7	1	227
Hybrid	Zhang et al. [4]	2011	10.37	25	1.3	24	200
Tip type	Khoo et al. [39]	2009	0.11	11.2	0.15	2	58
Radial-bending	Aoyagi et al. [48]	2004	106.40	25.4	12.4	69	-
	Lu et al. [41]	2010	24.14	20	5.8	58	-
	Lu et al. [44]	2011	23.27	25.4	2.7	20	-
Plate bending mode	Takemura et al.[45]	2004	2.00	40	0.06	-	50
	Goda et al.[46]	2009	0.06	6	0.5	-	-
	Aoyagi et al.[42]	2002	1.30	3	92.0	-	191
Surface acoustic wave	Tjeung et al. [5]	2011	0.13	1	238.7	5E-6	1900
Bulk traveling wave	Ting et al. [49]	2010	171.50	60	1.5	170	19
Multiple traveling wave actuators	Hoshina et al. [7]	2009	48.60	15	27.5	4	80
Multiple standing wave actuators	Shen [6]	2010	2.05	44.5	0.04	-	50
	Otokawa et al.[53]	2004	1.79	40	0.05	15	70
Inertia motor	Ueno et al. [8]	2006	33.51	4	6.75	0.2	8.33
Direct drive electromagnetic	Bederson et al. [25]	1992	120.00	30	8.5	8	14
	Wallace et al. [24]	1993	512.00	50	15.3	20	83
	Wang et al. [60]	1998	178.41	48	3.1	400	57
	Wang et al. [23]	2001	452.39	62	3.6	600	57
Stepping electromagnetic	Week et al. [1]	2000	12730.55	275	1.2	40E3	120
	Yano [19]	2010	348.45	78	1.4	13	300
Synchronous electromagnetic	Yano [21]	2007	4871.99	130	4.2	590	15
Induction	Kumagai et al. [22]	2013	1029.96	246	0.13	4000	300

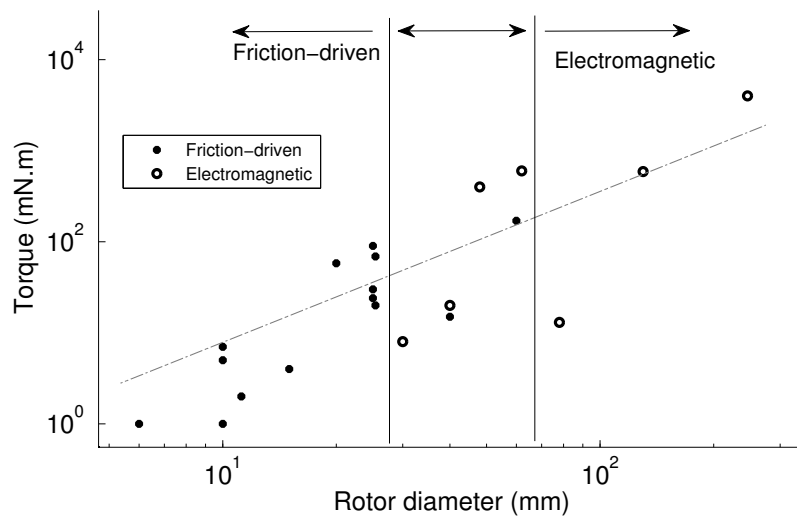


Figure 1.18: Torque as a function of rotor diameter for spherical single rotor MDOF motors. A large dispersion is observed in terms of torque due to the great variety of systems and the dependance of torque on a large amount of variables. Nevertheless, a tendency can be observed from the power law fitted. It can be noted that electromagnetic devices are well adapted to large mechanical systems while friction-driven actuators are preferred for small size rotors.

1.8.1 Electromagnetic systems

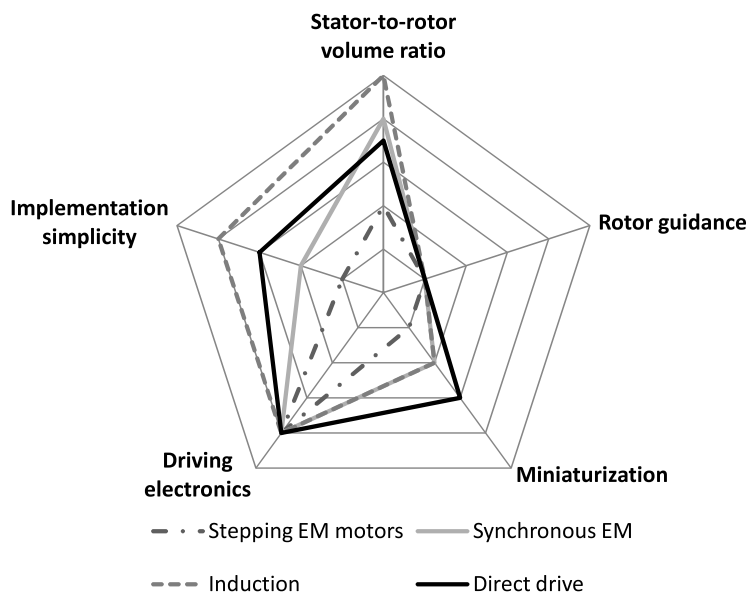


Figure 1.19: Qualitative comparison of electromagnetic spherical systems regarding the proposed criteria.

Figure 1.19 presents the qualitative comparison of electromagnetic spherical actuators. As shown in figure 1.18, electromagnetic systems are not well adapted to miniaturization

and no system below 120 cm^3 is found in literature. Electromagnetic actuators are composed of numerous mechanical parts and permanent magnets that make the realization of low size systems difficult. Direct drive electromagnetic actuators that use only one magnet associated with a limited number of coils are adapted to the realization of decimeter-scaled systems. Induction motors which do not require the use of permanent magnets and can be built using micro-fabrication technologies [61], are the electromagnetic technologies that have the best potential in terms of miniaturization. Induction motors have a low stator-to-rotor ratio that make them suitable for compact electromagnetic motors while stepping electromagnetic motors require the use of a high number of coils that limit their compactness. Electromagnetic actuators do not offer any guidance of the rotor. Therefore, they require bearings such as ball transfer units or spherical bearings. This requirement is one of the reason why their miniaturization is complicated. Electromagnetic technologies implementation can be difficult in terms of control. The use of a high inertia rotor associated with low torque in direct drive actuators and the high number of magnetic poles in synchronous and stepping electromagnetic motors require an adapted control of the actuator. Driving electronics of spherical electromagnetic motors are simple since they are similar to single degree-of-freedom motors which are well known technologies.

1.8.2 Single-stator ultrasonic technologies

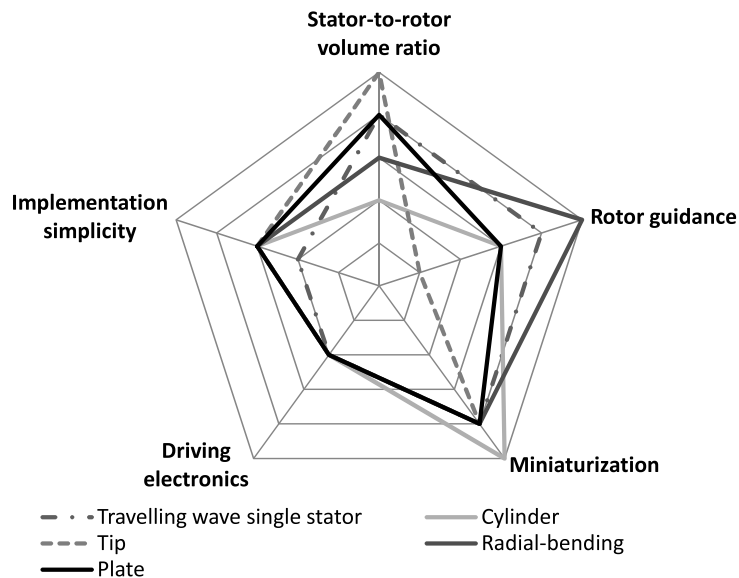


Figure 1.20: Qualitative comparison of single-stator spherical systems regarding the proposed criteria.

Figure 1.20 shows the qualitative comparison of single-stator spherical ultrasonic technologies. Single-stator ultrasonic technologies are the best suited for miniaturization among

spherical motors. The use of a monolithic stator simplifies the realization of small systems with prototypes existing at the millimeter scale. Stator-to-rotor ratio vary as a function of the used technology. Cylinder-based prototypes require the structure to have one longitudinal and a bending mode at the same frequency and result in a large stator as compared to the driven rotor. One solution to increase the compactness of the systems is to design tip-based longitudinal-bending actuators that are small but provide limited guidance to the rotor. Other solutions such as plate-based or radial-bending single stator motor are flat stator designs that provide good guidance of the spherical rotor. Single-stator spherical motors guide the rotor in one direction, however additional guidance is generally required for obtaining a completely constrained rotor. It can be based on a magnetic preloading force or on the use of a two part stator such as in radial-bending-actuators. The implementation of these systems is complicated because of the coupling of the different vibrations in the single stator that make the direction of motion difficult to control. Although ultrasonic actuators are more and more used in mechatronic systems, their electronics stay complicated because of the need for high voltage with high frequency power sources associated with a resonance tracking control algorithm.

1.8.3 Multi stator-ultrasonic technologies

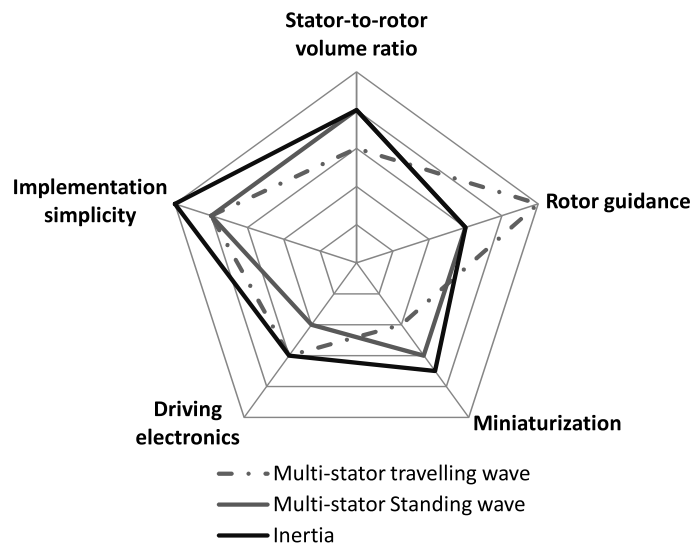


Figure 1.21: Qualitative comparison of multi-stator spherical systems regarding the proposed criteria.

Figure 1.21 shows a qualitative comparison of multi-stator spherical systems. The miniaturization of these systems is limited because of several mechanical parts that require to be assembled together. It limits their implementation to centimeter-sized systems. Multi-stator spherical motor are very versatile in terms of geometry since almost any single-degree of freedom ultrasonic actuator can be adapted to drive a spherical rotor in a multi-stator de-

sign. Therefore, their geometry can be adapted to obtain high stator-to-rotor ratio along with good guidance. The use of several ultrasonic traveling wave motors in parallel is interesting in terms of rotor guidance but the large size of these actuators limits their miniaturization and compactness. These actuators have an individual control over the rotation axes. Therefore, their implementation is easier than for single-stator ultrasonic spherical motors. Inertia motors use non-resonant driving technologies that are interesting since they do not require a resonance tracking system what simplify their implementation and driving electronics.

1.9 Target application of this work

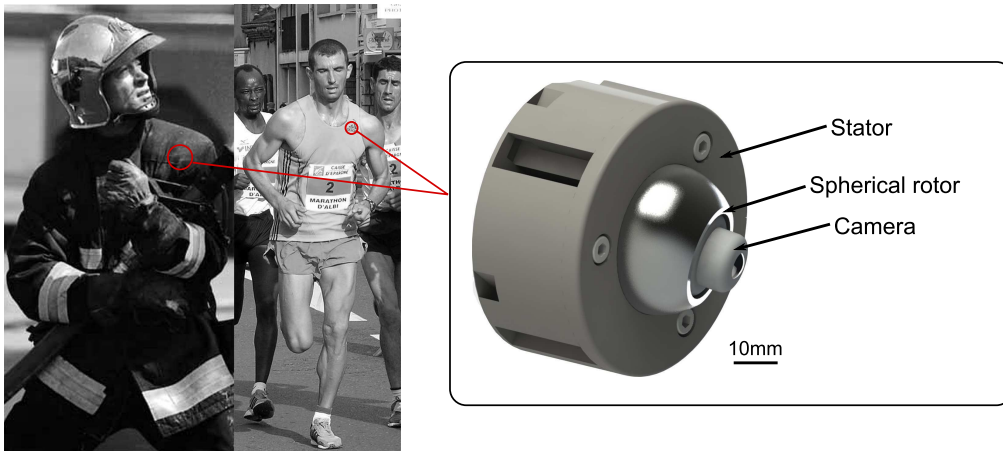


Figure 1.22: The target application of this work is a spherical motor adapted to the stabilization of a small camera placed on a person. The actuator should be small enough to fit on someone shoulder and have a sufficient dynamic response to provide stabilization in extreme situation such as on a running person.

In this chapter, numerous existing electromagnetic and friction-based prototypes are reported with various driving principles. From this review, important criteria for the design of multi-degree-of-freedom single rotor actuators have been proposed. Compromises have to be made between these criteria and it is important, before designing an actuator, to define the needs and application of the future motor.

In this thesis, the proposed application is the fast actuation of a partial sphere in order to achieve pan-tilt motion of an optical component such as a camera, a laser or a mirror. The system aims at being mounted on a person and should provide the dynamic performance and angular amplitude to be able to stabilize a camera in real time while the person is running or in extreme situation (figure 1.22). The system is expected to be placed on the shoulder in order to offer a large field of view while limiting intrusion for the user.

While running, the shoulder moves of about 40° at frequencies of 3.5 to 4 Hz (Smoliga [62], Cavagna et al. [63]). Based on these data and considering a spherical rotor with a diameter of 30mm, it is possible to estimate the required properties for the actuator. The estimation

is based on a typical response of the actuator which consists of a 40° movement at a 8Hz rate (125 ms period). 20% of the travel time is dedicated to acceleration and deceleration of the rotor while during the 80% remaining, the actuator is at constant maximum speed. From this characteristic, a maximum speed of $460^\circ/\text{s}$ and accelerations of $36000^\circ/\text{s}^2$ are required to actuate the spherical rotor. An inertia moment of $3000\text{g}\cdot\text{mm}^2$ is estimated from Solidworks, based on a partial sphere made of aluminum material. From classical dynamics, a torque of $2\text{mN}\cdot\text{m}$, required for proper rotor movement can be computed. Additional torque should be considered if the rotor is not balanced. A 15g mass off-centered of about 10mm generates a $1.5\text{mN}\cdot\text{m}$ torque due to gravity that should be taken into account.

Although these reflexions provide for only rough estimations of the required mechanical properties. They give a useful indicator to study computed and measured properties of the actuator. A $5\text{mN}\cdot\text{m}$ torque actuator will be considered enough for a stabilization application. The different systems that exist at the centimeter scale are friction-based actuators and particularly piezoelectric ultrasonic actuators. Several designs can be considered:

- Single-stator design have great potential in terms of miniaturization. However coupling between each axis limits their implementation simplicity. The use of a single stator limits also the geometries that can be considered.
- Multi-stator design and especially standing wave actuators allow for a high number of possible geometries, without problems of coupling between axis. It offers high compactness and is suitable to build centimeter-sized systems.
- Inertia motors are less complex to design than ultrasonic actuators but they are limited in terms of reachable speed and torque.

For the considered application, a multi-stator design will be used. It provides for a high versatility in actuator geometry along with a simple characterization of the actuator which is possible on a single degree-of-freedom motor assembly. The absence of coupling between the axes is also an advantage that simplifies motor implementation. Hoshina et al. [7] (Figure 1.16 on page 22) proposed a motor based on the association of multiple traveling wave actuators mounted in parallel while Shen and Huang [6] (Figure 1.15 on page 21) use standing wave actuators. Although the traveling wave design provide high rotor guidance, it is difficult to build a compact system with this approach. On the other hand, the standing wave prototypes are interesting since they offer great compactness and ability to be miniaturized. One limitation is the rotor guidance that requires additional mechanical parts and make the actuator difficult to integrate. A substantial improvement would be the design of a standing wave ultrasonic actuator that can provide good miniaturization and compactness while providing an excellent rotor guidance and easy integration.

Since ultrasonic actuators are friction-based actuators, they are subjected to wear and stresses. The common use of friction tips as contact transmission mechanism in current

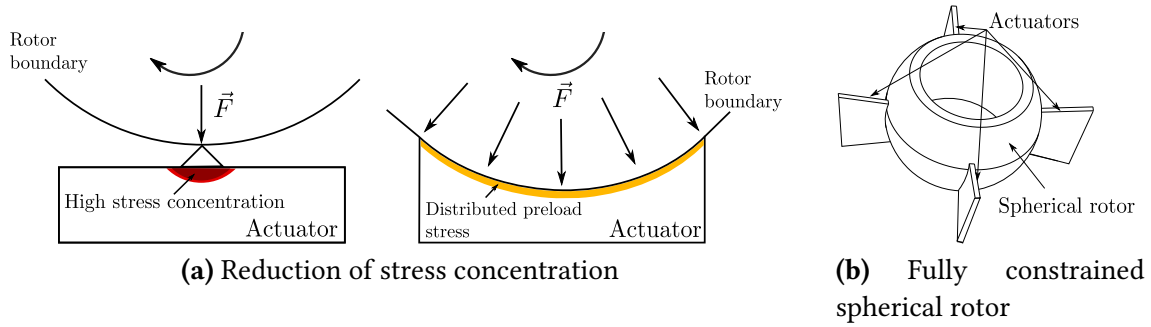


Figure 1.23: Expected improvements using an extended contact area for the ultrasonic actuator

standing wave linear actuators causes localized stresses around the friction head and therefore high wear of the contact layer for a given preloading force. An enlarged contact area could be interesting to obtain a better pressure distribution and reduced wear of the contact layer (figure 1.23a). In addition, this increased area could also be used to improve rotor guidance and to offer a completely constrained sphere similarly to the concept used for radial-bending actuators. A fully constrained rotor would be obtained by the association of three or more actuators as shown in figure 1.23b. A curved contact surface of the same radius as the rotor is proposed for our application. Two major working principles can be used to drive a rotor from standing waves:

- Single-mode asymmetric actuation: A single vibration mode of a structure is excited asymmetrically. This causes the formation of linear oblique motions at the interface that drive the rotor. Inversion of the asymmetry causes reverse motion of the rotor. (see figure 1.4e on page 10)
- Multi-mode actuation: two different modes of a structure are excited at the same frequency with a temporal phase shift in order to generate elliptical movements at the interface. A change in the phase shift causes reversed motion. (see figure 1.4c on page 10)

An extended contact surface for the actuator implies the interaction of multiple friction forces along the stator/rotor interface. Although these interactions can be constructive, some of the generated forces could also act against each other causing a diminution of the actuator efficiency. To our knowledge, only few literature has discussed the influence of the contact extent on standing wave ultrasonic actuators. Spanner and Koc [64] discussed briefly the use of an extended contact surface on an asymmetric single-mode actuator similar to those presented in figure 1.15. However, the use of a single vibration resulted in non-constructive movements that limited the performance. Lu et al. [65] developed a multi-mode actuator with several points of contact at the interface. Proper operation of the motor is reported

although no explicit comparison with a single foot motor is made. The use of a multi-mode actuation principle, although more difficult to design, presents an improved control over the motions produced at the interface that could be used to produce elliptical constructive motions. In this work, it is proposed to use a combination of two vibration modes as the working principle for the developed actuator.

1.10 Proposed design method

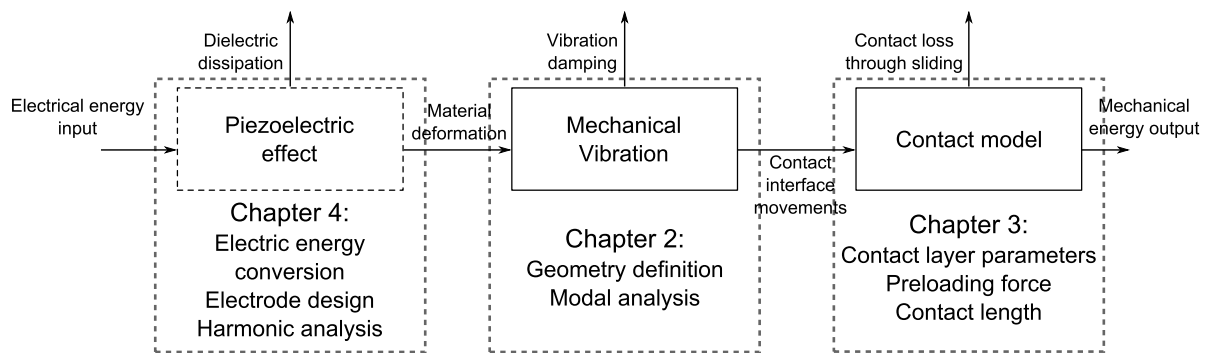


Figure 1.24: Overview of the two steps energy conversion in an ultrasonic motor. The electrical energy is injected into a piezoelectric material that causes the deformation of the material and vibration of the mechanical structure. These vibrations are transmitted to a rotor through friction so that finally useful mechanical energy is obtained. Chapter 2, 3 and 4 of this thesis describe a model for these conversion steps.

An ultrasonic motor is based on a two step energy conversion shown in figure 1.24:

- The first step is the conversion of electrical to mechanical energy in order to produce vibrations in the stator. This conversion step uses the piezoelectric effect that convert dielectric energy into material deformation. This repeated conversion leads to the generation of vibrations into the mechanical structure.
- The second step converts the vibratory energy stored in the stator into a displacement of the rotor. Repeated movements at the edge of the rotor cause a continuous movement of the rotor.

In the remaining of the work, a complete model of the ultrasonic motor is proposed. It is divided into three chapters:

- Chapter 2 proposes to design the mechanical structure. This step is essential to select the vibration modes and modes shapes necessary for the description of the first and second energy conversion steps. Theoretical vibratory concepts are presented along with the definition of the proposed actuator using finite element modal analysis.

- Chapter 3 describes the second conversion step. A contact model is proposed and applied to the developed actuator. Different contact parameters are analyzed.
- Chapter 4 focuses on the first conversion step. Theoretical concepts of piezoelectric devices are presented and applied to the case of our actuator. The effect of the excitation electrodes is specifically studied. This chapter, combined with chapters 2 and 3 allows to provide for a complete model of the ultrasonic motor.

Finally the chapter 5 presents an ultrasonic motor prototype based on the target application. Influence of multiple parameters is verified experimentally. The presented method, although specifically applied to our application, is general and could be used for the design of other ultrasonic actuators.

1.11 Conclusion

In this chapter the different approaches for multidegree-of-freedom ultrasonic motors are proposed. The review focuses on motors based on spherical rotors. They have a high potential for compact, low inertia multi-degree-of-freedom (MDOF) actuators. Several criteria for the evaluation of spherical motors are proposed. Ultrasonic friction-driven technologies are well adapted to the realization of miniature actuation systems. They are based on few mechanical parts and offer self-guidance to the rotor. Numerous prototypes are presented. Their design can either be based on a single-stator or several stators. The first approach is easily miniaturized. However, coupling between the driving vibrations might lead to parasitic motion of the desired rotation direction. The use of several stators placed in parallel does not suffer from such disturbances. However, their miniaturization is limited due to a higher number of mechanical parts.

The target application of this work is then presented. The objective is to design an ultrasonic spherical actuator that can be used for the stabilization of a micro-camera in extreme conditions. The proposed concept is based on multiple actuators placed in parallel. Their contact area fit the spherical rotor outer surface so that a complete guidance of the rotor is possible. Finally, the design methodology developed in the next chapters is presented.

Modal Analysis: Design of the resonant mechanical structure

2

Contents

2.1	Introduction	36
2.2	Vibrations theory	36
2.2.1	Mass-spring resonator	36
2.2.2	Vibration modes	40
2.2.3	Finite-element method	41
2.3	Modal analysis	44
2.3.1	Generic geometry	44
2.3.2	Finite element model	44
2.3.3	Tracking modes through geometric variations	45
2.3.4	Modes selection	48
2.3.5	Mode symmetry	51
2.3.6	Mode degeneration	52
2.3.7	Angle between movements at contact surface	52
2.3.8	Geometric variations	55
2.3.9	Geometry selection	59
2.4	Modal sensitivity	59
2.4.1	Geometric tolerances	60
2.4.2	Soldering points	61
2.4.3	Influence of contact layer	64
2.4.4	Experimental result of vibration modes tuning	64
2.5	Conclusion	66

2.1 Introduction

This chapter presents the first step of the proposed methodology for ultrasonic motor design. It is organized in three main sections:

- The first section introduces basics about vibration theory. The objective is to provide for vibrations concepts that are useful to improve the properties of ultrasonic motors. It focuses specifically on the use of standing waves and the amplification phenomenon caused by resonance in solids.
- The second section details modal finite element analysis of the actuator. A generic parametric geometry is proposed. Modes useful for actuation are presented and a specific mode combination is chosen based on several criteria. The geometric variations are analyzed and a final geometry of the actuator, adapted to the target application, is proposed.
- The last section proposes a modal sensitivity analysis. Modal analysis is useful to evaluate the effect of disturbances on the vibration modes. Although it does not have a direct theoretical interest, it is useful to predict the influence of geometric tolerances or soldering points on mode frequencies, therefore providing interesting results for experimentation.

2.2 Vibrations theory

Piezoelectric motors use vibration of solids in order to transmit forces to a rotor. Therefore, for their design, it is important to understand how mechanics of vibration and numerical methods can be used to predict vibratory characteristics of a structure. In this section, an overview of vibration theory is presented. First, resonance and natural frequency concepts are presented with the mathematical study of a single-degree-of-freedom system, then the vibration theory is extended to the notion of vibration modes. Finally, the finite element method and its application to the computation of natural frequencies is discussed.

2.2.1 Mass-spring resonator

Natural frequency

One of the most basic systems studied in vibrations is the mass-spring-damper system (see figure 2.1), it allows to understand analytically the basic concepts of vibrations. From the system in figure 2.1, the equation of motion can be written:

$$m\ddot{x} = F - kx - c\dot{x} \quad (2.1)$$

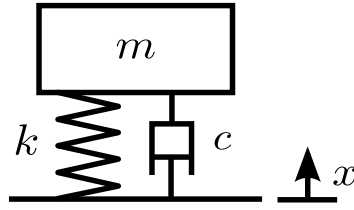


Figure 2.1: Mass-spring-damper mechanical model. The study of this system allows understanding the natural frequency and resonance concepts.

$$\ddot{x} + \frac{c}{m}\dot{x} + \frac{k}{m}x = \frac{F}{m} \quad (2.2)$$

k is the stiffness of the spring, m the mass and c the damping coefficient. This equation is a second order differential equation that have a solution $x(t) = x_h(t) + x_p(t)$. x_h is the solution to the homogenous equation ($F = 0$) and x_p a particular solution of the complete equation. The homogenous equation can be solved using the characteristic polynomial:

$$x_h(t) = Ae^{r_1 t} + Be^{r_2 t} \quad (2.3)$$

$$x_h(t) = e^{-\frac{c}{2m}t} [A' \sin(\omega_d t) + B' \cos(\omega_d t)] \quad (2.4)$$

with

$$\omega_d = \frac{\sqrt{4km - c^2}}{2m} \quad (2.5)$$

ω_d is defined as the *ringing* vibration of the system, it is the angular frequency at which the system vibrates when it is free of any external force. For an undamped system, a natural frequency $\omega_0 = \sqrt{\frac{k}{m}}$ is defined and can be related to the damped frequency:

$$\omega_d = \omega_0 \sqrt{1 - \frac{c^2}{4km}} \quad (2.6)$$

Harmonic forced excitation and resonance

If we suppose that the force F is an harmonic excitation of frequency Ω_F :

$$F = F_0 e^{j\Omega_F t} \quad (2.7)$$

The particular solution can be computed as:

$$x_p(t) = C e^{j\Omega_F t} \quad (2.8)$$

And the complete solution is written as:

$$x(t) = e^{-\frac{c}{2m}t} [A' \sin(\omega_d t) + B' \cos(\omega_d t)] + C e^{j\Omega_F t} \quad (2.9)$$

The first term represents a transient movement that does not have influence after a certain amount of time because of the exponential $e^{-\frac{c}{2m}t}$ that tends to 0 when $t \rightarrow \infty$. The steady state of the system is thus given by the particular solution x_p which can be derived and replaced into the main equation (2.2):

$$-\Omega_F^2 C e^{j\Omega_F t} + j \frac{c}{m} C \Omega_F e^{j\Omega_F t} + \frac{k}{m} C e^{j\Omega_F t} = F_0 e^{j\Omega_F t} \quad (2.10)$$

The amplitude C is obtained as:

$$C = \frac{F_0}{-\Omega_F^2 + \frac{k}{m} + j \frac{c}{m} \Omega_F} = \frac{F_0(-\Omega_F^2 + \frac{k}{m} - j \frac{c}{m} \Omega_F)}{(-\Omega_F^2 + \frac{k}{m})^2 + (\frac{c}{m} \Omega_F)^2} \quad (2.11)$$

And its module:

$$|C| = F_0 \left[\frac{1}{(-\Omega_F^2 + \frac{k}{m})^2 + (\frac{c}{m} \Omega_F)^2} \right] \quad (2.12)$$

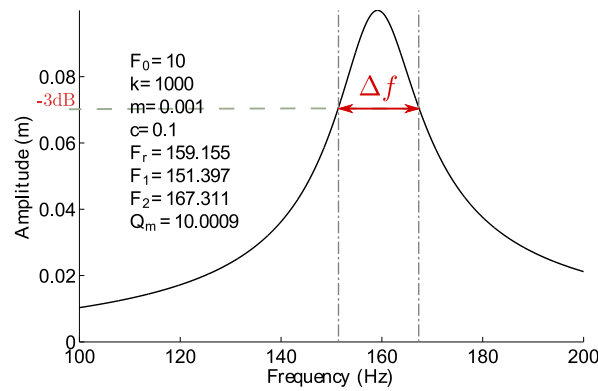


Figure 2.2: Forced response of a mass-spring-damper system. When the excitation force has a frequency close to the resonance frequency of the system, an amplification of the displacement occurs.

The module of the displacement is shown in figure 2.2 as a function of the pulsation Ω_F of the applied force. When the denominator of equation (2.12) is minimum, the module of amplitude C shows a maximum. It is reached when the pulsation is:

$$\Omega_1^2 = \frac{k}{m} - \frac{c^2}{2m^2} = \frac{2km - c^2}{2m^2} = \omega_0^2 - \frac{c^2}{2m^2} \quad (2.13)$$

This frequency is called the resonance frequency, it is defined as the frequency where the displacement amplitude of the system is maximum. It is also possible to solve for the frequency where the velocity is maximum:

$$\Omega_0^2 = \frac{k}{m} = \omega_0^2 \quad (2.14)$$

And where the acceleration is maximum:

$$\Omega_2^2 = \frac{2k^2}{2km - c^2} \quad (2.15)$$

It can be noted that when the damping coefficient c becomes zero, the three frequencies are the same and equals to $\Omega_0 = \frac{k}{m}$. This frequency is the natural frequency of an undamped system. In dynamics, resonance frequencies are usually computed in order to be avoided because the amplification effect is in dangerous. In piezoelectric motors, this effect is interesting because the displacements are low and it can be used to improve the amplitude of the stator without need for a high voltage power source. Around the resonance, it is practical to compute a quality factor in order to characterize the damping of the resonance. This quality factor Q_m is defined as the ratio of stored energy at resonance and energy dissipated per cycle.

$$Q_m = 2\pi \frac{\text{Energy stored}}{\text{Energy dissipated per cycle}} \quad (2.16)$$

Considering the energy stored in the spring:

$$E_{\text{stored}} = \frac{1}{2}k|C|^2 \quad (2.17)$$

And the energy dissipated in one cycle (which corresponds to the work of the force produced by the damper):

$$E_{\text{dissipated}} = \int -c\dot{x}dx \quad (2.18)$$

$$E_{\text{dissipated}} = \int_0^{2\pi/\Omega_c} -c\dot{x} \times \dot{x}dt \quad (2.19)$$

$$E_{\text{dissipated}} = \pi c\Omega_c C^2 \quad (2.20)$$

Q_m is then defined as:

$$Q_m = \frac{\sqrt{km}}{c} \quad (2.21)$$

When the damping is low, Q_m can be computed from the width of the peak at half power or at $\frac{\max(|C|)}{\sqrt{2}}$ when amplitude is considered (-3dB). An example of such calculation is shown in figure 2.2. Q_m is obtained from the equation:

$$Q_m = \frac{f_r}{\Delta f} \quad (2.22)$$

Where f_r is the resonance frequency and Δf the width at -3dB. In figure 2.2, an analytical quality factor of 10 is found. It is close to the peak width method (10.0009). Q_m is one of the essential parameter to qualify the damping of a resonance.

2.2.2 Vibration modes

When considering real structures, the atoms assembly can be considered as a set of mass-spring-damper systems. This result in an important number of possible resonant motions that are called vibration modes. Vibrations modes are defined as a combination of a specific shape of deformation associated with a resonance frequency of a solid. Exciting the specific mode at its frequency results in the movement amplification described in the previous section.

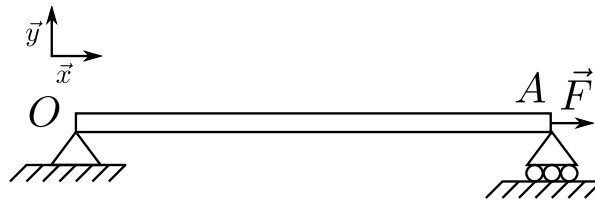


Figure 2.3: Simply-supported beam.

The longitudinal modes of a beam are one classical example of vibration mode calculation. Using linear mechanics, it is possible to find the vibration modes of a beam in the direction of an applied force. Considering a simply-supported beam (figure 2.3) with a length l , Young modulus E_y , density ρ and section S . It can be shown that there exists an infinity of resonant frequencies given by:

$$u(x, t) = A \sin(\omega t) \sin(\beta x) \quad (2.23)$$

$$\omega = \sqrt{\frac{E_y}{\rho}} \left(\frac{2n\pi}{l} \right) \quad (2.24)$$

$$\beta = \frac{2n\pi}{l} \quad (2.25)$$

u is the displacement amplitude as a function of time and position along the beam. β corresponds to the wave number which is inversely proportional to the wavelength λ of the vibration mode and ω is the natural frequency of the mode. A is the amplitude of the displacement and cannot be determined by a simple modal analysis since it depends on the excitation force. By analogy to the spring-mass-damper system, it can be noted that the frequency increases linearly with respect to $\sqrt{\frac{E_{young}}{\rho}}$ which is similar to $\sqrt{\frac{k}{m}}$ in equation (2.5). In general, the stiffer and lighter the structure is, the higher its resonance modes are. Another typical characteristic that can be noted is the effect of the length l . The larger the

structure is, the lower its mode frequencies are. This criterion is not always verified. For example, when considering bending vibrations of a beam, an increase in the height of the beam increases its stiffness and mode frequencies. The parameter n is called the mode order, it corresponds to the n^{th} solution of the differential equation. The larger n is, the higher the mode frequency is. n has a role in the mode shape, as it increases, the wave-number β increases and the wavelength decreases. This means that when n increases, there are more nodes (point with zero displacement) on the vibrating beam. Different vibration modes (bending, torsional...) can be analytically computed. But analytical models are limited when the geometry is complex and a finite element model becomes more appropriate for the modal analysis of the structure.

2.2.3 Finite-element method

The finite element method consists in a discretization of a geometry in order to numerically approach solutions of partial differential equations that are impossible to solve analytically. A given geometry is divided into a finite number of points at which specific properties are defined. Between these points, interpolation functions (in general polynomial) are considered and used to evaluate the physical interaction between the elements. The method results in a set of several vectors and matrices defining the physical values at each node and the interactions between neighboring nodes. Although not exact, the method has the advantage to be able to model almost any geometry with the inclusion of different materials and physical problems. In particular, it is appropriate to obtain eigenfrequencies (mode frequencies) and modal shapes of structures made of piezoelectric materials which are both orthotropic and coupled physics materials (for more detail on piezoelectric material properties refer to appendix A).

Modal analysis

In mechanical analyzes and more specifically in dynamics, two majors matrices are defined:

- The mass matrix $[M]$ is analogous to the density ρ , it models the mass of the material at the considered finite element.
- The stiffness matrix $[K]$ is analogous to the Young's modulus E_y . It can be defined in three dimensions and used to compute 3D vibration modes.

An eigenvalue problem allows to solve for the vibration modes of the structure and is defined as:

$$([K] - \omega^2[M]) \underline{X} = 0 \quad (2.26)$$

This expression is similar to equation (2.2). \underline{X} is a set of eigenvectors that represents mode shapes. Software such as COMSOL, ANSYS or ABAQUS are used to divide the geometry into elements (meshing), assemble the stiffness and mass matrices and solve the linear system for ω (eigenvalues) and \underline{X} (eigenvectors). It is usually possible to visualize different physical values through a post-processing unit and, in particular, the mode shapes. Solving the eigenvalue problem does not give information about the amplitude of the displacement. The eigenvectors are representations of the distribution of a physical value subjected to an excitation at a mode frequency. They can be used for relative amplitude comparison at different points of the mode shape but modal analysis does not allow to compare amplitudes of different mode shapes since the actual displacements depend on the location and magnitude of the excitation.

Damping modeling

In finite element analysis, damping is introduced using a damping matrix, so that the problem becomes:

$$([K] + j\omega[C] - \omega^2[M]) \underline{X} = 0 \quad (2.27)$$

There are several means to define the C modal damping matrix. The matrix can be defined using damping data obtained experimentally for each mode, $[C]$ is then a diagonal matrix. This technique is viable for a simple system with a low number of degree-of-freedom but is not usable for systems consisting of several hundreds DOF. One common simpler way to define the damping matrix is to use a linear combination of the mass and stiffness matrix:

$$[C] = \alpha[M] + \beta[K] \quad (2.28)$$

This definition is called Rayleigh damping. It requires experimental data from at least two modes to be defined. Modal proportional damping results in a speed dependent damping which leads to a quadratic equation of ω . The definition of $[C]$ as a function of $[M]$ and $[K]$ allows for a simplification of the problem that groups damping and stiffness matrices together. Another model that is often used is structural damping. It is a displacement dependent damping consisting in modifying the stiffness of the material in order to introduce complex terms. In the case of an isotropic material, the Young's modulus becomes:

$$E_y = E'_y + jE''_y = E'_y(1 + j \tan(\delta_m)) \quad (2.29)$$

The complex modulus is a standard used in highly damped materials such as polymers. δ_m is called the mechanical loss angle. This definition introduces a complex stiffness matrix but equation (2.26) stays a linear equation of ω . This last damping model is used in this work. It has the advantage to be easily defined and is similar to the dielectric losses modeling that

are defined by an electrical loss angle δ_e . Although this parameter is defined in the simulation, as discussed earlier, a more convenient parameter to quantify damping in a resonant mechanical structure is the quality factor Q_m . It can easily be obtained from finite element analysis using complex eigenfrequencies.

Complex eigenfrequencies

The resulting eigenvalues of the damped equation are complex frequencies (Li and Liang [66]):

$$\tilde{\omega} = \omega_0(1 + j\xi) \quad (2.30)$$

Where ξ represents the losses at the resonance. The strain at a point in the material can then be expressed as:

$$\vec{S} = \vec{S}_0 e^{-\xi\omega_0 t} e^{j\omega_0 t} \quad (2.31)$$

Thus, the energy in the resonant system decays as a function of time following the equation:

$$W = W_0 e^{-2\xi\omega_0 t} \quad (2.32)$$

The power loss, which is the derivative of the energy with respect to time is defined as:

$$P_L = -\frac{dW}{dt} = 2\xi\omega_0 W \quad (2.33)$$

The quality factor is defined as the ratio of stored to dissipated energy:

$$\begin{aligned} Q_m &= 2\pi \frac{\text{Energy stored}}{\text{Energy dissipated per cycle}} \\ Q_m &= 2\pi \frac{\text{Energy stored}}{\text{Power loss} \times 1/f_r} \\ Q_m &= \omega_0 \frac{W}{2\xi\omega_0 W} \\ Q_m &= \frac{1}{2\xi} \end{aligned} \quad (2.34)$$

Combining equation (2.30) and (2.34), the quality factor in finite element analysis is obtained from the complex resonance frequency:

$$Q_m = \frac{\text{real}(\tilde{\omega})}{2 \times \text{imag}(\tilde{\omega})} \quad (2.35)$$

2.3 Modal analysis

In this section, the proposed actuator concept is studied using finite element analysis. The objective is to understand how the geometric parameters of the structure may affect the ultrasonic motor properties. Since the actuator is based on the use of two vibration modes, modal analysis is used to study the effect of the geometry on these modes and select the proper modes for actuation.

2.3.1 Generic geometry

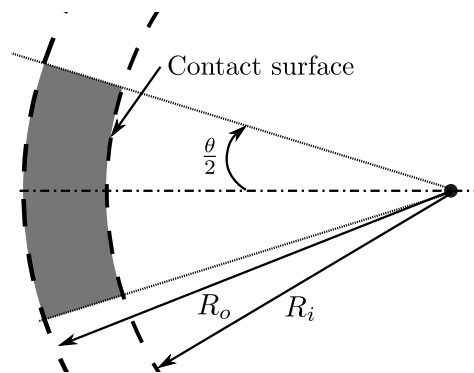


Figure 2.4: Generic geometry proposed for the design of the actuator. R_i is the inner radius, adapted to the rotor. R_o the outer radius and θ the portion angle of the actuator.

A large number of geometric parameters can be considered in the design of the actuator. In order to reduce the number of parameters that define the geometry, a generic geometry is proposed. It allows to consider a majority of cases. This geometry is based on a portion of a ring whose inner and outer radii can be varied independently. Three geometric variables define the geometry: the inner radius R_i , the outer radius R_o and the portion angle θ (figure 2.4). The radius R_i corresponds to the contact area and is adapted to the radius of the rotor. This arbitrary geometric restriction allows to study a large panel of different geometries with different mode shapes while providing a limited number of parameters. The resonant structure is entirely made of a piezoelectric material in order to reduce the number of mechanical parts required to build the spherical motor.

2.3.2 Finite element model

Once the geometry of the actuator is defined, modal analysis is necessary to find suitable modes for ultrasonic actuation. The structure proposed, although simple, does not have a simple modal analytical solution. The shape, the orthotropic material that is used and coupled physics result in a complex analytical modeling. For complicated cases, a finite element model is well adapted to describe the vibratory behavior of the mechanical structure. The

TABLE 2.1: PZ26 MATERIAL PROPERTIES. ALL UNITS ARE SI. (REPORT TO APPENDIX A.4 FOR MORE INFORMATION ON SYMBOLS DEFINITION)

Name	PZ26	c_{11}^E	1.68E+11	e_{31}	-2.80
Type	Hard	c_{12}^E	1.10E+11	e_{33}	14.7
ρ	7.70E+03	c_{13}^E	9.99E+10	e_{15}	9.86
$\varepsilon_{r,1}^S$	8.28E+02	c_{33}^E	1.23E+11	$Q_{m,p}^E$	2.7E+03
$\varepsilon_{r,3}^S$	7.00E+02	$c_{44}^E = c_{55}^E$	3.01E+10	$Q_{m,t}^E$	3.3E+03
$\tan \delta_e$	0.003	c_{66}^E	2.88E+10	$T_c >$	330°C

model proposed is based on the piezoelectric device module from the commercial software COMSOL Multiphysics¹. A parametric model is used for modal analysis and implemented using the Java application programming interface (API).

In the model, mechanical boundary conditions are left free everywhere since the actuator is intended to vibrate with minimal support points. The material used in simulations is Ferroperm Pz26 PZT with a thickness of 0.5mm and poled in the out-of-plane direction of the plate. Table 2.1 describes the properties of the ceramic. An explanation of the symbols along with the reasons for this material selection are further described in appendix A.

Modal analyzes are performed in three dimensions, allowing the study of out-of-plane modes and the control of the transverse electric field which is useful for harmonic analyzes presented in chapter 4. The electrodes are not modeled since they are considered of negligible thickness (10 μ m silver as compared to 500 μ m of ceramic). The electric field is directly applied to the ceramic. A zero E_3 field is applied to the piezoelectric element ensuring a constant electric field condition. The modal analysis computes two results:

- Mode frequencies that correspond to resonance frequencies. Complex modes frequencies give an additional information about the damping of the mode vibration.
- Mode shapes that are the expected deformations, strain, stresses and more generally any physical characteristic in the actuator subjected to an harmonic excitation at a modal frequency. These results are not absolute, and give only information about the relative distribution (shape) of the considered characteristic.

2.3.3 Tracking modes through geometric variations

Finite element analysis software does not classify modes as a function of their shapes but as function of their frequencies. A method is required to automatically track the modes and observe differences between geometries. The method used here is called *modal assurance criterion* (MAC). The MAC method compares the mode shapes to reference mode shapes

¹<http://www.comsol.fr/>

ϕ^{ref} that are selected manually. The MAC computes how close a mode is from the reference mode using the following equation (Allemang [67]):

$$MAC = \frac{|\phi_c^T \phi_{ref}^*|^2}{(\phi_c^T \phi_c^*) (\phi_{ref}^T \phi_{ref}^*)}$$

ϕ_c is the computed mode and ϕ_{ref} is the reference mode. MAC indicates a number between 0 and 1, the closer it is to 1, the more similar the mode is to the reference mode shape. Using MAC in order to track the modes in spite of the geometric variations supposes to select and classify manually the modes of a reference geometry. Then, when geometry is changed, the computed modes can be compared to the reference modal shapes. The mode with the highest MAC value is identified.

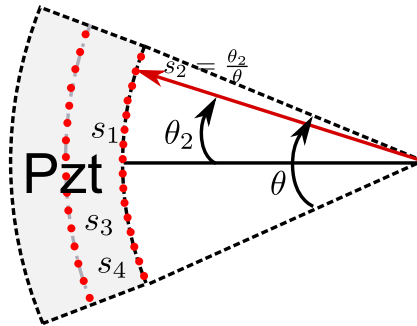


Figure 2.5: Set of points used for the application of the Modal Accordance Criterion (MAC). It is assumed that the modal deformation does not have important variations from one geometry to another if it is defined as a function of $s_i = \frac{\theta_i}{\theta}$.

Practically, the method is based on a discrete set of points that are representative of the studied modes. The set of points that is used for MAC computation is essential for accurate mode discrimination (and recognition). It should not be affected by a change in R_i , R_o or θ . The proposed solution is to use a discrete set of points (θ_i, \vec{u}) of the deformation along the edge of the actuator and at the neutral axis of the actuator $\frac{R_i+R_o}{2}$. Because the portion angle θ is changing, the selected points are defined by relative coordinates $s_i = \frac{\theta_i}{\theta}$ (figure 2.5) so that:

$$MAC = \frac{(\sum_{i=0}^n \vec{u}_c(s_i) \cdot \vec{u}_{ref}(s_i))^2}{(\sum_{i=0}^n \vec{u}_c(s_i) \cdot \vec{u}_c(s_i)) \cdot (\sum_{i=0}^n \vec{u}_{ref}(s_i) \cdot \vec{u}_{ref}(s_i))}$$

where $\vec{u}_c(s_i)$ and $\vec{u}_{ref}(s_i)$ are the compared and reference displacement vectors at the point of coordinate s_i . The set of points is validated using an evaluation criterion called autoMAC. It consists in taking a set of reference modes consistent with the future application of the modal accordance criterion and apply the MAC test between every mode of this series.

The proposed set of points is evaluated using the nine modes presented in figure 2.6. MAC results are represented as a matrix in figure 2.6a, abscissa axis lists the reference modes indexes while compared modes indexes are on the ordinate axis. In the case of autoMAC,

1	1.00	0.04	0.17	0.05	0.00	0.07	0.00	0.00	0.01
2	0.04	1.00	0.14	0.07	0.16	0.02	0.08	0.11	0.04
3	0.17	0.14	1.00	0.21	0.00	0.04	0.01	0.00	0.03
4	0.05	0.07	0.21	1.00	0.00	0.15	0.01	0.00	0.25
5	0.00	0.16	0.00	0.00	1.00	0.00	0.10	0.74	0.10
6	0.07	0.02	0.04	0.15	0.00	1.00	0.01	0.00	0.05
7	0.00	0.08	0.01	0.01	0.10	0.01	1.00	0.07	0.05
8	0.00	0.11	0.00	0.00	0.74	0.00	0.07	1.00	0.10
9	0.01	0.04	0.03	0.25	0.10	0.05	0.05	0.10	1.00
	1	2	3	4	5	6	7	8	9

Reference modes

(a) AutoMAC matrix. This table represents the computation of MAC values using the same set of modes for reference and compared modes. The diagonal of the matrix is one and corresponds to a perfect match between the two compared modes which are the same. Outside the diagonal, an important MAC value implies high computed similarity between two different modes that may affect the mode recognition process.

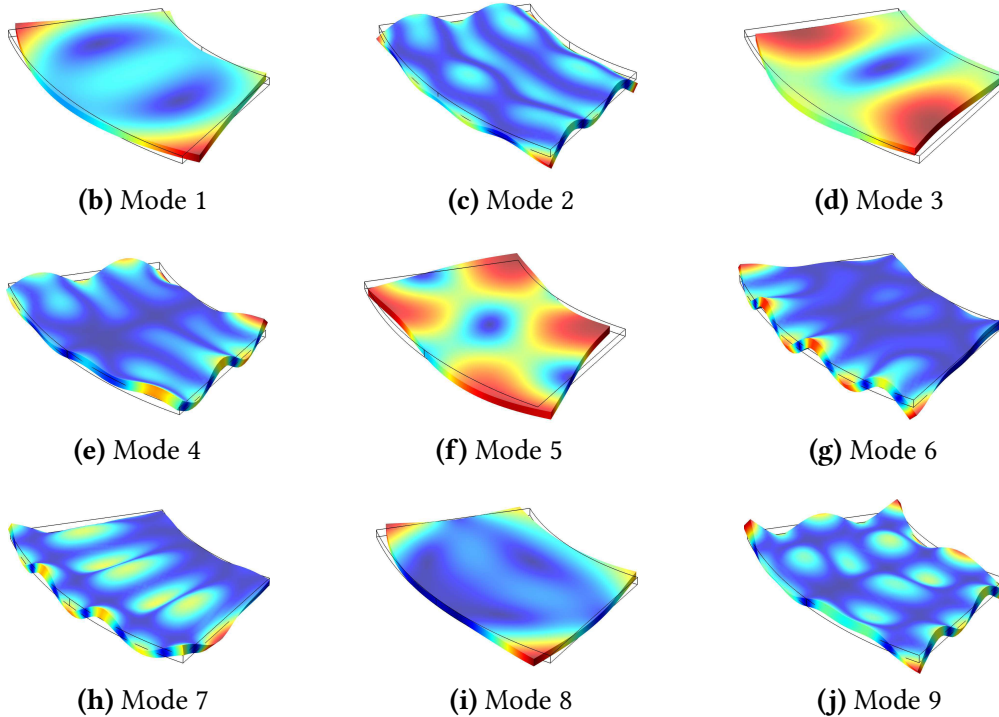


Figure 2.6: AutoMAC for a set of nine representative modes of a typical actuator geometry. MAC computation is performed using 30 points selected as described in figure 2.5. AutoMAC allows to determine the ability of the method to discriminate modes one from each other.

the two sets are the same. It can be observed that on the diagonal, MAC values are one, what correspond to a perfect match between the modes. It is an expected result since the compared modes and reference modes are exactly the same on the diagonal. Outside the diagonal, the matrix is symmetric because a switch between the compared and the reference mode does not affect the MAC result. If the points are well chosen, MAC values outside of the diagonal should be low since they correspond to the comparison of modes that are not the same. A high MAC value outside the diagonal can result in the confusion of two modes especially when geometry is changed. In the shown matrix, a majority of values are almost zero. Only one of them has a value of 0.74 which is the equivalent of a 74% mode similarity based on the MAC computation. These modes, labeled 5 and 8, may be confused if the change in geometry is too important between two simulations. Indeed, a high geometric change between the reference and the computed simulations would cause the computed modes shapes to be largely different from the reference mode shapes. Practically, the mode recognition process begins to show difficulties with autoMAC values above 0.9 outside the diagonal.

In order to avoid mode recognition failures, the geometric changes that are considered in the modal study are small (for example, a change in the parameter θ is not above 5°). High geometric variations are observed using a continuity principle. The reference modes are updated with the newly identified modes at each new geometry change, keeping the geometry changes at a low level. The advantage of this principle is illustrated in figure 2.7. MAC value is represented as a function of portion angle θ . Without continuity, the reference mode is always the same (i.e. the one identified manually at a 25° portion angle). Up to a 40° portion angle, MAC values are near one and the computed mode is very similar to the reference mode. Past this point, MAC starts to decrease what may cause failure of mode recognition. With mode continuity, the reference mode is updated at each step with the newly identified mode. Therefore, changes in mode shapes are kept at a reasonable level with MAC values that are not below 0.99.

2.3.4 Modes selection

Two different modes have to be chosen for a proper multi-mode ultrasonic actuation. Two major families of modes can be considered for a plate-like geometry:

- Out-of-plane modes are used in traveling wave ultrasonic motors. They cause a displacement perpendicular to the electrodes. The mode shape shown in figure 2.6c is a typical out-of-plane mode.
- In-plane modes (or contour modes) result in a displacement along the lateral edges of the actuator. Since the actuator is generally longer and larger than thick, these modes

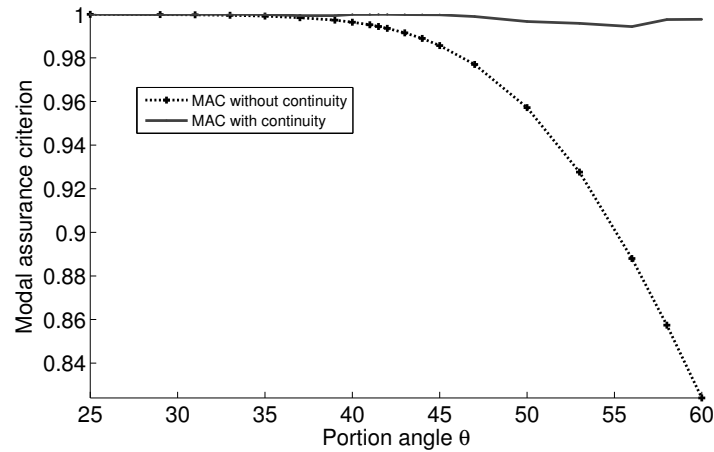


Figure 2.7: MAC of a specific mode as a function of the variation of the portion angle θ with or without continuity. The use of a continuity principle allows to observe large geometric variations without failure of the mode recognition procedure.

generate a larger total displacement at the contact area. Figure 2.6b shows an in-plane mode of a typical actuator geometry.

Given the proposed geometry, in-plane modes are more suitable. Considering an actuator geometry with an inner radius of 15 mm and an outer radius of 25 mm, it is possible to compute which modes are the most interesting for the design of an ultrasonic actuator. To avoid complex excitation and high resonance frequencies, high order modes are not considered. Indeed, as mode order gets high, resonance frequency increases and the mode excitation becomes complex because of a large number of individual areas with different type of strain (compressive and extensive) that implies the need for a high number of electrodes. In this work, only the first four in-plane modes of the structure are studied.

A classification similar to the one used for rectangular plates (Krushynska et al. [68]) is proposed to identify the in-plane modes of the structure. For rectangular plates, the modes are classified with respect to the two axis of symmetry of the rectangle. In our case, the geometry has only one axis of symmetry. A second axis is defined for classification. It is the neutral axis of the ring and corresponds to an arc of a circle of radius $\frac{R_o+R_i}{2}$. It is not possible to consider the displacement as strictly symmetric with respect to this axis since it is not a symmetry axis. Instead of this, the modes are classified as a function of the type of strain (compressive or extensive) on each side of the axis. If the strain type is the same, a “symmetric” strain type condition is considered and noted S, otherwise, an “antisymmetric” strain type condition noted A is considered. A number n is used to define mode order. For example, the mode shown in figure 2.8a is the first symmetric mode about axis 1 (the symmetry axis of the actuator) and anti-symmetric about axis 2 (the neutral curved axis proposed), it is noted SA_1 .

The four first order in-plane modes are shown in figure 2.8:

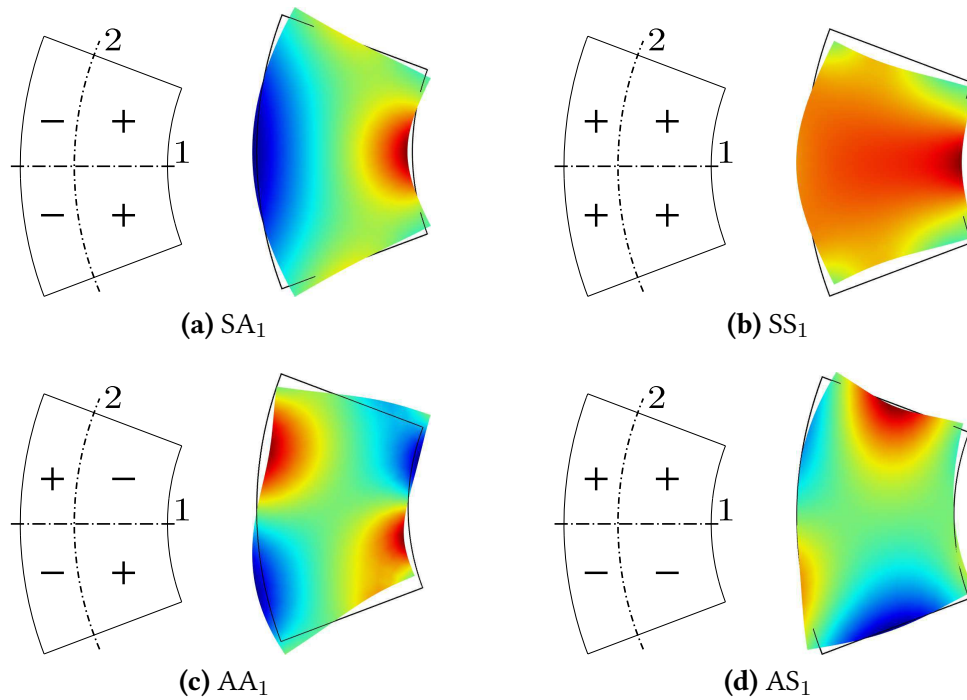


Figure 2.8: First order in-plane modes found for a typical actuator geometry. They are classified as a function of their strain type symmetry properties with respect to the axis 1 and 2. SA_1 for example is the first symmetric mode about axis 1 and antisymmetric about axis 2. Colors represent the S_3 (out-of-plane) strain of the considered modes. Blue areas correspond to negative out-of-plane strain and red areas to positive strain. A simplified schematic is proposed for better understanding of the symmetry properties.

- The first symmetric-antisymmetric mode SA_1 is similar to a first bending mode along the symmetry axis of the actuator (figure 2.8a).
- The first symmetric-symmetric mode SS_1 is a dilatation type mode, similar to a longitudinal mode of a beam (figure 2.8b).
- The first antisymmetric-antisymmetric mode AA_1 is similar to a diagonal mode of a plate or a second bending mode of a beam (figure 2.8c).
- The first antisymmetric-symmetric mode AS_1 is similar to a bending mode along the curved neutral axis of the actuator (figure 2.8d).

Several criteria are proposed to evaluate which mode combination is the most adapted to the development of an ultrasonic actuator:

- Mode symmetry: the symmetry of the movements at the contact surface of the actuator is an important criterion. A combination of two modes with the same symmetry at the contact interface causes non-constructive interferences.

- Mode frequency: the two modes considered for actuation should have the same resonance frequency for simultaneous resonant excitation.
- Mode displacement orthogonality: The two modes generate two independent motions at the interface with the rotor. The directions of their trajectories should be close to 90° to efficiently drive the rotor.

2.3.5 Mode symmetry

The objective for the proposed actuator is to use the largest contact surface of the actuator as possible. Therefore, elliptical motions that occur at the interface of the actuator should generate constructive motions and a tangential friction force in the same direction. This condition implies that the two modes that are used should *not* have the same type of symmetry about axis 1 (figure 2.9a) in their displacement at the contact edge of the actuator. As indicated in figure 2.9, when two modes with the same symmetry are excited with a $\frac{\pi}{2}$ temporal phase shift, the direction of elliptic paths is opposed on either side of the actuator. Therefore, the two movements cancel each other. On the other hand, the use of two modes with a different type of symmetry shows elliptic paths that are in the same direction and are constructive. Considering the modes proposed earlier, SA_1 and SS_1 are symmetric modes while AS_1 and AA_1 are antisymmetric modes in their movement along the contact edge of the actuator. The four possible combinations are therefore: SA_1+AA_1 , SA_1+AS_1 , SS_1+AS_1 , SS_1+AA_1 .

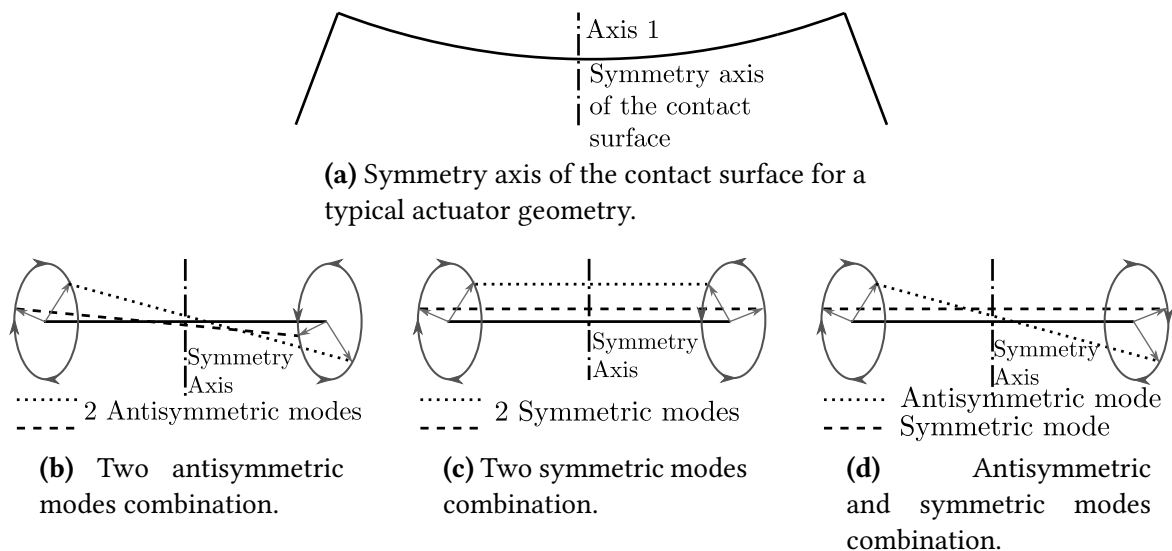


Figure 2.9: Differences in elliptic paths as a function of modes combination symmetry. The combination of modes with the same type of symmetry results in the creation of elliptical shapes with opposite driving direction.

2.3.6 Mode degeneration

In order to achieve the desired movement at the interface with the rotor and use the amplification effect of resonance, the resonance frequencies of the two modes should be the same. The four in-plane modes are tracked through changes in portion angle θ using modal accordance criteria. The objective is to observe if the modes can be found at the same frequencies.

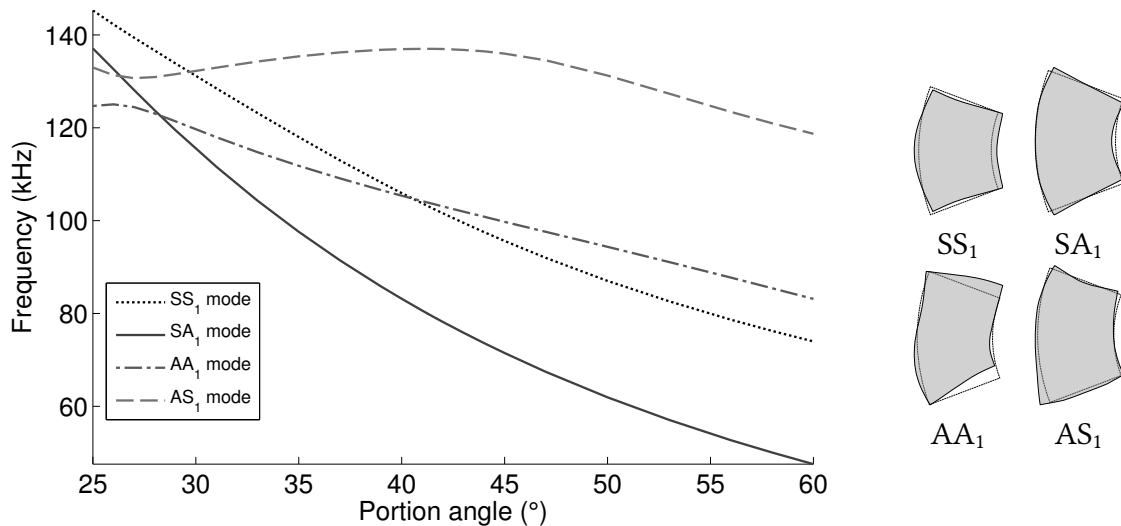


Figure 2.10: Evolution of the frequency of the modes as a function of the portion angle θ . Intersections show that some modes can be found at the same resonant frequency.

Figure 2.10 shows the evolution of mode frequencies of the four first order in-plane modes for an actuator of 15mm inner radius and 25mm outer radius. Four intersections are observed and indicate that for some angles θ it is possible to find modes at the same frequency. The first intersection is visible at $\theta = 26.3^\circ$ for which SA₁ and AS₁ frequencies are the same. The second intersection is visible at $\theta = 28.3^\circ$ where SA₁ and AA₁ intersect. The third one is at 29.7° for SS₁ and AS₁ modes and the last one at 40.5° for SS₁ and AA₁. At high portion angle the four modes are far apart and do not intersect. All these intersections correspond to mode combinations that do not have the same movement symmetry at the contact interface and are therefore compatible with the first criterion. From these observations any of the four proposed mode combinations can be used at the same frequency with a resonance effect.

2.3.7 Angle between movements at contact surface

The mode combination used for ultrasonic actuation generates elliptical motions at the interface between the rotor and the stator. Depending on the amplitude of the two modes and the direction of the generated motions, the elliptical motions can have various shapes. As it will be further studied in chapter 3 on page 67, the normal amplitude and tangential amplitude of these elliptical movements have both an important role in the performance of the

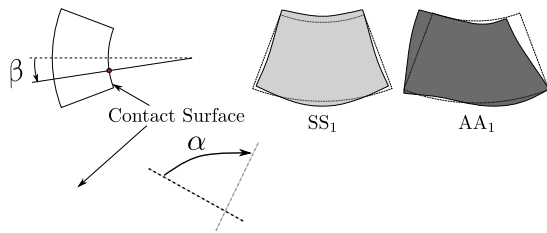
actuator. Normal amplitude influences contact time, maximum preloading force and maximum transmissible torque while tangential amplitude affects maximum speed of the motor. These two amplitudes should be maximized, and the elliptical movements should be as large as possible and eventually close to a circle.

Apart from mode amplitude, that cannot be studied using modal analysis, one parameter that have to be considered in elliptical movement size, is the angle between the mode trajectories at the interface. A 0° angle between the two modes trajectories result in collinear movements of both modes and therefore absence of elliptical movements. A 90° angle leads to circular shape when modes have the same amplitude, which is the best case for ultrasonic actuation. Mode movement orthogonality leads to a better control over the elliptical movements and therefore allows for a better tunability of the dynamic properties of the actuator and good controllability at low speed (Takano et al. [31]).

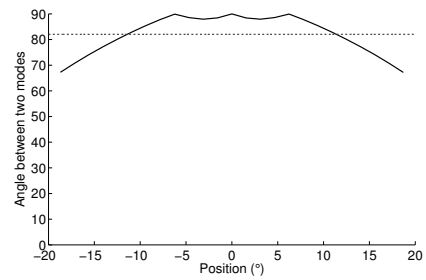
Although the mode amplitudes should not be considered using modal shape data because actual mode amplitudes depend on mode excitation, the angle between the two mode movements can be analyzed. Figure 2.11 presents the trajectories at the motor interface for various mode combinations. A representation of the expected movements is proposed along with the angle between the two mode trajectories as a function of the position on the contact surface. Each mode combination is studied at its degeneration portion angle computed in the previous section.

Figures 2.11a and 2.11b present the trajectories obtained using a combination of SS_1 and AA_1 modes. No collinear movement is observed along the contact area and the average angle between modes trajectories is 82° . At the center point of the actuator the two mode motions are orthogonal and the angle stays high for the central portion ($|\beta| < 6^\circ$) before falling down to 68° at the edges of the contact area. Figures 2.11c and 2.11d present the trajectories obtained using a combination of SS_1 and AS_1 modes. The same observation as the previous mode combination can be made with a 90° angle at the central point. However, the angle falls to below 55° as points far from the center ($|\beta| > 7.5^\circ$) of the actuator are considered. The average angle along the contact surface is about 62° . No collinear movement is observed along the contact area but a clear “flattening” of the ellipses is observed on the edges of the contact surface.

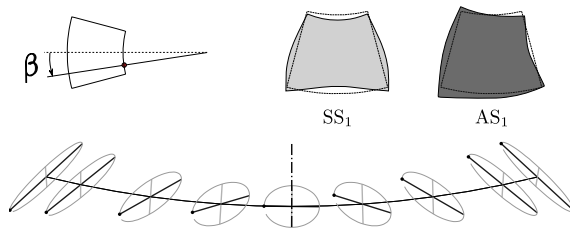
Figures 2.11e and 2.11f present the trajectories obtained using a combination of SA_1 and AA_1 modes. Again, orthogonal movements are observed at the middle point of the contact surface and an angle diminution similar to SS_1 and AS_1 combination is observed. The angle drops below 10° for some positions along the contact area and some trajectories on figure 2.11e are quasi-collinear. An average angle of 31° is observed. Figures 2.11g and 2.11h present the trajectories obtained using a combination of SA_1 and AS_1 modes. Again, the two movements have a 90° angle at the center point. As the considered position gets far from the center of the actuator, the angle drops to 76° and goes up to 90° . An average angle of 81.5° is



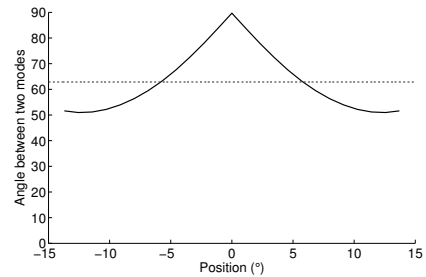
(a) Elliptical trajectories at the contact surface for AA₁ mode (dark) and SS₁ mode (light) combination.



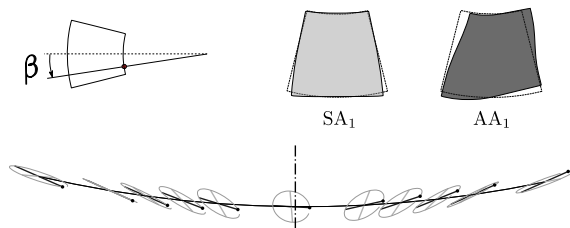
(b) Angle α as a function of position β for SS₁ and AA₁ mode combination. ($\theta = 40.5^\circ$)



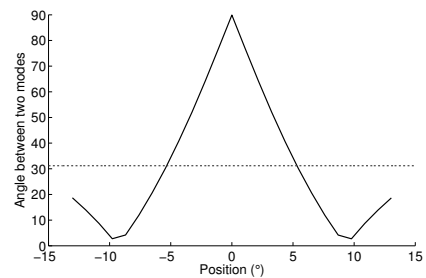
(c) Elliptical trajectories at the contact surface for AS₁ mode (dark) and SS₁ mode (light) combination.



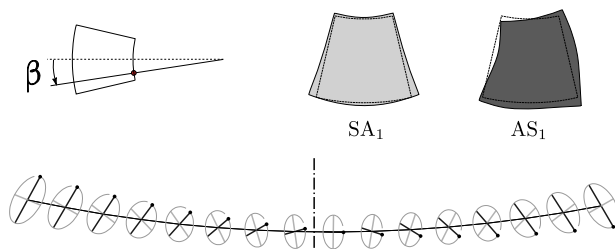
(d) Angle α as a function of position β for AS₁ and SS₁ mode combination. ($\theta = 30^\circ$)



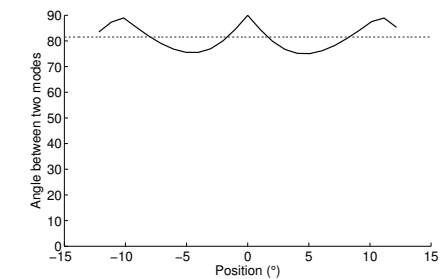
(e) Elliptical trajectories at the contact surface for AA₁ mode (dark) and SA₁ mode (light) mode combination.



(f) Angle α as a function of position β for AA₁ and SA₁ mode combination. ($\theta = 28^\circ$)



(g) Elliptical trajectories at the contact surface for AS₁ mode (dark) and SA₁ mode (light) combination.



(h) Angle α as a function of position β for AS₁ and SA₁ mode combination. ($\theta = 25^\circ$)

Figure 2.11: Trajectories of the points along the contact area for different mode combinations. They are presented at the portion angle θ where the two modes are at the same frequency. Angle α is the angle between modes trajectories and β is the position angle along the actuator contact surface. Amplitudes are normalized amplitudes from finite element modal analysis and should not be compared.

observed along the contact surface, which is close to the first considered combination at 82° .

SS_1+AA_1 and SA_1+AS_1 combinations offer the best average angle between the trajectories along the contact area. Although SS_1+AA_1 have a slightly better angle, the difference is not considered as significant and the two modes combinations can be used. SA_1+AA_1 and SS_1+AS_1 combinations are suitable for single point of contact transducers with orthogonal movements at the middle point of the actuator. The important drop of the angle on the whole contact area limits their utilization with an extended contact surface.

Different parameters have been considered for mode selection and the two combinations SS_1+AA_1 and SA_1+AS_1 are promising for actuator design. Nevertheless, geometrical variations might affect the results discussed in this section and it is proposed to analyze the four modes combinations properties as a function of geometric variations.

2.3.8 Geometric variations

Modal analysis is used to evaluate the influence of other geometrical parameters on the properties of the actuator. In this section, it is proposed to observe the changes in actuator properties as a function of variations of outer and inner radius R_o and R_i . Because changes in geometry affect mode frequencies, the portion angle θ where the two modes are degenerating is recomputed after each geometric variation. An automatic search algorithm for θ , based on MAC mode recognition, is implemented in COMSOL Java API. The algorithm can be described in four steps:

1. First two initial analyzes are conducted for two different angles θ_1 and θ_2 . Two different values for Δf , the frequency difference between the two considered modes are obtained.
2. From these values it is possible to compute a new value for θ assuming a linear dependence between Δf and θ : $\theta_3 = \frac{\Delta f_1 \theta_1 - \Delta f_2 \theta_2}{\Delta f_2 - \Delta f_1}$.
3. A new value Δf_3 is obtained from θ_3 .
4. If Δf_3 is not below a defined tolerance (in our case 10 Hz), a new θ_4 is estimated using Δf_2 and Δf_3 . Otherwise, the portion angle is found and the iteration loop stops.

Three properties are compared through geometric variation:

- Average angle between mode displacements: As explained in section 2.3.7, the angle between the modes movements is an important parameter since it is directly associated to the size of the elliptical movements that can be generated.
- Portion angle θ : Since the angle θ for mode degeneration is recomputed after each geometric change, it is possible to analyze how it evolves with respect to R_o and R_i .

- Mode frequencies are influenced by the geometry. As discussed in section 2.2.2, for longitudinal modes of a beam, mode frequencies increase as the size of the system is reduced. It can be expected to observe the same evolution with the size of the actuator.

Angle between movements

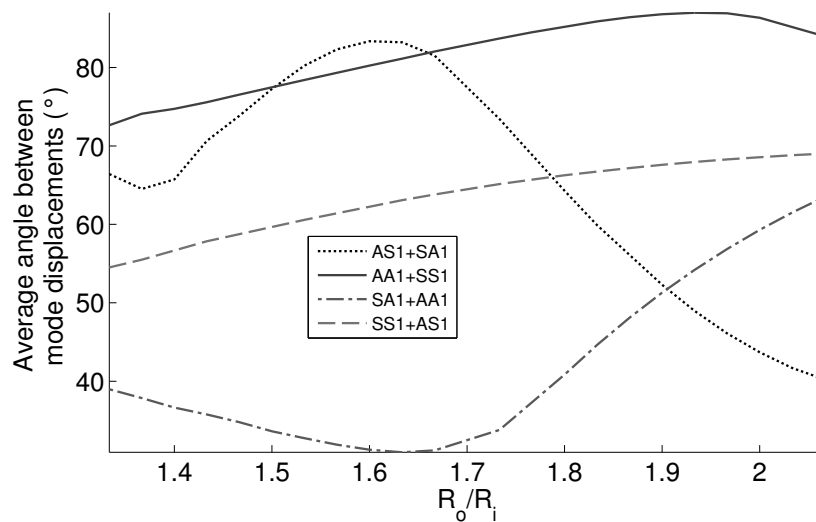


Figure 2.12: Average angle between mode movements as a function of R_o/R_i . AS_1+SA_1 and AA_1+SS_1 combinations offer the largest average angles between mode movements at contact interface.

The angle between the two movements generated at the interface is important in order to obtain good elliptical motions and controllability of the motor. Because a large contact surface is used for actuation, the average angle along the contact area is studied. Deformation directions are not affected by an homothetic transformation of the actuator and it is therefore possible to study this angle with respect to the dimensionless parameter $\frac{R_o}{R_i}$.

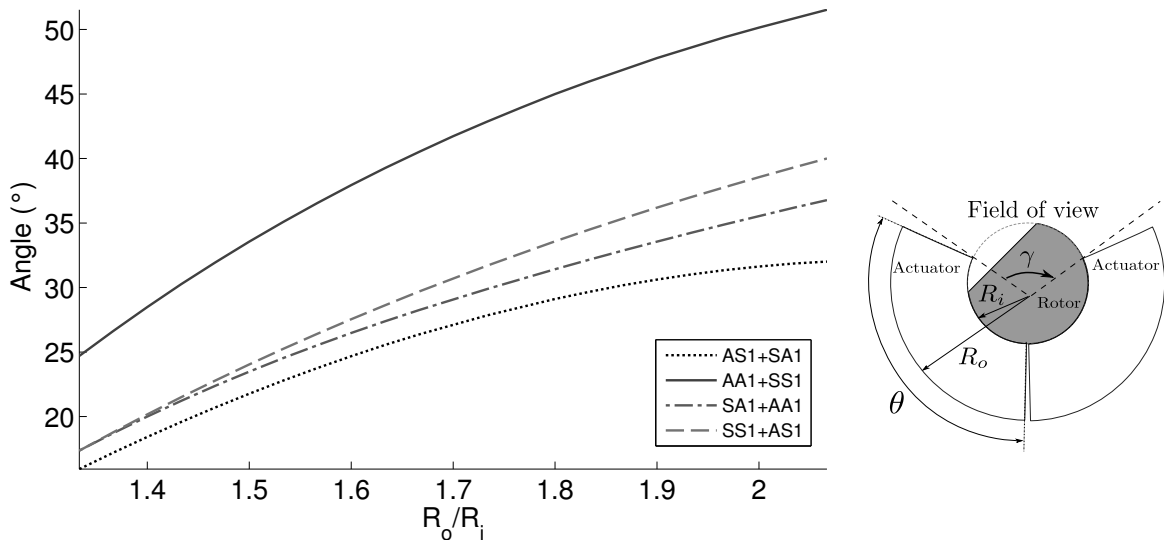
Figure 2.12 shows the evolution of the average angle between the two mode movements with respect to the outer to inner radius ratio of the actuator. The four potential modes combinations are represented. The association of SA_1 and AA_1 offers the lowest average angle at the contact area with values between 40° and 55° . In the precedent section it is evaluated as the worse combination with an average angle of 31° (with $\frac{R_o}{R_i} = 1.67$). While this observation is correct for a ratio below 1.9, above this value, SA_1+AA_1 becomes more interesting than the association of AS_1 and SA_1 . This indicates that no geometric parameter should be neglected in the mode selection process.

AS_1+SA_1 combination has an average angle that varies greatly with respect to R_o/R_i . Between 1.5 and 1.65, it is the most interesting mode combination, with an average angle close to 90° . As R_o/R_i increases, it becomes less interesting with an average angle that drops below 40° . At $\frac{R_o}{R_i} = 1.6$, this combination is particularly interesting as compared to the others with an average angle of 83° between movements generated at the contact surface.

AA_1+SS_1 and SA_1+AA_1 , observe steady variations of the average angle over the range of parameters studied. SA_1+AA_1 does not present high average angle between the movements at the contact interface, with values between 55° and 65° . AA_1+SS_1 is the most interesting combination. For a large range of R_o/R_i values, angles between 72 and 86° are observed with a peak value around $\frac{R_o}{R_i} = 1.9$.

Evolution of angle θ

The portion angle θ required to obtain mode degeneration changes as a function of the geometry. Finite element method shows that the angle is not affected by an homothetic transformation (i.e. a decrease of both the outer radius and inner radius by the same factor results in the same angle θ for mode degeneration). Therefore, it is possible to express θ as a function of the ratio of the outer radius to the inner radius. The results for a 1.3 to 2.1 R_o/R_i range are presented in figure 2.13. θ increases as R_o/R_i is increased. This evolution is polynomial, with an angle varying from 25° to 50° for the AA_1+SS_1 combination. The other modes combinations show angles θ that are smaller with a similar polynomial evolution. SS_1 and AS_1 degeneration is obtained at portion angles between 17° and 38° . At a 1.3 R_o/R_i ratio, two combinations can be used for the same geometry since a 17° actuator will have both SS_1+AS_1 and SA_1+AA_1 combinations. AS_1+SA_1 has the lowest θ angle for any given R_o/R_i ratio with portion angles varying from 16° to 32° .



(a) Portion angle θ as a function of the ratio R_o/R_i for the different modes combinations.

(b) Influence of actuator portion angle on field of view.

Figure 2.13: Study of portion angle θ evolution as a function of geometry. As R_o/R_i increases, the portion angle θ for mode degeneration increases. Depending on the required workspace for the actuator, portion angle may be an important parameter.

As explained in figure 2.13b, portion angle θ is a geometric parameter that has an influence on the workspace of the spherical motor when it is used as servomotor. Considering the case of an orientation platform for a camera, an actuator with a large portion angle may interfere with the line-of-sight of the camera, causing a diminution of the maximum field of view. On the other side, a high portion angle θ implies a larger contact area and better guidance of the rotor. The total size of the actuator is also increased, what results in a larger displacement at the contact area and better properties of the actuator. Therefore, it can be interesting to use an actuator with a large portion angle for the realization of omnidirectional wheels that use a single point of contact of a complete sphere as a driving system in a miniature robot for example.

Mode frequency

Mode frequency is directly related to the total size of the actuator and finite element analysis shows that a variation in the inner radius or the outer radius results in the same relation between actuator area and mode frequencies. Figure 2.14 shows the evolution of the frequency as a function of the actuator area for each considered combination. A global diminution of resonance frequency is observed as area increases. This result is similar to longitudinal modes of a beam which have a mode frequency proportional to $1/l$ where l is the length of the beam. The relation found for the considered actuator is a variation of the frequency as a function of $1/\sqrt{A}$, where A is the in-plane area of the actuator. Assuming a characteristic length $l_c = \sqrt{A}$ can be defined, it is similar to the relation observed between longitudinal modes and the length of a beam.

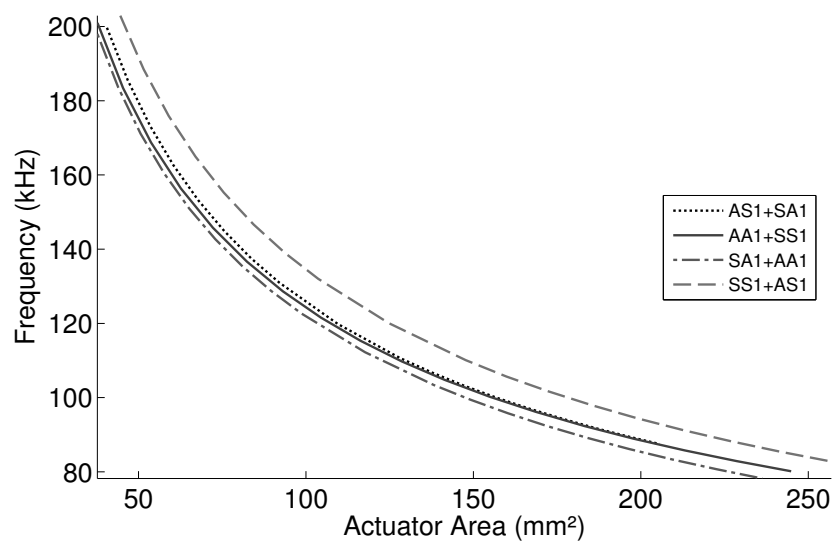


Figure 2.14: Evolution of the mode frequency as a function of the actuator area. Mode frequencies are proportional to the inverse of the square root of the actuator area.

For a given actuator area, the mode combinations have different mode frequencies. The use of the SS_1+AS_1 combination results in the highest resonant frequencies. Considering for example the case of a 150 mm^2 actuator, SA_1+AA_1 resonance frequency is at 99kHz, AA_1+SS_1 frequency is 2.7 % higher, AS_1+SA_1 3.13 % higher and SS_1+AS_1 is 10.2% higher. Resonance frequency can be an important parameter to select driving electronics that are used. In general, the larger the frequency is, the more difficult it is to find suitable electronics especially when high voltage is required.

2.3.9 Geometry selection

The various parameters that are exposed here can be tuned as a function of the actuator requirements. A large actuator can be designed for good rotor guidance with high amplitude and low driving frequency, while a small actuator can be proposed for integration in compact designs. In section 1.9, the target application of this thesis has been described. The objective is to obtain a spherical motor of 30mm in diameter capable of a minimum amplitude of 40° over 2 axes with a large contact area so that stresses at the interface are reduced and guidance of the rotor is ensured.

Based on these requirements, a design based on a piezoelement of 15 mm inner radius and 25 mm outer radius is proposed. Using a combination of SS_1 and AA_1 modes, the resulting actuator has a portion angle of 40.5° , which is below 45° and allows to propose a spherical pointing device with a 90° workspace. The obtained area of contact is large and the effect of contact length on actuator properties can be studied. Moreover, the actuator is easily manufactured since 50 mm diameter PZT disks are found as standard industrial parts.

The choice of SS_1 and AA_1 combination is based on several observations. The average angle between the movements at the contact surface of the actuator is close to 90° , the mode frequency of the actuator is around 100 kHz which is compatible with most amplifiers and digital acquisition card for characterization, and the two modes are similar to commonly used modes in plate-type longitudinal-bending linear actuators (Takano et al. [28], Shi and Zhao [69]). Because of this similarity, it is chosen to refer to the SS_1 mode as the first longitudinal mode L_1 and the AA_1 mode as the second bending mode B_2 in the remaining of this work. The obtained actuator can therefore be referred as a curved longitudinal-bending actuator.

2.4 Modal sensitivity

Since the working principle of the actuator is based on the combination of two modes of vibration, it is important to ensure that they are at the same frequency. Finite element analysis allows for the study of the sensitivity of the structure to manufacturing tolerances. In this section three types of disturbances are considered:

- Manufacturing tolerances. It is interesting to anticipate what consequences a geometric uncertainty has on mode degeneracy and what precision is required for proper actuator fabrication.
- Soldering points are added masses to the actuator that may cause a shift in the mode frequencies.
- Contact layer is also an added mass to the actuator that may shift resonance frequencies in an undesirable way. Predicting how modes are affected allows for anticipation and correction using for example a modified geometry.

2.4.1 Geometric tolerances

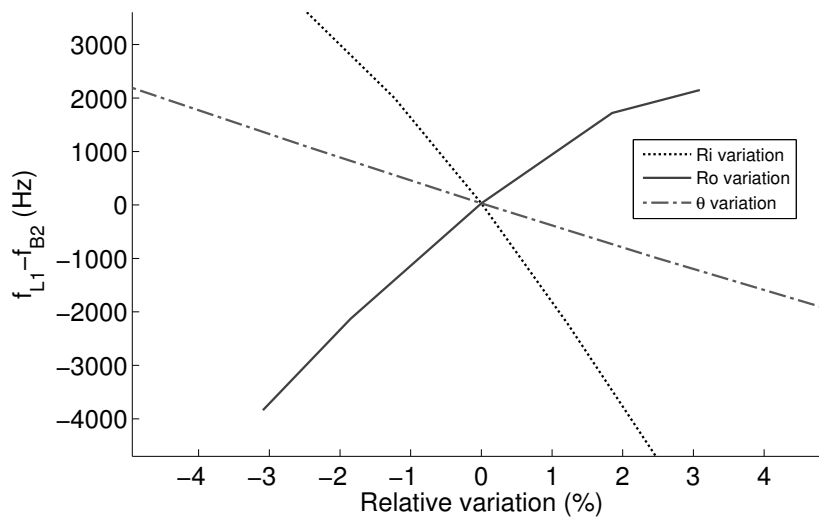


Figure 2.15: Geometric tolerances effect on mode degeneracy. Imprecision in the manufacturing process may affect mode frequencies.

Figure 2.15 shows the effect of small relative variations of the actuator geometric parameters on mode degeneracy. A slight increase in the inner radius of the actuator causes the longitudinal mode to drop below the bending mode. The effect is important with a frequency shift of 1.2kHz between the modes for an increase of 0.67% (0.1mm) of the inner radius. A reduction of R_i has a less pronounced effect with a bending mode 1kHz below the longitudinal mode for a -0.67% variation. The tolerance on R_o has the inverse effect with a longitudinal mode above the bending mode when the outer radius is increased. The sensitivity is less important, with a 440Hz shift for a -0.4% variation (0.1mm). The variation is not symmetric and an increase of 0.4% in R_o causes a frequency shift of 395Hz. Portion angle change has a symmetric and linear effect for variations of $\pm 5\%$. A relative increase of 1% (0.4°) leads to a bending mode 460Hz above the longitudinal mode.

A piezoelectric material manufacturer such as Ferroperm, provides tolerances down to 10 μ m. The maximum frequency shift from this uncertainty is 100Hz which is an acceptable

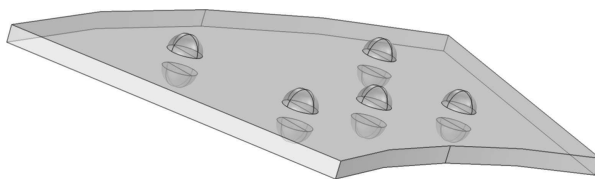
tolerance on mode degeneracy at it is shown in chapter 3. A laser cutting method, for example, is very precise but divergence of the laser cause tolerances that can be around 0.1mm. This error is repeatable and can be taken into account into the design process.

2.4.2 Soldering points

Various ways have been used in order to supply electric power to piezoelectric elements. Springs are used in Shen and Huang [6], conductive glue in Rogers [2] and soldering in most applications. Soldering ensures both strong mechanical and electrical connections and is widely used in electronics. With actuators at a macroscopic scale, soldering points are usually negligible as compared to the mass of the actuator. As size reduces their mass begin to matter. As an illustration, an actuator of 25mm in outer radius and 15mm in inner radius with a portion angle $\theta = 40.5^\circ$ made of Ferroperm Pz26 material, weights 544 mg. Because there is a need for multiple electrodes in order to excite each mode, a total of 10 soldering points is needed on the actuator. Considering soldering points as half spheres of 0.5mm in diameter, the total added mass is 21.8mg (4% of the total weight).

Frequency shift due to solder mass

We propose to study the effect of soldering points using finite element modal analysis. A solder point is modeled as a perfect half sphere of eutectic Tin/Lead alloy with properties listed in figure 2.16b. Figure 2.16a shows how soldering points are modeled. They are positioned at the expected location of excitation electrodes. Their radius is changed to observe the effect of mass on mode frequency shift.



(a) Solder positions.

Density	8340 kg.m ⁻³
Young's modulus	31.5 GPa
Poisson's ratio	0.36

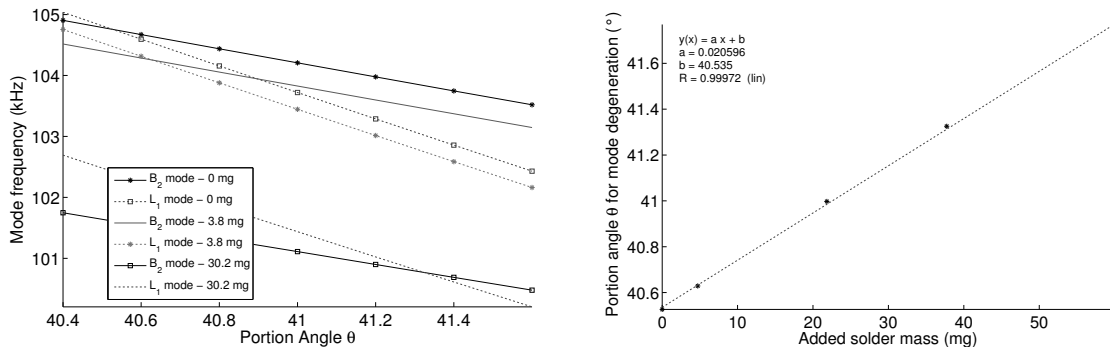
(b) Eutectic Tin/Lead Alloy (67% Tin) Material properties. From eFunda online database: http://www.efunda.com/materials/solders/tin_lead.cfm.

Figure 2.16: Soldering points are modeled as half spheres of Tin/Lead alloy.

Although the simulation does not take into account the mass due to connection wires and other external interactions, it allows to estimate how the modes are affected and whether it is possible to develop a strategy to keep both modes at the same frequency. Figure 2.17 shows the result of finite element analysis for solder points of different masses. The direct effect

CHAPTER 2. MODAL ANALYSIS: DESIGN OF THE RESONANT MECHANICAL STRUCTURE

of an added mass is a drop in mode frequencies while the linear evolution of the frequency with respect to the portion angle keep the same slope. The frequency diminution is not the same for each vibration mode and this causes the two modes to be shifted apart. Both modes can still be found at the same frequency if the portion angle is increased. In figure 2.17b, it is observed that the larger the mass is, the larger the shift in θ is. This evolution is linear with a 0.02° shift per milligram of added mass.



(a) Mode frequency evolution with respect to added soldering mass and portion angle θ .

(b) Degeneration angle θ with respect to added solder mass.

Figure 2.17: Effect of soldering deposit on modal frequencies and degeneration portion angle. The soldering points cause an added mass to the actuator that shift down the resonance frequencies. The bending mode drops more quickly than the longitudinal mode, causing a shift in the degeneration portion angle which is larger than expected.

Influence of solder points location

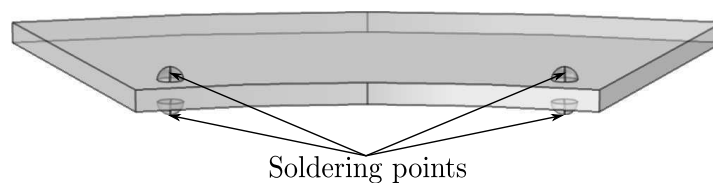


Figure 2.18: Solder points modeling for location influence study. Four points are placed and moved symmetrically on the actuator surface to avoid asymmetries and changes in modes shapes.

The location of soldering points has an important effect on the frequency shift due to added mass. A solder point placed in areas of large displacement cause a larger change in mode frequency. In the finite element model, four solder points of radius 0.3 mm (total mass: 1.88 mg) are modeled as shown in figure 2.18. Two soldering points are disposed on each face of the actuator with respect to the symmetry axis of the structure. This disposition avoid asymmetries and deformation of the mode shapes. These soldering points are moved

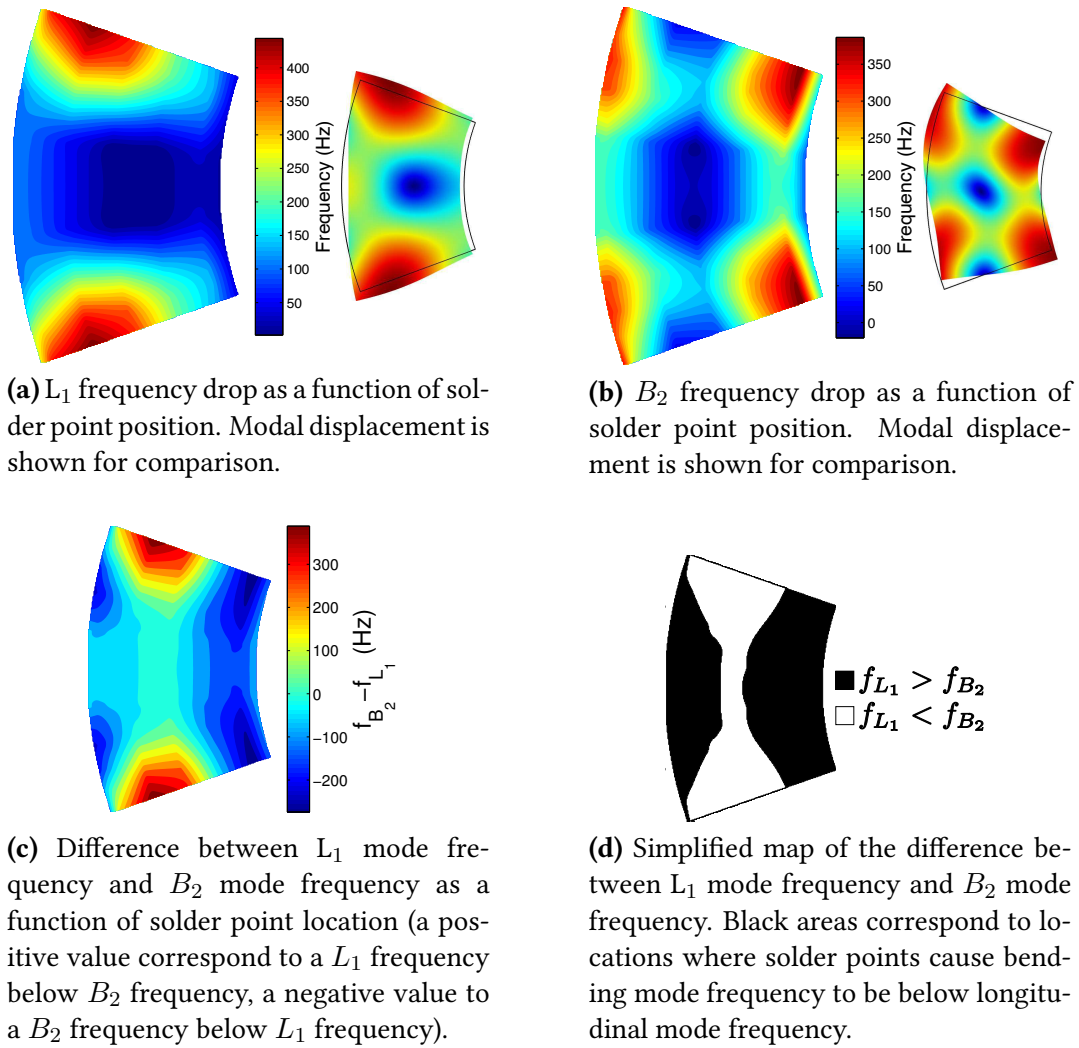


Figure 2.19: Modal frequencies changes as a function of the position of four hemispheric solder points of 0.3 mm in radius disposed symmetrically onto the actuator.

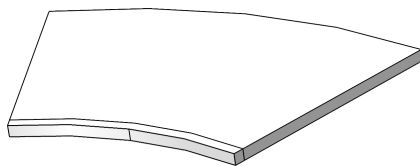
symmetrically around the actuator and the frequency shift is observed. The mass of solder is kept constant while position is varied.

Figure 2.19a and 2.19b show the resonance frequency change as a function of soldering points location. The modal shape displacements are shown for comparison. It can be observed that the frequency drop is larger when the solder points are placed at a location where modal displacement is large. In the case of the longitudinal mode, a maximum drop of 440 Hz is observed for a total mass of 1.88mg placed at maximum displacement location. For B_2 mode, this maximum drop is reduced to 380 Hz.

It is possible to observe the frequency difference between the two modes as a function of solder point location. In figure 2.19c, positives values correspond to locations where a solder point causes the longitudinal mode frequency to drop below the bending mode frequency while negative values correspond to a longitudinal mode frequency above the bending mode frequency. Depending on solder point position it is possible to have either mode below

the other. The simplified map 2.19d emphasizes this characteristics with black areas that correspond to a location that causes L_1 frequency to be above B_2 frequency and white areas where it is below. This phenomenon shows that there is a need for precise control of soldering location and mass in order to keep the two modes at the same frequency. On the other hand, this effect can be used as a way to tune the actuator modes experimentally. An iterative process based on admittance characterization for mode frequency measurement can be set-up. If a frequency difference between modes is observed, soldering points locations or masses can be adjusted until modes are tuned together.

2.4.3 Influence of contact layer



(a) Epoxy layer modeling.

Density	Young's modulus	Poisson's ratio
1100 kg.m ⁻³	10 GPa	0.4

(b) Epoxy properties used. From Matweb online database <http://www.matweb.com/>.

Figure 2.20: Modeled contact layer in finite element analysis. An epoxy contact layer is modeled in COMSOL, its radius is the same as R_i (15mm).

The deposition of a contact layer causes also added mass to the actuator. The material chosen for contact is epoxy resin. It is a commonly used matrix material for composite contact materials [70, 71] and is easily deposited onto the actuator. The shape and properties of the simulated contact layer are presented in figures 2.20a and 2.20b. It is interesting to observe whether the contact layer will have an influence on mode degeneracy. Simulation shows that the second bending mode is more affected by the contact layer with a shift of approximately -440 Hz for a 1 mm layer thickness against 170 Hz/mm for the longitudinal mode (figure 2.21a). The same effect is observed on mode damping, with a more pronounced drop in bending mode quality factor than longitudinal mode (figure 2.21b).

The influence of the contact layer can be anticipated or compensated using a smart placement of the soldering points or a slight increase in the portion angle of the actuator since it will allow to increase bending mode frequency.

2.4.4 Experimental result of vibration modes tuning

The tuning method based on soldering point location has been performed on an actuator with an inner radius of 15mm, an outer radius of 25mm ($R_o/R_i = 5/3$) and a portion angle $\theta = 41.4^\circ$, slightly above the angle for mode degeneracy. Figure 2.22 shows the evolution of mode frequency through a tuning process. The initial admittance measurement of the

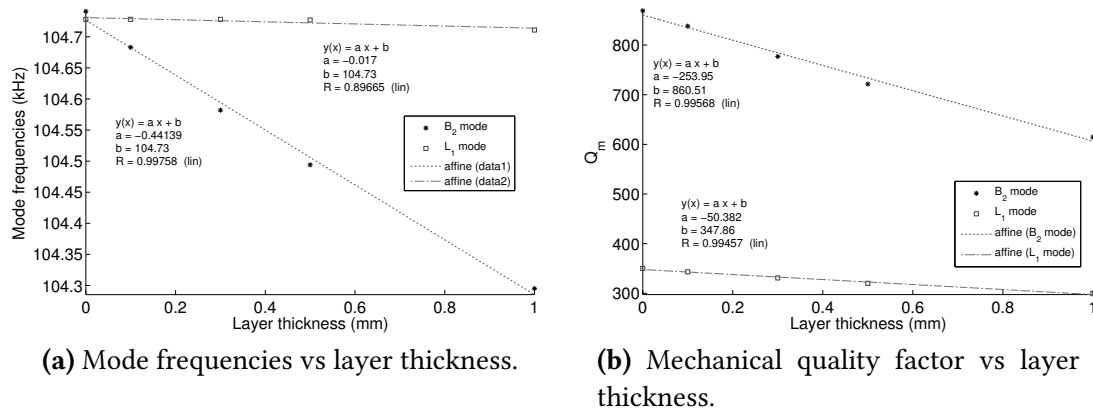


Figure 2.21: Influence of contact layer on mode frequencies and mechanical quality factor.

actuator in its holding mechanism shows a bending mode 2 kHz above the longitudinal mode at 1N preloading. Solder mass is added according to the map shown in figure 2.19c. Rather than moving the solder points, solder is added to the existing soldering points. Results show that the modes can be tuned together with only 309 Hz remaining. Bending mode drops from 107750 Hz to 104676 Hz in frequency whereas longitudinal mode drops from 105732 Hz to 104367 Hz indicating that added masses at high bending displacement lead to mode tuning of an actuator with a bending mode above the longitudinal mode.

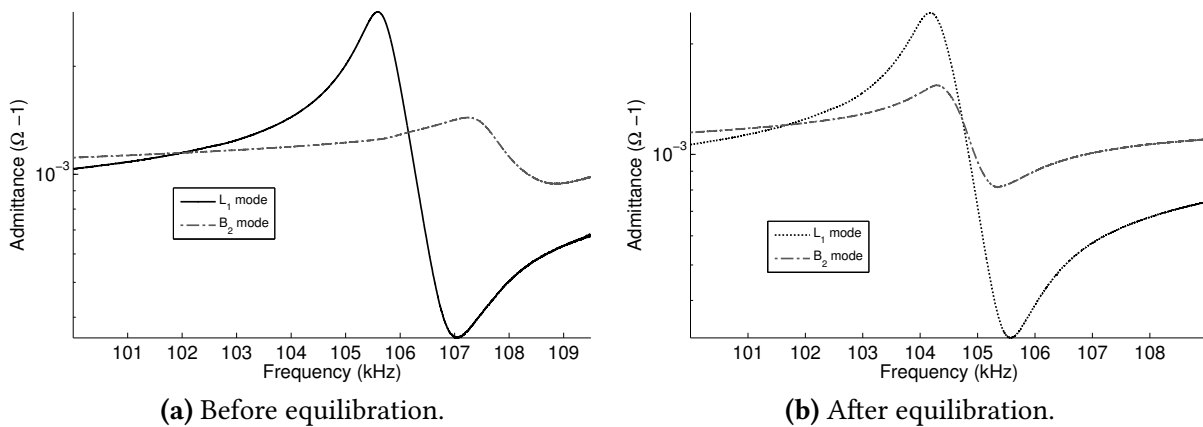


Figure 2.22: Mode frequency tuning using soldering points on the actuator. A smart positioning of the soldering points allows to improve mode degeneracy.

As it will be further discussed in section 3.8, this process improves the mechanical output power of the motor. For a quality factor of 50, contact analysis shows that a 2 kHz difference between mode frequencies results in an output power which is 25 % of the maximum power expected when modes are degenerating. If the modes are tuned to a 309 Hz difference, this percentage is above 95% of the maximum power output. This result shows the importance of mode tuning for proper actuator operation and efficiency.

2.5 Conclusion

In this chapter, an introduction to vibrations theory is proposed. It includes the presentation of vibrations modes and resonance, useful for the realization of ultrasonic motors. A specific geometry for the actuator is defined with three parameters: the outer radius R_o , the inner radius R_i and the portion angle θ . The possible modes for ultrasonic actuation are identified and studied using modal finite element analysis. Several mode combinations can be used. The optimal mode combination is selected based on several criteria: the angle between motions at the contact interface, mode frequencies, portion angle θ and size of the actuator. A final set of geometric parameters ($R_o = 25\text{mm}$, $R_i = 15\text{mm}$, $\theta = 40.5^\circ$) is proposed. The obtained actuator uses a combination of a longitudinal mode and a bending mode at 105 kHz.

Modal analysis is used to study the influence of geometric tolerances and added masses such as solder points and contact layer on the actuator. The results show that these parameters affect mode degeneracy. A smart positioning of the solder points allows tuning the modes. This tuning process is essential for optimal actuator performance as it is discussed in the next chapter.

Contact analysis: From vibration to motor mechanical output

3

Contents

3.1	Introduction	68
3.2	Tribology of ultrasonic motors	68
3.2.1	Friction model	68
3.2.2	Ultrasonic motor contact modeling	70
3.2.3	Friction material for ultrasonic motors	75
3.3	Coordinates change for the proposed actuator	76
3.4	Mode displacement amplitudes	77
3.4.1	Contact time	78
3.4.2	Motor output characteristics	78
3.5	Preloading force	81
3.5.1	Contact time	81
3.5.2	Motor output characteristics	81
3.5.3	Torque versus speed characteristics	82
3.6	Contact layer stiffness	83
3.6.1	Contact time	83
3.6.2	Motor output characteristics	84
3.7	Contact length	85
3.7.1	Contact time	86
3.7.2	Motor output characteristics	87
3.8	Frequency response of the actuator	89
3.8.1	Modes frequency response	89
3.8.2	Motor frequency response	90
3.8.3	Maximum output power	92
3.9	Conclusion	92

3.1 Introduction

This chapter proposes to model the output mechanical characteristics of an ultrasonic motor. It focuses on the description of the conversion of mechanical vibration to rotor rotation. This chapter applies a transfer model which is derived from the work of Guo et al. [72] and adapted to our design methodology. The major difference with Guo et al. is the numerical implementation which allows to study any geometry with various contact conditions. The chapter is organized into several sections:

- First an introduction to ultrasonic motors tribology is proposed. The contact model is introduced along with typical contact materials that are used in literature.
- In the following sections, the model is applied to the actuator concept studied in the previous chapter. Several parameters are studied:
 - Mode displacement amplitude
 - Preloading force
 - Contact layer stiffness
 - Contact layer length
 - Modes non-degeneracy

These studies allow to better understand how each parameters may affect the motor properties and how the contact may be tune to the required mechanical properties.

3.2 Tribology of ultrasonic motors

In this section, we want to address specifically the contact mechanics that allow the stator to transmit its energy to the rotor. A contact model based on friction forces is proposed along with examples of contact materials used in literature.

3.2.1 Friction model

Friction is described in its simplest form by Coulomb friction model:

$$F_t = \mu P \text{sign}(\Delta v) \quad (3.1)$$

Where F_t is the tangential force, P the normal force, μ the friction coefficient and Δv the relative velocity difference between the two considered surfaces. The tangential friction force is proportional to both the friction coefficient and the normal force. In general, two different coefficients are considered, the static friction coefficient μ_s describing the friction

properties when the stator and rotor are not moving relatively to each other and the dynamic coefficient μ_d , slightly lower which models the friction behavior when the stator and rotor are moving relatively to each other. A more general model for friction includes viscous effects so that the friction force equation becomes:

$$F_t = \mu P \text{sign}(\Delta v) + k_1 \times \Delta v \quad (3.2)$$

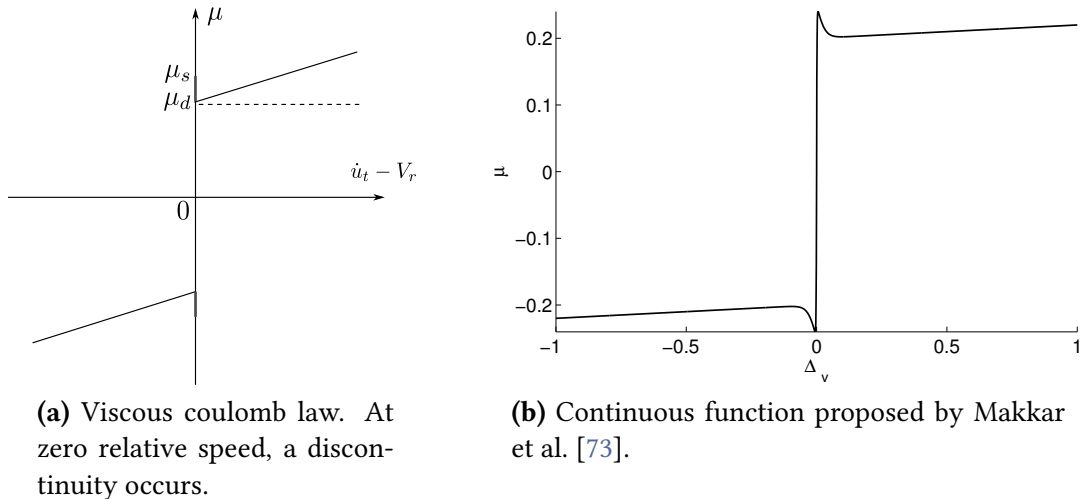


Figure 3.1: Two different friction models that can be used to compute friction forces.

In figure 3.1a, the resulting expression for the friction coefficient presents a singularity at 0 which is difficult to use in numerical modeling. The Δv have very low chances to be exactly 0 and the singularity at $\Delta v = 0$ causes highly non-linear behavior that may cause problems with the numerical solver. Therefore, several different models are proposed in literature in order to obtain fully differential friction description. One of them has been proposed by Makkar et al. [73] and gives good accordance with conventional friction models. It includes Stribeck effect that models partial lubrication at low speed. Although it is not necessary in our case, it offers a convenient way to take into account static friction effects. Some models include stiction description, such as in the Dahl model (Canuda De Wit et al. [74]). Although it is useful for quasi-static actuators such as stick-slip actuators (Breguet [75]), ultrasonic motors are almost always in a “slip” contact condition. Therefore, stiction is not included in our model.

Tribology at the micro-metric scale is complex. The roughness of the two surfaces placed in contact results in an actual contact surface much lower than the considered surface at the macro-scale. Moreover, displacements of ultrasonic actuators are at the micrometer scale which is about the same size of the irregularities present at the surface of the material used as stator and rotor. This is the reason why this simplified model is only an approximation of the contact model at the micro-metric scale. Improvements could be expected by taking

into account a possible partial sliding of the stator against the rotor considering the low amplitude of the ultrasonic vibration (Garbuio [76]), the tangential stiffness could also be taken into account in the case of low stiffness contact materials. Nevertheless, results in the literature have shown that the model proposed here is sufficient to describe the friction behavior of an ultrasonic motor (Wallaschek [77]).

3.2.2 Ultrasonic motor contact modeling

Different models have been used to describe the torque transmission in ultrasonic motors. Wallaschek [77] proposed a model well adapted to traveling wave motors while Guo et al. [72] proposed a model for a longitudinal-torsional standing wave actuator that shows good agreement with experimental results. In this work, it is proposed to adapt this model to a standing wave actuator with arbitrary geometry. The goal is to be able to predict effects such as contact length based on modal displacement obtained analytically or using finite element methods.

Stator displacement

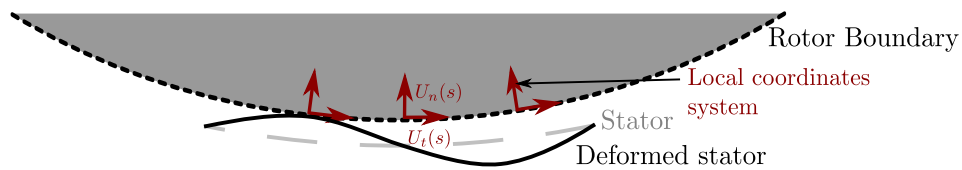


Figure 3.2: Local coordinates system used to define the contact model. Displacement of the stator is expressed in the coordinates system defined by the normal and tangential vectors to the rotor surface.

The displacement of the rotor is caused by the deformation of the stator both in the normal and tangential direction to the rotor. A motion of the stator only in the normal direction to the rotor does not result in a macroscopic movement and it is the formation of elliptical or oblique movements which causes the displacement of the rotor. Considering that rotor and stator can have complex shapes, there is a need to express the displacement of the contact point of the stator in a local coordinates system defined by the normal and tangential vectors to the rotor surface (see figure 3.2). The components of the movement at the edge of the rotor are divided in a combination of a normal amplitude and a tangential amplitude:

$$u_n(s, t) = u_n(s) \cos(\omega t) \quad (3.3)$$

$$u_t(s, t) = u_t(s) \cos(\omega t) \quad (3.4)$$

$u_n(s)$ and $u_t(s)$ are complex amplitudes as a function of the curvilinear abscissa s on the actuator. They can be written as a function of the phase and the module of the displacement:

$$u_n(s, t) = |u_n(s)| \cos(\omega t + \phi_n) \quad (3.5)$$

$$u_t(s, t) = |u_t(s)| \cos(\omega t + \phi_t) \quad (3.6)$$

with $\phi_n = \arg(u_n(s))$ and $\phi_t = \arg(u_t(s))$.

Impact force

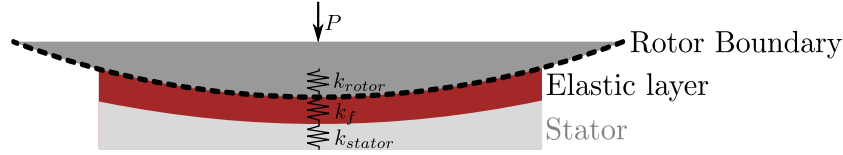


Figure 3.3: Friction layer is considered as an elastic layer. Its stiffness k_f should be lower than rotor and stator stiffness for the model to be valid.

The interface between the rotor and stator is composed of an elastic sheet of material which has an equivalent stiffness $k = \frac{E_y \times S_c}{h}$ where E_y is the Young's modulus of the contact material, S_c the contact area and h the thickness of the contact layer (figure 3.3). It is assumed that the rotor does not move or deform, and that the stator imposes a deformation to the friction layer. This means that the stiffness of the friction layer has to be small as compared to the rotor and stator stiffness. Defining $[t_a; t_b]$ as the time interval during which there is contact between rotor and stator, the normal force P can be written as:

$$\begin{cases} P = 0 & t \in [0; t_a[\\ P = k(u_n(s, t) - u_n^a(s)) & t \in [t_a; t_b] \\ P = 0 & t \in]t_b; T] \end{cases} \quad (3.7)$$

Where $u_n^a(s)$ is the minimum displacement of the actuator for which there is contact.

Contact time

The normal force is a sinusoidal function and a reasonable hypothesis is that the time interval when contact occurs is centered on the maximum normal amplitude. From the previous definitions, this maximum is reached when $\omega t = -\phi_n(s) = \varphi_{max}(s)$. It is assumed that, during steady state operation, there is contact during each frequency cycle. It means that the total acceleration exerted during one period of the movement is zero:

$$\int_0^T \ddot{u}_n dt = 0 \quad (3.8)$$

$$\frac{1}{m} \int_0^T (P - P_0) dt = 0 \quad (3.9)$$

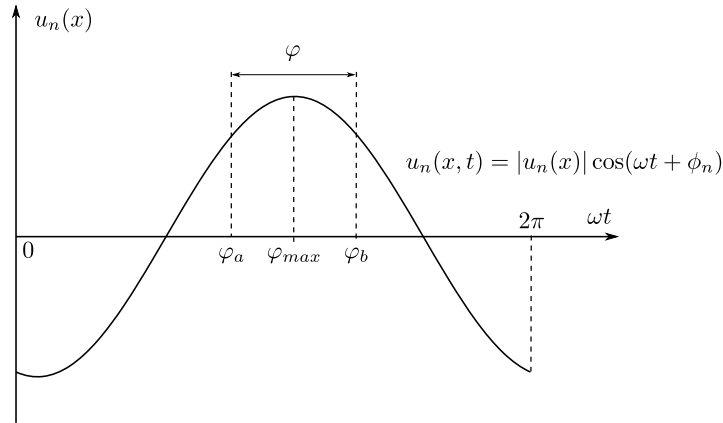


Figure 3.4: Normal displacement as a function of movement phase. φ_a correspond to the starting phase angle of the contact and φ_b to the end of the contact.

Where P is the force applied by the actuator as defined previously in equation (3.7) and P_0 is the preloading force on the rotor. Since the movement is periodic, it is convenient to use the phase of the periodic function as the integration variable:

$$\frac{1}{\omega \times m} \int_0^{2\pi} (P - P_0) d\varphi = 0 \quad (3.10)$$

$$\int_0^{2\pi} P d\varphi = 2\pi P_0 \quad (3.11)$$

Assuming contact occurs between phase φ_a and φ_b (see figure 3.4) we have:

$$\int_{\varphi_a}^{\varphi_b} k [|u_n(s)| \cos(\omega t + \phi_n(s)) - u_n^a(s)] d\varphi = 2\pi P_0 \quad (3.12)$$

$$k |u_n(s)| [\sin(\varphi_b + \phi_n) - \sin(\varphi_a + \phi_n)] - k u_n^a(s) [\varphi_b - \varphi_a] = 2\pi P_0 \quad (3.13)$$

Since contact occurs symmetrically around maximum normal amplitude phase, it is possible to write, for φ_a and φ_b :

$$\varphi_a = \varphi_{max} - \frac{\varphi_c}{2} = -\phi_n - \frac{\varphi_c}{2} \quad (3.14)$$

$$\varphi_b = \varphi_{max} + \frac{\varphi_c}{2} = -\phi_n + \frac{\varphi_c}{2} \quad (3.15)$$

Where φ_c is the phase angle when the stator and rotor are in contact. From equation (3.3), the displacement at $\varphi = \varphi_a$ is $u_n^a(s) = u_n(s) \cos(\frac{\varphi_c}{2})$. Substituting in (3.13):

$$|u_n(s)| \left[\sin\left(\frac{\varphi_c}{2}\right) + \sin\left(\frac{\varphi_c}{2}\right) \right] - |u_n(x)| \cos\left(\frac{\varphi_c}{2}\right) \varphi_c = \frac{2\pi P_0}{k} \quad (3.16)$$

$$|u_n(s)| \left[2\sin\left(\frac{\varphi_c}{2}\right) - \varphi_c \cos\left(\frac{\varphi_c}{2}\right) \right] = \frac{2\pi P_0}{k} \quad (3.17)$$

This non-linear equation can be solved numerically for the contact time φ_c from which φ_a and φ_b are deduced.

Critical preloading

When the rotor and stator are always in contact, the contact phase span is $\varphi_c = 2\pi$. Replacing φ_c in (3.16), the critical preloading P_c can be obtained:

$$|u_n(s)| 2\pi = \frac{2\pi P_c}{k} \quad (3.18)$$

$$P_c = \frac{E_y S_c}{h} |u_n(s)| \quad (3.19)$$

It can be observed from this equation that the stiffer the contact layer is, the easier it is to obtain levitation of the rotor for a given preloading. Over the critical load, torque of the motor is constant while the speed drops (Guo et al. [72]).

Generated torque

The process that sets the rotor in rotation is due to the friction force that the tangential motion creates. It is possible to model the friction force using friction laws presented earlier:

$$F_t = \mu P \quad (3.20)$$

F_t is the tangential friction force and μ the friction coefficient between the two surfaces. For a simple viscous Coulomb law and neglecting the static friction coefficient it is given by:

$$\mu = (\dot{u}_t - V_r) \left(\frac{\mu_d}{|\dot{u}_t - V_r|} + k_1 \right) \quad (3.21)$$

V_r is the rotor velocity, \dot{u}_t is the speed of the considered point of the interface, μ_d is the dynamic friction coefficient and k_1 is the viscous friction coefficient. A different definition of μ presented in figure 3.1b is used for numerical stability. Considering a contact length L , the average tangential force during one cycle will be given by:

$$F_t = \frac{1}{T} \int_0^T \int_0^L \mu(s, t) P(s, t) ds dt \quad (3.22)$$

And the transmitted torque will be:

$$M_r = F_t \times R \quad (3.23)$$

Where R is the radius of the rotor.

Stall torque and maximum speed

From these equations, it can be observed that the actuator will generate a torque that accelerate the rotor. This transmitted torque depends on the speed of the rotor. Figure 3.5 shows the different regimes of the motor. At start, transmitted torque is maximum. Eventually, the rotor reaches a speed higher than the tangential speed of the stator. The friction force changes sign and a torque in the opposite direction is generated slowing down the rotor (braking torque). Therefore, the net transmitted torque is lowered. An equilibrium state is reached when generated torque is close to 0 and constantly changing sign between cycles, then motor speed is maximum. Using a time-dependent solver, it is possible to obtain the transient response and torque-speed response of the motor.

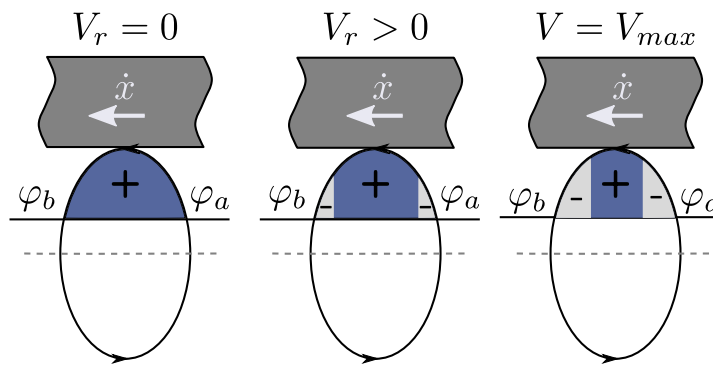


Figure 3.5: Evolution of torque transmission with respect to rotor velocity. Areas marked with a plus sign correspond to contact time where the speed of the stator is higher than the rotor. Minus sign correspond to instants where the velocity of the stator is lower than the rotor and braking forces occur. At first (left), speed of the rotor is 0 so that every instant of the contact time produce torque that accelerate the rotor. When speed increases, velocity of the rotor motion will eventually be below rotor speed and braking occurs, causing a decrease in the average transmitted torque. When useful torque and braking torque cancel each another, the rotor reaches maximum speed.

Contact efficiency

During the time when the stator is in contact with the rotor, contact surfaces slide against each other because of their speed difference. Some energy is dissipated through sliding friction and the contact efficiency resulting can be expressed as:

$$\eta = \frac{P_{out}}{P_{out} + P_d} \quad (3.24)$$

where P_d is the dissipated power by the contact and P_{out} is the output power. P_d is the power lost when there is sliding between rotor and stator, it is defined as:

$$P_d = \frac{1}{T} \int_0^T F_t \Delta V dt \quad (3.25)$$

with $\Delta V = \dot{u}_t - V_r$ and F_t the tangential friction force. P_{out} is the output mechanical power given by the product of torque M_r and speed V_r .

$$P_{out} = M_r \times V_r \quad (3.26)$$

The dissipated power P_d is important to take into account since it will generate heat that can affect actuator properties.

3.2.3 Friction material for ultrasonic motors

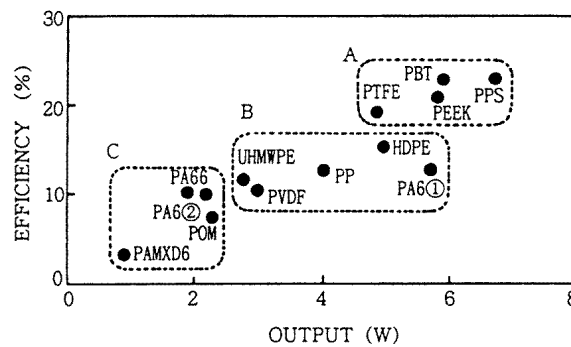


Figure 3.6: Classification of some materials used in traveling wave ultrasonic motors. These polymers are classified as a function of their potential output power and efficiencies in an ultrasonic motor application.

Various materials have been used for ultrasonic motors fabrication. Uchino [78] discussed the different materials for ultrasonic traveling wave motors. The presented materials are polymers and great differences are found in terms of output power varying from 1 W to 7W and efficiencies from 4 to 23 % (figure 3.6). Zhao [71, page 59] discusses different materials that can be used for ultrasonic motors. A matrix of polymeric material (PTFE, Epoxy, Polyimide...) is associated with a reinforcing filler (Alumina, Carbon fiber...) which improves the stiffness and temperature dependent properties of the material. A friction regulator (PTFE, copper oxide, graphite...) is added and improves the anti-wear properties of the material. Zhao [71] discusses also hard type contact layer based on alumina. They provide quicker response time but are hard to spread onto the contact surfaces. The specific case of a working longitudinal-torsional prototype showed that the best friction pair is an aluminum stator associated with a resin-based tribomaterial placed onto the rotor. In Ishii et al. [79], the effect of added lubricant on a hard/hard (steel/steel) contact in ultrasonic motor is discussed. It is observed that efficiency is highly improved at high preloading force using a lubricated condition. The phenomenon is attributed to a change in friction regime during a cycle which goes from a boundary type lubrication (when normal displacement is maximal) to a hydrodynamic lubrication regime (when normal displacement is minimum). The phenomenon is confirmed and modeled in a more recent study by Qiu et al. [80]. In Ko

et al. [81], various hard material such as TiN or diamond like carbon are discussed for stator coating in ultrasonic traveling type motors. The dynamic response of the actuator is good but wear of the contact layer causes instabilities appearing after 20 hours of operation.

As a summary, various type of contact materials are used in literature, it is not clear which kind of material provides the best contact properties. Hard materials (such as sapphire) are always used in inertia motors and surface acoustic wave motors because of the low induced displacement and the need for a precise roughness control. For ultrasonic motors, it is less clear about how to define a best suitable material. Prototypes using soft and hard materials are found in the literature and it is difficult to find a general design rule. In our case, unloaded epoxy resin will be used as a contact material. Although it may not be the most suitable contact material because of its low stiffness, it is easily manipulated and machined. Moreover, once a deposition method is well mastered, adding fillers to the epoxy matrix is a convenient way to tune contact material properties.

3.3 Coordinates change for the proposed actuator

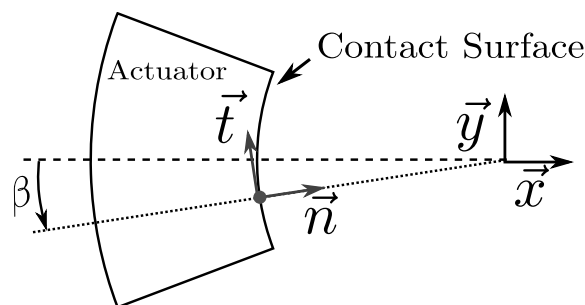


Figure 3.7: Change in coordinates from global (\vec{x}, \vec{y}) to local (\vec{n}, \vec{t}) coordinate system. The application of the contact model requires to express the modal deformation at the contact surface in the normal/tangential coordinate system.

Modes shapes obtained from modal analysis in chapter 2 are represented in a global coordinate system (\vec{x}, \vec{y}) . The force transfer model requires the displacement at the contact interface to be expressed in a local normal/tangential system. These two coordinate systems are presented in figure 3.7. It is convenient to express the change in coordinates using a transformation matrix:

$$\begin{bmatrix} u_n(\beta) \\ u_t(\beta) \end{bmatrix}_{\vec{n}, \vec{t}} = \begin{bmatrix} \cos(\beta) & \sin(\beta) \\ -\sin(\beta) & \cos(\beta) \end{bmatrix} \begin{bmatrix} u_x(\beta) \\ u_y(\beta) \end{bmatrix}_{\vec{x}, \vec{y}}$$

u_n and u_t are normal and tangential amplitudes and β is the position angle along the contact surface. u_x and u_y are complex numbers that include the displacements associated with the longitudinal and the bending mode. The temporal phase shift φ is included in the amplitude as a complex contribution, by multiplying the bending amplitude with $e^{j\varphi}$. For

example a 90° phase shift is obtained by multiplying the bending mode with the complex number j ($e^{j\frac{\pi}{2}} = j$):

$$u_x(\beta) = u_x^{L_1} + ju_x^{B_2} \quad (3.27)$$

$$u_y(\beta) = u_y^{L_1} + ju_y^{B_2} \quad (3.28)$$

Before this calculation, modes amplitudes are normalized by the maximum displacement of the considered mode ($\sqrt{(u_x^{L_1})^2 + (u_y^{L_1})^2}$ for L_1 mode) observed at the contact area. The resulting modes amplitudes in the local coordinate system are represented in figure 3.8. It can be observed that the two modes have significant components in both normal and tangential directions especially when the considered contact points are far from the center of the actuator. It can be problematic regarding to the control of the actuator as it is generally better to have an independent control on normal and tangential components for low speed control as explained by Takano et al. [31]. Nevertheless, it should not affect the global capabilities of the actuator.

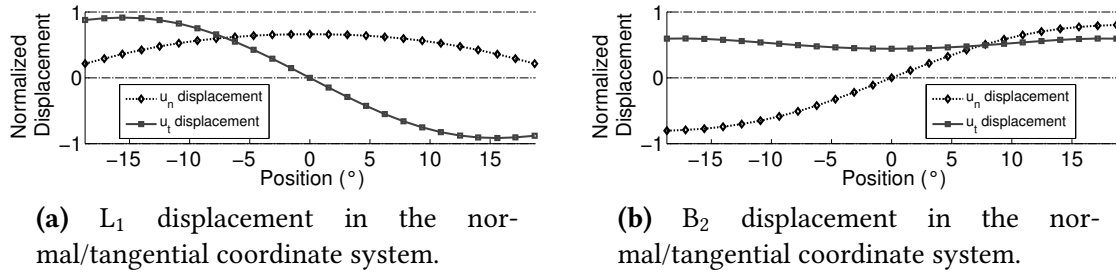


Figure 3.8: Normalized modes displacements at the contact interface. Displacements are expressed in the normal/tangential coordinate system, as a function of the position angle β described in figure 3.7.

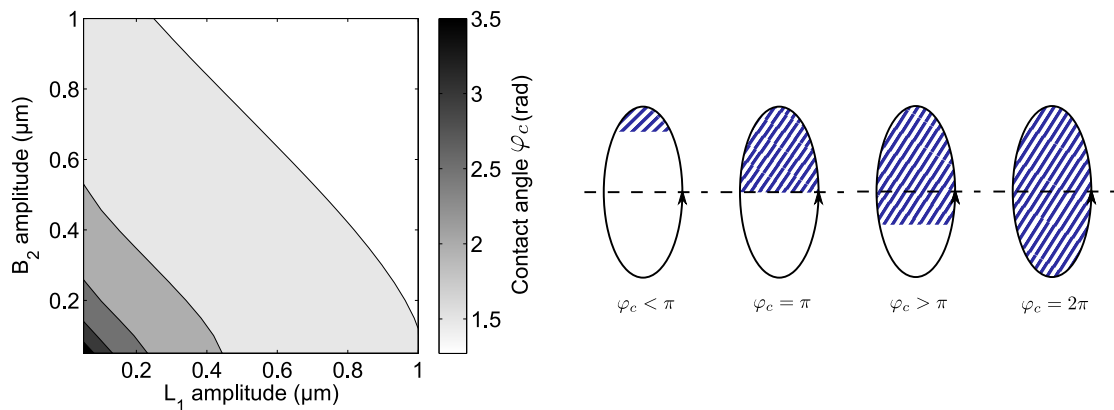
In the following studies, these normalized amplitudes will be used as input for the contact model. An actuator with an epoxy contact layer of 1mm is considered. A Young's modulus of 10 GPa is assumed with a friction coefficient of 0.2 between epoxy and aluminum. The motor is modeled with a small static friction torque of 0.1mN.m that corresponds to the friction torque caused by common bearings.

3.4 Mode displacement amplitudes

The first characteristic that is analyzed in the contact model is the mode displacement amplitudes. Amplitudes between 0 and $1\mu\text{m}$ are analyzed at a 1N preloading force considering an actuator with its total length of contact against the rotor. Contact time, output speed, torque and power are discussed along with the contact efficiency of the actuator.

3.4.1 Contact time

The amplitudes of the modes have a direct effect on the contact phase angle φ_c which represents the time during which the actuator is in contact with the rotor (see figure 3.9b). As discussed in the previous section, since the both modes have important contributions to the normal amplitude at the contact interface of the actuator, both modes should affect the average contact time along the actuator surface. Figure 3.9 shows the evolution of contact time as a function of both modes amplitudes. It shows a comparable effect of each mode amplitude on φ_c , with a diminution of contact time as amplitude is increased. The L_1 mode has a slightly more pronounced effect and, at a constant $0.2\mu\text{m}$ in bending mode amplitude, it is possible to observe a contact angle below 1.5 rad (for a $0.95\mu\text{m}$ L_1 amplitude). With a constant $0.2\mu\text{m}$ L_1 amplitude, a $1\mu\text{m}$ B_2 amplitude is not sufficient to bring contact time below 1.5 rad. Contact time decrease is non linear, with a fast decrease from 3.5 rad to 2.5 rad and a slower decrease with higher the amplitudes.



(a) Contact phase angle φ_c as a function of both displacement amplitudes.

(b) Representation of the portion of the elliptical motion during which stator is in contact with the rotor (hatched area) as a function of contact angle φ_c .

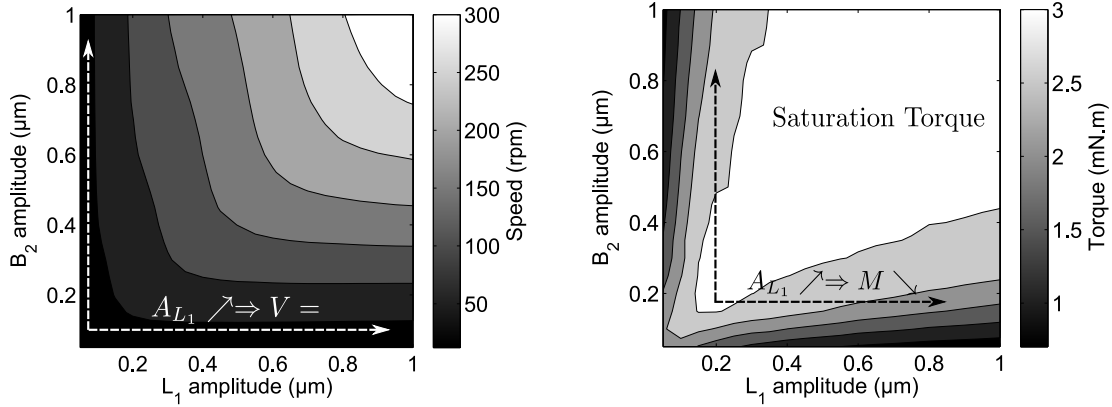
Figure 3.9: Evolution of mean contact time along the contact area with respect to both mode amplitudes at $P_0 = 1N$. The actual considered parameter is the contact phase angle φ_c , it is often referred to as *contact time* to avoid the confusion with the angle of the movement at contact interface. Since the contact phase angle changes along the surface of the actuator, an averaged value is considered.

3.4.2 Motor output characteristics

The mechanical output characteristics can be observed as a function of the modes amplitudes. From the contact time evolution it can be expected that a saturation torque will be reached as φ_c decrease is slowed down. Speed should not find a saturation point since an increase in

3.4. MODE DISPLACEMENT AMPLITUDES

the amplitude of the mode will cause stator tangential speed to be higher. Figure 3.10 and 3.11 sums up the model predictions.



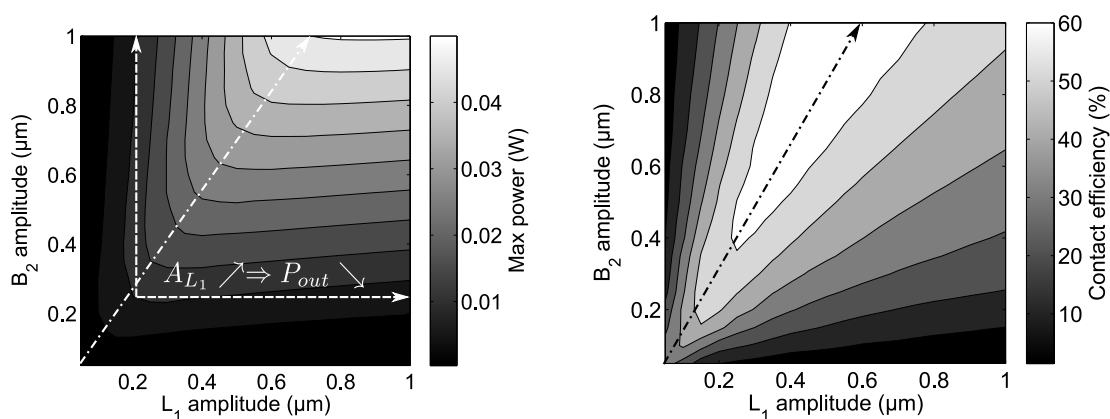
(a) Evolution of speed with respect to both modes amplitudes at $P_0 = 1N$. At low amplitude, when one mode amplitude is kept constant (dotted white lines), the speed is not affected by a change in the other mode amplitude. No saturation is observed and speed keep increasing above $1\mu\text{m}$ amplitude.

(b) Evolution of torque with respect to both modes amplitudes at $P_0 = 1N$. A saturation torque is reached above $0.2\mu\text{m}$ (for both modes at the same amplitude). An increase in the amplitude does not always result in a increase in torque M (see dotted arrows).

Figure 3.10: Evolution of speed and torque characteristics as a function of the two mode displacement amplitudes.

Figure 3.10a shows the evolution of speed as a function of mode amplitudes. Both amplitudes have comparable effect and should be increased in order to improve speed. A threshold effect is observed and for example if B_2 is increased up to $1\mu\text{m}$ but L_1 is kept at low amplitude ($<0.1\mu\text{m}$), the speed does not increase much. This confirms the fact that both modes are necessary for proper motor operation.

Figure 3.10b shows the evolution of torque as a function of mode amplitudes. The first characteristic that can be observed is the saturation torque of 3mN.m which is reached when B_2 and L_1 amplitudes are both slightly over 200nm . It is represented as a large white area. Further increase in the amplitude do not result in any torque improvement. It can also be noted that an increase in mode amplitude do not necessary result in an improvement of the transmitted torque. In figure 3.10b, the dashed arrows show this phenomenon. As saturation torque is reached, an increase in L_1 mode amplitude while keeping B_2 mode amplitude constant result in a drop of the maximum transmitted torque. This is due to a diminution of the average contact time that is not completely compensated by the increase in the normal force $P = k(u_n - u_n^a)$. Therefore, the average transmitted force during a period is reduced. The torque evolution confirms the importance of both amplitudes to obtain interesting torque performance.



(a) Evolution of maximum power output with respect to both mode amplitudes at $P_0 = 1N$. It is observed that an increase in one amplitude can result in a drop of output power that may affect greatly motor efficiency.

(b) Evolution of contact efficiency with respect to both mode amplitudes at $P_0 = 1N$. A B_2 amplitude 1.3 times higher than L_1 amplitude result in a better contact efficiency and therefore reduced generated heat at the interface as compared to output mechanical power.

Figure 3.11: Evolution of output power and contact efficiency as a function of the two modes amplitudes.

Figure 3.11a represents the evolution of output power as a function of mode amplitudes. The output power does not observe a saturation point since speed is always increased by an augmentation of the mode displacement. It is observed that an increase in one mode amplitude while the other is kept constant may result in a drop of the output power. This has an important effect on motor efficiency as an augmentation of L_1 mode amplitude will require more electrical energy to be injected and since it results in a drop of the output power, the total motor efficiency decreases. The dotted-dashed line represents the path where output power is best for a given $\sqrt{A_{L_1}^2 + A_{B_2}^2}$. If both modes have the “same cost” in terms of energy usage, this will be the path for best efficiency. Unfortunately both modes do not have the same damping factors, and an increase of 1W electrical input for L_1 mode excitation is not likely to have the same effect on mode amplitude as 1W additional power for B_2 mode excitation.

Figure 3.11b represents the evolution of the contact efficiency, that is to say the energy lost in contact sliding as compared to the output energy. Bending mode have a beneficial effect on contact efficiency. The dashed-dotted arrow shows that a B_2 amplitude about 1.3 times higher than L_1 amplitude results in a better contact efficiency with a maximum of 60% obtained at a $1\mu\text{m}$ amplitude on the bending mode and 600nm on longitudinal mode. Contact efficiency does not give information about actual efficiency of the actuator, but about heat generation due to friction as compared to the mechanical output power.

3.5 Preloading force

In this study the effect of preloading force on the actuator performance is analyzed. The layer is kept at 1mm thickness, with the full area in contact. Maximum amplitudes of both modes are set to $1\mu\text{m}$.

3.5.1 Contact time

Similarly to the amplitude parameter, the preloading force affects contact time and therefore the average tangential speed of the actuator. Figure 3.12 shows the evolution of the average contact phase angle φ_c as a function of the preloading force. The relation shows a fast increase of contact time between 0 and 5 N which slows down until a critical preloading force is reached at ~ 40 N. A constant contact condition ($\varphi_c = 2\pi$) is kept for higher preload. The output torque is expected to increase as preloading force increases since the contact time and average generated tangential force is improved. Speed, on the other hand, is reduced as contact time increases because average tangential speed is lowered.

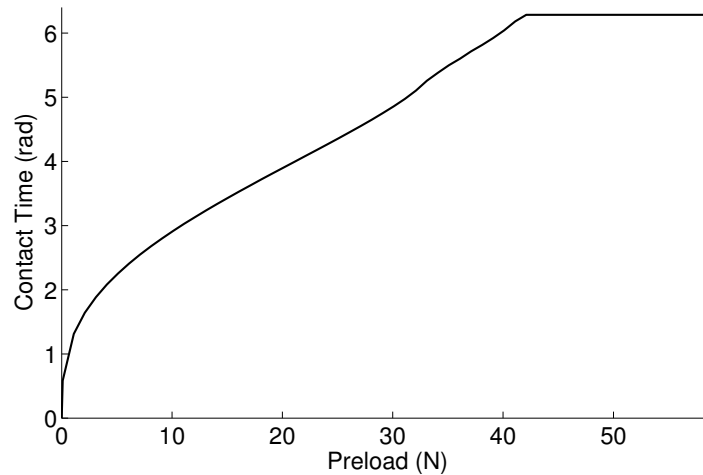


Figure 3.12: Mean contact phase angle φ_c along the contact surface vs preloading force for a given amplitude of $1\mu\text{m}$ on both modes. A saturation effect is observed above 40N at which a constant contact condition is reached ($\varphi_c = 2\pi$).

3.5.2 Motor output characteristics

From the equations derived in section 3.2, the preloading force do not affect directly the torque of the actuator. P_0 is not directly taken into account in the generated tangential force. In fact, increasing the preloading force causes an increase in the contact phase angle, thus, the tangential force is applied for a longer time and the factor $u_n - u_n^a$ expressed in equation (3.7) is larger. The model shows (figure 3.13a) that for a given amplitude, torque increases with the preloading force but once full contact time is reached ($P_0 > P_c$, where

CHAPTER 3. CONTACT ANALYSIS: FROM VIBRATION TO MOTOR MECHANICAL OUTPUT

P_c is the critical force expressed in equation (3.19)), torque stops to increase because of a constant contact time. In the case of the considered model parameters, a maximum torque of 70 mN.m is observed at critical preloading force. On the opposite, mean tangential speed is reduced as contact time is increased. This causes a drop of the maximum speed of the rotor as preloading force is increased. This decrease is continuous, with no visible change as preloading force is above critical force.

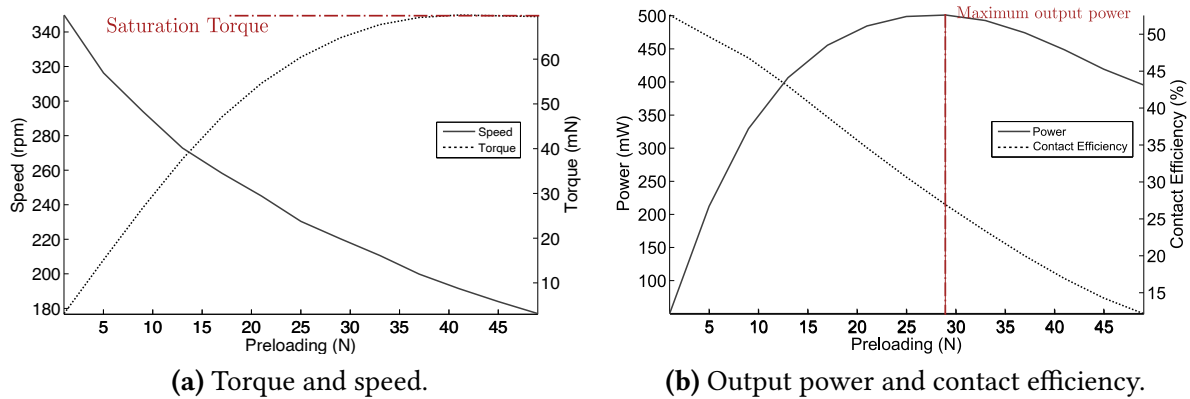


Figure 3.13: Motor output characteristics as a function of preloading force. The actuator is modeled for a $1\mu\text{m}$ maximum amplitude on both modes and a contact layer of 1mm thickness.

Power and contact efficiency are presented in figure 3.13b. The output power increases as preloading force increases and a maximum output power is found for a preload of 29N. It corresponds to a preloading force below the critical force, with a contact time of 4.75rad (i.e. rotor loses contact with stator for about 25% of the time). This indicates that there exists an optimal preloading force for actuator maximal efficiency. Contact efficiency drops as preloading force is increased. When contact time increases, more energy is lost through sliding. The additional energy lost in the sliding of the actuator is greater than the output energy gained from the increased preloading force, causing contact efficiency to decrease.

3.5.3 Torque versus speed characteristics

Contact model returns transient characteristics of the motor, therefore, it is possible to represent speed as a function of torque. Unlike a conventional electromagnetic motor, which has a linear relationship between torque and speed, ultrasonic motors have a non-linear response that depend highly on the contact properties. Figure 3.14 shows the evolution of speed as a function of torque for different preloading force. For a 41 N preloading force the response is flat and close to a linear relationship. As preloading force is reduced, an almost constant torque is observed at low speed. For example at a 5N preloading force, a 15mN.m torque is kept up to a 125 rpm speed. For higher speed, torque tends to have a linear dependence

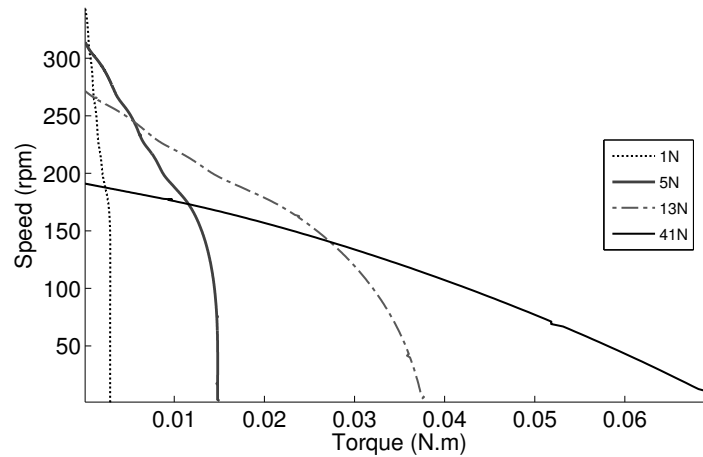


Figure 3.14: Evolution of speed vs torque actuator response as a function of preloading. As preloading force is reduced, torque tend to be almost constant for a large speed range.

with speed. This constant torque can be explained by a high average tangential speed during contact. Indeed, the torque diminution as speed increases is due to instants of contact during which the tangential speed of the stator is lower than the rotor speed which cause the generation of braking forces that slows down the rotor (as explained in figure 3.5). If the tangential speed is high and the contact time is low, the speed of the rotor has to be higher for braking forces to appear. One consequence of this phenomenon is that at low preloading force, the power peak of the actuator tends to be at low speed. As preloading force is high, it tends to be close to electromagnetic motors power peak which is at half maximum speed of the motor.

3.6 Contact layer stiffness

In this section, it is proposed to observe the influence of contact layer stiffness on the motor mechanical characteristics. Contact layer stiffness is defined as $k = \frac{E_y S_c}{h}$ where E_y is the Young's modulus of the contact layer, S_c the area of contact and h the thickness of the layer. It is possible to increase the stiffness of the layer by either increasing Young's modulus or decreasing contact layer height (S_c is difficult to vary since it depends on the actuator geometry). It is proposed to observe the influence of a change in the height of the contact layer on the properties of the actuator. Modes amplitudes are 500nm and the entire contact area is in contact with the rotor.

3.6.1 Contact time

The contact time increases as the layer thickness increases (i.e. stiffness decreases). Figure 3.15 shows a symmetric effect of layer thickness and preloading force on contact time. This

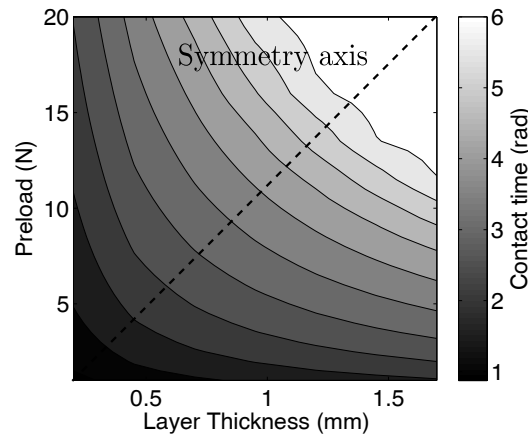


Figure 3.15: Contact phase angle φ_c as a function of the layer thickness and the preloading force P_0 . The symmetry axis shows a common effect of preloading force and contact thickness on the contact phase angle φ_c .

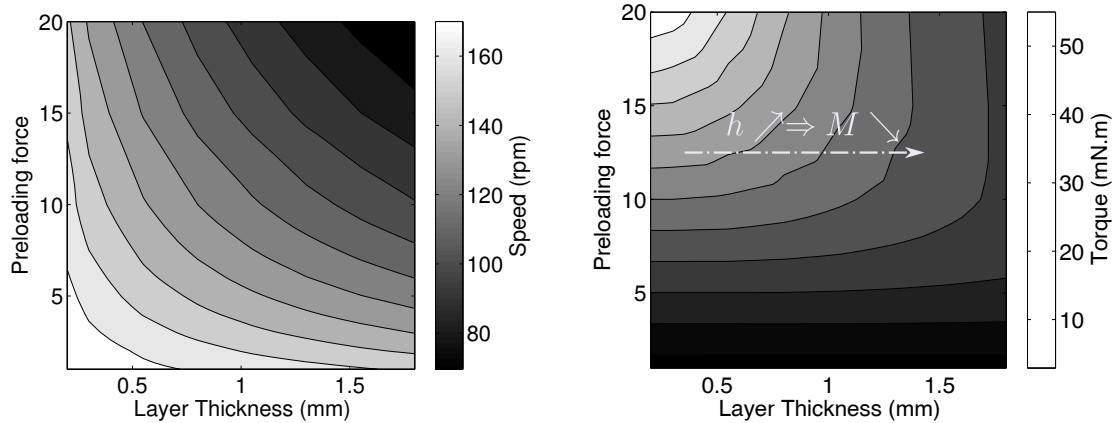
symmetry is expected from equation (3.17) which shows that contact time depends on the ratio $\frac{2\pi P_0}{k}$. It means that at lower layer thickness, higher torque can be reached since the critical preloading force P_c is higher. Another result that can be expected is an increased maximum speed for a given preloading force since a reduced contact time implies an increased average tangential speed during contact at the interface.

3.6.2 Motor output characteristics

Figure 3.16 shows the evolution of speed and torque as a function of layer thickness and preloading force. A reduction of layer thickness causes the output speed of the motor to be higher for a given preloading force. This is in accordance with a reduction of contact time and an increased average tangential speed. Figure 3.16a shows a symmetrical graph indicating that the relative influence of layer thickness and preloading force on motor speed is the same, and that at constant mode amplitudes, the contact time is the only parameter that influences speed of the motor.

Torque presented in figure 3.16b shows that the influence of preloading force and contact thickness is different. At low preloading force, a change in layer thickness does not visibly affect the output torque of the motor. At these forces, the contact time is low and a saturation torque similar to the one discussed in section 3.4 on amplitude effect is likely to be reached. As preloading force is increased, changes are observed with a diminution of the maximum transmissible torque as layer thickness is increased. This is essentially due to the maximum contact time which is reached at higher preloading force when the contact layer is thin.

Figure 3.17 shows the evolution of maximum output power and contact efficiency as a function of layer thickness and preloading force. It shows that the output power is maximal where preloading force is maximal and contact layer thickness is minimal. The preloading



(a) Evolution of speed as a function of layer thickness and preloading force for mode amplitudes of 500nm. A reduction of contact layer thickness causes an increased stiffness and a higher rotor speed at a given preloading force. The symmetry of the graph suggests a high dependence of rotor speed on the contact time.

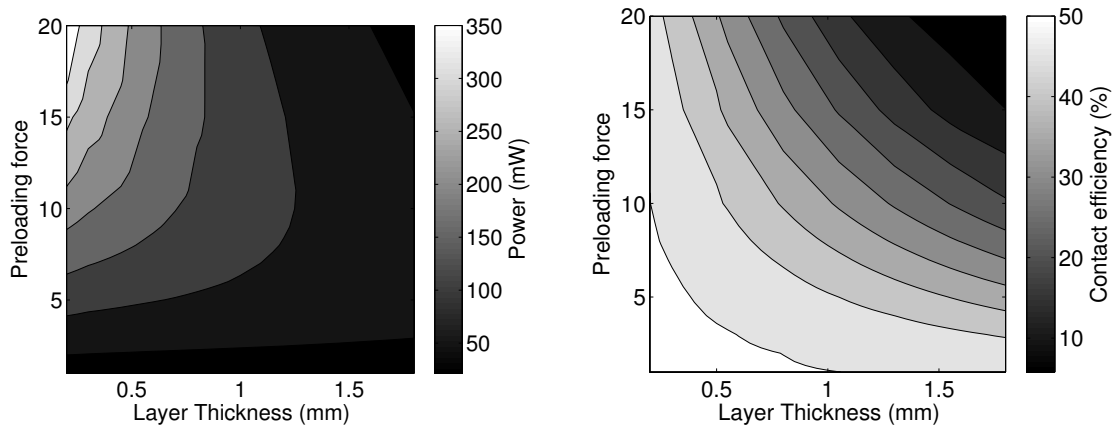
(b) Evolution of torque as a function of layer thickness and preloading force for mode amplitudes of 500nm. At low preloading force the layer thickness does not affect maximum output torque. At higher preloading force, a lower thickness causes the output torque to be higher.

Figure 3.16: Evolution of speed and torque characteristics as a function of the layer thickness and preloading force.

force affects maximum transmissible torque while contact layer stiffness keep the contact time low so as to obtain a high rotor speed. At low preloading force, the effect of the layer thickness is low and increases as preloading force increases. This is due to low contact time variations at low preloading force. As preloading force increases, the effect of layer thickness on output power is much more visible since contact time is high and the increase in layer stiffness allows to reduce the contact time. Contact efficiency is high for low preloading forces and low layer thickness. Its variations are highly dependent on contact time as the graph is very similar to contact time evolution. As contact time is reduced, the slipping time of the stator against the rotor is shorter and the dissipated energy due to sliding friction is lower. These observations are also valid for a change of contact material. A stiffer material is equivalent to a diminution of layer thickness.

3.7 Contact length

The contact length is one of the properties that make the novelty of the actuator proposed in this work. It is possible to apply the contact model to different contact layer lengths and analyze how it may affect the actuator mechanical characteristics. In this study, the length of the contact is changed. The extremities of the actuator are always kept in contact with the rotor and the contact area is increased symmetrically from the extremities to the



(a) Evolution of output power with respect to layer thickness and preloading force for mode amplitudes of 500nm. The maximum power point is reached at low layer thickness (high stiffness) and high preloading force. The preloading force causes the maximal transmissible torque to increase while layer thickness causes the contact time to stay low enough so that rotor speed is high.

(b) Evolution of contact efficiency with respect to layer thickness and preloading force for mode amplitudes of 500nm. The evolution of contact efficiency is symmetric with respect to preloading force and layer thickness. It shows that contact efficiency is essentially dependent on contact time and that it is improved with a low contact time (i.e. low preloading force and low layer thickness).

Figure 3.17: Evolution of power and contact efficiency as a function of the layer thickness and preloading force.

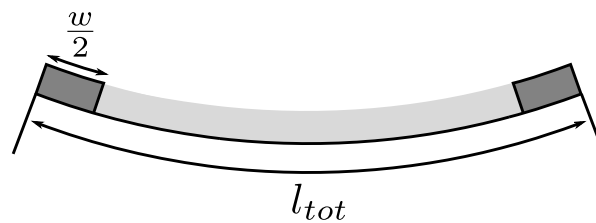


Figure 3.18: Definition of the parameters used for the change in contact length. w is defined as the length of the contact used for actuation.

center of the actuator until full contact is reached (see figure 3.18). Lengths of contact w between 1mm to 10mm are considered and the maximum length of the contact area is $l_{tot} = 40.5[\text{deg}] \frac{\pi}{180} \times 15[\text{mm}] = 10.5\text{mm}$. The preloading force is distributed all over the contact area so that locally the pressure is decreased when the contact length is increased (with constant P_0). The contact model is applied through a set of preloading forces between 1 and 20 N at an amplitude of 500 nm on both modes.

3.7.1 Contact time

A map of contact time as a function of preloading force and contact length is shown in figure 3.19. As discussed before, contact time increases as the preloading force is increased. Because

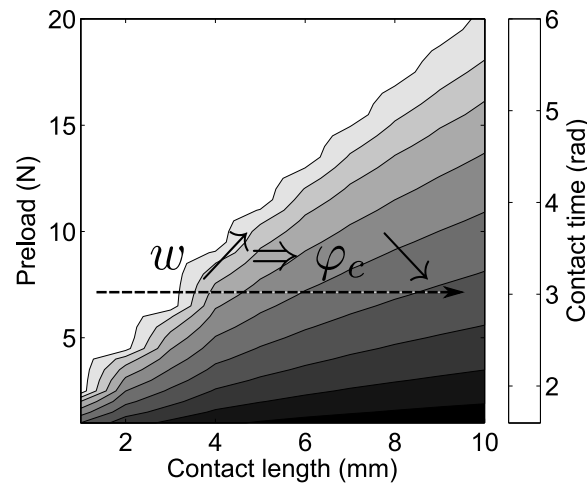


Figure 3.19: Mean contact time φ_c as a function of the length of contact w and preloading force P_0 . When contact length is increased, preloading force is better distributed, causing the mean contact time to decrease.

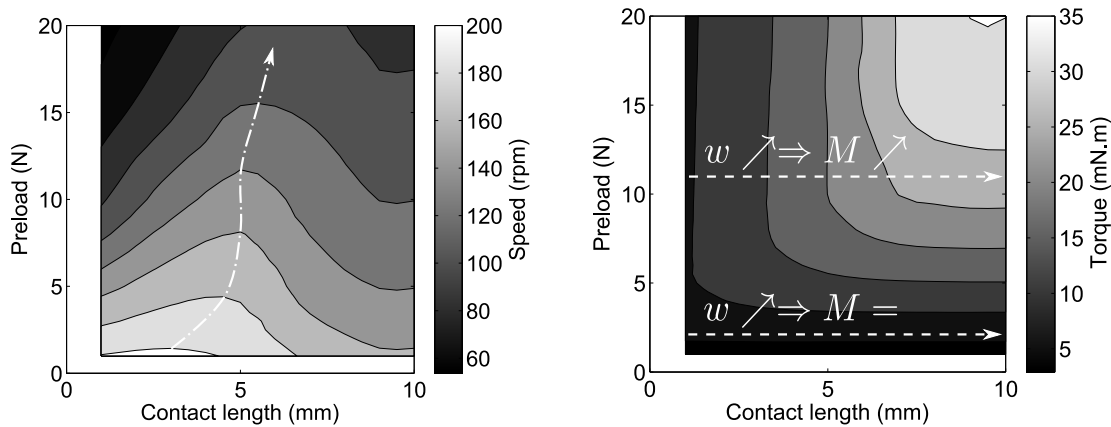
of the distributed preloading force, the critical force for which $\varphi_c = 2\pi$ increases as contact length is increased. Therefore the maximum transmissible torque might be improved by this phenomenon and a higher output power may be reached, indicating better efficiency of the actuator. On the other hand, the amplitudes are not the same along the actuator, and an increase in contact length might include non-constructive contact motions that may affect motor performance.

3.7.2 Motor output characteristics

Torque and speed characteristics of the motor are presented in figure 3.20. The maximum speed is reached at low preloading force where contact time is low. The diminution of the average contact time has a role along with the newly included points of contact that may reduce the average tangential speed during contact and along the contact area. For a given preloading force, there is an optimal length where speed is maximum. This optimal length is represented as a dotted-dashed arrow in figure 3.20a. The result shows that an increase of the contact length as preloading force is increased provides better speed performance. The optimal contact length for maximum speed is about 3mm at 1N preload. As preloading force is increased to 15N, a contact length of 5mm is optimal.

Torque is improved by an increase in the contact length. As contact length increases, the preload is better distributed over the contact area and contact time is reduced. Therefore, the critical preload and maximum torque observed in figure 3.13a are reached at higher force and higher torque can be transmitted. Below the critical regime (i.e. at low preloading force), it could be expected that a larger contact area would produce less torque than the shorter one since contact time is reduced because of force repartition. Contact model shows that

CHAPTER 3. CONTACT ANALYSIS: FROM VIBRATION TO MOTOR MECHANICAL OUTPUT



(a) Motor speed as a function of contact length and preloading force. There is an optimal length for which motor speed is maximal. This length tends to increase as preloading force is increased. At low preloading force a contact length around 3 mm provides highest speed while above 15 N a contact length above 5 mm is optimal in terms of maximum reachable speed.

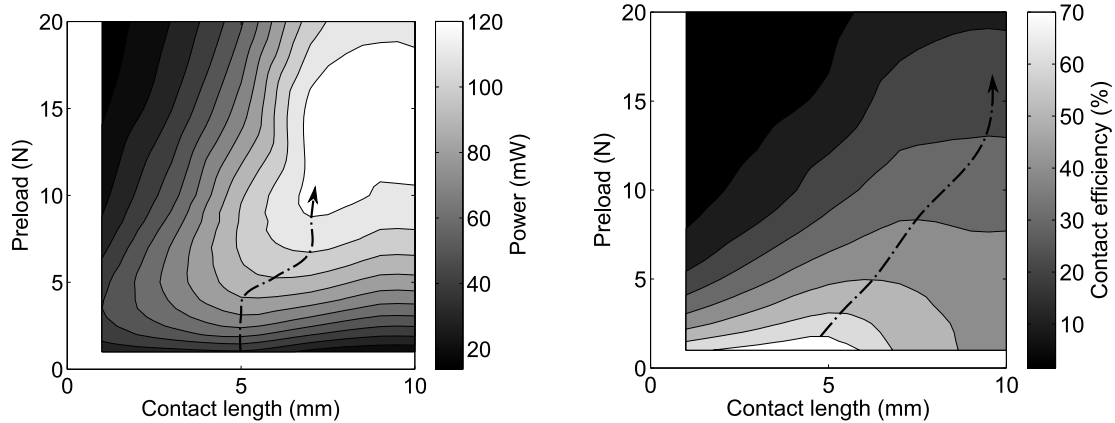
(b) Maximum transmissible torque as a function of contact length w and preloading force. At low preloading force, the torque is not affected by a change in contact length. With preloading force above 4 N, the maximum torque is increased when the contact length is increased.

Figure 3.20: Evolution of speed and torque as a function of contact length and preloading force.

similar torque is observed, therefore confirming the constructive interactions between the different contact points along the actuator. The benefits of an increased contact length on torque become visible for preloading forces above 4 N.

Output power and contact efficiency are represented in figure 3.21. An optimal contact length value for best output power can be found for a given preloading force. It is shown as a dotted-dashed arrow. This optimal value tends to increase as preloading force is increased. A contact length of 5 mm is optimal at a 1 N preloading force while a 7 mm contact length provides better output power at a preloading force of 8.5 N. Motor output characteristics are results that should be considered carefully since the model does not take into account the possible losses in the vibration caused by an increase of the contact length. However, the result shows that in terms of contact, without considering a possible damping effect, an adaptation of the contact length depending on the preloading force may improve output power and efficiency of the motor.

Contact efficiency is presented in figure 3.21b. An optimal contact length for maximal contact efficiency exists at a given preloading force. This optimal length tends to increase as preloading force increases and is represented as a dashed-dotted black arrow. This optimal length is a tradeoff between contact time minimization and tangential speed maximization.



(a) Evolution of motor output power as a function of contact length and preloading force. The optimal path for best output power is shown as the dotted-dashed arrow. It indicates an optimal contact length of 5mm at low preloading force that tends to be larger as preloading force is increased.

(b) Contact efficiency as a function of contact length and preloading force. The optimal contact length for maximum contact efficiency at a given preloading force is shown as a dotted-dashed black arrow. It shows that an increase in the contact length is interesting to improve contact efficiency as preloading force increases.

Figure 3.21: Evolution of output power and contact efficiency as a function of contact length and preloading force.

An increase in contact length reduce contact time while inclusion of points with low tangential speed may reduce contact efficiency.

3.8 Frequency response of the actuator

One last characteristic that is proposed to be analyzed is the frequency response of the actuator and more specifically the influence of mode non-degeneration on the actuator performance. In practice, it is almost impossible to obtain a perfect match between both mode frequencies and it is therefore interesting to observe how mode separation influences the actuator response.

3.8.1 Modes frequency response

A typical mode frequency response for the two vibrations modes is assumed. It is proposed to consider the modes as classic resonant systems with a normalized amplitude. The response is defined by two parameters: resonant frequency f_s and quality factor Q_m . The resonance frequency defines the frequency point where normalized amplitude is 1 and the quality factor describes how the amplitude drops near this frequency. A typical example of modes responses is shown in figure 3.22. Bending and longitudinal modes are assumed to

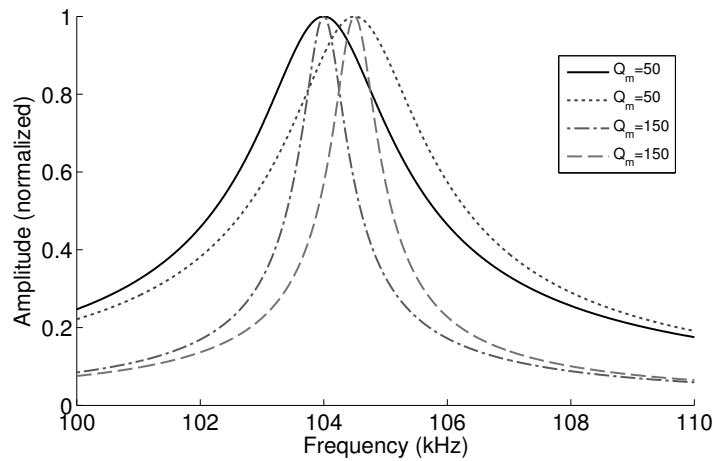


Figure 3.22: Example of two modes amplitude frequency responses for a 500 Hz shift and 50 and 150 quality factors. Two peaks with the same quality factor correspond to the response of two modes used together for actuation. Amplitudes are normalized so that Q_m only affects peak width.

have the same quality factor and in the figure two different quality factors with a 500 Hz frequency shift are presented. The two modes with $Q_m = 150$ have sharper frequency response than the modes with a $Q_m = 50$. Therefore the mode responses with a $Q_m = 50$ are assumed to be less sensitive to a mode shift than modes with higher quality factors. As it can be observed, the quality factor is assumed to only influence the distribution of the amplitude around the resonant point and it does not change the maximum amplitude. This assumption is not true since a high quality factor resonance has less mechanical dissipation and higher displacement amplitude. The objective here is to observe the influence of mode non-degeneration on frequency response and not on the maximum performance of the actuator, absolute speed and torque comparisons between different mechanical quality factors results are therefore incorrect.

3.8.2 Motor frequency response

Motor frequency response is computed at a fixed preloading force of 5 N and a peak amplitude of $1\mu\text{m}$ on both modes. Contact layer is 1 mm thick and full contact is considered. Figure 3.23 shows the evolution of velocity as a function of driving frequency for different frequency shifts Δf and quality factors Q_m . When modes are not shifted, the velocity follows the amplitude response of the actuator, with a peak velocity at resonance frequency. For the low quality factor case, as the modes are shifted one from another, the maximum velocity drops. When quality factor is higher (150), inversion in speed is observed due to the phase shift of first mode movement and is visible with a 1 kHz frequency shift. After the second resonance peak, the actuator has a similar speed response as in the case where the modes are not shifted. When the frequency shift between the two modes is increased,

3.8. FREQUENCY RESPONSE OF THE ACTUATOR

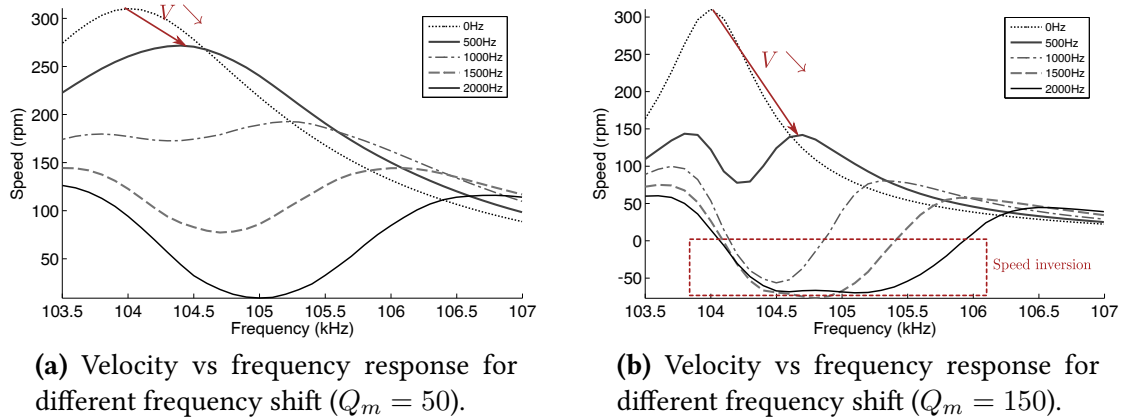


Figure 3.23: Effect of mode non-degeneracy on motor speed as a function of frequency.

the frequency span where speed is inverted increases also. This behavior is prejudicial to the motor operation since it reduces greatly motor efficiency. It might be useful in order to set-up a frequency controlled direction of motion if the phase shift between the modes cannot be controlled.

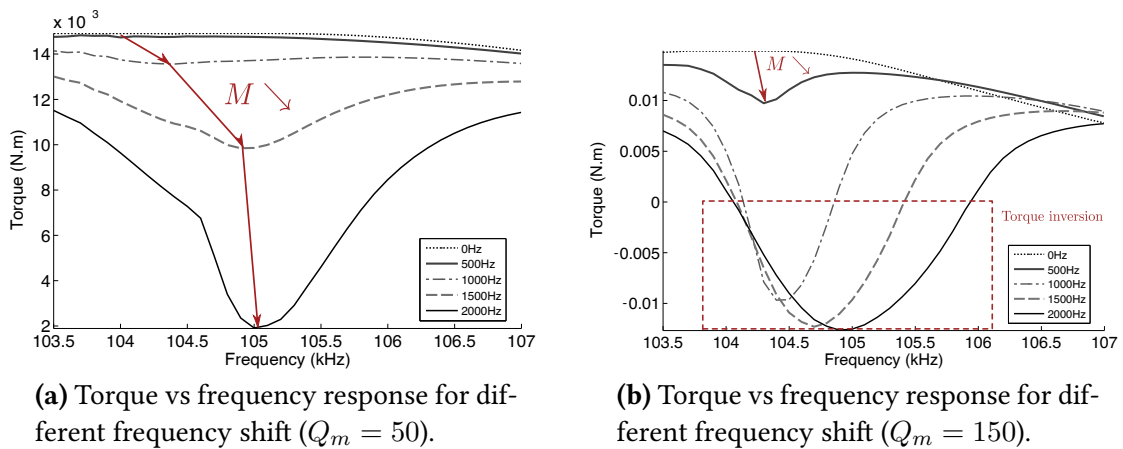


Figure 3.24: Effect of mode non-degeneracy on motor torque as a function of frequency.

Figure 3.24 shows the evolution of torque frequency response for different frequency shift and quality factor. For a 0 Hz shift (mode degeneracy), the torque has less important variations than speed with respect to frequency. The reason is that at the considered contact conditions, the torque does not vary much with respect to normal amplitude (an amplitude dependent saturation torque is reached). At $Q_m = 50$, mode separation starts to have a significant effect for a frequency shift of 1 kHz, with a drop of 1 mN.m in torque. At 2 kHz shift, the torque drops to 2 mN.m at 105kHz. For $Q_m = 150$, the effect is important at a frequency shift of 500 Hz with a torque decrease of 5 mN.m. An inversion of torque

direction is observed at a 1 kHz frequency shift. Mode non-degeneracy affects similarly speed and torque, with high loss in terms of actuator performance.

3.8.3 Maximum output power

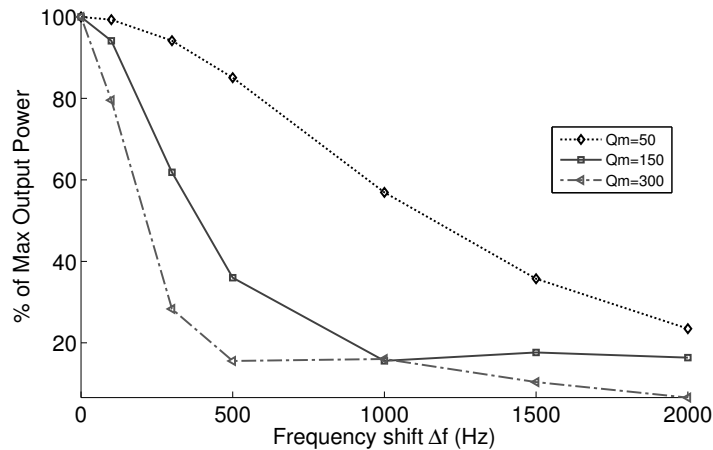


Figure 3.25: Evolution of maximum output power as a function of frequency shift between the two modes.

A good indication of how mode frequency shift is prejudicial to the actuator operation is the output power. Figure 3.25 shows the evolution of the output power as a function of the frequency shift for different quality factors. It can be observed that a 1kHz shift with $Q_m = 50$ causes the output power of the actuator to drop to 60% of the maximum output power. At a quality factor $Q_m = 150$, the consequences of a 1kHz shift are much more important with an output power below 20%. These observations show how much the proposed process for mode tuning in section 2.4 is important.

3.9 Conclusion

In this chapter, the conversion of vibration to rotor rotation is described. A contact model is proposed and applied to the actuator. It is used to predict the motor output characteristics as a function of displacement amplitudes, preloading force, contact layer properties and mode frequency shift. The model leads to several recommendations for the ultrasonic motor design:

- The two modes should be of the same amplitude for optimal motor performance.
- The torque of the actuator strongly depends on preloading force. Above the critical preloading force, the transmitted torque is saturated. This critical preloading force can be increased by a contact time decrease. A normal amplitude increase or a stiffer contact layer reduce the contact time.

- The speed of the actuator depends on mode amplitude and contact time. An important tangential speed is associated with a large rotor speed. Speed is also improve by a contact time reduction.
- The contact layer length modifies the motor properties. A large contact area can be useful to provide higher torque, since it distributes the preload hence reducing the contact time.
- As modes frequencies are set apart, the output power of the motor decreases. An actuator with low quality factor is less sensitive to this frequency shift. As quality factor increases, inversions of rotation direction are observed.

Electrodes pattern: Electrical energy to mechanical energy conversion

4

Contents

4.1	Introduction	96
4.2	Electromechanical model of a piezoelectric resonant actuator	96
4.2.1	Admittance circle	97
4.2.2	Mechanical quality factor	100
4.2.3	Electromechanical coupling factor	101
4.3	General discussion on electrode design and efficiency	102
4.4	Effective electromechanical coupling factor computation	104
4.5	Experimental verification	105
4.5.1	Geometry and mode selection	105
4.5.2	Experimental set-up	107
4.5.3	Experimental measurements	108
4.5.4	Influence of electrode pattern on quality factor	108
4.6	Optimization of the actuator	110
4.6.1	Electrodes for longitudinal-bending actuators	110
4.6.2	Single mode optimization	111
4.6.3	Two mode optimization problem	114
4.6.4	Relation between mode amplitude and equivalent circuit parameters	115
4.6.5	Ultrasonic motor complete modeling	117
4.7	Summary of the ultrasonic motor modeling method	119
4.8	Conclusion	120

4.1 Introduction

Several steps of the design of an ultrasonic motor have been presented. Chapter 2 focuses on the definition of the mechanical vibratory structure, the choice of its geometry and the vibration modes that are used. Chapter 3 describes the transformation of vibratory energy to rotation of the rotor. In this chapter, the first step of the energy conversion is described. The objective is to provide for an accurate description of the transformation from electrical to mechanical vibratory energy. An important design parameter that will be considered is electrode design. The chapter is organized in four different sections:

- The first section presents an equivalent electromechanical model which is commonly used to describe piezoelectric material properties around resonance. It is useful to explain how the energy conversion can be modeled.
- Important criteria for actuator excitation efficiency are determined. Two main parameters are found to be useful: quality factor Q_m and electromechanical effective coupling factor k_{eff} .
- An analytical model for k_{eff} determination as a function of the electrodes pattern is proposed and verified experimentally.
- A complete model of the actuator is proposed based on harmonic finite element analysis and results from chapters 2 and 3. It allows to optimize the electrode pattern for our actuator.

4.2 Electromechanical model of a piezoelectric resonant actuator

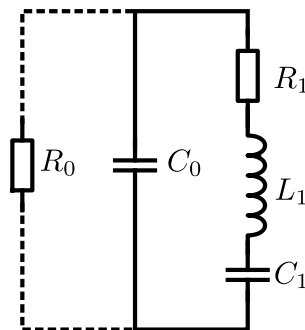


FIGURE 4.1: Equivalent Butterworth van Dyke (BVD) circuit used to model the behavior of a piezoelectric crystal response around resonance. C_0 and R_0 model the low frequency response of the actuator while the RLC circuit model behavior of the crystal around a resonance frequency.

4.2. ELECTROMECHANICAL MODEL OF A PIEZOELECTRIC RESONANT ACTUATOR

Piezoelectric materials have been studied for more than 130 years. Their working principle and physical properties are well known and understood. A detailed description of piezoelectric materials is proposed in appendix A. In this section, the equivalent model of a piezoelectric resonator around resonance is presented.

Numerous models have been used to describe the piezoelectric materials electromechanical conversion. The Mason model is useful to describe the behavior of a structure composed of a piezoelectric material and a resonant mechanical part and can, therefore, be used to model an ultrasonic motor (Budinger [82]). In our case, the piezoelectric material is the resonator and a good method to describe its behavior is an admittance analysis.

The coupling between the electrical and the mechanical characteristics of a piezoelectric crystal leads to the determination of a lot of information from an electrical measurement. Around resonance, the crystal frequency response can be considered as the response of a RLC circuit associated with a capacitor in parallel (C_0) which models the static capacitance of the crystal. A resistor R_0 can be added in parallel to model the dielectric losses in the crystal. This model is known as the Butterworth Van Dyke model (BVD) and shown in figure 4.1.

4.2.1 Admittance circle

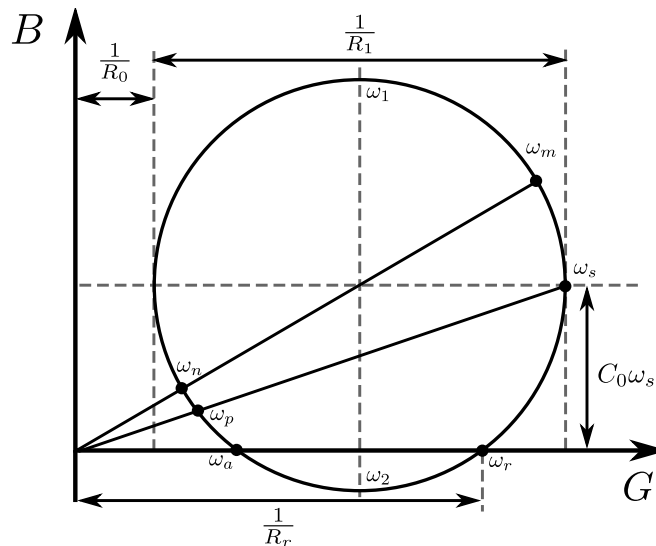


Figure 4.2: Typical Admittance circle around resonance. G is the real admittance and B the imaginary admittance. Characteristic frequencies are represented along with methods to obtain equivalent circuit properties.

One useful method to obtain the equivalent circuit parameters is the admittance circle. The admittance of the circuit described in figure 4.1 is:

$$Y = \frac{1}{R_0} + i\omega C_0 + \frac{1}{R_1 + i\omega L_1 + \frac{1}{i\omega C_1}} \quad (4.1)$$

$$Y = \frac{1}{R_0} + \frac{R_1}{R_1^2 + \left(L_1\omega - \frac{1}{C_1\omega}\right)^2} + i \left(C_0\omega - \frac{\left(L_1\omega - \frac{1}{C_1\omega}\right)}{R_1^2 + \left(L_1\omega - \frac{1}{C_1\omega}\right)^2} \right) \quad (4.2)$$

$$Y = G + iB \quad (4.3)$$

G is the real part of admittance called conductance and B , the imaginary part, is the susceptance. Around resonance, the graph $B = f(G)$ shows a circle which can be used to determine the equivalent circuit parameters (figure 4.2).

Static dissipation R_0 From the admittance equation, $\frac{1}{R_0}$ is defined as the minimum of real admittance G . The $\frac{R_1}{R_1^2 + \left(L_1\omega - \frac{1}{C_1\omega}\right)^2}$ term cannot be zero, but tends to very low values when ω is high or low as compared to resonance frequency. Thus, it is possible to find $\frac{1}{R_0}$ as the lowest conductance point of the circle.

Dynamic dissipation R_1 At the point where the real admittance is maximum we have:

$$\left(L_1\omega - \frac{1}{C_1\omega}\right)^2 = 0 \quad (4.4)$$

It corresponds to the point marked as ω_s on the figure 4.2, which is the series resonance frequency. The dynamic capacitance and inductance C_1 and L_1 compensate so that there is only the dynamic dissipation R_1 in the dynamic branch. Looking at the figure, $\frac{1}{R_1}$ can be computed as $\max(G) - \frac{1}{R_0}$ which is the diameter of the circle.

Dynamic capacitance C_1 and inductance L_1 In order to find the dynamic branch parameters, everything cannot be read from the circle and the frequencies are also important to take into account. The admittance circle has to be used in conjunction with regular frequency-admittance plots. As it has been seen earlier, the point where the real admittance is maximal corresponds to the frequency ω_s , the series resonance frequency. This frequency can easily be found using a $G = f(\omega)$ graph. Admittance circuit equation shows that:

$$\begin{aligned} L_1\omega_s - \frac{1}{C_1\omega_s} &= 0 \\ L_1C_1\omega_s^2 &= 1 \\ \omega_s &= \sqrt{\frac{1}{L_1C_1}} \end{aligned} \quad (4.5)$$

4.2. ELECTROMECHANICAL MODEL OF A PIEZOELECTRIC RESONANT ACTUATOR

It is also possible to find the extrema of the susceptance which correspond to ω_1 and ω_2 on figure 4.2. They are frequencies where the real part of the admittance is equal to $1/R_0 + 1/(2R_1)$. So it is possible to write for these points the equations:

$$\frac{R_1}{R_1^2 + \left(L_1\omega - \frac{1}{C_1\omega}\right)^2} = \frac{1}{2R_1} \quad (4.6)$$

$$\frac{2}{1 + \left(\frac{L_1\omega - \frac{1}{C_1\omega}}{R_1}\right)^2} = 1 \quad (4.7)$$

$$\left(\frac{L_1\omega - \frac{1}{C_1\omega}}{R_1}\right)^2 = 1 \quad (4.8)$$

$$L_1\omega - \frac{1}{C_1\omega} = \pm R_1 \quad (4.9)$$

$$C_1L_1\omega^2 \pm R_1C_1\omega - 1 = 0 \quad (4.10)$$

This second order polynomial has four solutions:

$$\omega_{\pm}^2 = \frac{R_1C_1 \pm \sqrt{(R_1C_1)^2 + 4C_1L_1}}{2C_1L_1} \quad (4.11)$$

$$\omega_{\pm}^1 = \frac{-R_1C_1 \pm \sqrt{(R_1C_1)^2 + 4C_1L_1}}{2C_1L_1} \quad (4.12)$$

The solutions ω_{\pm}^2 and ω_{\pm}^1 are not suitable because they correspond to negative values of the frequency ω . There are two solutions ω_{+}^1 and ω_{+}^2 that we choose to note ω_1 and ω_2 ($\omega_2 > \omega_1$) and correspond to the ω_1 and ω_2 shown on the figure 4.2. From (4.12) and (4.11):

$$\omega_2 - \omega_1 = \frac{R_1}{L_1} \quad (4.13)$$

Dynamic inductance can then be deduced:

$$L_1 = \frac{R_1}{\omega_2 - \omega_1} \quad (4.14)$$

And dynamic capacitance is deduced using the series resonance frequency:

$$\omega_s = \sqrt{\frac{1}{L_1C_1}} \quad (4.15)$$

$$C_1 = \frac{1}{\omega_s^2 L_1} \quad (4.16)$$

The parameters found from the admittance circle analysis are a good initial guess for a non-linear regression of the full frequency data.

Specific frequencies Six specific frequencies are marked on figure 4.2:

- ω_m corresponds to the maximal admittance point, where current flowing in the element is maximal.
- ω_r corresponds to the frequency where the current is in phase with the voltage and the piezoelectric element has a purely resistive behavior.
- ω_s corresponds to the series resonant frequency, it is the frequency point where the current flowing into the dynamic branch is purely resistive and therefore corresponds to the resonance frequency of the dynamic part.
- ω_a corresponds to another point where the current is in phase with the voltage but it correspond to the minimum purely resistive admittance that can be reached and can be defined as an anti-resonance frequency.
- ω_p corresponds to the maximum real impedance point of the system. It is also known as the parallel resonance frequency.
- ω_n corresponds to the maximum impedance frequency, it is the frequency point where the current flowing into the piezoelectric element is at its lowest value.

When quality factor is high, one can consider that $\omega_m = \omega_r = \omega_s$ and $\omega_a = \omega_p = \omega_n$ [83]. This property is interesting for resonance tracking of the actuator. ω_s is difficult to track using an electronic circuitry but ω_r can be tracked using a phase measurement and ω_m can be tracked using a power measurement. Therefore, a high quality factor simplify resonance tracking of the actuator.

4.2.2 Mechanical quality factor

The quality factor is given by the ratio of the energy stored in the system to the energy lost per cycle. Considering the energy in the dynamic branch, it is possible to compute the mechanical quality factor of the system which will be the same as the quality factor defined in (2.22):

$$Q = 2\pi \frac{\text{Stored Energy}}{\text{Dissipated Energy per cycle}} \quad (4.17)$$

The maximum energy stored in the inductor is given by:

$$E_{\text{stored}} = E_L = \frac{1}{2} L_1 I_{\text{max}}^2 \quad (4.18)$$

The energy lost during one cycle is the energy dissipated in the resistor R_1 :

4.2. ELECTROMECHANICAL MODEL OF A PIEZOELECTRIC RESONANT ACTUATOR

$$E_{lost} = \int_0^{\frac{2\pi}{\omega_s}} R_1 I_{max}^2 \cos^2(\omega t) dt \quad (4.19)$$

$$E_{lost} = R_1 I_{max}^2 \frac{\pi}{\omega_s} \quad (4.20)$$

The quality factor is then given by:

$$Q_m = 2\pi \frac{E_{stored}}{E_{lost}} \quad (4.21)$$

$$Q_m = 2\pi \frac{\frac{1}{2} L_1 I_{max}^2}{R_1 I_{max}^2 \frac{\pi}{\omega_s}} \quad (4.22)$$

$$Q_m = \frac{L_1 \omega_s}{R_1} \quad (4.23)$$

It can also be written in terms of the dynamic capacitance C_1 given that $\omega_s = \frac{1}{\sqrt{C_1 L_1}}$.

$$Q_m = \frac{1}{R_1} \sqrt{\frac{L_1}{C_1}} \quad (4.24)$$

It has been shown earlier in equation (4.13) that the ratio $\frac{L_1}{R_1}$ can be expressed from frequencies of lowest and highest susceptance ω_2 and ω_1 thus:

$$Q_m = \frac{\omega_s}{\omega_2 - \omega_1} \quad (4.25)$$

The mechanical quality factor computed here is similar to the one defined in equation (2.21) and is useful to qualify the damping of the resonant motion.

4.2.3 Electromechanical coupling factor

The electromechanical coupling factor (k) is an interesting parameter to estimate the efficiency of the energy conversion in the actuator. The higher k is, the better the conversion from electrical to mechanical energy is performed. The electromechanical coupling factor is defined as the ratio of converted mechanical energy (or electrical energy in the case of a sensor) to the total stored energy in the device during one period (Yaralioglu et al. [84]):

$$k^2 = \frac{E_{mech}}{E_{tot}} = \frac{E_{mech}}{E_{elec} + E_{mech}} \quad (4.26)$$

For static cases, it can be computed using the piezoelectric coefficients of the material [85]. At resonance, an *effective* coupling factor is defined. From the equivalent circuit description, it is possible to write (Takano et al. [28]);

$$k^2 = \frac{E_{mech}}{E_{elec} + E_{mech}} = \frac{C_1}{C_0 + C_1} \quad (4.27)$$

$$k^2 = \frac{1}{1 + \gamma} \quad (4.28)$$

with

$$\gamma = \frac{C_0}{C_1} \quad (4.29)$$

γ is called the capacitance ratio of the considered resonance. The effective electromechanical coupling factor can be determined, at resonance, using the equivalent parameters C_0 and C_1 . It is also possible to define the electromechanical coupling factor as a function of characteristic frequencies [85]:

$$k_{eff}^2 = \frac{\omega_p^2 - \omega_s^2}{\omega_s^2} \quad (4.30)$$

Another definition of the electromechanical coupling factor is based on energy calculation in the device and is defined as the ratio of mutual elasto-dielectric energy squared to the geometric mean of stored electric and elastic energy [85]:

$$k^2 = \frac{U_{12}^2}{U_1 U_2} \quad (4.31)$$

Where U_{12} , U_1 and U_2 are computed from the state equations described in appendix A.

4.3 General discussion on electrode design and efficiency

When considering a resonant piezoelectric actuator several parameters can be used to characterize the efficiency of the resonant excitation:

Quality factor: Q_m characterizes the damping in the actuator. It is defined as the ratio of stored energy in the actuator to lost energy during one cycle. In a simple spring-mass-damper system it is directly linked to the properties of the system (stiffness, damping and mass) but not to the excitation whether it is its location or its amplitude. In a complex mechanical system, Q_m depends on the properties of the material, the geometry of the structure and the excited mode. The excitation only influences how much energy can be transferred to the mode during one period, but it does not influence how much energy can be stored as compared to the dissipated energy. When using a piezoelectric material, mechanical properties of the actuator depend on the electrical boundary conditions. An area of the actuator where a field is imposed have a different stiffness (c^E) as an area with open-circuit boundary condition (c^D). Therefore, the mechanical stored energy is different and quality factor

4.3. GENERAL DISCUSSION ON ELECTRODE DESIGN AND EFFICIENCY

is influenced. As an example, in the case of Ferroperm PZ26, the constant field stiffness c_{33}^E (123GPa) is 28% lower than the open-circuit stiffness c_{33}^D (158GPa). In the case of an ultrasonic actuator, we will consider the hypothesis that the actuator is mostly covered with electrodes thus leading to very low variation of quality factor influenced by electrode design (stiffness is assumed to be c^E everywhere).

Effective electromechanical coupling factor: The effective coupling factor k_{eff} represents the efficiency of the piezoelectric conversion in the case of a resonant actuator. It characterizes how much of the electric energy injected in the system is converted into mechanical energy and is highly associated to electrode design. Similarly to a resonant beam that is efficiently excited if the harmonic force is placed at a point where the displacement is important, the piezoelectric element vibration mode is efficiently excited where the strains or stresses are important (since the piezoelectric effect is directly linked to them). Therefore, the electrodes should be placed where modal strain or stresses are high in order to allow high energy injection in the resonant system. k_{eff} is an interesting parameter to characterize the efficiency of an excitation and should be the main parameter in electrode design of an actuator.

Excitation efficiency as a function of k_{eff}^2 and Q_m It is possible to give a full description of the efficiency of the excitation of a piezoelectric actuator as a function of the two parameters, k_{eff} and Q_m . Mechanical energy in a resonant piezoelectric structure is analogous to the energy in the dynamic branch of the Butterworth Van Dyke model that is given by:

$$E_d = \frac{1}{2}L_1 i_1^2 \quad (4.32)$$

where L_1 is the dynamic inductance and i_1 the current in the dynamic branch. At resonance, L_1 and C_1 impedance cancel so that:

$$i_1^2 = \left(\frac{U}{R_1}\right)^2 = \frac{U^2 Q_m^2 C_1}{L_1} \quad (4.33)$$

$$E_d = \frac{1}{2}U^2 Q_m^2 C_1 \quad (4.34)$$

For a given displacement amplitude, the energy losses are due to mechanical and dielectric losses. While mechanical losses are due to the material and the mechanical constraints of the actuator and cannot be affected by the electrode design, the dielectric loss is directly linked to the field and thus to the electrode area. The energy dissipated during one cycle is given by:

$$E_{loss} = \pi \varepsilon_0 \varepsilon_r E_0^2 \tan \delta_e \times A \times d \quad (4.35)$$

$$E_{loss} = \pi \varepsilon_0 \varepsilon_r U_0^2 \tan \delta_e \times \frac{A}{d} \quad (4.36)$$

$$E_{loss} = \pi \tan \delta_e C_0 U_0^2 \quad (4.37)$$

So that finally the actual ratio of stored mechanical energy to lost electrical energy during each cycle is given by:

$$\Gamma = \frac{E_d}{E_{loss}} = \frac{Q_m^2 C_1}{2\pi \tan \delta_e C_0} = \frac{Q_m^2 k_{eff}^2}{2\pi \tan \delta_e (1 - k_{eff}^2)} \quad (4.38)$$

This last equation gives the ratio of the useful energy to the lost energy. It shows that it is interesting to optimize k_{eff} and Q_m in order to obtain the best efficiency.

4.4 Effective electromechanical coupling factor computation

As discussed earlier, k_{eff} is an interesting parameter for optimizing electrodes of a piezoelectric resonant actuator. In this section, an analytical model in order to obtain a fast, practical tool for electrodes optimization is proposed. k_{eff}^2 can be defined as:

$$k_{eff}^2 = \frac{U_{12}^2}{U_1 U_2} \quad (4.39)$$

U_{12} the coupling energy, U_1 the elastic energy and U_2 the dielectric energy are computed from the state equations of piezoelectricity:

$$\frac{1}{2} \int_V T S^* dV = \frac{1}{2} \int_V c^E S S^* dV - \frac{1}{2} \int_V e^T E S^* dV = U_1 + U_{12} \quad (4.40)$$

The total electrical energy is given by :

$$\frac{1}{2} \int_V D E^* dV = \frac{1}{2} \int_V e^E S E^* dV + \frac{1}{2} \int_V \varepsilon^S E E^* dV = U_{12} + U_2 \quad (4.41)$$

S and T are the strain and stress in the actuator, E and D the electric field and displacement. e is the piezoelectric matrix, c^E the stiffness matrix at constant field and ε^S is the permittivity at constant strain. The star operator $*$ corresponds to the transposed conjugate of the considered matrix (self-adjoint operator). Considering the excitation of a in-plane mode of a plate with constant field electric boundary conditions, a relation between the out-of-plane modal strain S_3 and k_{eff} can be written. Based on the piezoelectric mathematical formalism explained in appendix A, the relation can be written as:

$$k_{eff}^2 = K \frac{\left(\int_{V_{electrode}} S_3 dV \right)^2}{A_{electrode}} \quad (4.42)$$

Where K is a constant depending on the properties of the actuator and the considered mode. S_3 is the out-of-plane strain and $A_{electrode}$ is the area of the actuator. The detailed derivation of this relation can be found in appendix B. For the simple case of an in-plane mode of a plate which has a delimited excitation electrode with constant field elsewhere, the electromechanical coupling factor can be optimized by considering the distribution of the out-of-plane strain S_3 .

4.5 Experimental verification

In order to verify the relationship developed for the optimization of the effective coupling factor, it is proposed to observe the influence of different electrodes patterns on resonance properties.

4.5.1 Geometry and mode selection

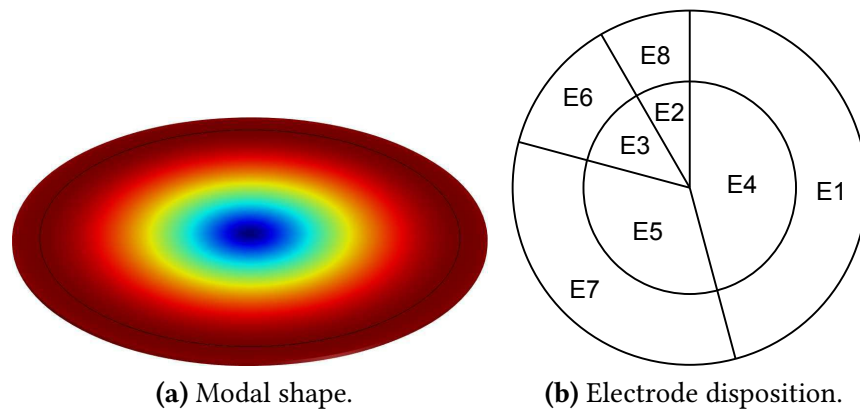


Figure 4.3: Modal shape and electrode disposition of the sample used for experimental verification. An in-plane mode with a circular symmetry is excited using various electrode patterns.

The sample that is used for validation of the model is a piezoelectric disk of 50 mm in diameter and 0.5 mm in thickness. The material used is a Lead Zirconate Titanate (PZT) ceramic Ferroperm PZ26. The top electrode of the sample is patterned as shown in figure 4.3b. The 8 electrodes allow for 255 different patterns to be tested and confronted to the model. Each electrode has an associated number and each electrode configuration corresponds to a 8 bit number, each bit corresponding to one electrode (see table 4.1).

TABLE 4.1: EXAMPLE OF AN ELECTRODE CONFIGURATION DESIGNATION.

Configuration number	Binary representation	E8	E7	E6	E5	E4	E3	E2	E1
100	1100100	On	On	Off	Off	On	Off	Off	Off

CHAPTER 4. ELECTRODES PATTERN: ELECTRICAL ENERGY TO MECHANICAL ENERGY CONVERSION

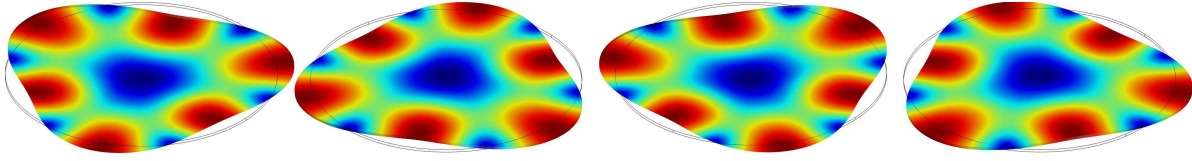


Figure 4.4: Four degenerating non-rotational invariant in-plane modes with the same modal shape. An infinity of modes with this same mode shape exist by rotation along the disc axis.

To simplify the theoretical calculation of k_{eff}^2 , a mode with a rotational invariance is chosen. This mode corresponds to the first radial mode of the disk. COMSOL finite element modal analysis shows it can be found at 44195 Hz with the modal shape in figure 4.3a. Choosing a mode with a rotational invariance simplify k_{eff}^2 computation for an arbitrary set of electrodes. Due to the circular symmetry of the disk, there exists an infinity of degenerating modes at the same frequency with the same mode shape. If modes are not rotational invariant (e.g figure 4.4), the electromechanical coupling factor of an electrode set will change for each degenerating mode. Although it is possible to compute theoretically the k_{eff}^2 for one mode, experimentally, there is no guarantee that it will be the excited mode as the degenerating mode with the best k_{eff}^2 will be excited. This phenomenon implies to find, by rotating the electrode set, the angle that gives the best k_{eff}^2 in order to compare experimental and theoretical data. Choosing a mode with rotational invariance makes the problem simpler since each rotation of the electrode results in exactly the same k_{eff}^2 .

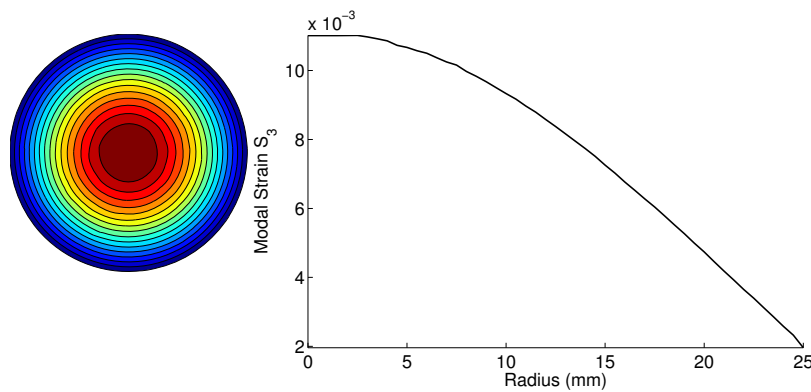


Figure 4.5: Strain S_3 distribution of the first radial mode of a piezoelectric disk as a function of the radius from the center of the disk.

The theoretical coupling efficiency for different sets of electrodes can be evaluated for each pattern using equation (4.42) and modal strain S_3 represented in the figure 4.5. Figure 4.6 shows that, although the shape of the mode is simple, it is possible to evaluate a large range of effective coupling factors with the same electrode area.

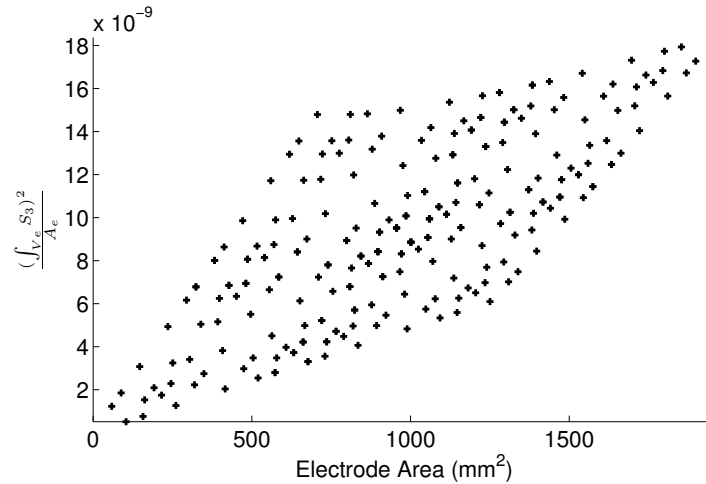


Figure 4.6: Theoretical total strain squared density versus electrode area for all possible electrode patterns.

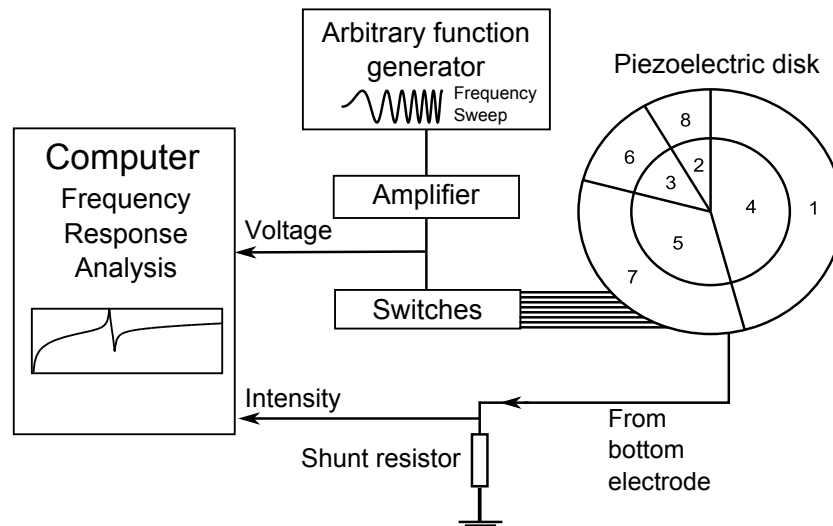


Figure 4.7: Experimental setup for admittance measurement. A frequency sweep is generated and amplified before being sent to the sample. A set of switches is used to select which electrodes are excited. Current is measured using a shunt resistor.

4.5.2 Experimental set-up

A scheme of the setup used to measure the resonance characteristics of the piezoelectric disk is represented in figure 4.7. An arbitrary function generator Tektronix AFG3021B is used to generate a frequency sweep (chirp signal between 10 and 120 kHz). This signal is amplified and sent through a series of switches that allow for connecting or grounding the patterned electrodes. Intensity measurement is performed using a shunt resistor. Both voltage and intensity are measured through a National Instrument PCI-6251 acquisition card. Admittance data are computed from raw voltage and intensity signals acquired at a 600 kHz sampling frequency. A fast Fourier transform is performed in Labview to obtain the frequency response of the system. These data are analyzed using a Butterworth van Dyke

(BVD) model computed with Matlab in order to obtain properties of the resonance. It is possible to evaluate k_{eff}^2 from the admittance model using the relation:

$$k_{eff}^2 = \frac{1}{1 + \frac{C_0}{C_1}} \quad (4.43)$$

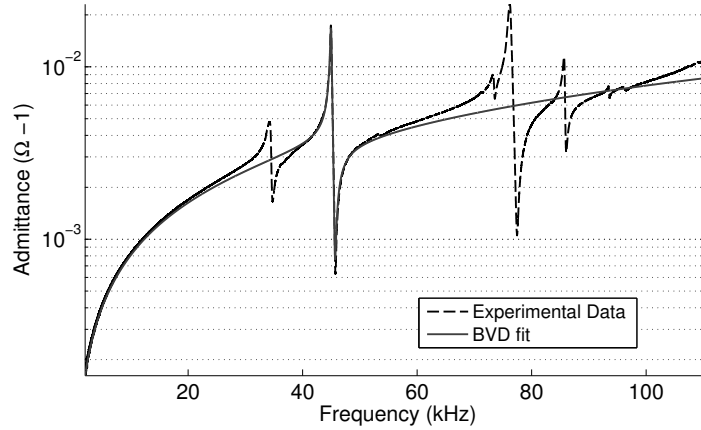


Figure 4.8: Fit of experimental data. The radial mode response is observed at 5V for the electrode configuration 1.

4.5.3 Experimental measurements

The patterns are tested through the set of switches. All non used electrodes are connected to the bottom electrode in order to have a zero electric field in passive areas of the piezoelectric element. An example of an obtained admittance curve is shown in figure 4.8. From the Butterworth van Dyke model fit, k_{eff}^2 is evaluated and compared to the analytical predictions. The figure 4.9 shows the correlation. A linear relationship is found, hence validating the semi-analytical model proposed for electromechanical coupling factor computation of a given electrodes set.

4.5.4 Influence of electrode pattern on quality factor

In theory, it is predicted that the quality factor is not influenced by the electrode pattern if the piezoelement has an imposed electric field boundary condition everywhere. The experimental measurements show that there is a dispersion of the quality factor as a function of the excited electrodes. For this comparison, quality factor is computed from the BVD model using the equation (4.24).

Figure 4.10a shows the evolution of the quality factor as a function of k_{eff}^2 . The quality factor clearly changes as a function of the excited electrode pattern. Although the correlation is not very clear, it can be noted that there is a decrease in Q_m as k_{eff}^2 increases. Since several different values of Q_m can be found for a single k_{eff}^2 , no direct correlation can be established.

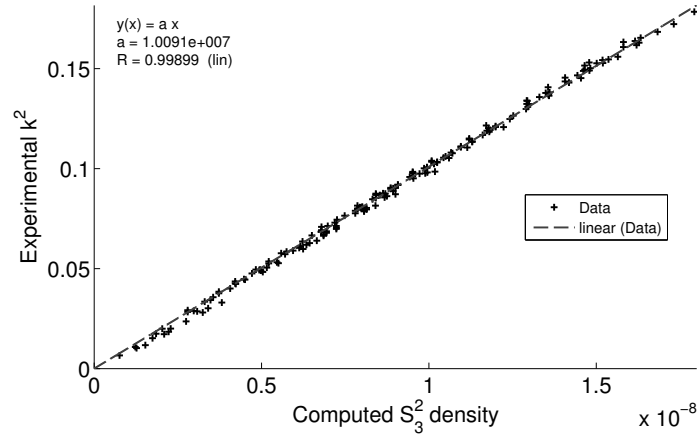
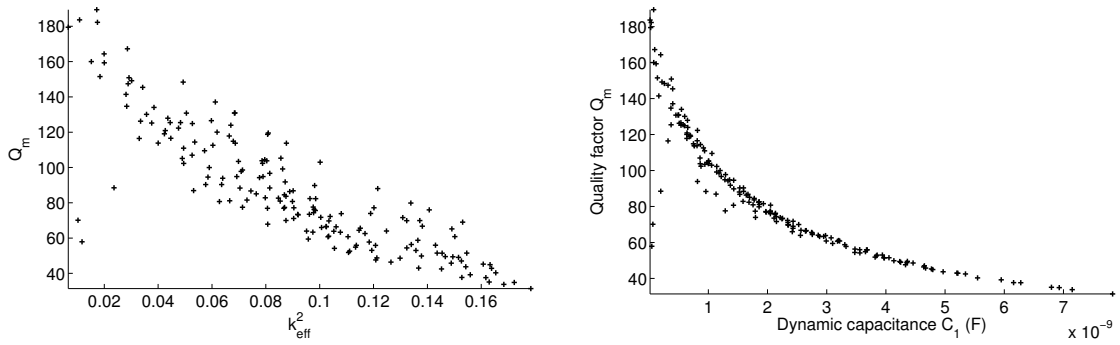


Figure 4.9: Experimental electromechanical coupling factor vs computed $(\int S_3)^2$ density. The result shows a linear correlation validating the development proposed earlier.

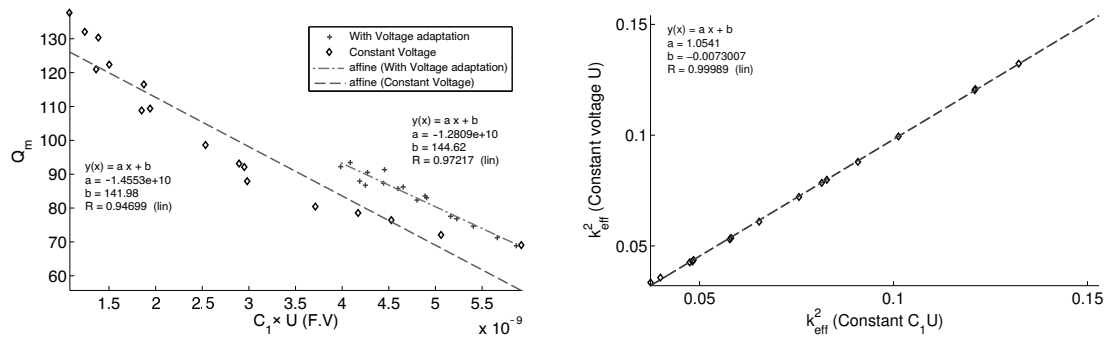


(a) Q_m as a function of effective coupling factor k_{eff}^2 . A global decrease is observed while no clear correlation between the two parameters can be observed.

(b) Q_m as a function of dynamic capacitance. A clear relation between the two parameters is observed.

Figure 4.10: Quality factor Q_m as a function of excitation parameters for constant voltage harmonic excitation.

Figure 4.10b shows the relation between dynamic capacitance C_1 of the equivalent model and quality factor Q_m . C_1 is a parameter that depends on excitation efficiency k_{eff}^2 and electrode capacitance C_0 . A clear relation between C_1 and Q_m is observed with a diminution of quality factor as dynamic capacitance increases. A hypothesis that can be considered is non-linear damping. It has been shown (Uchino and Hirose [86], Tashiro et al. [87]) that the damping $\tan \delta_m$ can be influenced by the vibration velocity and therefore the mechanical energy stored in the material. Supposing that Q_m is constant when mechanical energy is constant it would be possible to keep a constant Q_m by maintaining a constant $C_1 U^2$. It is proposed to test this hypothesis by modulating the excitation voltage as a function of the dynamic capacitance C_1 .



(a) Dependence between C_1U and quality factor. With a constant excitation voltage, the Q_m has important variations that are reduced when the voltage is adapted to maintain a constant C_1U^2 . The figure suggests a non-linear damping that depends on C_1U rather than C_1U^2 .

(b) Comparison of electromechanical effective coupling factor k_{eff}^2 for a constant C_1U^2 factor and a constant excitation voltage U .

Figure 4.11: Resonator properties comparison for a constant C_1U^2 factor and a constant excitation voltage U .

Figure 4.11a shows the result of this experiment. When modulating the excitation voltage in order to have a constant C_1U^2 , the quality factor Q_m is more uniform with a standard deviation reduced from 22 % to 9%. Variations are still present and experiment suggests a dependance on C_1U rather than C_1U^2 . This is consistent with a non-linear damping which is not proportional to the mechanical energy. Although no further investigations were carried on, this phenomenon does not affect the theoretical propositions made earlier about independence of quality factor from electrode pattern since the relation observed is clearly associated with the excitation amplitude. In addition, it can be noted in figure 4.11b that the electromechanical coupling factor k_{eff}^2 is not affected by the change in the voltage as unitary slope is observed between k_{eff}^2 from both experiments.

4.6 Optimization of the actuator

4.6.1 Electrodes for longitudinal-bending actuators

In the case of a two modes standing wave actuator, several choices can be made to excite the actuator modes. A first solution is to use two sets of electrodes that both excite the two vibrations modes. A second solution is to use two independent sets that are each used to drive one mode of vibration. The first method uses the fact that the modes do not have the same symmetry, it is therefore possible to excite them using one signal that is composed of a

symmetric component and an anti-symmetric component. Zhang et al. [3] proposed such a method. They chose two sets of two coupled electrodes, both sets received different signals:

$$V_1 = V_L e^{i\omega t} + V_B e^{i\phi} e^{i\omega t} \quad (4.44)$$

$$V_2 = V_L e^{i\omega t} - V_B e^{i\phi} e^{i\omega t} \quad (4.45)$$

Where V_B and V_L are the excitation voltage of both modes, ω is the excitation frequency and ϕ the phase shift between the signals. The corresponding electrode pattern is shown on the left side of figure 4.12. In the case where an electrode optimization is wanted, this method is not advantageous, because the sets of electrodes have to be optimized for both modes at a time. Still, this method could be proven useful for pattern with large common strain areas. Another advantage is the possibility to use a common ground on the other side of the actuator.

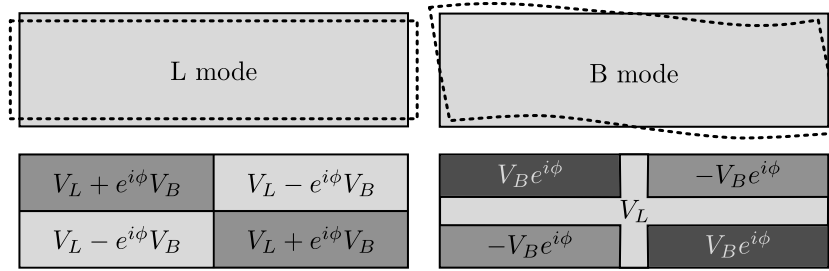


Figure 4.12: Modal shapes and possible electrodes configuration for a longitudinal-bending actuator. The first electrode configuration is composed of two sets of electrodes that both excite the two modes of the structure. The second configuration is composed of two sets of independent electrodes that each excite one mode of the structure.

The second method uses two different sets which are each dedicated to the excitation of one mode as shown on the right of figure 4.12. The advantage of such a configuration is that each electrode geometry can be adapted to the mode it excites. As seen in figure 4.12, the sign of the bending signal is not the same on each electrode. That does not mean that a third signal is needed, two solutions can be used: the piezoelectric poling direction can be locally changed or the field direction can be inverted by connecting the signal on the other side of the actuator using the same electrode pattern. This last method does not allow to use the other electrode as a common ground. For the actuator developed in this work, a two independent set is chosen since it simplifies the optimization of each mode excitation. Nevertheless, the method presented is general and could be adapted to the first type of excitation electrodes.

4.6.2 Single mode optimization

It is interesting to study single mode excitation optimization to better understand the criteria for electrodes optimization and how they may apply to a two modes excitation. The

CHAPTER 4. ELECTRODES PATTERN: ELECTRICAL ENERGY TO MECHANICAL ENERGY CONVERSION

optimized geometry is the 15mm inner and 25mm outer radius actuator proposed in the previous chapters. Figure 4.13 represents S_3 modal strain patterns for longitudinal and bending modes that are used for actuation. These out-of-plane strains are used to find the effective coupling factor for longitudinal (k_L^2) and bending mode (k_B^2) for any electrode pattern.

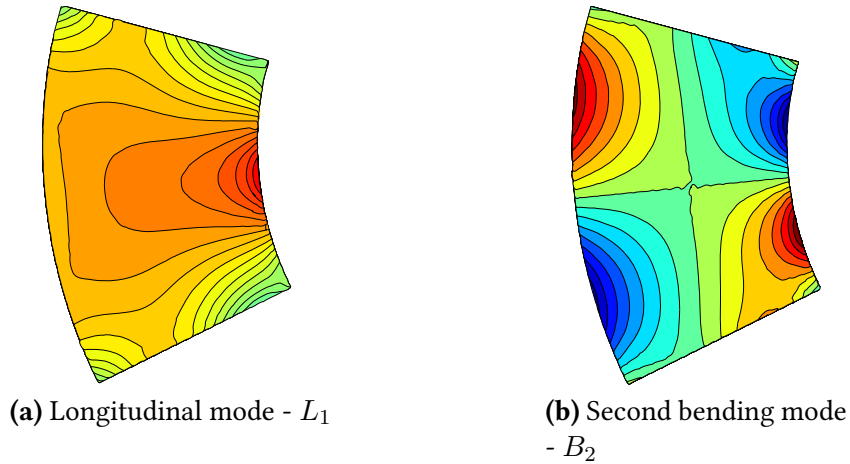


Figure 4.13: S_3 strain distribution for the considered actuator modes. Red areas correspond to large positive strain, green areas to near zero strain and blue areas to large negative strain.

Relationship between k_{eff}^2 and $\frac{(\int_{V_e} S_3 dV)^2}{A_e}$

The first step of the optimization principle is the realization of several finite element harmonic simulations with different electrodes patterns in order to find the relation between $\frac{(\int_{V_e} S_3 dV)^2}{A_e}$ and k_{eff}^2 . Although it is not strictly necessary to know the absolute value of k_{eff}^2 for a single mode optimization process since a relative comparison of $\frac{(\int_{V_e} S_3 dV)^2}{A_e}$ values is enough, it will be useful for the next steps of the electrode design.

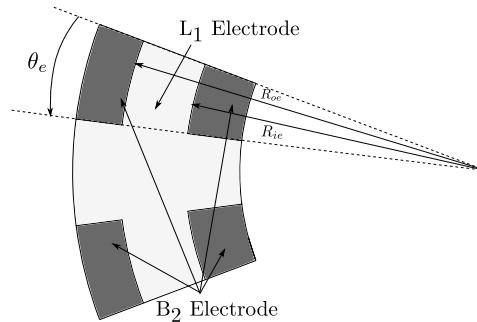


Figure 4.14: Parametric electrode pattern. The pattern is defined via three parameters, inner electrode radius R_{ie} , outer electrode radius R_{oe} and angle θ_e .

The parametric electrode configuration used is shown in figure 4.14. It is similar to patterns found in the literature for rectangular actuators (Takano et al. [28]). Several different

electrode pattern responses are obtained using harmonic finite element analysis. The equivalent Butterworth Van Dyke model is applied to the obtained electric responses and allow to find the electromechanical coupling factor for the different electrode patterns. The values are compared to $\frac{(\int_{V_e} S_3 dV)^2}{A_e}$ for each pattern and the linear relations shown in figure 4.15 are obtained. The electromechanical coupling factor for each mode can then be computed using the relations:

$$\begin{cases} k_L^2 = 3.02 \frac{(\int_{V_e} S_3^L dV)^2}{A_e} \\ k_B^2 = 7.82 \frac{(\int_{V_e} S_3^B dV)^2}{A_e} \end{cases} \quad (4.46)$$

Using these relations, it is possible to evaluate k_{eff}^2 for any electrode configuration based solely on modal analysis strain results and without requiring an harmonic analysis.

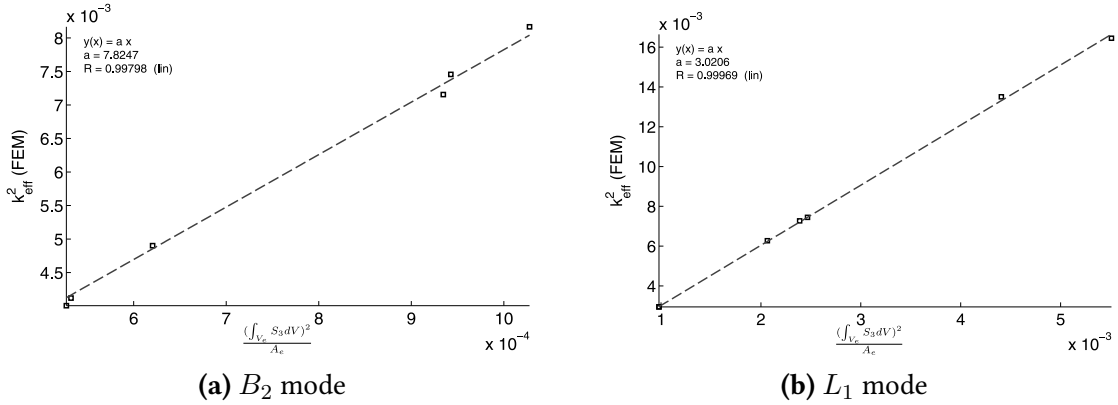
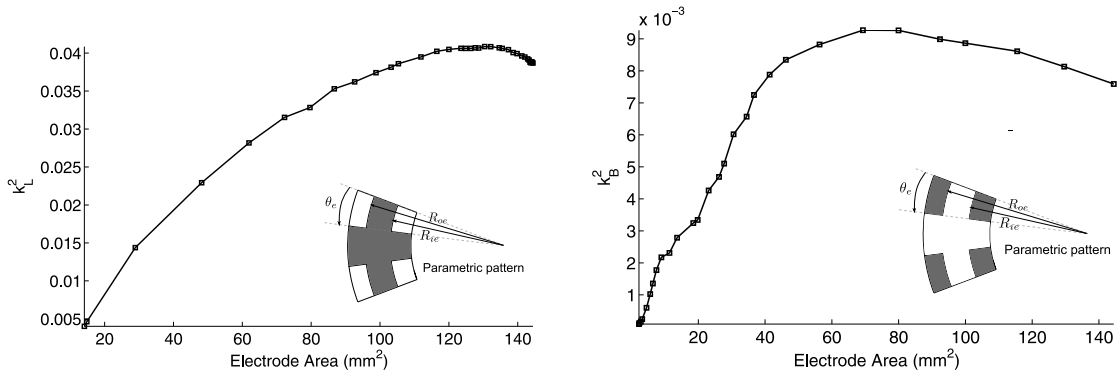


Figure 4.15: Relation between the total strain squared density $\frac{(\int_{V_e} S_3 dV)^2}{A_e}$ and the electromechanical coupling factor k_{eff}^2 for the two considered modes. This relation allows to find k_{eff}^2 for any electrode configuration without requiring an harmonic analysis since $\frac{(\int_{V_e} S_3 dV)^2}{A_e}$ is computed based on modal strain.

Optimization results

It is possible to compute k_{eff}^2 for a large number of parametric patterns using variations of R_{ie} , R_{oe} and θ_e . Several different values of k_{eff} are found for a single electrode area indicating that the shape of the electrode is as important as its size. Figure 4.16 represents the maximum coupling factor that is observed for a given electrode area using parametric patterns. It can be observed that for each mode, there is an optimal area where the excitation efficiency is maximum. For the longitudinal mode, the optimal electrode covers 88.4 % of the total actuator area (125 mm² for a total electrode area of 141.4mm²). The bending mode has an optimal electrode area between 70 and 80 mm² (49.5 % and 56.5% of the total electrode

CHAPTER 4. ELECTRODES PATTERN: ELECTRICAL ENERGY TO MECHANICAL ENERGY CONVERSION



(a) Evolution of electromechanical coupling factor of longitudinal mode L_1 as a function of electrode area for parametric patterns. The parametric patterns k_{eff}^2 are computed for a large number of parameters. The results for the ones with the best electromechanical factor given an electrode area are shown in the figure.

(b) Evolution of electromechanical coupling factor of longitudinal mode B_2 as a function of electrode area for parametric patterns. The parametric patterns k_{eff}^2 are computed for a large number of parameters. The results for the ones with the best electromechanical factor given an electrode area are shown in the figure.

Figure 4.16: Best electromechanical coupling factor as a function of area using parametric electrodes. Both longitudinal and bending mode presents an optimal electromechanical coupling factor.

area). The two resulting optimal electrode patterns cover each other and cannot be optimized at the same time for a two modes excitation problem.

4.6.3 Two mode optimization problem

The definition of the actuator efficiency developed in equation (4.38) is not valid in the case of a two modes excitation. With two different sets of electrodes for modes a and b , the dynamic branch energies can be expressed as:

$$2E_d^a = U_a^2 Q_{ma}^2 C_1^a \quad (4.47)$$

$$2E_d^b = U_b^2 Q_{mb}^2 C_1^b \quad (4.48)$$

And dielectric losses are:

$$E_{loss} = \pi \tan \delta' (C_{0a} U_a^2 + C_{0b} U_b^2) \quad (4.49)$$

$$E_{loss} = \pi \tan \delta' \left(\frac{2E_d^a}{Q_{ma}^2} \frac{1 - k_a}{k_a} + \frac{2E_d^b}{Q_{mb}^2} \frac{1 - k_b}{k_b} \right) \quad (4.50)$$

So that the efficiency becomes:

$$\Gamma = \frac{U_a^2 Q_{ma}^2 C_1^a + U_b^2 Q_{mb}^2 C_1^b}{2\pi \tan \delta' (C_{0a} U_a^2 + C_{0b} U_b^2)} \quad (4.51)$$

In the case of a two electrodes design, the different losses of the two vibration modes have to be considered. Moreover, although it is shown in section 3 that the two modes should have similar amplitude for best output power of the actuator. The contact model does not take into account the energy cost to increase one mode amplitude over the other. Therefore, a complete model of the actuator should be used for proper electrode optimization. From equation (4.50), the minimization of the loss and the optimization of k_a and k_b will depend mostly on the expected energies in both modes and therefore the expected mode amplitudes. Two major cases can be considered:

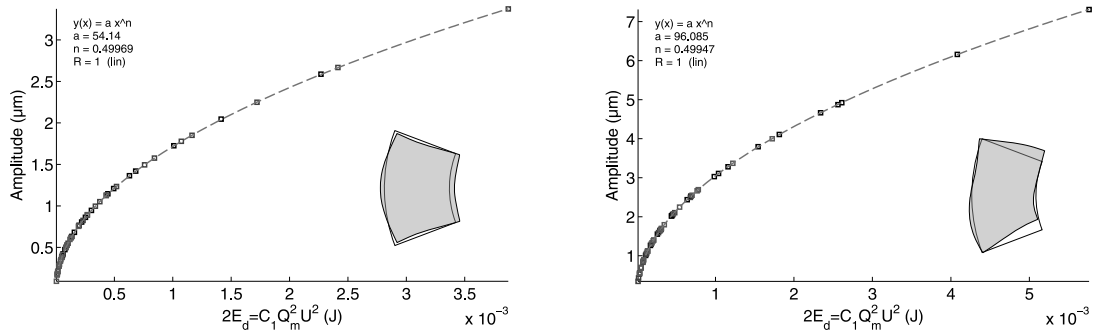
- Maximum k_a and k_b can be obtained at the same time. The electrode definition is easily set since it corresponds to the electrodes for best k_{eff}^2 on both modes. The two optimal electrodes should not be overlapping and high differences in modal strain are therefore required.
- k_a and k_b are not independent and for example an increase in k_b leads to a decrease in k_a . In this case, the problem is more complicated and depends on the expected converted and stored energy in each mode and their influence on the total motor efficiency.

In our case, the maximum efficiency of the longitudinal mode is obtained when the electrode is almost completely covering the actuator. Therefore, the creation of electrodes for the bending mode excitation will always cause a drop in the conversion efficiency of the longitudinal mode. Therefore, a compromise based on a full motor description has to be found between the longitudinal mode and bending mode electrodes.

4.6.4 Relation between mode amplitude and equivalent circuit parameters

A relation exists between the dynamic energy branch and the mode displacement amplitude, and it is possible to use equivalent circuit parameters to compute the amplitude of the displacement at the edge of the actuator. A finite element analysis is performed on various parametric electrodes patterns, damping factors and voltages so that the dependance between $2E_d = C_1 Q_m^2 U^2$ and mode amplitude is verified. Mode amplitude is computed based on the normalized mode shapes obtained from modal analysis that are used in the chapter 3. Figure 4.17 shows the relationship between mode amplitude and dynamic branch energy for both modes. It can be observed that the amplitude is proportional to the square root of the energy. This confirms that the dynamic branch energy E_d is analogous to the mechanical energy E_m , since mechanical energy depends on the square of the displacement amplitude.

CHAPTER 4. ELECTRODES PATTERN: ELECTRICAL ENERGY TO MECHANICAL ENERGY CONVERSION



(a) Longitudinal mode amplitude as a function of the dynamic branch energy.

(b) Bending mode amplitude as a function of the dynamic branch energy.

Figure 4.17: Mode amplitudes as a function of dynamic branch energies for both longitudinal and bending modes. These results are obtained using multiple finite element harmonic simulations. Several voltages and damping factors are used along with multiple electrode patterns. The displacement amplitude is computed from normalized modes shapes.

These two results are useful and have the potential to derive amplitude of displacement for any electrode pattern and any damping of the material. Coupled with the contact model analysis proposed earlier, they allow to obtain an estimation of the total efficiency of the actuator. The efficiency of the motor is defined as:

$$\eta = \frac{P_m}{P_{elec}^{B_2} + P_{elec}^{L_1}} = \frac{P_m}{U_{B_2}^2 \left(\omega C_0^{B_2} \tan \delta_e + \frac{1}{R_1^{B_2}} \right) + U_{L_1}^2 \left(\omega C_0^{L_1} \tan \delta_e + \frac{1}{R_1^{L_1}} \right)} \quad (4.52)$$

The resistor from dynamic branch is obtained from:

$$C_1 = \frac{k^2}{1 - k^2} C_0 \quad (4.53)$$

$$L_1 = \frac{1}{(2\pi)^2 C_1 f_s^2} = \frac{1}{(2\pi)^2 f_s^2} \frac{1 - k^2}{k^2 C_0} \quad (4.54)$$

$$R_1 = \frac{1}{Q_m} \sqrt{\frac{L_1}{C_1}} \quad (4.55)$$

$$R_1 = \frac{1 - k^2}{2\pi Q_m f_s k^2 C_0} \quad (4.56)$$

Using these relations it is possible to obtain a full description of the actuator admittance response. For power supply convenience, both modes are usually driven with the same voltage so that we consider $U_{B_2}^2 = U_{L_1}^2 = U^2$. Dielectric loss tangent angle is given by the material properties ($\tan(\delta_e) = 3 \times 10^{-3}$ for Ferroperm Pz26). Combining all these results, it is possible to estimate the efficiency of the resulting motor and find the appropriate electrode pattern for mode excitation.

4.6.5 Ultrasonic motor complete modeling

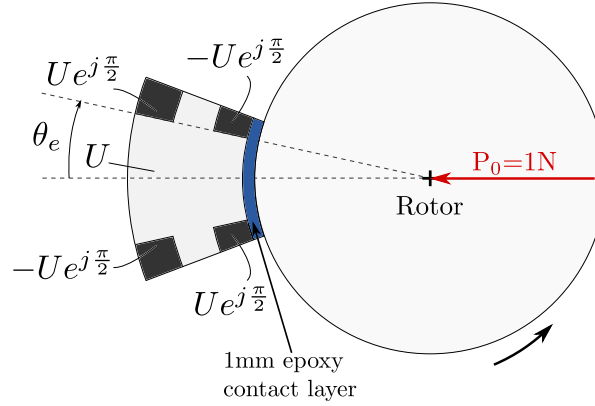


Figure 4.18: Motor parameters for full motor modeling. The motor is based on a $R_i = 15\text{mm}$, $R_o = 25\text{mm}$ actuator with a 1mm thickness epoxy layer. A 1N preloading force is applied between the rotor and the contact layer. The actuator is patterned with a parametric electrode pattern. R_{ie} is set to 18mm and R_{oe} is set to 20.5mm. The angle θ_e is changed for electrode area variations. The electrodes are excited with the same voltage amplitude, according to the strain pattern of the considered modes. The two modes excitations have a phase shift of 90° .

A parametric pattern similar to figure 4.14 is proposed for electrodes optimization using a complete ultrasonic motor model. R_{ie} is set to 18mm and R_{oe} to 20.5mm in order to covers the maximum strain areas of bending mode. Electrode area is changed using angle θ_e . The equivalent circuit parameters are obtained using the semi-analytical method developed earlier. Quality factors are computed from finite element analysis assuming an isotropic loss factor $\tan(\delta_m) = 3 \times 10^{-3}$. The obtained values are $Q_{mB_2} = 293$ and $Q_{mL_1} = 117$.

As shown in figure 4.18, the motor uses a 1mm epoxy contact layer with similar properties as in chapter 3. A preloading force of 1N is applied between the rotor and the contact layer. The electrodes are excited with the same voltage amplitude U , the phase of the electrode excitation is adapted depending on the strain distribution of the considered mode. A phase shift of 90° is applied between both modes excitation and the modes are assumed to be at the same resonance frequency. Using the method described in the previous section, the amplitude at the edge of the actuator can be derived as a function of voltage. This amplitude is used in the contact model to obtain the motor output characteristics.

Figure 4.19a shows the output mechanical power of the motor as a function of bending mode area and voltage. It can be observed that as voltage is increased, the output power is increased. An optimal electrode area for maximum output power exists, it represents a compromise between longitudinal mode excitation and bending mode excitation. In figure 4.19b, the optimal bending mode electrode for maximum output power is shown as a function of the input voltage. Slight variations between 53.5mm^2 and 67mm^2 are observed with an

CHAPTER 4. ELECTRODES PATTERN: ELECTRICAL ENERGY TO MECHANICAL ENERGY CONVERSION

average optimal electrode area of 61.9mm^2 . A maximum output power of 68 mW is observed for the maximum considered voltage of 20V and with an electrode area of 64.6 mm^2 .

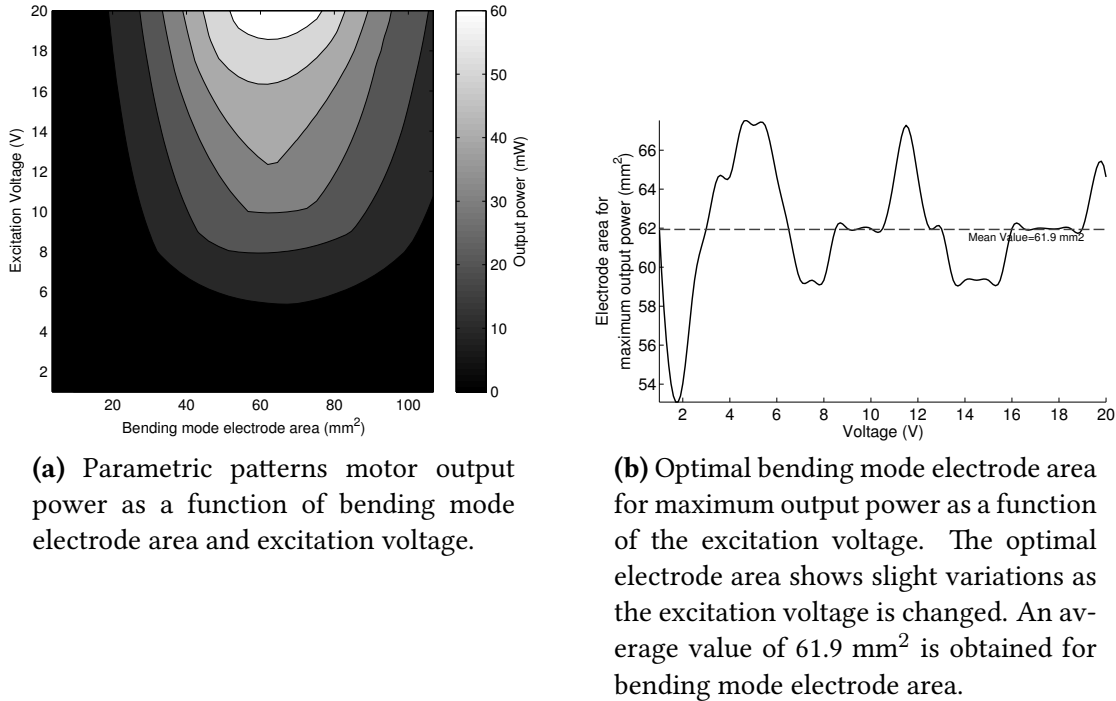


Figure 4.19: Electrode area optimization for maximum output power.

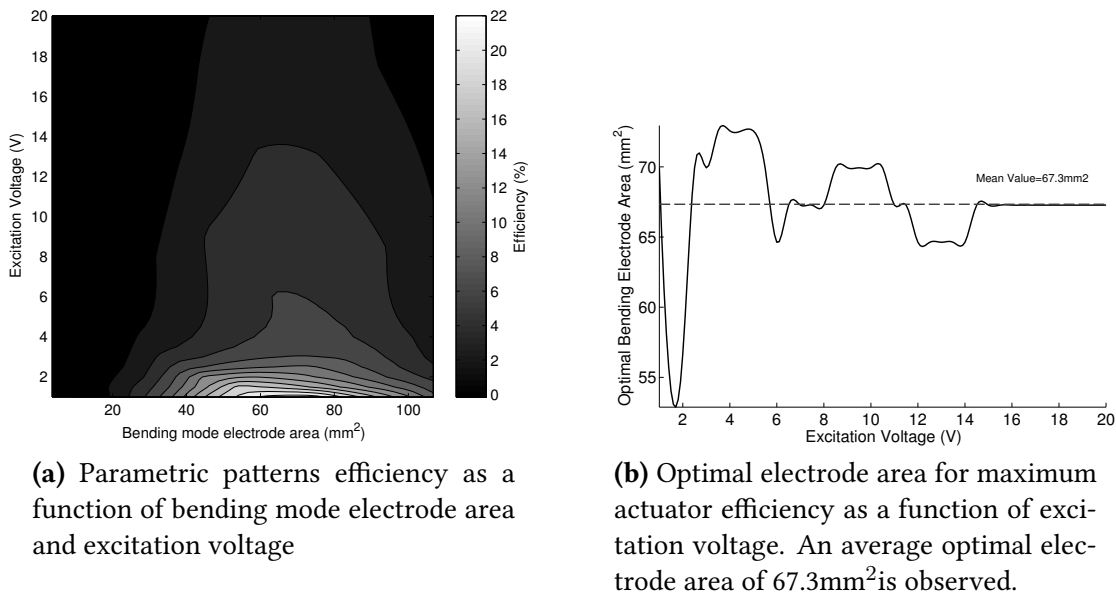


Figure 4.20: Electrode area optimization for maximum motor efficiency.

Figure 4.20a shows the evolution of motor efficiency as a function of bending mode electrode area and excitation voltage. Similarly to power, an optimal electrode value can be

observed for which motor efficiency is maximal. The efficiency decreases quickly as the excitation voltage is increased. A maximum efficiency of 23.2% is reached at the minimum excitation voltage of 1V and an electrode area of 69.9mm². It decreases to 3.5% at an excitation voltage of 15 V. This important drop is attributed to a limited increased of output mechanical power due to a saturation effect on torque. The efficiency can be improved by an increase of the preloading force. The optimal electrode area for maximum efficiency is represented as a function of input voltage in figure 4.20b. Variations of the optimal values are observed as excitation voltage is changed and an optimal average value of 67.3mm² is observed. The optimal electrode area for maximum efficiency is different from the one for maximum power. Efficiency computation takes into account the gain in output power as compared to the increase in electrical input power, this ratio depends on mechanical losses of both vibration modes what explains the difference in optimal electrode area.

4.7 Summary of the ultrasonic motor modeling method

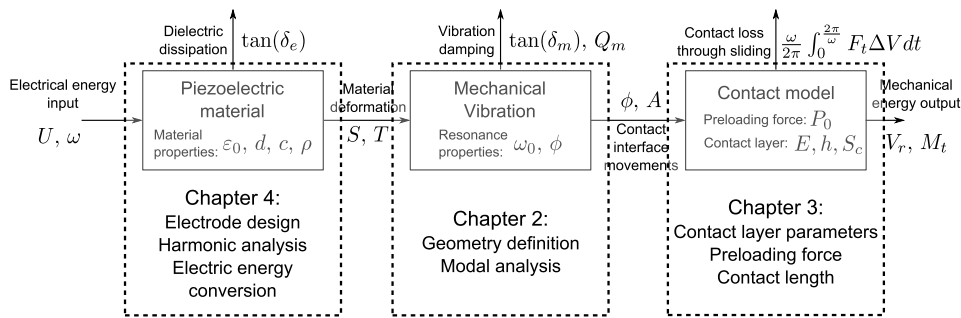


Figure 4.21: Summary of the proposed ultrasonic modeling method.

In the last three chapters a complete method for ultrasonic motor design and modeling is proposed. Figure 4.21 summarizes the three important steps of the developed method:

- First, in chapter 2, the mechanical resonant structure is proposed. A parametric geometry is defined and simulated using modal analysis. The effect of geometric parameters is studied and vibration modes are chosen. The final geometry for the proposed actuator is a 25mm outer radius, 15mm inner radius piece of a ring with a portion angle of 40.5°. Modal analysis allows to study disturbances such as soldering points that affect mode degeneration.
- In chapter 3, using the computed modes shapes and frequencies, the output properties of the actuator are discussed as a function of the various parameters that influence contact model. Contact layer properties are discussed along with effect of modes amplitudes and preloading force. The influence of mode non-degeneration, that can be

caused by the disturbances described in chapter 2, is found to be prejudicial to motor operation.

- In chapter 4, a semi-analytic method for computing electrodes properties is proposed. Analytical considerations are combined with harmonic finite element method to obtain modes amplitudes as a function of the input power and the electrode design. Association of these results with contact analysis allows to obtain a complete description of the motor characteristics from electrical input power to motor output power.

A complete modeling of the ultrasonic motor is obtained. It can be used to tune the different parameters to obtain the required motor characteristics. Nevertheless, it suffers from some limitations that are mainly associated with the difficulty to predict the damping of the actuator that depends on numerous parameters such as the holding mechanism, the electrical contacts or the preloading force. Therefore, a full optimization of the ultrasonic motor is not possible unless we have a precise knowledge of the damping of the actuator. Ideally, the final electrode optimization should be performed after a first experimental characterization of the actuator.

On the other hand, the model is very versatile and can be applied to numerous geometries of actuator. The modal and contact properties can be optimized without requiring knowledge about the damping properties of the actuator. Also, the model is easily applied for comparison with experimental data. Q_m and C_1 can be measured using admittance measurements and the equivalent Butterworth Van Dyke model. From these measurements, the amplitude of the modes can be estimated and applied to the contact model so that expected output power of the motor can be compared to the experimental results.

4.8 Conclusion

In this chapter a model for electrical to mechanical energy conversion is proposed. It shows that the efficiency of a harmonic excitation depends mainly on two parameters: The effective electromechanical coupling k_{eff}^2 and the quality factor Q_m of the resonance. Although Q_m is not significantly affected by the electrodes arrangement, k_{eff}^2 strongly depends on the shape and size of the electrodes. A semi-analytical method for the computation of k_{eff}^2 is proposed and verified through experiments. It allows computing the admittance properties of any electrode set given the quality factor and the resonance frequency of the mechanical structure. Although simulation shows that an optimal electrode pattern exists for a single-mode excitation, it is difficult to apply to a two modes excitation since optimal electrodes overlap. A full model of an ultrasonic motor is therefore used for electrode optimization. A relation between electrode admittance properties and amplitude of the excited mode is determined using finite element harmonic analysis. From this result, it is possible, using

contact model in chapter 3, to derive the actuator output power and efficiency as a function of voltage and electrodes area. The model shows that it is possible to find an optimal electrode area for maximum output power or maximum efficiency of the actuator. The optimization process depends on numerous parameters that are difficult to obtain through simulation. In particular, the quality factor of the resonance depends on numerous factors such as internal damping, holding mechanism or electrical contacts interactions.

Ultrasonic motor experimental characterization

5

Contents

5.1	Introduction	124
5.2	Actuator implementation	124
5.2.1	Actuator fabrication	124
5.2.2	Holding mechanism	125
5.2.3	Contact wires	127
5.2.4	Contact layer deposition	128
5.3	Experimental set-up	129
5.3.1	Mechanical set-up	129
5.3.2	Measurement set-up	130
5.3.3	Measurement procedure	133
5.3.4	Model comparison	134
5.4	Voltage dependance	134
5.4.1	Admittance response	135
5.4.2	Mechanical response of the actuator	136
5.5	Phase shift influence	139
5.5.1	Speed and torque	139
5.5.2	Power and efficiency	140
5.6	Preloading force dependance	141
5.6.1	Effect of preload on resonance characteristics	141
5.6.2	Preloading force and frequency response of the actuator	142
5.6.3	Torque and speed as a function of preloading force	143
5.6.4	Preloading and efficiency of the actuator	144
5.7	Contact length	145
5.7.1	Influence of contact pattern on resonance characteristics	145
5.7.2	Influence of contact length on speed-torque characteristics	146
5.8	Resonance tracking of the actuator	147
5.8.1	Phase-based resonance tracking	149
5.8.2	Phase tracking for highly damped vibrations	150
5.9	Conclusion	152

5.1 Introduction

This chapter presents the experimental studies of a prototype actuator. The goal is to verify the actuator concept introduced in the previous chapters in an ultrasonic motor. Experimental results are compared to the model of the actuator and used to provide general rules for the design of the actuator. The chapter is divided into several sections:

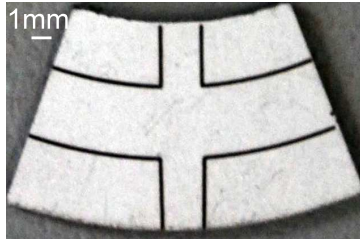
- The first one introduces the actuator and holding structure fabrication.
- The second one presents the experimental setup and procedure.
- The following sections discuss the response of the actuator as a function of different parameters such as voltage, phase shift, preloading force and contact length.
- Finally, insights about the control required for the actuator are proposed especially in terms of resonance tracking.

5.2 Actuator implementation

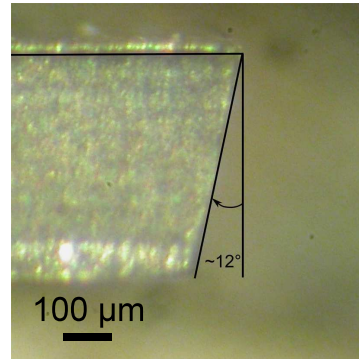
5.2.1 Actuator fabrication

Actuators are engraved and cut using picoseconds laser technology (See figure 5.1). This technology allows for fast and precise cutting and engraving of the piezoelectric material using short pulses that limit heat generation. However, one drawback is the divergence of the laser beam that causes a slight angle in the thickness. Although it is not problematic for the 10 μ m thick electrodes, it can cause tolerance problems on 0.5mm cut features.

The divergence angle is measured on figure 5.1b. It is in the range of 12° and causes an uncertainty of 0.1mm on the length of 0.5mm cut features. This tolerance can affect mode degeneracy which is dependent on portion angle of the actuator. Assuming a portion angle at half thickness of 40.5° is required, the target cutting angle should be 40.8° to take into account the divergence angle. In addition, soldering is expected to affect mode degeneration. Solder points positioned on bending electrodes cause at least 400 Hz frequency difference between the two modes, with B_2 mode below L_1 mode (see section 2.4). The contact layer affects similarly mode degeneration with a shift of the bending mode below the longitudinal mode. One solution to anticipate this effect is to modify the angle of the actuator so as to have bending mode above longitudinal mode before electrical contact and friction layer are deposited. The two modes are unlikely to be found at the same frequency and a tuning step similar to the one described in section 2.4.4 is required. Because of the electrodes position, the tuning process is simplified for an actuator with a bending mode above longitudinal mode (see figure 2.19c on page 63).



(a) Cut actuator with engraved electrode pattern using picoseconds laser technology.



(b) Angle due to laser divergence. The angle is estimated to 12° . Manufacturing tolerance is estimated to 0.1mm due to this problem.

Figure 5.1: A picture of the laser-cut actuator. The actuator is cut using picoseconds laser technology that limits heat generation in the piezoelectric element while providing precise electrode engraving and material cutting.

An actuator with its bending mode 600Hz above longitudinal mode when it is completely free of masses is estimated to be adapted. Around portion angle for mode degeneracy, the sensitivity of frequency with respect to θ is $-1.168 \text{ kHz}/^\circ$ for B_2 mode and $-2.209 \text{ kHz}/^\circ$ for L_1 mode. One added degree to θ causes the actuator to have the bending mode 1.041 kHz above the longitudinal mode. Therefore, added masses and margin for actuator tuning requires the portion angle to be $0.6/1.041=0.58^\circ$ larger than predicted. Considering the laser beam tolerance and added masses, the final target angle of the actuator is 41.4° .

The electrode pattern used in this chapter is a square electrode pattern with a B_2 electrode area of 67mm^2 and a L_1 electrode area of 77mm^2 (pattern is similar to figure 4.14 with $R_{ie} = 18\text{mm}$ and $R_{oe} = 20.5\text{mm}$).

5.2.2 Holding mechanism

The actuator has to be held and connected while still being able to vibrate with minimal loss due to the friction against the support. Holding the actuator correctly is a critical problem in order to ensure good quality factor and stability of the motor. The actuator should not be affected by the force it generates and it should not be excessively constrained at the risk of an important damping of the vibration. In literature, various holding mechanisms have been used. One method consists of using springs or soft materials as means to hold the actuator. Shi and Zhao [69] use silicon rubber to ensure actuator fixation while Chen et al. [88] use a spring-based fixation. These methods are easily implemented on large scale systems but may be difficult to apply when actuators are scaled down because of small mechanical parts. Numerous examples are found where one or a few points are used for constraining

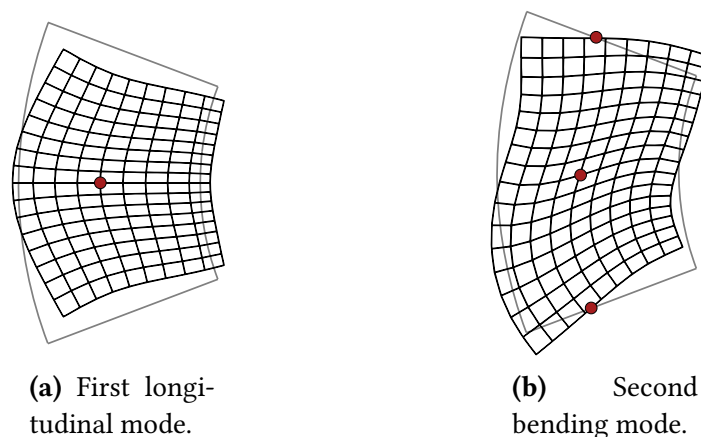


Figure 5.2: Modal shapes of the two modes. Zero displacement points (nodes) are shown as red dots.

the actuator (Shen and Huang [6], Funakubo and Tomikawa [89], Hemsell and Wallaschek [90]). Fixations are generally placed at nodal points of the actuator resonant modes what cause minimal damping of the vibration. However, holding the actuator using only a few points is a delicate procedure that may result in some actuator movement and change the actuator properties. Other examples such as the resonant holding mechanism proposed by Yun et al. [91] offer great performance at the expense of miniaturization and implementation simplicity.

In our case, because of the size of the actuator, the most appropriate clamping technique is a point clamping mechanism with ideally, the nodal points (points of minimal modal displacement) fixed. In figure 5.2, the modal shapes of the two modes used are presented. Their nodal points are located as red dots. Three nodal points are present on the B_2 mode and one on the L_1 mode. The only common zero displacement point for both modes is the center of gravity of the actuator. Two actuators support have been tested.

The first design (figure 5.3a) uses three contact points with two of them at minimum bending displacement. A spring is machined into the support to offer a constant force boundary condition that limits damping of the longitudinal mode. This spring pushes the actuator against two contact points on the edges of the actuator. This design constrains well the actuator in the plane, however it is difficult to constrain the out-of-plane displacement without tightening the actuator at the points of contact (what damps the longitudinal vibration). The second holding mechanism that is investigated uses a central fixation point to avoid out-of-plane displacement. The three others contact points are maintained with a housing larger than the actuator so that the contact points only prevent the actuator from rotating, without applying important stresses on the actuator (figure 5.3b).

The two holding mechanisms are compared by measuring resonance characteristics. Admittance measurements of the unloaded actuator at 4Vpp are performed to obtain quality

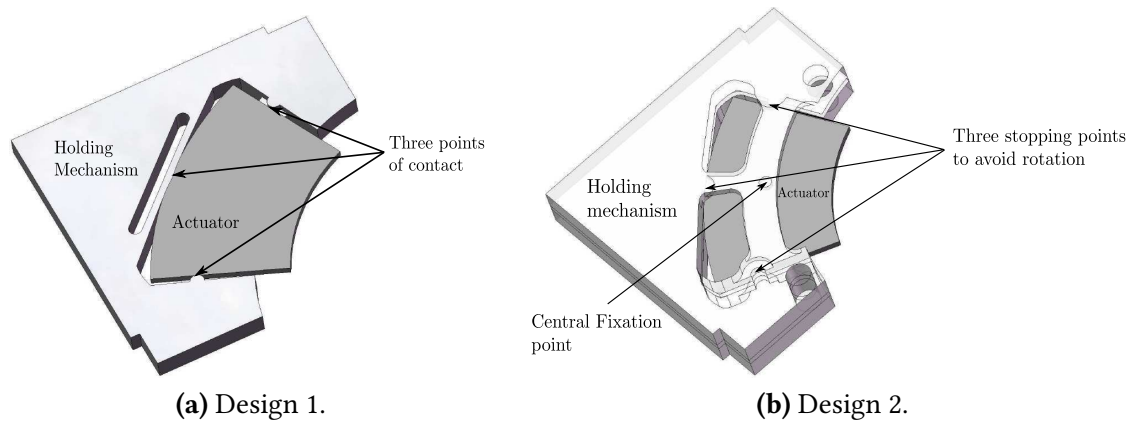


Figure 5.3: Two different possible holding mechanisms. The first one is based on an elastic fixation where three points of contact corresponding to minimal bending mode displacement are used. The second one is based on a clamping of the center of gravity of the actuator and three support points.

	Design 1	Design 2
Q_{mL_1}	120.17	353.73
Q_{mB_2}	413.35	596.05

TABLE 5.1: QUALITY FACTOR FOR BOTH MODES AS A FUNCTION OF THE HOLDING MECHANISM USED. MEASUREMENTS ARE PERFORMED ON THE SAME ACTUATOR MOUNTED IN A DIFFERENT SUPPORT. A SUPPORT BASED ON A FIXATION OF THE CENTER NODE OF THE ACTUATOR SHOWS MUCH LESS DAMPED VIBRATIONS.

factors Q_m . Results are shown in table 5.1. The use of the three points holding mechanism causes a drop of 31 % of the bending mode quality factor as compared to the centered one point fixation. Longitudinal mode is more affected with a drop of 66% of the quality factor when using three holding points. The centered fixation mechanism is the one used in the remaining of the experimental work due to the better obtained performance.

The holding mechanisms are milled into printed circuit board material so that it is possible to use the copper part for electrical connections between the electrodes. This is especially useful for bending mode excitation since there are four electrodes on each side that have to be in phase opposition.

5.2.3 Contact wires

Electrical connections are achieved using soldered wires. They introduce mechanical constraints and increase the mechanical losses at resonance. There is a tradeoff between wire diameter for current conduction and reduced damping. Measurements performed on the same actuator and with two sets of wires, one with a 0.24mm diameter and one with a 0.14mm diameter, show that wire diameter has an important influence on the damping of the actuator. Table 5.2 shows the changes in quality factor at low excitation amplitude (4Vpp). The quality

	\varnothing 0.24mm	\varnothing 0.14mm
Q_{mL_1}	50.21	321.11
Q_{mB_2}	36.52	331.01

TABLE 5.2: COMPARISON OF QUALITY FACTORS WITH RESPECT TO WIRE DIAMETER. MEASUREMENTS ARE PERFORMED ON THE SAME ACTUATOR. A LARGE DAMPING EFFECT IS CAUSED BY AN INCREASE IN WIRE DIAMETER.

factor drops significantly on both modes when the 0.24mm wires are used with a decrease of 84% of Q_{mL_1} and 89% of Q_{mB_2} . Wires with a 0.14mm diameter are therefore used for actuator fabrication.

5.2.4 Contact layer deposition

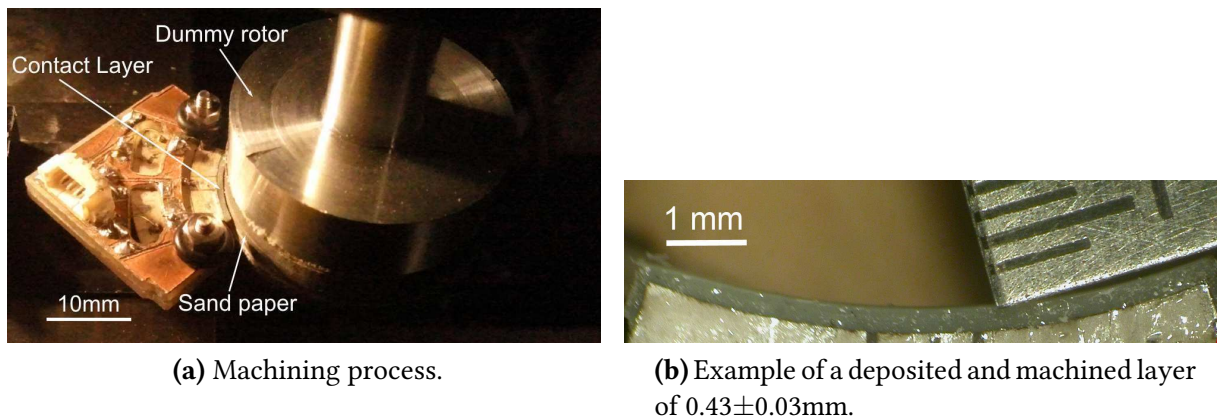


Figure 5.4: Contact layer deposition process. A thick raw layer is molded onto the actuator. Excess of material on the actuator faces is removed using a sharp blade. The layer is then machined to the necessary thickness using sandpaper placed on a dummy rotor.

A contact layer is deposited onto the actuator to avoid damage and optimize the contact surface. Different materials are discussed in section 3.2.3. Although it has a low stiffness that implies limited performance of the actuator, epoxy is chosen as the contact material. It has the advantage to be easily deposited and is an appropriate matrix material for composites used in ultrasonic motors (Zhao [71, page 62]). A raw layer is deposited onto the actuator using a Delrin mold. Any excess of material is removed using a sharp blade. A thick layer is first deposited and then adjusted using a dummy rotor covered with sandpaper to obtain the desired thickness (see figure 5.4). The viscosity of the resin affects the properties of the actuator. The phenomenon is represented in figure 5.5, where, after 12H, the resonance frequencies are shifted up and damping is reduced indicating a drying effect that affects stiffness and damping of the layer.

The resin used is a 3M DP110 adhesive epoxy. A friction coefficient of 0.218 is measured between the resin and aluminum. Epoxy resin have various Young's modulus with a typical

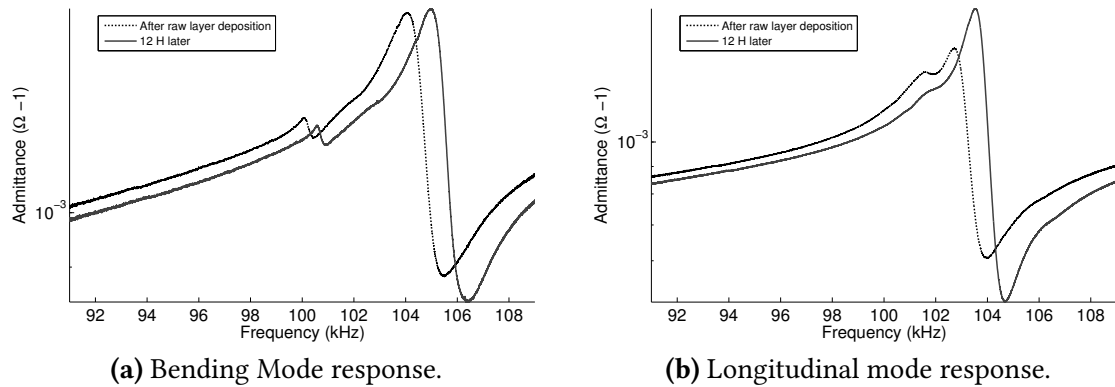


Figure 5.5: Drying effect on the contact layer. As the epoxy resin dries, mode frequencies are shifted up with a narrower peak (especially for longitudinal mode) indicating a stiffer and less viscous layer.

range of 2 to 20 GPa. To apply the contact model, it is important to have a good estimation of the resin properties. Data about this specific epoxy material are hardly found in literature. One reference (Hildebrand and Vessonen [92]) indicates a tensile modulus of 1470 MPa well below the data used for modeling in chapter 4 (10 GPa). This new value is used for comparison with the model.

5.3 Experimental set-up

5.3.1 Mechanical set-up

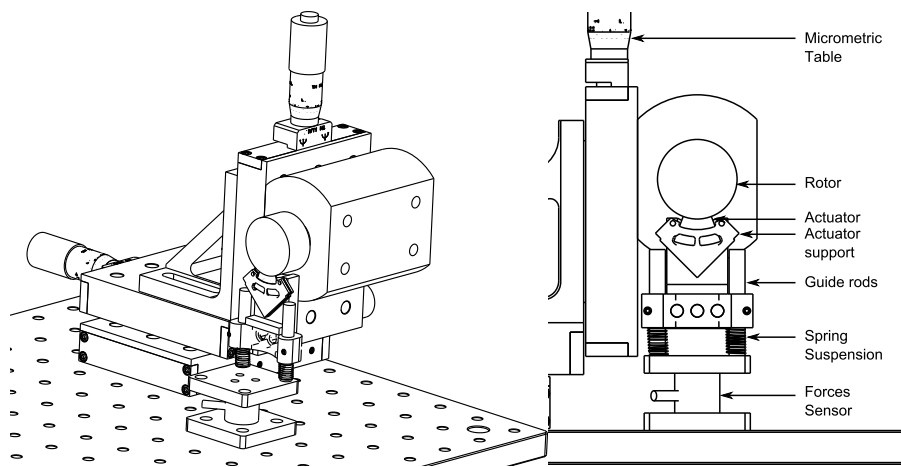


Figure 5.6: Mechanical set-up used for actuator characterization. The actuator is placed on an elastic suspension allowing to compensate for rotor irregularities and experiment at constant force. The rotor is positioned using a 3-D micro-metric platform. Force sensor is used for both actuator positioning and preloading force measurement.

Figure 5.6 represents the mechanical set-up used for the actuator characterization. The rotor is positioned against the actuator using a 3-D micropositioning platform. The actuator itself is held in a support which is mounted on a guiding system associated with a spring suspension. The objective is to observe the characteristics of the actuator at constant preloading force. The springs allow for the compensation of geometric irregularities of the rotor (e.g: diameter, coaxiality) without a large increase in the preloading force. The shaft used for characterization is made of aluminum. Its moment of inertia is $4499.84 \text{ g}\cdot\text{mm}^2$. The static friction torque of the rotor in its guidance mechanism is $0.11 \text{ mN}\cdot\text{m}$.

An ATI nano17¹ force sensor is placed below the suspension for the measurement of forces in all directions. It is primarily used to measure normal force although it can be used to evaluate the torque in a static or quasi-static manipulation. The force sensor is used for positioning the rotor against the actuator. The moment about the axis of the rotor has to be zero at rest if the rotor is well placed against the actuator. The position is measured using a 500 steps Avago HEDS-5500 encoder. The encoder is used in quadrature X4 mode, which means it produces 2000 counts per turns leading to an angular resolution of 3.14 mrad (0.18°).

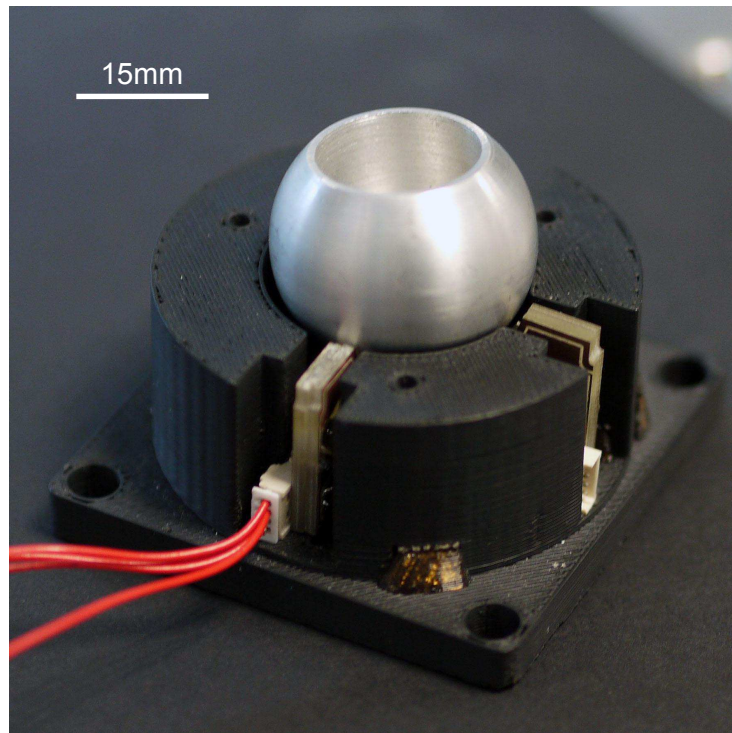
A spherical motor has been validated (figure 5.7a). Nevertheless the measurement of forces and displacement of a spherical rotor are complicated and the single degree-of-freedom motor using a cylindrical rotor is better suited for the actuator characterization (figure 5.7b).

5.3.2 Measurement set-up

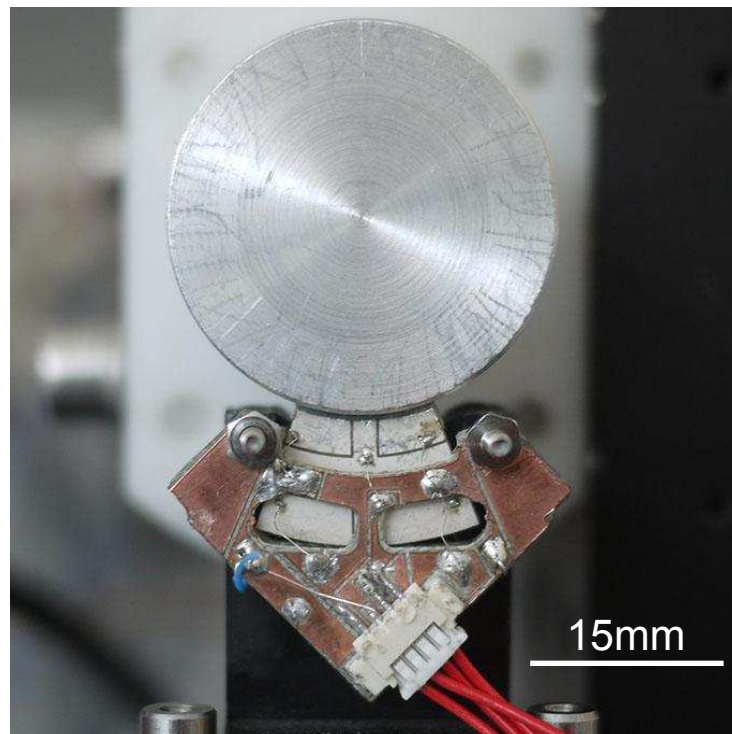
The measurement set-up used for characterization is shown in figure 5.8. A Labview interface controls two function generators (Tektronik AFG3021B) via USB. The two signals generated are synchronized and fed to an amplifier unit (Elbatech T-503) which uses high-power operational amplifiers to drive the actuator. The two output voltages are measured using voltage dividers that are directly connected to the analog input of a National Instrument PCI-6251 acquisition card. The currents sent to the actuator are measured using 10Ω shunt resistors.

A low-pass filter is observed between the voltage divider and input capacitance of the card and a calibration is required to obtain correct voltage and current measurement. It is performed using an admittance measurement of a known impedance (typically a 50Ω 0.1% resistor). A comparison of non-calibrated and calibrated measurements of a 1.5 mH inductor are shown in figure 5.9. The non-calibrated measurements show good characteristics in terms of gain, with the inductance only slightly over-evaluated. The main problem is the phase term which diverges from the inductor model prediction. This effect is largely compensated using a calibration. Incremental Encoder is read using a specific counter input of the NI Card and 6 analog inputs of the 6251 card are used to obtain forces readings.

¹<http://www.ati-ia.com/>



(a) Spherical motor assembly.



(b) Single degree-of-freedom assembly used for actuator characterization.

Figure 5.7: Validated ultrasonic motor prototypes. A single degree-of-freedom actuator using a spherical rotor has been validated. A cylindrical rotor is used for characterization allowing for a simplified measurement of the actuator characteristics.

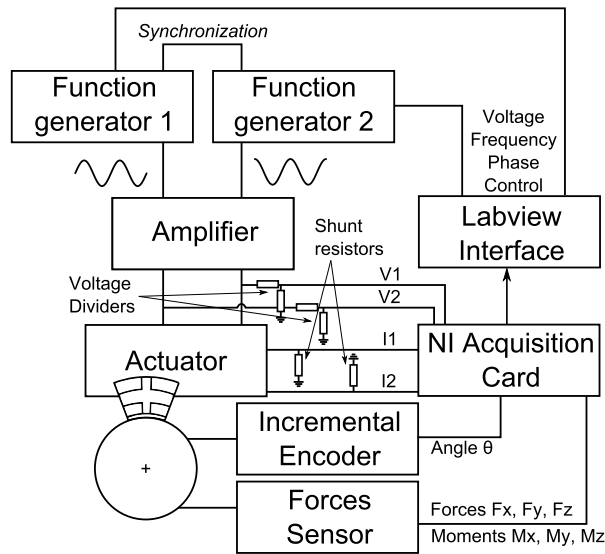


Figure 5.8: Measurement set-up for actuator characterization. A Labview interface is used for control of the instruments and acquisition of the data. Two arbitrary function generators are synchronized to generate the signals for both modes excitations. A high voltage amplifier is used to drive the actuator while a National Instrument acquisition card allows to acquire electrical and mechanical data from the experiment.

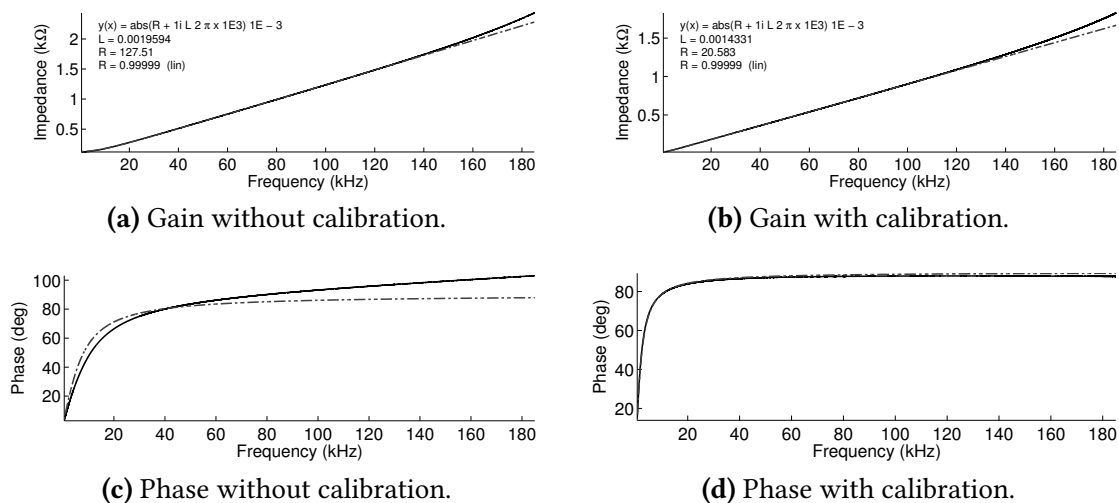


Figure 5.9: Impedance measurement of a 1.5mH inductor with and without calibration. The dashed-dotted line represents the inductor model while the solid line is the experimental data.

5.3.3 Measurement procedure

The measurement procedure is divided into several steps:

- The preloading force is applied using the micro-metric platform and the force sensor. Rotor is centered using a measurement of the torque exerted along the axis of the rotor (it should be zero for proper alignment).
- A search of the frequency span where speed of the actuator is maximum is performed at the excitation voltage. It allows to find the frequency points where the actuator is characterized.
- Mechanical characteristics are measured. Five measurements of transient speed and forces are performed at the found frequencies.
- Electrical characteristics are measured. Input voltage and current are measured. Electrical and mechanical measurements cannot be performed simultaneously because of the limited sampling frequency of the National Instrument card.

This procedure allows to obtain frequency response of the actuator with indications about the stability of the actuator (thanks to the multiple measurements). Static torque measurements can be performed using the force sensor but its bandwidth is too limited for dynamic torque measurements. An approximate method described by Nakamura et al. [52] is used. Transient speed response is fitted with an exponential:

$$\dot{\theta}(t) = \dot{\theta}_0(1 - \exp(\frac{-t}{\tau})) \quad (5.1)$$

Maximum speed of the actuator $\dot{\theta}_0$ is obtained and starting acceleration is estimated from the fit parameters:

$$\dot{\theta}(\delta t) \approx \dot{\theta}_0(1 - 1 + \frac{\delta t}{\tau}) \quad (5.2)$$

$$\ddot{\theta} = \frac{d\dot{\theta}}{dt}(0) = \frac{\dot{\theta}_0}{\tau} \quad (5.3)$$

Using inertia of the rotor, the torque can be calculated:

$$C = J\ddot{\theta} \quad (5.4)$$

$$C = J\frac{\dot{\theta}_0}{\tau} \quad (5.5)$$

An example of this procedure is shown in figure 5.10. A good correlation is observed between the fit and the experimental data although speed variations are observed on the

measurements. These variations are due to the tolerances of the rotor associated with the mobility of the actuator in its support. The fit gives a good average of the established value and the correlation of the slope at the start-up of the actuator indicates a good estimation of the starting acceleration which is proportional to the torque.

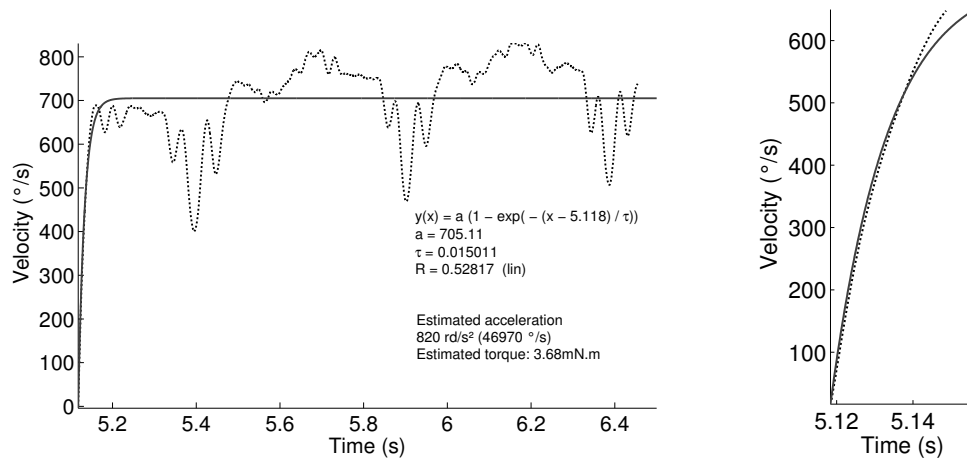


Figure 5.10: Example of a transient speed response of the actuator. The speed variations are attributed to the rotor eccentricity and cylindrical tolerance that are amplified by the mobility of the actuator in its support.

5.3.4 Model comparison

To validate the model, a comparison with experimental data is proposed. Model computation requires to know precisely the equivalent model parameters of the actuator. Damping of the actuator is difficult to evaluate from modeling because of the interactions between the actuator, its support and the rotor. Therefore, it is proposed to use low voltage experimental admittance measurements as inputs for the model:

- A low voltage admittance measurement of the actuator is performed. Using a non-linear regression of the data, the equivalent circuit parameters are obtained.
- C_1 and Q_m are used to estimate the amplitude of the mode displacement at the edge of the actuator. The relation between amplitude and dynamic branch energy obtained from finite element harmonic analysis is used (figure 4.17 on page 116).
- The modes amplitudes are used as input to the contact model and allow to obtain an estimation of the mechanical output of the motor.

5.4 Voltage dependance

In this section, the influence of excitation voltage on actuator properties is studied. The electrical and mechanical responses of the actuator are analyzed. The actuator has a large

surface in contact with the rotor but the central part of the layer is cut out to improve contact and limit the influence of layer uncertainties. The resulting layer length is 7.4mm (3.4 mm removed).

5.4.1 Admittance response

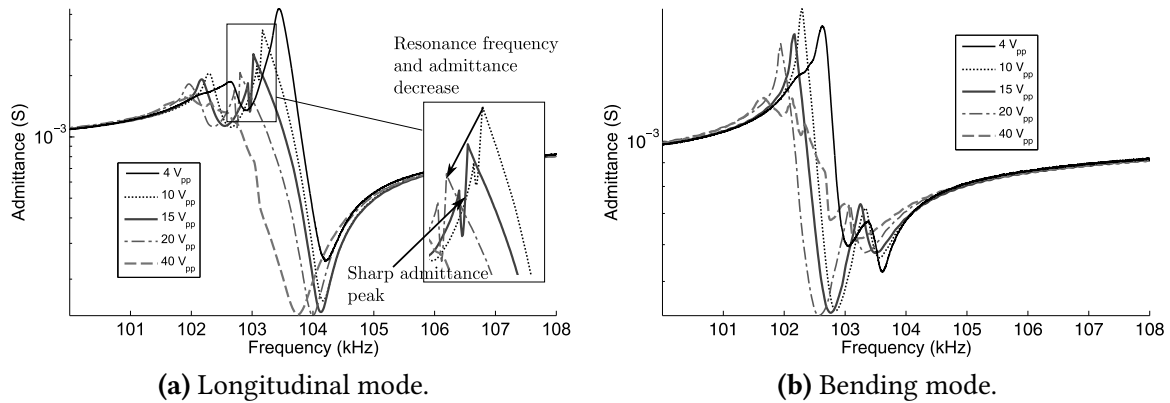
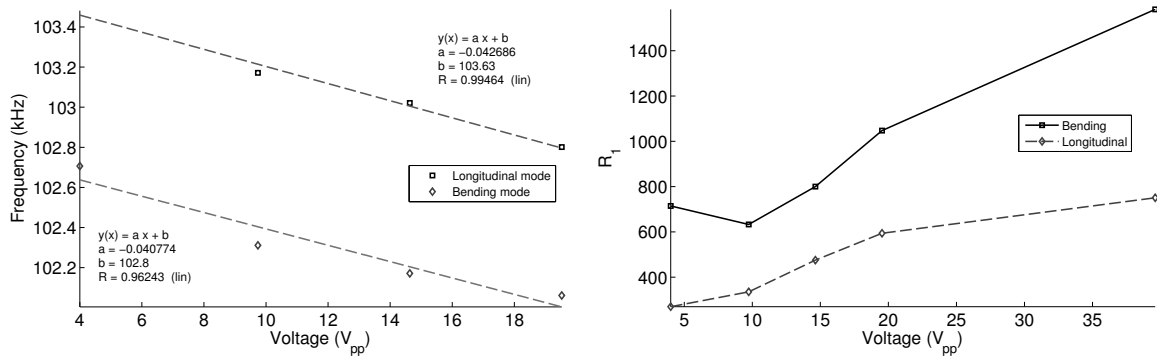


Figure 5.11: Evolution of admittance response as a function of the voltage. A displacement of the resonance frequency along with the deformation of the admittance peak are observed as voltage increases. Maximum admittance point is reduced indicating an increased damping of the actuator.

Admittance response is greatly affected by the excitation voltage. Figure 5.11 shows the evolution of admittance response for amplitudes between 4 and 40 V_{pp}. Results show a shift of resonance to lower frequencies. A deformation of the resonance peak when amplitude increases is also observed. At low amplitude, admittance changes smoothly and symmetrically around resonance frequency. As amplitude increases, the peak is sharper and non-symmetric (especially for longitudinal mode). Zhao [71, p. 362] described similar phenomena. Parasitic peaks are more visible and maximum admittance drops until it becomes difficult to distinguish resonance. This last characteristic indicates a drop in quality factor of the actuator. Although it is difficult to evaluate quality factor from conventional equivalent model because of the deformation of the response, R_1 can be estimated based on maximum real admittance point. This behavior had already been identified in chapter 5 (section 4.5 on page 105), where quality factor is found to be dependent on excitation voltage. It is similar to phenomena described by Uchino and Hirose [86] and attributed to non-linear damping in the material.

The evolution of resonance frequency and dynamic resistor R_1 are shown in figure 5.12. The two resonance frequencies decrease similarly. This evolution is well approximated by affine functions. The frequency change is -42.6Hz/V_{pp} for longitudinal mode and -40.7Hz/V_{pp} for bending mode. The non-significant difference of 1.9 Hz/V_{pp} in mode frequency shift does



(a) Longitudinal and bending modes resonance frequencies as a function of excitation voltage.

(b) Evolution of dynamic resistor R_1 as a function of excitation voltage.

Figure 5.12: Evolution of series resonance frequency and dynamic resistor as a function of the voltage applied to the electrodes. A drop in resonance frequency is observed as amplitude is increased on the two modes. This shift is about the same on both modes and do not affect mode degeneracy.

not affect mode degeneration. The dynamic resistor indicates an increased damping as voltage increases. R_1 tends to reach a saturation point on bending mode when voltage is high. The major consequence of this high damping is a possible over-evaluation of the quality factor used for the model evaluation, since actuators properties are measured at low voltage.

5.4.2 Mechanical response of the actuator

An actuator with a 1 mm contact layer is preloaded with a 1N force and the motor characteristics are measured as a function of voltage. The goal is to analyze the behavior of the actuator with a change in the voltage and to compare the experimental results with the model.

Frequency response

Figure 5.13 shows the evolution of speed and torque as a function of frequency and voltage. The frequency response is different from contact model predictions. The model predicts a symmetric response of the motor around the resonance frequency. The obtained response is non-symmetric with a sharp speed increase at resonance frequency. This is in accordance with the admittance response in figure 5.11, that shows a deformation of the maximum admittance peak as voltage is increased. Around the maximum speed point, the behavior of the actuator is erratic and the actuator stops within a few seconds. This phenomenon is attributed to a resonance frequency displacement. Heat generation and change in the mechanical load of the actuator shift resonance frequencies of the actuator and the sharpness of the resonance peak may stop motor rotation. Ferreira and Minotti [93] reported a similar

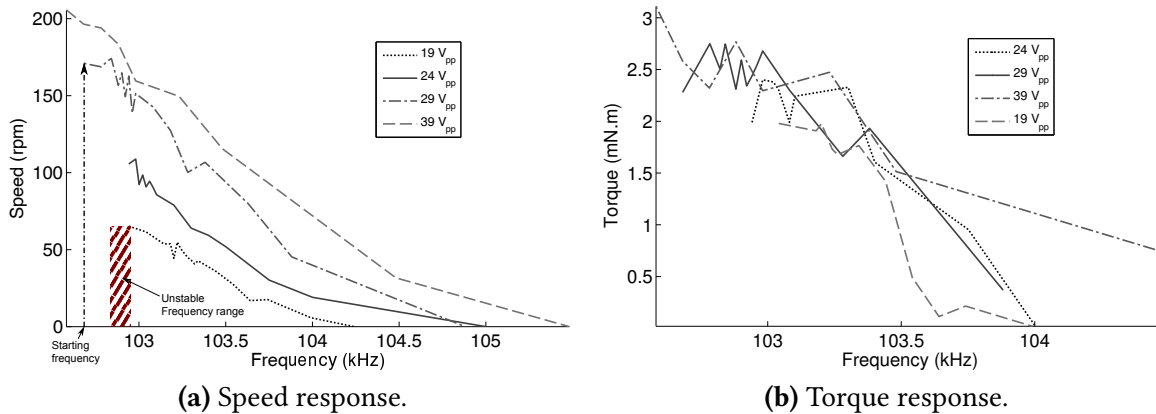


Figure 5.13: Motor frequency response with respect to excitation voltage. The frequency for which maximum speed is reached decreases as the amplitude increases. Around resonance frequency a sharp increase of speed is observed. An unstable frequency range is observed before resonance.

unstable behavior in ultrasonic traveling motors which is consistent with our observations. The starting frequency of the actuator is lower as voltage increases. This result is similar to the observations made on admittance measurements. As expected, the speed of the motor increases as voltage increases.

The torque response shows a saturation effect with an almost constant torque for a large frequency span. As frequency is increased, an abrupt drop in motor torque is observed when amplitude becomes too low to transmit torque to the rotor. The saturation effect is consistent with a phenomenon described in chapter 4 (figure 3.10b) with a torque saturation as the amplitude of displacement is increased.

Torque and speed characteristics

Figure 5.14, shows the evolution of maximum speed and torque as a function of the amplitude. The model is computed from low voltage admittance of the actuator that is used for mode amplitude calculation. These amplitudes are used as input in the contact model that allows to obtain the characteristics of the actuator shown in the figure. In terms of speed, the model shows the same tendency as the experimental data, the average relative error of the experimental data as compared to the model is -27 % with a maximum error of -32 % at high amplitude. Although this error is high, it is still considered a good approximation of the performance of the actuator considering that numerous parameters and especially amplitude at the interface is estimated directly from low amplitude electrical measurements. Several causes for these differences can be considered. The increased damping with respect to amplitude is an important effect that is difficult to take into account in the model and causes the mode amplitudes to be over-estimated. Finite element approximation assume a perfectly symmetric system and asymmetries in the mounting of the actuator, contact layer

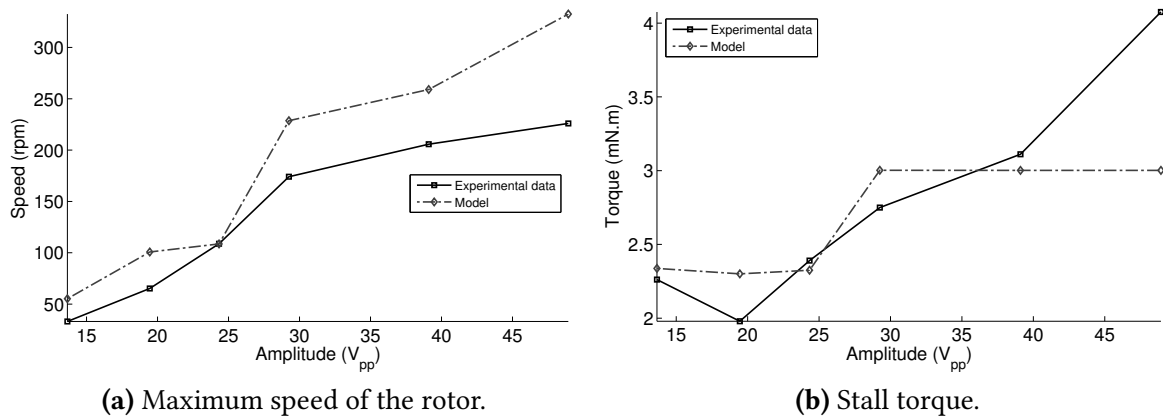


Figure 5.14: Motor characteristics with respect to excitation voltage. Torque and speed increase as voltage increases. There is a saturation effect in speed which is attributed to an increased damping of the vibration. The model predicts a quick saturation of the output torque which is not observed experimentally and is associated to uncertainties on the contact layer properties and asymmetries of the actuator assembly.

machining and repartition of soldering points may have an influence on the mode shapes of the actuator. Experimental data shows an increase of the torque up to 4mN.m as voltage increases. The model predicts a similar increase with a saturation torque of 3mN.m reached at 30V_{pp}. The average error is 11% with a maximum of 37 % at maximum voltage. This difference is attributed to asymmetries of the assembly.

Efficiency

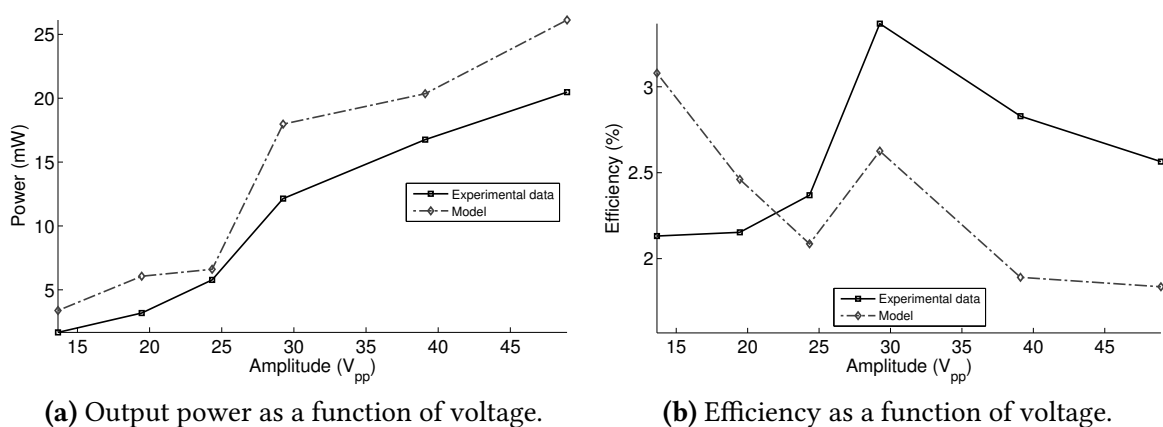


Figure 5.15: Power and efficiency as a function of the excitation voltage. Power increases as the voltage increases. This evolution is similar to the evolution of the speed of the actuator. A maximum of 3.4% efficiency is reached at 30V_{pp}.

Figure 5.15 shows the evolution of output power and motor efficiency as a function of voltage. An output power between 5 and 20 mW is measured, which is about the same

order of magnitude as what is predicted by the model. A maximum efficiency of 3.4% is measured at 30 Vpp. The model, based on low voltage admittance measurements, predicts efficiencies of the same order of magnitude. Lower values are observed at higher excitation voltage. They are due to non-linear damping that cause an overestimation of the quality factor. The low efficiency is explained by several factors. The stiffness of the layer is an important parameter since it is associated with contact phase angle φ_c . Increasing the layer stiffness should result in a diminution of φ_c and an increase in the motor power at constant input energy. Improvements of the holding mechanism can improve the quality factor of the modes and reduce the damping of the modes.

5.5 Phase shift influence

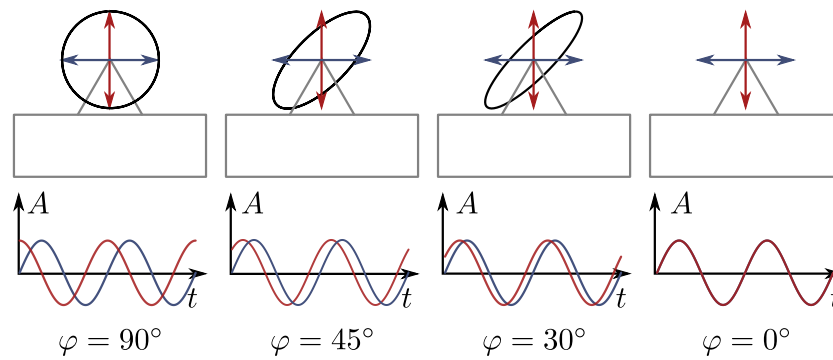


Figure 5.16: Evolution of elliptical trajectories as a function of phase shift. Two orthogonal modes are represented in blue and red. As the temporal phase shift tends to zero, the elliptical trajectory becomes a straight line.

The phase shift between the two excitations has an important role in the performance of the actuator. As shown in figure 5.16, it affects the shape of the elliptical trajectories and is used to reverse the direction of the motor. Theoretically, the mechanical properties of the actuator are maximal at phase shifts of -90° and 90° , where the two mode displacements cause the larger elliptical motions. When the two modes are in-phase, the movements at the interface are rectilinear and oblique. Although oblique trajectories can be used to generate rotor motion such as in asymmetric single-mode excitation, in our case, the symmetric motions on both sides of the contact area should result in a zero net tangential force and no rotation of the motor.

5.5.1 Speed and torque

The experiment is performed on an actuator with a 1mm contact layer at a 1N force. Figure 5.17 shows the evolution of speed and torque as a function of the phase shift. It can be observed that it is possible to change the direction of the rotation of the actuator by changing

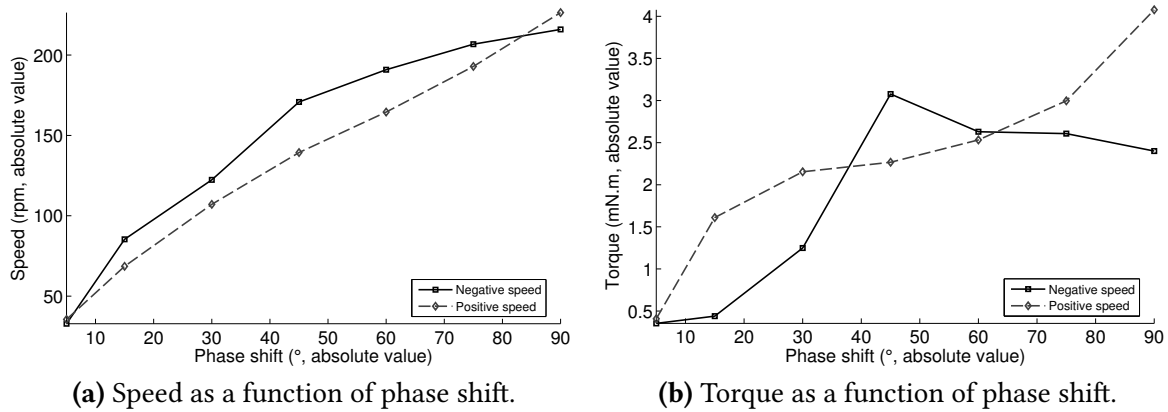


Figure 5.17: Motor properties as a function of the phase shift between the two signals. The maximum speed points are reached for phase shift values of 90°. The actuator speed response is slightly asymmetric, with the negative rotation direction 13.6% faster than the positive one.

the sign of the phase shift and as expected, the closer the phase shift is to 90° the faster the actuator is. This experiment gives indication about the symmetry of the actuator vibration modes and whether a direction of motion is privileged over the other. In our case, the average difference in terms of speed from one direction to the other is 13.6%. A maximum of 22.5% of difference is observed at a 43° phase shift. This indicates that there exists asymmetries in the mechanical holding mechanism or contact layer.

The torque response is similar to the speed response with an inversion of torque as the sign of the phase changes. The asymmetry is more pronounced on torque measurement with positive torque values 30% higher on average than the negative ones. Maximum torque for the negative rotation direction is not reached at the highest speed but at 41° of phase shift. Again, these divergences are attributed to asymmetries.

5.5.2 Power and efficiency

As expected, the maximum output power is reached around a 90° phase shift with 20mW for positive speed and 14mW for negative values confirming the asymmetries discussed previously. When phase shift is reduced the output power is reduced while the electric power stays the same. This result in an important drop of efficiency around the 0° phase shift with efficiencies below 0.5%. A maximum efficiency of around 2.5% is reached at 90° phase shift with an excitation voltage of 50Vpp. From a control perspective, the phase shift can be used to change motor speed. However, poor linearity and low efficiency at low phase shift are two important limitations.

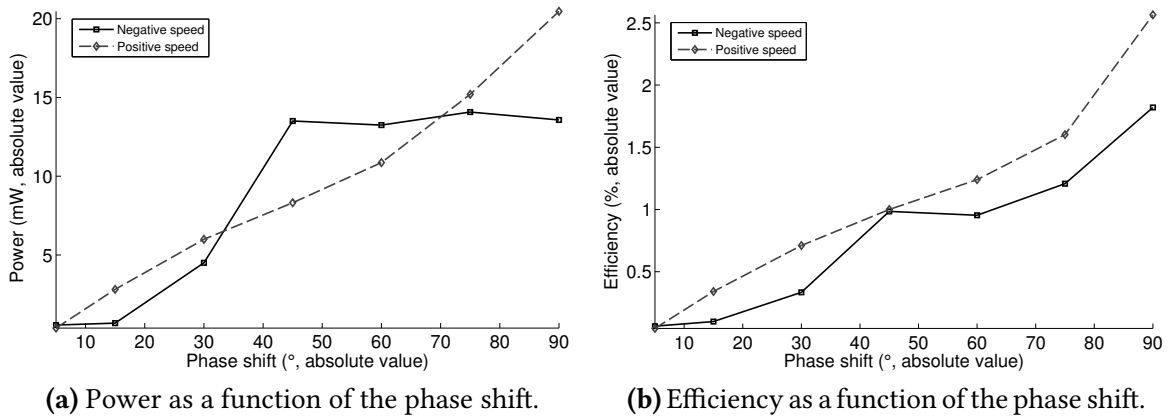


Figure 5.18: Output power and efficiency of the actuator as a function of the phase shift between the two signals. Output power is maximal at a 90° phase shift. Efficiency decreases highly as phase shift is reduced.

5.6 Preloading force dependance

The preloading force has a major role on the actuator performance. As explained in chapter 3, increasing the normal force should result in an increased transmitted torque and a lower speed of the rotor. In this section, experimental results of the preloading effect is presented. Low voltage admittance measurements are analyzed and mechanical characteristics of the motor are studied with respect to preloading force. Results are compared to the model developed in the previous chapters.

5.6.1 Effect of preload on resonance characteristics

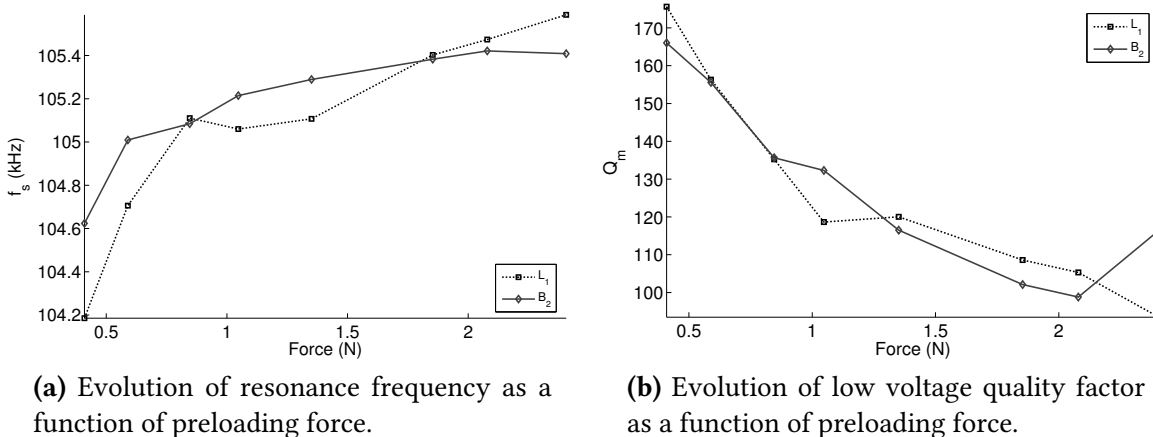


Figure 5.19: Evolution of resonance characteristics as a function of preloading force. The resonance frequency of the actuator increases as preloading force is increased. A decrease of Q_m is observed as the preloading force is increased, this indicates an increased damping of the vibration.

Resonance characteristics of the actuator are measured at low amplitude using admittance measurement for different preloading forces. In figure 5.19a, it can be observed that the resonance frequency tends to increase as the preloading force increases. Arnold and Mühlen [94] reported similar effect on pre-stressed piezoelectric transducers. The quality factor is similar on both modes and tends to decrease as the preloading force increases. A limit value around 100 is reached above 1.5 N preloading force, indicating that mechanical damping saturates as preloading force increases.

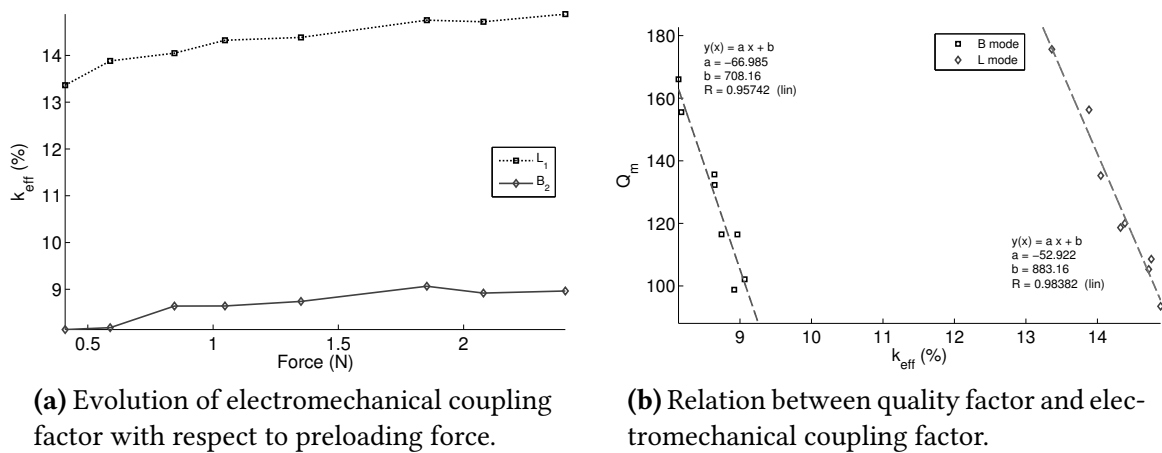


Figure 5.20: Evolution of resonance characteristics as a function of preloading force.

Figure 5.20 shows the evolution of the electromechanical coupling factor as a function of preloading force. k_{eff} increases as preloading force increases. The evolution of k_{eff} as a function of Q_m is shown in figure 5.20b. A linear relation is observed between quality factor and coupling efficiency. It is similar to the observations made in section 4.5.4 where the divergences in quality factor Q_m are attributed to an energy dependent damping. Here, the electromechanical coupling factor change is due to the preloading force. One hypothesis for this change is the pre-stressed condition of the actuator that affect modal strain distribution and therefore k_{eff} .

5.6.2 Preloading force and frequency response of the actuator

The preloading force influences the frequency response of the actuator. In figure 5.21 the speed and torque evolution are shown as a function of preloading force. The maximum speed of the actuator decreases as the preloading force increases. In the same way as for the amplitude study presented previously, around the resonance frequency, the actuator is unstable. The speed decreases as frequency increases similarly to what has been observed in the voltage study. Between 0.6 and 1.4 N the speed to frequency slope is quite similar and the curves coincide. The frequency where speed reaches its maximal value increases with

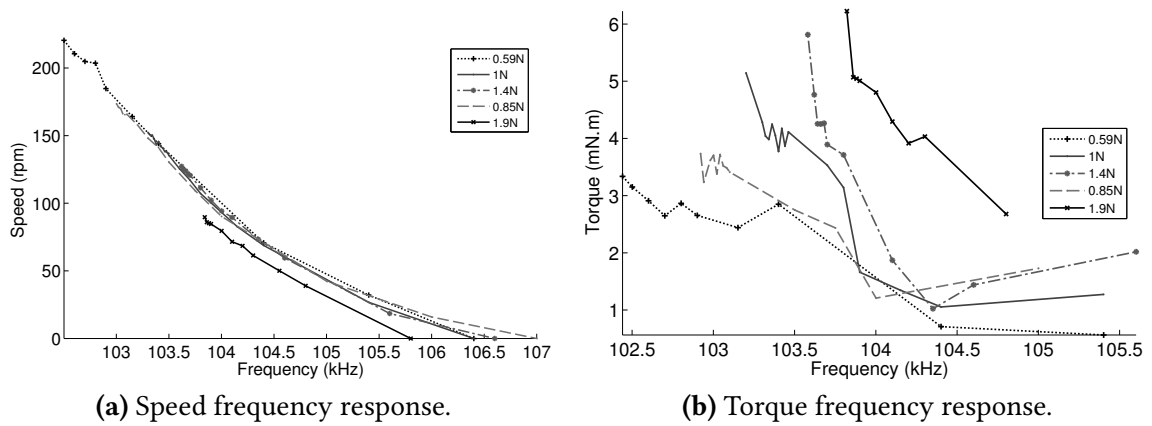


Figure 5.21: Frequency response of the actuator as a function of the preloading force. As preloading force increases, maximum speed decreases and is reached at higher frequency.

the preloading force. This is consistent with the observations on low voltage admittance measurements that show an increase in resonance frequency as preloading force is larger.

The maximum torque is shifted to higher frequencies as preloading force is increased and higher torque is observed with respect to preloading force. The torque decreases significantly faster with respect to frequency as preloading force increases. This phenomenon is due to the saturation torque effect observed with amplitude in contact model. At low preloading force, this saturation torque is reached quickly and thus increasing the frequency causes a drop in the amplitude that has no effect on the torque which is already saturated. When preloading force is increased, this saturation torque is reached for a lower frequency span and the torque drops quickly with respect to frequency.

5.6.3 Torque and speed as a function of preloading force

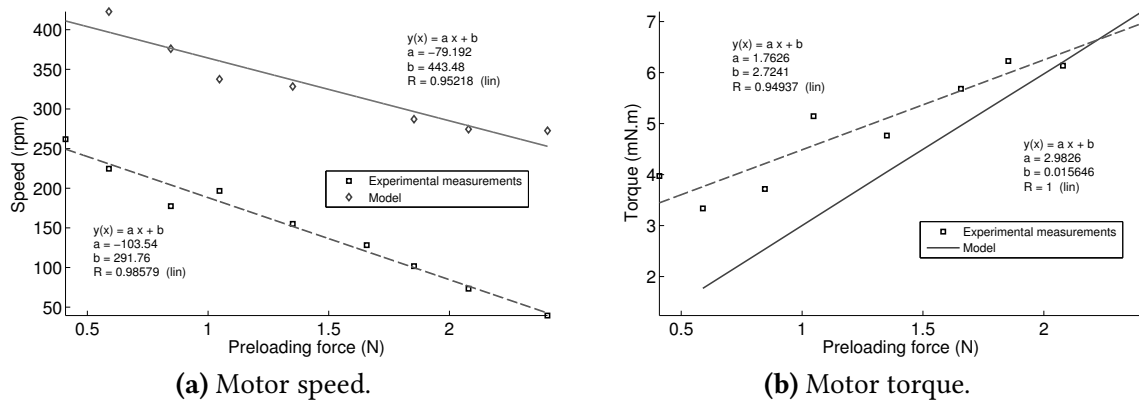


Figure 5.22: Mechanical characteristics of the motor as a function of the preloading force.

Figure 5.22 shows the motor speed and torque as a function of preloading force. The model is also shown for comparison. As observed in the frequency responses, speed tends to decrease as the preloading force increases, experimental data shows an average drop of 103 rpm/N at 50Vpp. Prediction from the model shows a speed of about 60 % higher than the experimental speed, with a drop of 79 rpm per Newton. This difference is attributed to the additional damping due to high voltage excitation and increased preloading force that is not taken into account in the model. These divergences may be due to other considerations such as mode shapes and contact material properties that affect this relation and show the limits of the model. Torque characteristics have similar divergences. Experimental results show a variation of about 1.76 mN.m/N while model predicts 2.98 mN.m/N. At low preloading force, the difference between model and experimental measurements is strong and may be due to an asymmetry of the actuator that generates a torque similarly to asymmetric excitation single-mode actuator.

5.6.4 Preloading and efficiency of the actuator

Figure 5.23 shows the evolution of the efficiency as a function of preloading force. An optimal efficiency of 3.5% is observed at a 1.5N preloading force. Above this force, the efficiency drops because of lower speed and limited increase in torque. The model efficiency values are computed using two different methods, one uses the low voltage admittance characteristics to estimate the input power while the other uses experimental electric power for efficiency calculation. Although similar order of magnitudes is observed between model based on experimental electric power and experimental data, results computed from low power admittance measurements cause the electric power estimation to be above the measured values. At higher preloading force, model predicts an increase in efficiency that is not observed experimentally. It is believed that high damping caused by holding mechanism interaction limits the properties of the actuator at larger preloading force.

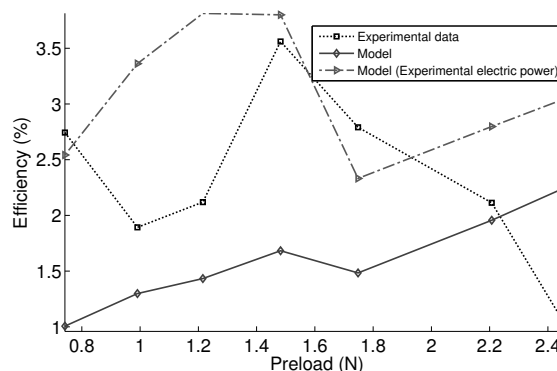


Figure 5.23: Efficiency as a function of preloading force. An optimal efficiency of 3.5% is observed for a preloading force of 1.5N.

As a summary, the ultrasonic motor performance depends on both amplitude and preloading force. The amplitude has an important influence on motor speed and torque but non-linear damping show a loss of efficiency of the motor when amplitude is high. An optimal excitation voltage point that depends on the contact conditions exists. Preloading force has an important effect on the torque of the actuator and it is the major parameter that should be tuned to obtain the desired stall torque of the motor. On the other hand it has a negative effect on the speed of the motor and an increase of amplitude is required to improve speed of the motor. Theoretically the speed of the actuator could also be improved by an increased stiffness of the layer that reduces the contact time while providing similar torque. Experimentally, it is found that the maximum efficiency of the actuator depends both on excitation voltage and preloading force (an optimal preloading force of 1.5N is found at 50Vpp while a 30Vpp excitation provides the maximal efficiency at 1N).

5.7 Contact length

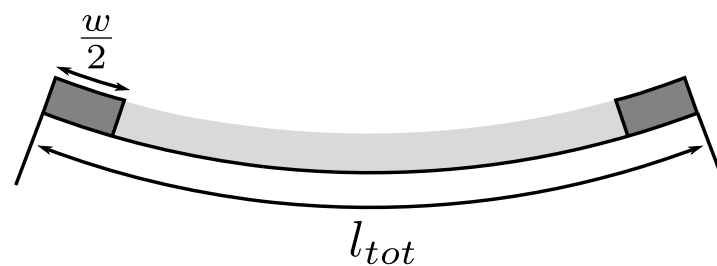


Figure 5.24: Contact layer length change. The contact layer is removed starting from the center of the actuator which is the point where the tangential speed is minimal.

As discussed in chapter 3, the contact length affects motor performance. We propose to analyze the influence of the contact using a 0.4mm layer which is progressively reduced. The layer is removed as described in figure 5.24. Low amplitude admittance responses are analyzed along with motor characteristics as a function of the length of layer. Because removal of some layer mass may cause the modes to shift, frequencies are tuned before each set of experiments.

5.7.1 Influence of contact pattern on resonance characteristics

Figure 5.25 shows the evolution of low voltage quality factor as a function of contact length for a given preloading force of 1N. It can be observed that the quality factor tends to decrease as the contact length is increased. this is especially true for bending mode with an important drop above a 8 mm length of contact. Amplitude at the contact area of the actuator should therefore be improved as contact length is reduced.

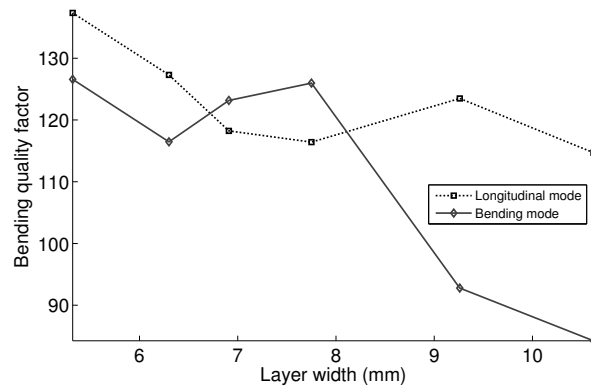


Figure 5.25: Q_m as a function of contact extent for a preloading force of 1N. The quality factor is evaluated from low voltage admittance measurements.

5.7.2 Influence of contact length on speed-torque characteristics

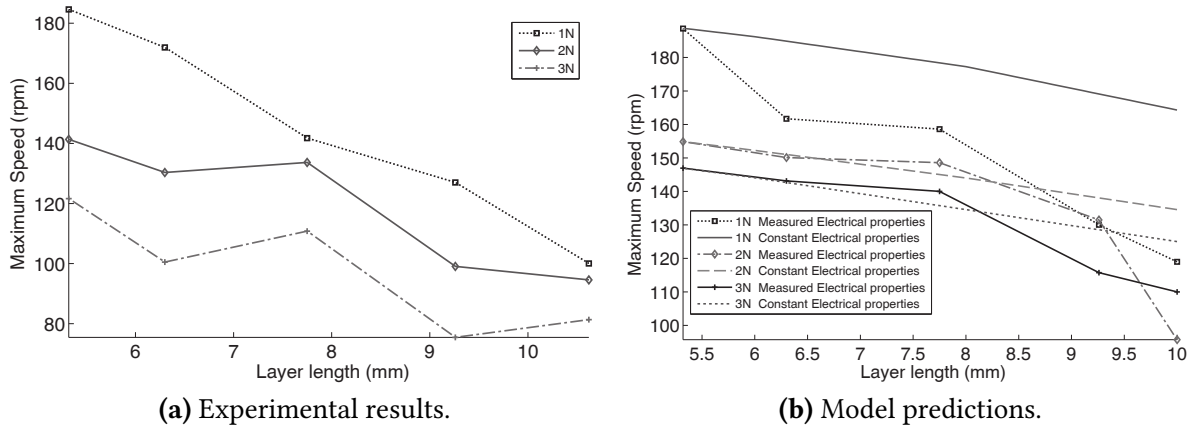


Figure 5.26: Speed versus contact length for various preloading force. An important decrease in motor speed is observed as contact length is increased. Model predicts this decrease.

The response of the actuator is observed for different contact lengths. Speed of the actuator is presented in figure 5.26 as a function of the contact length. It is observed that as the length of the layer is reduced, the speed is increased. For the three considered preloading forces, the effect is important with an increase from 100 rpm to 184 rpm at 1N when the contact length is reduced to about half its total length (5.4 mm).

Figure 5.26b shows the model predictions. The quality factor used for model prediction is adjusted to correspond to experimental speed values at low contact layer length and 1N. This allows to study how the contact model predicts relative changes in rotor velocity. The first set of data consider constant electrical properties. The quality factor is kept at a constant value, which correspond to the $w = 5.4$ mm estimated quality factor. A decrease in speed is observed as the layer length increases. At a 1N preloading force, the speed changes from 188 rpm at 5.4 mm to 164 rpm at 10 mm which is a lower speed drop than observed exper-

imentally. This underestimation of speed diminution is due to a change in damping caused by the modifications of the contact conditions. Using measured quality factor for each layer length give better correlation with a speed of 188 rpm at 5.4 mm that drops to 95 rpm at 10 mm with a 1 N preloading force. This indicates the limit of the model that does not predict the damping evolution due to changes in contact conditions.

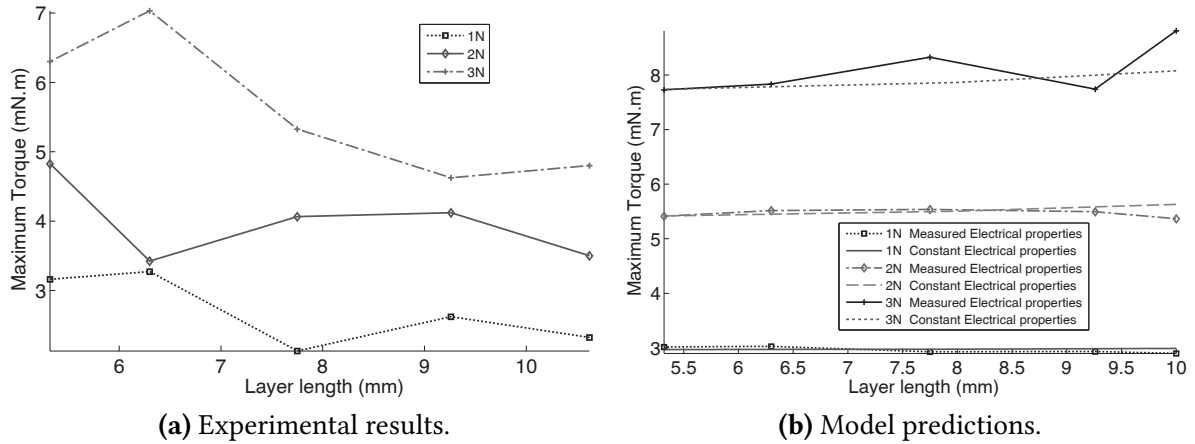


Figure 5.27: Torque versus layer length for various preloading forces. A slight decrease in torque is observed as layer length is increased. The model predicts quasi-constant torque with layer length.

Torque evolution is represented in figure 5.27. A diminution of torque is observed as contact length increases. At a 3N preloading force, the torque drops from 6.2 mN.m to 5mN.m when contact layer is changed from 5.4mm to 10mm. Similar torque decrease is observed at 1N and 2N. The model predicts different results. When constant quality factor are considered, the torque tend to increase as contact layer length increases. However when measured electrical properties are used, the torque decreases as contact length increases for 1N and 2N preloading forces. For 3N, the torque is still predicted to improve. It is due to an overestimation of the quality factor which is adjusted to correspond to 1N preloading experimental data. The model variations are small as compared to measured experimental data. Asymmetries in the contact that increase as the contact length is increased could be a reason why such differences are observed.

5.8 Resonance tracking of the actuator

The designed actuator is based on the excitation of resonant modes in order to obtain lower admittance of the actuator and controlled deformation shapes. Resonance is excited using a specific frequency which corresponds to the mode frequency. This frequency depends on the actuator state whether it is the temperature, humidity or the load it is subjected to. There is a need to find and keep track of the resonance frequency in order to have a good behavior of

- ω_r corresponds to the frequency where the system is completely resistive. At this frequency, the phase shift between voltage and intensity is zero.

ω_m and ω_r are easily tracked based on maximum power or zero phase frequencies while ω_s , the actual mechanical resonance frequency is difficult to track. When $1/R_1$ is large as compared to $C_0\omega_s$, these three frequencies are close, and tracking ω_m or ω_r is enough for proper motor operation.

5.8.1 Phase-based resonance tracking

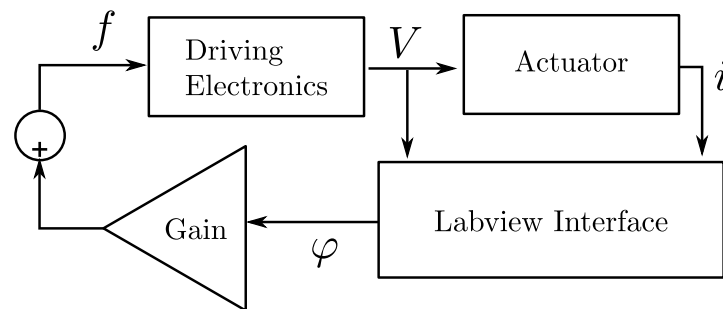


Figure 5.29: Control for zero phase tracking implemented in Labview.

A tracking method based on intensity phase measurement has been implemented in Labview. The objective is to keep track of the point where the phase between current and voltage is zero. The control loop is shown in figure 5.29. An initial driving frequency below the resonance is sent to the actuator. A National Instrument acquisition card is used to measure the phase between the two voltage and current. The measured phase is multiplied by a gain and added to the current driving frequency. When the phase between current and voltage is zero, the resonance frequency is found.

Figure 5.30 shows the influence of resonance frequency tracking on stability of the actuator. The tracking algorithm is activated for the first minute of the experiment to find the resonance frequency of the system. Then tracking is set off and the actuator is driven at the constant frequency of 102.6 kHz. In the first 10 minutes of the experiment, the velocity decreases from 150rpm to 100 rpm. Irregularities in the speed are observed with variations of 20 rpm. These variations are due to resonance frequency shift of the actuator associated with heating and cooling cycles of the actuator. After 75 minutes, tracking is set back on, a change in frequency is observed and velocity of the actuator increases up to 160 rpm. The speed stays constant for the last 75 minutes of the experiment. Small oscillations in speed are observed and attributed to the low resolution in phase due to sampling frequency (600kHz) of the NI card. At high speed, the actuator is sensitive and high resolution in phase is required in order to keep constant properties. Using an analog tracking circuit should result in a better speed homogeneity.

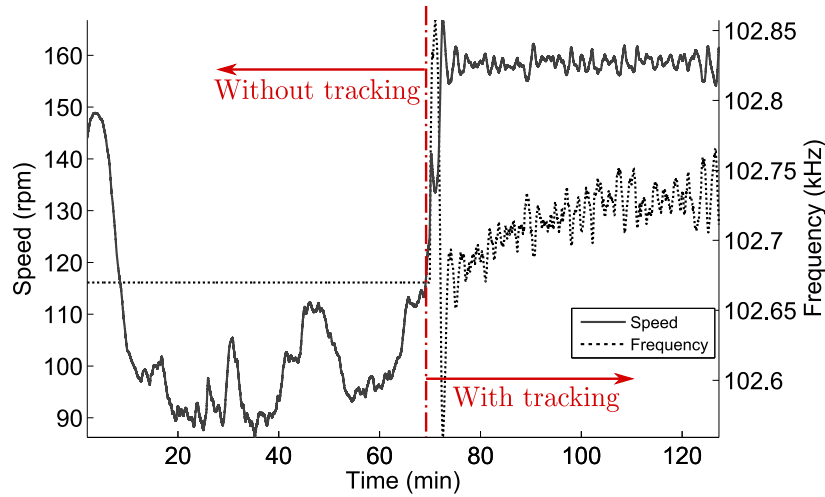


Figure 5.30: Influence of a resonance tracking system on the performance of the actuator. First, the tracking algorithm is launched to find the resonance frequency. Once it has been found, tracking is set off and speed is measured over time at constant driving frequency. After 75 minutes, tracking is put back on for comparison.

5.8.2 Phase tracking for highly damped vibrations

Piezoelectric materials are highly non-linear and as voltage is increased, the damping of the system increases. An important added damping can also be due to the preloading force of the actuator. If the quality factor of the resonance is low, the zero phase point cannot be considered as the resonance point and it is possible that below some quality factor, the zero phase point do not exist anymore, because static capacitance imaginary admittance is not totally compensated. A solution to avoid this problem is to compensate static capacitance using a parallel inductor. Admittance of the static capacitance is given by:

$$A_{C_0} = iC_0\omega \quad (5.6)$$

The admittance of an inductor is given by:

$$A_L = \frac{1}{iL\omega} \quad (5.7)$$

So that at resonance the inductor used to compensate static capacitance is:

$$L = \frac{1}{C_0\omega_s^2} \quad (5.8)$$

Considering a 1.2nF static capacitance at 104kHz, the obtained inductor value is 1.9mH. Figure 5.31 shows the shift caused by a 1.5mH parallel inductor on the considered actuator. Although the maximum real admittance point ω_s is at a phase shift slightly below zero, ω_r is closer to series resonance frequency than before compensation

This method is efficient for tracking a single mode because of a large phase change at resonance and the proximity of ω_r and ω_s . In the case of a multi-modes actuator, coupling

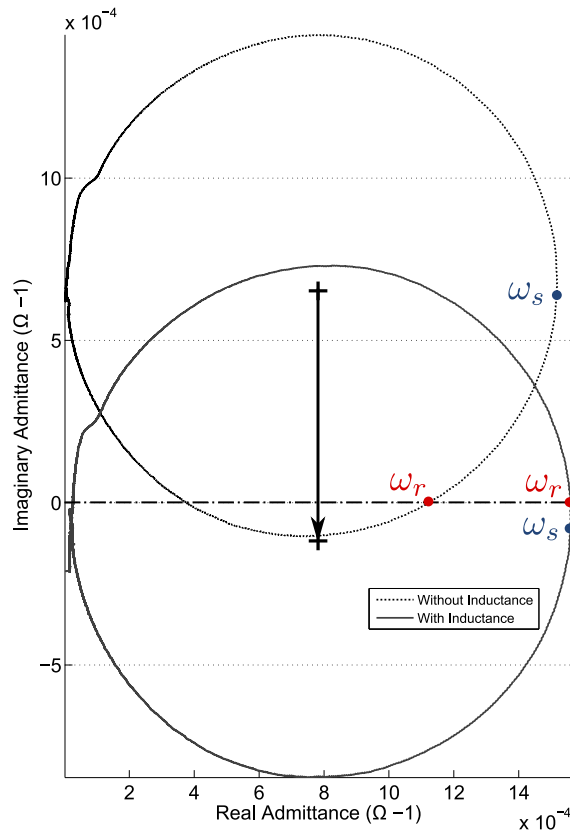


Figure 5.31: Admittance circle shift caused by a parallel inductor.

between the modes can cause difficulties in resonance tracking. Theoretically, the bending mode is anti-symmetric and should not generate any current on the longitudinal electrode because of a zero deformation integral. Experimentally, the electrode pattern manufacturing tolerances and mechanical asymmetries cause a non negligible current to be generated on the longitudinal electrode, leading to a phase shift of the measured current. Considering the current on the longitudinal electrode:

$$I = I_0 \cos(\omega t) + I_B \sin(\omega t) \quad (5.9)$$

In this equation, it is assumed that the phase of the current is zero on both modes. This approximation supposes that both modes are at the same resonance frequency and current and voltage are in phase on both modes at this frequency. The intensity can be expressed in the complex form as:

$$I = (I_0 + iI_B) e^{i\omega t} \quad (5.10)$$

So that the actual phase of the current is not zero but:

$$\phi = \arctan \frac{I_B}{I_0} \quad (5.11)$$

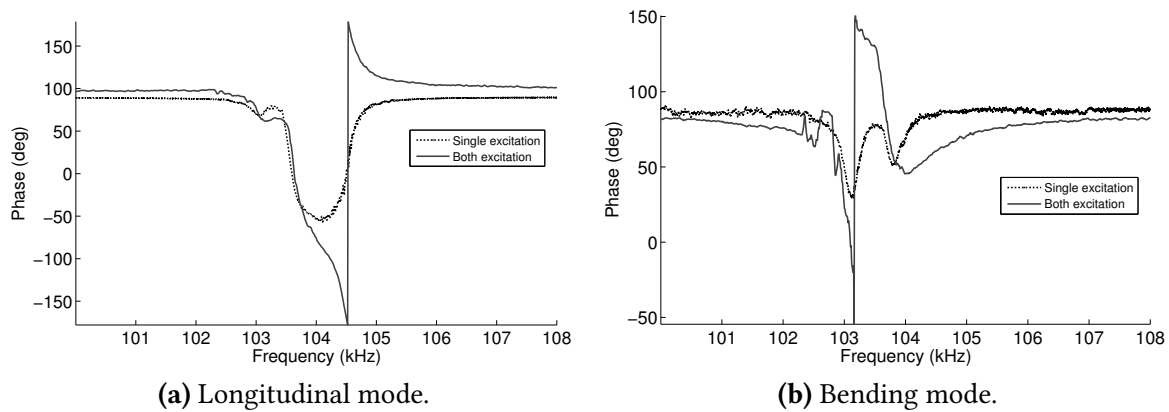


Figure 5.32: Influence of two modes excitation on admittance phase for both considered modes. The cross-coupling between the two excitations changes the phase measurement of the current on one mode. The resonance tracking algorithm is affected.

Although this lead to only 5° phase difference if I_B is 10 times smaller than I_0 . Experiment shows that it is significant enough to cause problems with mode tracking especially with an inductor in parallel. Figure 5.32 shows the interaction between the two modes excitation for a low excitation amplitude. Important differences in phase response are observed when a single mode is excited or both modes are excited at the same time. The zero phase point of longitudinal mode is not affected but tracking becomes problematic when an inductor is added in parallel. Phase for the bending mode is greatly affected with an important jump in phase around the zero phase point that makes the mode very difficult to track with a phase going from -50 to $+150^\circ$.

Mode excitation coupling is an important problem to consider for resonance tracking of a multi-mode ultrasonic actuator. This problem may be avoided by taking high care in the realization of the actuator especially in terms of symmetry. A control algorithm based on a deported electrode is also interesting assuming it is possible to find an area of the actuator where the strain is essentially dependent of one mode deformation. The use of a single-mode working principle is also an interesting solution for resonance tracking implementation.

5.9 Conclusion

In this chapter, an experimental characterization of an ultrasonic motor prototype is proposed. The prototype is fabricated using laser cutting technology. Manufacturing tolerances and effect of added masses such as soldering points are taken into account for the actuator realization. A portion angle θ of 41.4° instead of the 40.5° predicted by modal analysis is proposed to ensure mode degeneration. The effect of the holding mechanism and electrical contact is discussed as they have an important role on actuator damping.

A characterization set-up is proposed. It is used to evaluate actuator properties as a function of several parameters. An increase of the excitation voltage causes the mode frequency to be shifted down and an improvement of both speed and torque. An optimal excitation of 30 V_{pp} is found for maximum actuator efficiency with a 1mm thick layer and a 1N preloading force. The frequency response of the actuator before resonance differs from model prediction. A sudden speed peak of the motor is observed around resonance frequency. Past the resonance frequency, the actuator shows a behavior similar to the model predictions with a smooth decrease in motor speed as frequency is increased.

Preloading force has an important effect on the actuator properties. Transmitted torque is particularly affected and increases significantly as preloading force is increased. Rotor speed, on the other hand, decreases as the force is increased. These observations are in accordance with the model predictions. Contact length affects actuator properties and in particular the maximum speed of the actuator. A reduction of the layer length causes the actuator speed to increase and low changes in torque are observed. A decrease of the quality factor as contact length is increased is observed. It points out one limitation of the model that does not predict changes in damping.

In the last section of this chapter, considerations about actuator control are discussed. The importance of resonance tracking is shown. A high decrease of the speed is observed when the implemented frequency tracking system is disabled. Furthermore, the actuator asymmetry has an important effect on control since coupling between the two mode excitation affects the current phase measurement.

The experimental work points out some limitation of the model and the sensitivity of the proposed actuator. The model is unable to predict the damping factor of the actuator due to high non-linearities of the piezoelectric material and interactions of the holding mechanism. The sensitivity of the actuator to asymmetries requires an important control on the mechanical fabrication of the motor.

Conclusion and perspectives

6

The research work presented in this thesis focuses on the design and realization of ultrasonic motors. These actuators are adapted to the fabrication of small scale systems because of their high torque capabilities and their simple structure, with a limited number of mechanical parts. Their working principle, based on the generation of friction forces allows using various shapes of rotors achieving both rotary and linear motors. These actuators are particularly interesting for multidegree-of-freedom motors that use a single spherical rotor. This thesis proposes a design methodology for piezoelectric ultrasonic actuator adapted to the fabrication of spherical motors. The intended application is the stabilization of micro-cameras in extreme conditions. The objective is to obtain a stable image from a camera mounted on a person who is, for example, running. Finally, experimental results of a prototype actuator are discussed.

6.1 Design methodology

The design methodology proposed in this work, analyzes the two steps of energy conversion in an ultrasonic motor. It is divided into three parts: Mechanical structure design, contact analysis and electrode design. The first step is the definition of the mechanical structure. Ultrasonic stator geometries are numerous. The definition of the mechanical structure should be adapted to the target application. The size and the type of movement (rotation, translation) required for the actuator are the two main parameters for the design of the structure. However, specific geometric constraints can help defining specific features of the stator (e.g. flat stator, semi-circular shape...). Although the design methodology described in this work focuses on the use of the ceramic directly as a vibrator, a different material is possible for the realization of the resonant structure. The change of material does not significantly change the design method proposed in chapter 2 but may affect the practical realization of the actuator. In fact, different parts will be used for electrical to mechanical conversion and for energy storage using resonance.

The mechanical design method uses finite element modal analysis to study the vibration of the structure as a function of the geometry. The method is applied to a multi-mode actuator that requires two vibration modes to be at the same frequency. The vibration modes selection is discussed. An important criterion is the angle between the movements produced by the two modes at the contact interface between rotor and stator. The two modes displacement directions should be as close as possible to orthogonality in order to produce large elliptical movements. Modal analysis is used to optimize the geometry in order to ensure that the two modes required for actuation are at the same frequency. A sensitivity analysis of the actuator to geometric tolerances, soldering points and contact layer is proposed. It shows that disturbances can cause the modes to shift one from each other. A tuning strategy based on a smart positioning of electrical contacts is then proposed.

The second step of the design process is the contact analysis. The study of the properties of the actuator using a contact model allows estimating the mechanical properties of the final motor. The parameters such as contact layer, mode amplitude or preloading force may affect the properties of the actuator. The study of the proposed actuator is based on a force transfer model and the modal shapes of the actuator. Contact model shows that the output mechanical properties of the actuator depends on numerous parameters. It is possible to tune the contact properties in order to obtain the desired actuator output performance:

- Torque: To obtain a specific torque, the main parameter that should be analyzed is the preloading force. The preloading force determines the maximum transmissible torque (assuming friction coefficient does not change). It should be increased until the desired torque is reached. Nevertheless, the preloading force is not the only parameter taken into account since there exists a critical preloading force from which torque stops to increase. If this critical preloading force is reached, contact phase angle φ_c has to be reduced. This can be achieved by increasing the layer stiffness or the normal amplitude of the modes. Another approach would be to increase the contact length so that a distributed preloading force is obtained.
- Speed: Tangential amplitude and contact time are the two main parameters that affect speed. The tangential amplitude is associated to the tangential speed which defines the maximum reachable speed. It is impossible to obtain a rotor speed above the tangential speed. This parameter is essential to define the maximum speed of the actuator. Contact time is directly linked to the average speed of the stator. Therefore, increasing the contact layer stiffness or the normal amplitude reduces the contact time and improve the average tangential speed. An optimization of the contact length can also be used to increase the speed of the actuator.
- Speed/Torque characteristics. The actuator can be tuned to have a specific speed/torque characteristic. If a high torque at low speed is required, the contact time should be low.

If a linear relationship between torque and speed is required, contact time should be high and preloading should be close to critical preloading force.

- Output Power/Efficiency: Maximizing the output power of the actuator with fixed mode amplitudes depends on two major parameters, contact stiffness and preloading force. The contact stiffness should be as high as possible to minimize the contact time. The preloading force should also be high to maximize the transmissible torque. However, in practice, preloading force and contact stiffness have an influence on the quality factor of the actuator. This effect makes the optimization problem more complex.

Finally contact analysis shows that a shift between the two modes used for actuation deteriorates the motor properties. Depending on the quality factor of the resonance, a shift of 1kHz may cause a loss of 80% of the output power as compared to the degenerating mode case.

The last part of the design method addresses with the electrical to mechanical energy conversion. The piezoelectric effect is used to convert the electrical energy into mechanical energy. The mode shapes may affect the efficiency of the energy conversion due to harmonic excitation. A useful parameter to quantify this efficiency is the effective electromechanical coupling factor k_{eff} . A semi-analytical method for the calculation of this parameter is proposed. It combines modal and harmonic finite element analysis in an analytic description to propose an optimal size of the electrodes. An optimal electrode pattern for single mode excitation is easily found based solely on k_{eff} optimization but hardly applicable to the case of a two-mode excitation. The complete motor model is therefore used for the optimization. Based on specified contact model condition and modes damping, it allows to define an optimal electrode size for maximum output power or maximum efficiency of the motor. These two optimal electrodes areas differs. Maximum output power is only associated with the optimal amplitude of each mode whereas maximum efficiency supposes a tradeoff between output power and dissipated energy. The proposed optimization method requires a good knowledge of the damping properties of the actuator. The damping depends on numerous variables such as the holding mechanism, the electrical contacts or the preloading force. The optimization method should therefore be applied after a first characterization of the system in its nominal conditions.

6.2 Motor fabrication

An ultrasonic motor prototype is built based on the proposed methodology. The objective is to propose a stator adapted to the realization of compact spherical motors. The novel concept of this actuator is based on the adaptation of its contact surface to the driven spherical rotor. It allows to constrain completely a spherical rotor without requiring additional mechanical

parts for guidance. The actuator is machined into Ferroperm PZ26 piezoelectric material using picoseconds laser technology. This technology allows for a fast engraving and cutting of the material. The divergence angle of the laser beam causes geometric deviations that have to be taken into account in the actuator design. To compensate the effect of soldering points and contact layer, the actuator is designed with geometrical properties that causes one mode to be at higher frequency than the other. The two modes are then tuned using a change in location and mass of the soldering points. An epoxy resin of low stiffness is deposited onto the actuator contact area. Although this material has low stiffness, its deposition is easy and it is possible to increase its stiffness using solid fillers.

The resulting motor is characterized on an single degree of freedom mechanical setup. The dependance of actuator properties on excitation voltage is studied. The frequency response of the actuator shows an unstable frequency range where behavior of the actuator is unpredictable. A sudden increase of velocity is observed around resonance with a progressive speed reduction as frequency is increased. An increase of the voltage excitation causes the maximum speed of the rotor to increase while a limited variation of the transmitted torque is observed. Although the behavior of a voltage variation are well predicted by the model, non-linear damping affects the actuator properties and makes the estimation of the absolute displacement amplitude at the edge of the actuator difficult. An increase in the preloading force causes an increase in the transmitted torque (3mN.m at 1N preloading force and 7mN.m at 3N). A reduction of the maximum velocity is observed as preloading force is increased. Because the preloading force affects the actuator damping, the decrease of speed predicted by the model is found to be lower than the measured properties. Contact layer length affects significantly the speed of the motor with an important increase of the speed as the contact length is reduced (at a 1N preloading force velocity is increased by 76% when contact layer is reduced from 10.5mm to 5mm). The low efficiency of the motor around 4% can be explained by the low stiffness of the contact layer that limits the speed of the actuator. This efficiency could be greatly increased by the use of a more appropriate contact material and a better holding mechanism for the piezoelectric ceramic. The actuator can provide the required performance for the stabilization of a micro-camera placed on a running person. These required characteristics were estimated to a 5mN.m torque and 80rpm speed.

Investigations on frequency tracking are proposed. A resonance frequency tracking control electronics is proposed for proper actuator operation. The use of a parallel inductor can improve the performance of the tracking system. However, coupling between the two mode due to asymmetries disturbs the intensity phase measurement and the resonance frequency tracking.

6.3 Perspectives

Several improvements can be proposed for better actuator operation. One is the contact layer which has a very low stiffness that limits the actuator performance. The use of hard particles in the layer should improve the speed of the actuator for a given preloading force and therefore improve efficiency of the actuator. Figure 6.1a shows the perspectives in terms of actuator geometry. The properties of the actuator are greatly affected by asymmetries and holding mechanism. A better fixation of the actuator based on a fixation hole could lead to an improved stability of the actuator. Although, it has been discussed in the model, electrode optimization effect has not been observed yet since it requires a good experimental knowledge of the actuation system. Experimental studies of the optimization are planned. The proposed actuator aims at being used in small scale systems. Actuators four times smaller than current actuators will be investigated.

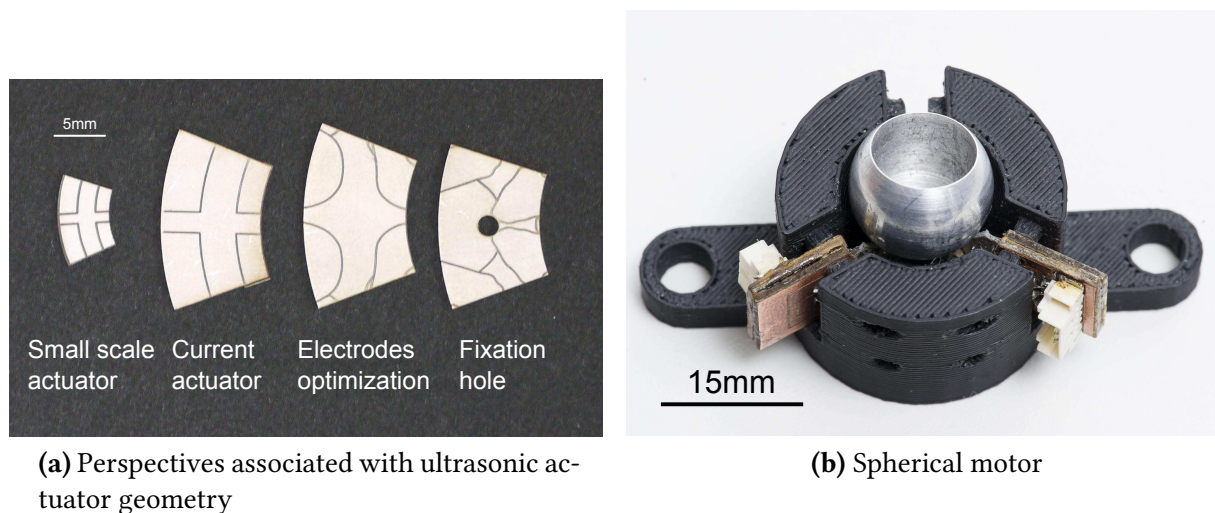


Figure 6.1: Actuator perspectives. Current investigations focus on the improvement of the holding mechanism of the actuator along with a better estimation of the effect of the electrode optimization. Small scale actuators are also studied for their application in a spherical motor assembly.

The objective of these actuators is to be integrated in a spherical motor design. An adapted mechanical structure associated with a proper position sensing system based on magnetic technologies is under investigation (figure 6.1b). This spherical motor requires also adapted electronics which are miniaturized and able to provide an accurate resonance tracking of the actuator. Analog circuitry based on phase locked loop are particularly interesting but requires a good stability of the actuator before being successfully implemented. The two-mode working principle is convenient to generate constructive elliptical movements at the edge of the actuator. Nevertheless, the required mode tuning is problematic as mode frequencies are very sensitive to disturbances. The use of another working principle based on the same geometry could be investigated. An asymmetric single-mode excitation could be

CHAPTER 6. CONCLUSION AND PERSPECTIVES

interesting since it simplifies also the resonance tracking by avoiding any coupling between two excitations.

Finally, the design method presented in this work is specifically applied to a multi-mode curved longitudinal-bending actuator made entirely of piezoelectric material. One perspective is the application of this method to the realization of high torque actuators with different geometries and applications. The method aims at being easily adapted to other actuators geometry and principles and a first adaptation would be the use of an independent resonator made of a different material than the piezoelectric element.

Appendices

Piezoelectric materials



This appendix contains an introduction to piezoelectric materials. History and applications are presented along with the mathematical formulation for their physical description.

A.1 Definition and History

The word *piezoelectric* comes from the Greek prefix *pies-* which means squeeze or press, it defines an existing relation between the electric field and the stress in a material. Piezoelectricity was discovered by Jacques and Pierre Curie in 1880. They observed that pressure variations applied along the hemihedral axes of a pyroelectric crystal lead to the development of polar electricity inside the crystal. This effect is called direct piezoelectricity (figure A.1a). A crystal is called pyroelectric when there exist a relationship between temperature and electric field in a material. Pyroelectric crystals have been studied since the 1700s ([95, pages 7-8 (french)]). The inverse piezoelectricity (figure A.1b) is the reciprocal effect which occurs when an applied electric field causes deformation of a piezoelectric crystal. It has been predicted in October 1881 by Gabriel Lippmann ([96, page 166-167]). Mathematical formalism for piezoelectricity has not been defined until 1894, when Woldemar Voigt established the tensorial relationships for piezoelectric constants along with the identification of 20 piezoelectric classes. ([97]).

A.2 Applications

One of the first application of piezoelectricity was the development of sonar by Paul Langevin during the first World War. In his device, Langevin proposed to use quartz as a material that could both emit and receive acoustic waves for the active detection of submarines ([98]). Another precursor application was the quartz oscillator proposed by Walter Guyton Cady in 1921. The discovery of ferroelectric oxides (e.g BaTiO₃ and PZT) led to improvements

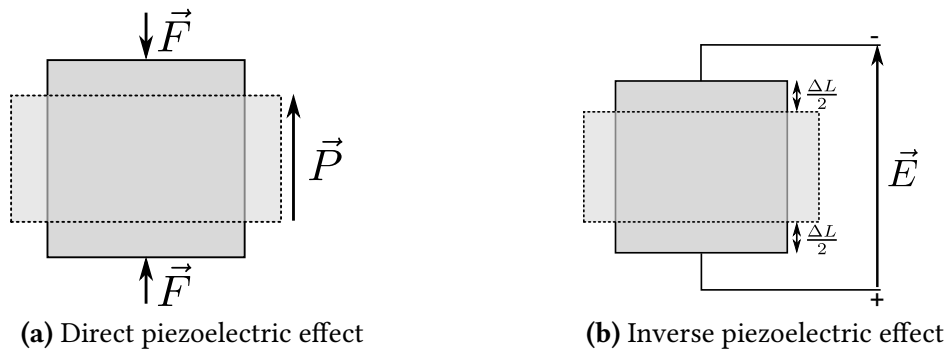


Figure A.1: Direct and inverse piezoelectric effects. (a): External forces cause deformation of the crystal and apparition of an electric polarization inside the piezoelectric element. (b): External electrical field cause deformation of the crystal (and eventually forces if the element is not free).

TABLE A.1: EXAMPLES OF APPLICATIONS THAT USE PIEZOELECTRIC EFFECTS

<i>Inverse piezoelectric effect</i>	<i>Both effects</i>	<i>Direct piezoelectric effect</i>
Ultrasonic Welding	Sonar	Force sensors
Ultrasonic scalpel	Echography	Weighing scale
Nanopositioning	Quartz Clocks	Energy Harvesting
Motors	MEMS (Gyroscope)	Microphones
Speakers	Surface acoustic (SAW) Filters	Lighters (spark generation)
Ultrasonic Cleaning	Vibration control	Pressure gauges
Fuel injectors	Non-destructive testing	
	Electric Transformers	

in existing applications and new developments. Today, piezoelectric materials are used in numerous engineering areas including new type of sensors and actuators. Some of the applications are presented in table A.1.

The inverse effect is used for applications that require actuators and in general, for any application that requires the generation of ultrasonic waves. Ultrasonic welding uses vibrations in order to weld plastics together, the method is commercialized and widely used in the industry¹. Ultrasonic cleaning consists in creating cavitation bubbles using high frequency waves in a solvent in order to clean an object (typically a glass lens). Ultrasonic waves are also used as dust reduction systems in Digital Single Lens Cameras². Inverse piezoelectric effect is used in motors when standard electromagnetic motors cannot be used (e.g. in highly electromagnetic environment such as MRI) and has also been used to produce waterproof speakers³.

¹<http://www.emersonindustrial.com/en-US/branson/Products/plastic-joining/ultrasonic-plastic-welders>

²http://www.olympusamerica.com/cpg_section/cpg_dust.asp

³http://www.murata.com/new/news_release/2010/0608/

Numerous applications use both inverse and direct effect, the most famous example being the sonar cited earlier. Echography and non-destructive testing use also generation and sensing of acoustic waves in order to produce images of the human body or a mechanical structure. Resonant piezoelectric crystals are used to produce stable clock sources or sense displacement (in MEMS gyroscopes for example). An important consumer electronics application of piezoelectricity is Surface Acoustic Wave (SAW) filters. Delay time of an acoustic wave in a mechanic structure is used to filter high frequency electromagnetic waves. The surface wave is produced in a piezoelectric material on which electrodes are deposited. One set of electrodes is used to generate the wave while the other one is used to sense it once it has propagated. These filters are widely used in telecommunications (Cellular phones, Wifi, GPS, Bluetooth...). Piezoelectric materials can be used to damp actively the vibrations in a structure for noise reduction applications and have also been used as voltage transformers.

Finally the direct piezoelectric effect is used to produce various force and torque sensors⁴ and build precise weighing scales. Microphones and hydrophones have been built based on this effect. Another example of the use of direct effect is the electronic lighter which uses the high voltage peak produced by a shock on a piezoelectric material in order to obtain an ignition spark.

A.3 Ferroelectric materials

Piezoelectricity depends mostly on the symmetry of the atomic arrangement in the crystal. In some materials, an asymmetry caused by a displacement of a charge in the atomic arrangement causes the material to exhibit a spontaneous polarization. These materials are called polar and they present pyroelectric and piezoelectric properties. Other kind of asymmetries in the atomic arrangement can cause non-polar materials to be piezoelectric. Quartz, for example, is non-polar and not pyroelectric but it exhibits piezoelectric properties. Among pyroelectric materials, some materials can have their spontaneous polarization reversed. These materials, usually ceramics, are said to be ferroelectric. All ferroelectric materials are pyroelectric but some pyroelectric materials do not exhibit ferroelectric properties (e.g. Tourmaline). These materials are particularly interesting since they present a high piezoelectric coupling.

Typical examples of ferroelectric ceramics are oxides with Perovskite structure (see figure A.2) such as BaTiO₃ or Lead Zirconate Titanate (PZT) materials. These ceramics can be found in two different phases. Above a given temperature T_c (Curie temperature), their structure is cubic and they are paraelectric materials which do not exhibit piezoelectric properties. Below T_c , the perovskite structure can adopt a tetragonal structure in which a metallic ion (Ti⁴⁺ or Zr⁴⁺ in the case of PZT) can find a stable off-centered position which leads to the

⁴<http://www.kistler.com>

APPENDIX A. PIEZOELECTRIC MATERIALS

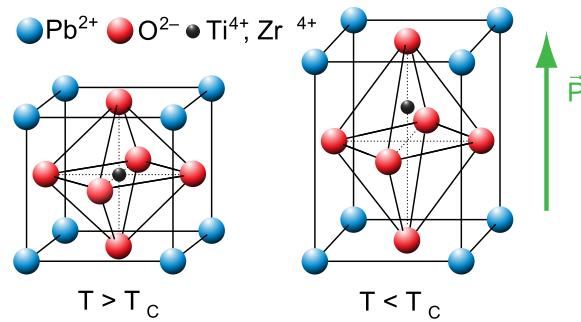


Figure A.2: Perovskite structure (ABO_3) of Lead Zirconate Titanate (PZT) exhibiting ferroelectric properties. On the left, above the Curie temperature T_c , the micro-structure is cubic and do not have piezoelectric properties. The electric behavior of the crystal is paraelectric. On the right side, below the Curie temperature, the central titanium or zirconium ion can be off-centered within the oxygen octahedron resulting in tetragonal structure and a net polarization of the crystal. The ferroelectric behavior is the ability to change the position of the ion from the top to the bottom, resulting in an inverted polarization.

polarization of the material. By applying an electric field in the material it is possible to invert the position of the ion and the remanent polarization. The capacity of ferroelectric materials to stay polarized in the wanted direction makes them suitable for use in ferroelectric random access memory used in computers ([99]).

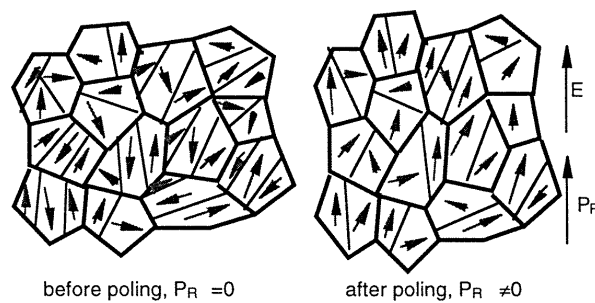


Figure A.3: Poling of a ferroelectric ceramic. Before poling, domains inside the material have different polarization that oppose each other and result in a macroscopical zero polarization. After the crystal is poled, the polarizations of the domains orient with each another and a net polarization is created in the material.

Poling process Ferroelectric materials are in general made by high temperature powder fritting and do not present a net polarization when cooling down. The different domains (Weiss domains) have locally the same electric polarization, but domains cancel each other so that the total polarization is zero.

A process called poling of the material consists in applying a strong electric field to the ceramic ($\sim 10 - 100 \text{ kV} \cdot \text{cm}^{-1}$) usually at high temperature in order to reorient the polarization of each domain and obtain a net macroscopic polarization (figure A.3).

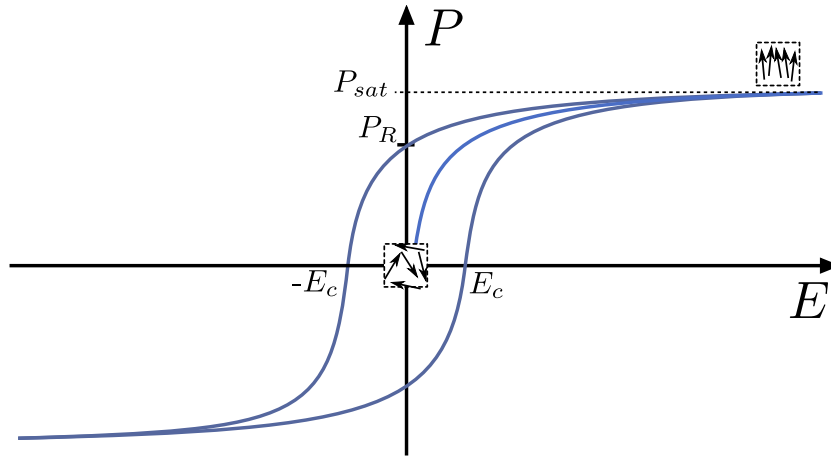


Figure A.4: Hysteresis loop in a ferroelectric material. The evolution of the polarization in the material as a function of the applied electric field present an hysteresis and a remanent field similarly to ferromagnetic materials.

Electrical response The electric polarization in a ferroelectric crystal is shown as a function of the applied electric field in figure A.4. At the zero point (zero field and zero polarization), the material is not polarized, the domains have different polarization that result in a zero macroscopic field. Applying a field results in an alignment of the domains in the material which causes a net macroscopic polarization. Once a certain field is reached, all the domains are aligned and a saturation point occurs where no more extra polarization can be reached in the material, and its dielectric permittivity becomes the vacuum permittivity ε_0 .

Once a polarization is created in the material, lowering the applied field to zero will result in a remanent polarization P_r in the material. In order to cancel this remanent polarization, an opposite coercive field E_c have to be applied.

Because of their spontaneous polarization, ferroelectric materials exhibit interesting dielectric properties, in particular high permittivity. The permittivity of a material is its ability to cause an electric displacement under the effect of an external field. In vacuum, it is described by the expression:

$$D = \varepsilon_0 E \quad (\text{A.1})$$

where $\varepsilon_0 = 8.85418782 \times 10^{-12} \text{ m}^{-3} \cdot \text{kg}^{-1} \cdot \text{s}^4 \cdot \text{A}^2$ is the vacuum permittivity and E is the electric field. In the case of ferroelectric materials, a high level of polarization is obtained and the electric displacement is:

$$D = \varepsilon_0 (E + P) \quad (\text{A.2})$$

$$D = \varepsilon_0 (1 + \chi) E \quad (\text{A.3})$$

$$D = \varepsilon_0 \varepsilon_r E \quad (\text{A.4})$$

Where χ is called the electric susceptibility. Therefore, the electric displacement depends on the relative permittivity ε_r which can be very large in a ferroelectric material ($\varepsilon_r = 1300$ for Ferroperm⁵ Pz26 whereas $\varepsilon_r \approx 1$ for air). The electric displacement quantify the amount of electric charges that are moved when an electric field is applied to a material, it is expressed in C/m^2 (Coulomb per square meter). A large electric displacement is interesting in order to build large capacitors. The amount of charges created in a capacitor consisting in two plates of area A with a dielectric material in between is:

$$Q_{charge} = D \times A \quad (A.5)$$

$$Q_{charge} = \varepsilon_0 \varepsilon_r E \times A \quad (A.6)$$

$$Q_{charge} = \varepsilon_0 \varepsilon_r \frac{V}{d} \times A \quad (A.7)$$

where d is the space between the two plates, V the voltage imposed and Q_{charge} the amount of charges created in the plates. The capacitance is defined as the number of charges created per volt:

$$C = \frac{Q_{charge}}{V} = \varepsilon_0 \varepsilon_r \frac{A}{d} \quad (A.8)$$

Ferroelectric materials, because of their high dielectric constant ε_r , are very interesting in order to obtain high capacity at small scale.

The dielectric constant is often represented in a complex form

$$\varepsilon^* = \varepsilon' - i\varepsilon'' \quad (A.9)$$

ε'' is useful to define dielectric loss in the material. Indeed the dissipated energy under a sine external field gives a net emitted energy ([86]):

$$w_e = \int DdE = \pi\varepsilon''\varepsilon_0 E_0^2 = \pi\varepsilon'\varepsilon_0 E_0^2 \tan \delta_e \quad (A.10)$$

Where E_0 is the amplitude of the field and $\tan(\delta_e) = \frac{\varepsilon''}{\varepsilon'}$ is the tangent of the electrical loss angle. Dielectric losses are due to charges movement within the material, they are important at high voltage stimulation and cause heating of the piezoelectric material. They can directly affect the behavior of a piezoelectric motor at high voltage.

Soft vs Hard materials In general PZT ceramics are doped by adding either donor or acceptor atoms in the material. This allows for fine tuning of the material properties. Donor dopants such as La^{3+} or Nb^{5+} ([101]), results in the formation of cation vacancies in the structure that lead to the synthesis of “soft” ceramics with higher piezoelectric constants

⁵<http://www.ferroperm-piezo.com/>

TABLE A.2: DIFFERENCES BETWEEN SOFT AND HARD CERAMICS (FROM [100])

Characteristic	Soft Ceramic	Hard Ceramic
Piezoelectric Constants	larger	smaller
Permittivity	higher	lower
Dielectric Constants	larger	smaller
Dielectric Losses	higher	lower
Electromechanical Coupling Factors	larger	smaller
Electrical Resistance	very high	lower
Mechanical Quality Factors	lower	higher
Coercive Field	lower	higher
Linearity	poor	better
Polarization / Depolarization	easier	more difficult

TABLE A.3: COMPARISON OF DIFFERENT MATERIALS (PIEZOELECTRIC AND DIELECTRIC PROPERTIES)

	Quartz	Tourmaline	Barium Titanate	PZT-4
Dielectric constant ϵ_{33}	4.68 [102]	7.9 [103]	450[104]	1300[104]
Piezoelectric coupling e_{31}	0.17 [104]	0.21[105]	-4.3[104]	-5.2[104]
Curie point	573°C (phase change)	900°C (melting point)	115°C[104]	328°C[104]

and permittivity but increased losses and lower quality factor. Acceptor doped ceramics (e.g. Fe^{3+}) show smaller piezoelectric constants but less losses and higher quality factor, their coercive field and Curie temperature are also generally higher. Advantages and disadvantages of each type of doped ceramic are presented in table A.2.

Ferroelectric ceramics are very interesting materials, they present high piezoelectric constants and high dielectric constants as compared to other piezoelectric materials (see table A.3). Their major limitations is the need for a poling phase and the existence of a Curie Temperature that limits their use at high temperature.

In the case of ultrasonic motors, ferroelectric ceramic are materials of choice because of their high piezoelectric coupling. In our case, we chose to use a Ferroperm ceramic PZ26 which is a hard PZT that offer good properties for building ultrasonic motors with high Curie temperature (330°C) and high quality factor.

A.4 Piezoelectric mathematical formalism

A.4.1 Piezoelectric effect in ceramics

In ferroelectric ceramics three major inverse effects can be considered (see figure A.5, direct effects exist in similar fashion):

- The d_{33} inverse effect which affects the extension of the material in the direction of the polarization when an electric field is applied in the direction of the polarization.
- The d_{31} inverse effect which affects the extension of the material in the direction perpendicular of the polarization when an electric field is applied in the direction of the polarization.
- The d_{15} inverse effect which creates a shear deformation of the material when an electric field is applied in an orthogonal direction to the polarization.

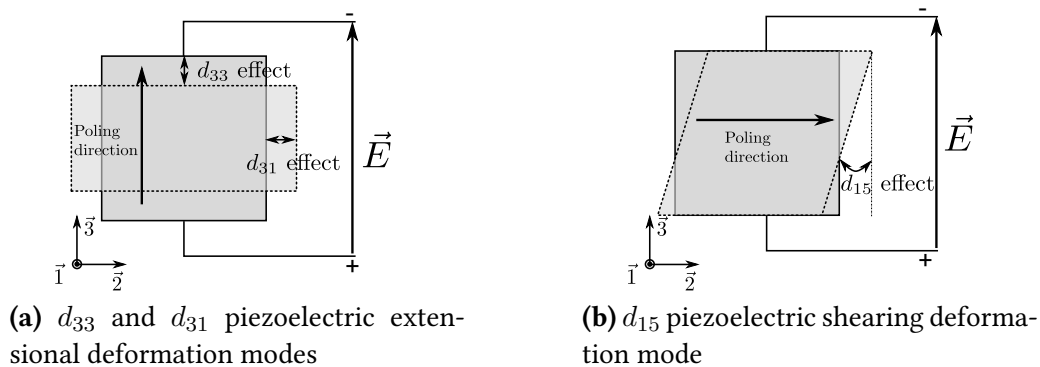


Figure A.5: Typical piezoelectric deformation modes used with PZT ceramics

The d constant comes from the d piezoelectric matrix that is defined in the next section. d_{33} and d_{31} effects are in general the most used effects, one reason is that the same electrodes can be used for the polarization and the operation of the ceramic while d_{15} effect requires two different sets. Some piezoelectric materials may have different deformation modes (e.g. d_{11} or d_{14} for quartz).

A.4.2 State equations

Piezoelectricity is in general modeled using electromechanical tensorial relations called state equations. Two major tensorial relations are used:

$$\begin{cases} S = s^E T + d^t E \\ D = d T + \varepsilon^T E \end{cases} \quad (\text{A.11})$$

The first one links the strain S in the material to the electric field E and the applied stress T . s^E is defined as the compliance at constant electric field and d^t is the transposed piezoelectric constant tensor. The second equation links the electric displacement D to the stress T and the electric field E in the material. ε^T is the permittivity of the material at constant stress. S and T are 6 components vectors, E and D are 3 components vectors.

Considering a ferroelectric ceramic poled along the $\vec{3}$ direction (see figure A.5), these two equations can be sum up into a single matrix relation given by:

$$\begin{bmatrix} S_1 \\ S_2 \\ S_3 \\ S_4 \\ S_5 \\ S_6 \\ \hline D_1 \\ D_2 \\ D_3 \end{bmatrix} = \begin{pmatrix} s_{11} & s_{12} & s_{13} & 0 & 0 & 0 & | & 0 & 0 & d_{31} \\ s_{12} & s_{11} & s_{13} & 0 & 0 & 0 & | & 0 & 0 & d_{31} \\ s_{13} & s_{13} & s_{33} & 0 & 0 & 0 & | & 0 & 0 & d_{33} \\ 0 & 0 & 0 & s_{44} & 0 & 0 & | & 0 & d_{15} & 0 \\ 0 & 0 & 0 & 0 & s_{44} & 0 & | & d_{15} & 0 & 0 \\ 0 & 0 & 0 & 0 & 0 & s_{66} & | & 0 & 0 & 0 \\ \hline 0 & 0 & 0 & 0 & d_{15} & 0 & | & \varepsilon_{11} & 0 & 0 \\ 0 & 0 & 0 & d_{15} & 0 & 0 & | & 0 & \varepsilon_{22} & 0 \\ d_{31} & d_{31} & d_{33} & 0 & 0 & 0 & | & 0 & 0 & \varepsilon_{33} \end{pmatrix} \begin{bmatrix} T_1 \\ T_2 \\ T_3 \\ T_4 \\ T_5 \\ T_6 \\ \hline E_1 \\ E_2 \\ E_3 \end{bmatrix} \quad (\text{A.12})$$

This relation is valid for transversely isotropic materials which are materials that have the same properties in the two directions of a plane but different properties out of this plane. PZT materials and most of ferroelectric ceramics are transversely isotropic materials. The d matrix represents the piezoelectric effect, it is expressed in terms of coulomb per newton (C/N) and associates the force applied to and the charges generated (or the opposite).

There exists four different matrix for modeling the piezoelectric effect and four associated pairs of equations as (A.11) ([106], [107]):

- d matrix links electric displacement to stress (C/N). It is used in the strain-charge relations presented in (A.11).
- g links electric field to stress ($V.m/N$). It is used in the strain-field relations:

$$\begin{cases} S = s^D T + g^t D \\ E = -g T + \beta^T D \end{cases} \quad (\text{A.13})$$

- e links electric displacement to deformation (C/m^2). It is used in the stress-charge relations:

$$\begin{cases} T = c^E S - e^t E \\ D = e S + \varepsilon^S E \end{cases} \quad (\text{A.14})$$

- h links electric field to deformation (V/m). It is used in the stress-field relations:

APPENDIX A. PIEZOELECTRIC MATERIALS

TABLE A.4: RELATIONS BETWEEN THE DIFFERENT PIEZOELECTRIC PROPERTIES. c AND s ARE THE MECHANICAL STIFFNESS AND COMPLIANCE MATRICES, d , e , g AND h ARE PIEZOELECTRIC COEFFICIENT MATRICES AND β AND ε ARE DIELECTRIC MATRICES. THE EXPONENT T INDICATE A CONSTANT STRESS, S A CONSTANT STRAIN, E A CONSTANT FIELD AND D A CONSTANT ELECTRIC DISPLACEMENT. TRANSPOSED OF MATRIX M IS NOTED M^t .

Elastic properties	Piezoelectric properties	Dielectric properties
$s^D = s^E - d^t g$	$d = \varepsilon^T g$	$\beta^S = \beta^T + h g^t$
$c^D = c^E + e^t h$	$e = d c^E$	$\varepsilon^T = \varepsilon^S + e d^t$
$c^E = (s^E)^{-1}$	$g = \beta^T d$	$\beta^T = (\varepsilon^T)^{-1}$
$c^D = (s^D)^{-1}$	$h = g c^D$	$\beta^S = (\varepsilon^S)^{-1}$

$$\begin{cases} T = c^D S - h^t D \\ E = -h S + \beta^S D \end{cases} \quad (\text{A.15})$$

β is the inverse tensor of permittivity, it is a diagonal tensor of the 3rd order with $\beta_{ii} = 1/\varepsilon_{ii}$. c^D is the stiffness tensor of the material at constant electric displacement (D). Relations between each property exist and are presented in table A.4.

Depending on the boundary conditions, one specific relation may be more appropriate. In the example of modeling the inverse effect in a free piezoelectric element in which an electric field is imposed, the strain-charge form is interesting because it allows to compute directly the deformation and electric displacement that the element will experience.

Electromechanical coupling factor computation

B

k_{eff} is an interesting parameter for optimizing electrodes of a piezoelectric resonant actuator. It is proposed to develop an analytical model in order to obtain a fast, practical tool for electrodes optimization. k_{eff}^2 can be defined as:

$$k_{eff}^2 = \frac{U_{12}^2}{U_1 U_2} \quad (\text{B.1})$$

U_{12} the coupling energy, U_1 the elastic energy and U_2 the dielectric energy are computed from the state equations of piezoelectricity:

$$\frac{1}{2} \int_V T S^* dV = \frac{1}{2} \int_V c^E S S^* dV - \frac{1}{2} \int_V e^T E S^* dV = U_1 + U_{12} \quad (\text{B.2})$$

The total electrical energy is given by :

$$\frac{1}{2} \int_V D E^* dV = \frac{1}{2} \int_V e^E S E^* dV + \frac{1}{2} \int_V \varepsilon^S E E^* dV = U_{12} + U_2 \quad (\text{B.3})$$

S and T are the strain and stress in the actuator, E and D the electric field and displacement. e is the piezoelectric matrix, c^E the stiffness matrix at constant field and ε^S is the permittivity at constant strain. The star operator $*$ corresponds to the transposed conjugate of the considered matrix (self-adjoint operator). From this, we can write:

$$k_{eff}^2 = \frac{(\int_V e^E S E^* dV)^2}{(\int_V c^E S S^* dV) (\int_V \varepsilon^S E E^* dV)} \quad (\text{B.4})$$

Considering the excitation of a single mode, one can assume, with good approximation that the strain distribution in the actuator will be the strain distribution that can be found through a modal analysis multiplied by a factor α . Thus elastic energy during one period will be given by:

APPENDIX B. ELECTROMECHANICAL COUPLING FACTOR COMPUTATION

$$U_1 = \alpha^2 U_1^{Modal} = \frac{1}{2} \alpha^2 \left(\int_V c^E S_{Modal} S_{Modal}^* dV \right) \frac{\pi}{\omega} \quad (B.5)$$

Where α depends on the amplitude of the excitation and U_1^{Modal} is the elastic energy computed from modal strain. Coupling energy is given by:

$$U_{12} = \frac{1}{2} \int_V e^E S E^* dV \int_0^{\frac{2\pi}{\omega}} \sin^2(\omega t) dt \quad (B.6)$$

$$U_{12} = \frac{1}{2} \alpha \int_V e^E S_{Modal} E^* dV \frac{\pi}{\omega} \quad (B.7)$$

k_{eff}^2 from modal analysis is given by:

$$k_{eff}^2 = \frac{\left(\int_V e^E S_{Modal} E^* dV \right)^2}{\left(\int_V c^E S_{modal} S_{modal}^* dV \right) \left(\int_V \varepsilon^S E E^* dV \right)} \quad (B.8)$$

Hypotheses In the case of our actuator, we consider several hypothesis in order to simplify the problem:

- In-plane modes are considered so that S_4 and S_5 components of strain are zero everywhere.
- All areas of the actuator apart from the excitation electrodes are kept at constant electrical field (as shown in figure B.1).

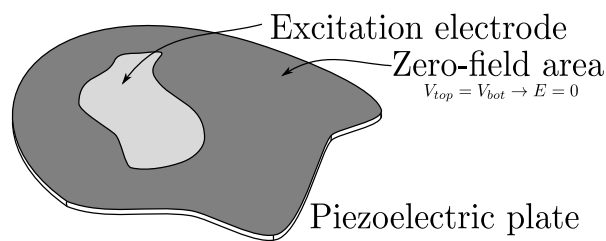


Figure B.1: Piezoelectric plate considered. A zero field boundary condition is considered wherever there is no excitation electrode.

Coupling Energy The coupling energy during one period can be computed evaluating the matrix multiplication:

$$U_{12} = \frac{1}{2} \int_0^{\frac{2\pi}{\omega}} \int_V e^E S_{modal} E^* dV dt \quad (B.9)$$

$$U_{12} = \frac{1}{2} \int_0^{\frac{2\pi}{\omega}} \int \left(\begin{array}{cccccc} 0 & 0 & 0 & 0 & e_{15} & 0 \\ 0 & 0 & 0 & e_{15} & 0 & 0 \\ e_{31} & e_{31} & e_{33} & 0 & 0 & 0 \end{array} \right) \begin{array}{c} S_1 \\ S_2 \\ S_3 \\ S_4 \\ S_5 \\ S_6 \end{array} \left[E_1 \quad E_2 \quad E_3 \right] dV dt \quad (\text{B.10})$$

We consider an in-plane vibration mode, shear strains S_4 and S_5 are zero. The problem can then be reduced to:

$$U_{12} = \frac{1}{2} \int_0^{\frac{2\pi}{\omega}} \int_V (e_{13}S_1 + e_{13}S_2 + e_{33}S_3) E_3 dV dt \quad (\text{B.11})$$

Because of Poisson's coefficient, there exists a relation between S_1 , S_2 and S_3 which is given by:

$$(S_1 + S_2) = -(v_{13} + v_{23})S_3 \quad (\text{B.12})$$

$$U_{12} = \frac{1}{2} \int_0^{\frac{2\pi}{\omega}} \int_V ((e_{33} - (v_{13} + v_{23})e_{13})S_3) E_3 dV dt \quad (\text{B.13})$$

E_3 is constant wherever there is no excitation electrode and because S_3 is a periodic function everywhere, the integration gives a zero coupling energy in those areas. Assuming E_3 is uniform on the electrode:

$$U_{12} = \frac{\pi}{2\omega} ((e_{33} - (v_{13} + v_{23})e_{13})) E_3 \int_{V_{\text{electrode}}} S_3 dV \quad (\text{B.14})$$

Dielectric energy The dielectric energy represents the stored energy into the piezoelectric element, it is given by:

$$U_2 = \frac{1}{2} \int_0^{\frac{2\pi}{\omega}} \int_V \varepsilon^S E E^* dV dt \quad (\text{B.15})$$

$$U_2 = \frac{1}{2} \int_0^{\frac{2\pi}{\omega}} \int_V \begin{bmatrix} \varepsilon_1^S & 0 & 0 \\ 0 & \varepsilon_2^S & 0 \\ 0 & 0 & \varepsilon_3^S \end{bmatrix} \begin{bmatrix} E_1 \\ E_2 \\ E_3 \end{bmatrix} \left[E_1 \quad E_2 \quad E_3 \right] dV dt \quad (\text{B.16})$$

$$U_2 = \frac{\pi}{2\omega} \int_V \varepsilon_1^S E_1^2 + \varepsilon_2^S E_2^2 + \varepsilon_3^S E_3^2 dV \quad (\text{B.17})$$

E_3 is known and E_1 and E_2 can be derived by the fact that there is no electric displacement in the 1 and 2 directions (open-circuit condition). Thus:

$$D = e^E S + \varepsilon E \quad (\text{B.18})$$

$$\begin{bmatrix} 0 \\ 0 \\ D_3 \end{bmatrix} = \begin{bmatrix} 0 & 0 & 0 & 0 & e_{15} & 0 \\ 0 & 0 & 0 & e_{15} & 0 & 0 \\ e_{31} & e_{31} & e_{33} & 0 & 0 & 0 \end{bmatrix} \begin{bmatrix} S_1 \\ S_2 \\ S_3 \\ S_4 \\ S_5 \\ S_6 \end{bmatrix} + \begin{bmatrix} \varepsilon_1^S & 0 & 0 \\ 0 & \varepsilon_2^S & 0 \\ 0 & 0 & \varepsilon_3^S \end{bmatrix} \begin{bmatrix} E_1 \\ E_2 \\ E_3 \end{bmatrix} \quad (\text{B.19})$$

Deriving this equation leads to:

$$E_1 = -\frac{e_{15}S_5}{\varepsilon_{11}} = 0 \quad (\text{B.20})$$

$$E_2 = -\frac{e_{15}S_4}{\varepsilon_{11}} = 0 \quad (\text{B.21})$$

Because the in-plane deformation S_5 and S_4 are zero, the fields E_1 and E_2 are zero. E_3 field is constant wherever there is no excitation electrode and assuming that E_3 is uniform on the electrode:

$$U_2 = \frac{\pi}{2\omega} \varepsilon_3^S E_3^2 \int_{V_{electrode}} dV \quad (\text{B.22})$$

$$U_2 = \frac{\pi}{2\omega} \varepsilon_3^S E_3^2 A_{electrode} \quad (\text{B.23})$$

Elastic energy The elastic energy does not depend on the electrode geometry because the electric boundary conditions do not change when electrode geometry is changed (field is imposed everywhere):

$$U_1 = \frac{\pi}{2\omega} \alpha^2 \left(\int_V c^E S_{Modal} S_{Modal}^* dV \right) \quad (\text{B.24})$$

Electromechanical coupling factor Based on these definitions of each energy term, the electromechanical coupling factor is:

$$k_{eff}^2 = \frac{\left(\int_V e^E S_{Modal} E^* dV \right)^2}{\left(\int_V c^E S S^* dV \right) \left(\int_V \varepsilon^S E E^* dV \right)} \quad (\text{B.25})$$

$$k_{eff}^2 = \frac{\left((e_{33} - (v_{13} + v_{23})e_{13}) \right) E_3^2 \left(\int_{V_{electrode}} S_3 dV \right)^2}{\left(\int_V c^E S_{Modal} S_{Modal}^* dV \right) \varepsilon_3^S E_3^2 A_{electrode}} \quad (\text{B.26})$$

$$k_{eff}^2 = K \frac{\left(\int_{V_{electrode}} S_3 dV \right)^2}{A_{electrode}} \quad (\text{B.27})$$

Where K is a constant depending on the properties of the actuator and the considered mode. For the simple case of an in-plane mode of a plate which has a delimited excitation electrode with constant field elsewhere, the electromechanical coupling factor can be optimized by considering the distribution of the out-of-plane strain S_3 .

Bibliography

- [1] E.h.M. Week, T. Reinartz, G. Henneberger, and R.W. De Doncker. Design of a spherical motor with three degrees of freedom. *CIRP Annals - Manufacturing Technology*, 49(1): 289–294, 2000. ISSN 0007-8506. doi:10.1016/S0007-8506(07)62948-5. (Cited on pages vi, 7, 8 and 25)
- [2] G. Rogers. Three degree-of-freedom piezoelectric ultrasonic micro-motor with a major diameter of 350 μm . *Journal of Micromechanics and Microengineering*, 20:125002, 2010. doi:10.1088/0960-1317/20/12/125002. (Cited on pages vi, 15, 25 and 61)
- [3] Minghui Zhang, Wei Guo, and Lining Sun. A multi-degree-of-freedom ultrasonic motor using in-plane deformation of planar piezoelectric elements. *Sensors and Actuators A: Physical*, 148(1):193–200, November 2008. ISSN 0924-4247. doi:10.1016/j.sna.2008.07.022. (Cited on pages vi, 16, 25 and 111)
- [4] Xiaofeng Zhang, Guangbin Zhang, Kentaro Nakamura, and Sadayuki Ueha. A robot finger joint driven by hybrid multi-DOF piezoelectric ultrasonic motor. *Sensors and Actuators A: Physical*, 169(1):206–210, sep 2011. ISSN 0924-4247. doi:16/j.sna.2011.05.023. (Cited on pages vi, 4, 16, 17 and 25)
- [5] Ricky T. Tjeung, Mark S. Hughes, Leslie Y. Yeo, and James R. Friend. Surface acoustic wave micromotor with arbitrary axis rotational capability. *Applied Physics Letters*, 99(21):214101, 2011. ISSN 00036951. doi:10.1063/1.3662931. (Cited on pages vi, 21 and 25)
- [6] Sheng-Chih Shen and Juin-Cherng Huang. Design and fabrication of a high-power eyeball-like microactuator using a symmetric piezoelectric pusher element. *Microelectromechanical Systems, Journal of*, 19(6):1470–1476, 2010. ISSN 1057-7157. doi:10.1109/JMEMS.2010.2076788. (Cited on pages vi, 21, 22, 25, 30, 61 and 126)
- [7] M. Hoshina, T. Mashimo, and S. Toyama. Development of spherical ultrasonic motor as a camera actuator for pipe inspection robot. In *Intelligent Robots and Systems, 2009. IROS 2009. IEEE/RSJ International Conference on*, pages 2379–2384, 2009. doi:10.1109/IROS.2009.5354315. (Cited on pages vi, 22, 25 and 30)
- [8] Toshiyuki Ueno, Chihiro Saito, Nobuo Imaizumi, and Toshiro Higuchi. Miniature spherical motor using iron-gallium alloy (galfenol). *Sensors and Actuators A: Physical*, 154(1):92–96, August 2009. ISSN 0924-4247. doi:10.1016/j.sna.2009.01.029. (Cited on pages vi, 23 and 25)
- [9] T.B. Lauwers, G.A. Kantor, and R.L. Hollis. A dynamically stable single-wheeled mobile robot with inverse mouse-ball drive. In *Proceedings 2006 IEEE International Conference on Robotics and Automation, 2006. ICRA 2006*, pages 2884–2889, 2006. doi:10.1109/ROBOT.2006.1642139. (Cited on page 4)
- [10] Doruk Senkal and Hakan Gurocak. Spherical MR-Brake with nintendo wii sensors for haptics. In Astrid M. L. Kappers, Jan B. F. van Erp, Wouter M. Bergmann Tiest, and Frans C. T. van der Helm, editors, *Haptics: Generating and Perceiving Tangible Sensations*, number 6192 in Lecture Notes in Computer Science, pages 160–165. Springer Berlin Heidelberg, jan 2010. ISBN 978-3-642-14074-7. doi:10.1007/978-3-642-14075-4.

BIBLIOGRAPHY

(Cited on page 4)

- [11] J.M. Hilkert. Inertially stabilized platform technology concepts and principles. *Control Systems Magazine, IEEE*, 28(1):26–46, 2008. ISSN 0272-1708. doi:10.1109/MCS.2007.910256. (Cited on page 4)
- [12] T. Shimizu, S. Nagata, S. Tsuneta, T. Tarbell, C. Edwards, R. Shine, C. Hoffmann, E. Thomas, S. Sour, R. Rehse, O. Ito, Y. Kashiwagi, M. Tabata, K. Kodeki, M. Nagase, K. Matsuzaki, K. Kobayashi, K. Ichimoto, and Y. Suematsu. Image stabilization system for hinode (solar-b) solar optical telescope. *Solar Physics*, 249(2):221–232, October 2007. ISSN 0038-0938. doi:10.1007/s11207-007-9053-z. (Cited on page 4)
- [13] F. Souvestre, M. Hafez, and S. Regnier. A novel laser-based tracking approach for wide field of view for robotics applications. In *International Symposium on Optomechatronic Technologies, 2009. ISOT 2009*, pages 328–333, 2009. doi:10.1109/ISOT.2009.5326043. (Cited on page 4)
- [14] C.M. Gosselin, E. St. Pierre, and M. Gagne. On the development of the agile eye. *Robotics & Automation Magazine, IEEE*, 3(4):29–37, 1996. ISSN 1070-9932. doi:10.1109/100.556480. (Cited on page 6)
- [15] Thomas Villgrattner and Heinz Ulbrich. Design and control of a compact high-dynamic camera-orientation system. *IEEE/ASME Transactions on Mechatronics*, 16(2): 221–231, April 2011. ISSN 1083-4435, 1941-014X. doi:10.1109/TMECH.2009.2039223. (Cited on page 6)
- [16] Zongjie Tao and Qi An. Interference analysis and workspace optimization of 3-RRR spherical parallel mechanism. *Mechanism and Machine Theory*, 69:62–72, November 2013. ISSN 0094114X. doi:10.1016/j.mechmachtheory.2013.05.004. (Cited on page 6)
- [17] Xuan-yin Wang, Yang Zhang, Xiao-jie Fu, and Gui-shan Xiang. Design and kinematic analysis of a novel humanoid robot eye using pneumatic artificial muscles. *Journal of Bionic Engineering*, 5(3):264–270, September 2008. ISSN 1672-6529. doi:10.1016/S1672-6529(08)60034-7. (Cited on page 7)
- [18] T. B. Wolfe, M. G. Faulkner, and J. Wolfaardt. Development of a shape memory alloy actuator for a robotic eye prosthesis. *Smart Materials and Structures*, 14:759, 2005. doi:10.1088/0964-1726/14/4/035. (Cited on page 7)
- [19] T. Yano. Basic characteristics of a hexahedron-octahedron based spherical stepping motor. In *Power Electronics Electrical Drives Automation and Motion (SPEEDAM), 2010 International Symposium on*, pages 1748–1753, 2010. doi:10.1109/SPEEDAM.2010.5544960. (Cited on pages 8 and 25)
- [20] L. Rossini, O. Chetelat, E. Onillon, and Y. Perriard. Force and torque analytical models of a reaction sphere actuator based on spherical harmonic rotation and decomposition. *IEEE/ASME Transactions on Mechatronics*, 18(3):1006–1018, 2013. ISSN 1083-4435. doi:10.1109/TMECH.2012.2195501. (Cited on page 8)
- [21] T. Yano, Y. Kubota, T. Shikayama, and T. Suzuki. Basic characteristics of a multi-pole spherical synchronous motor. In *Micro-NanoMechatronics and Human Science, 2007. MHS '07. International Symposium on*, pages 383–388, 2007. doi:10.1109/MHS.2007.4420885. (Cited on pages 8 and 25)

- [22] Masaaki Kumagai and Ralph L. Hollis. Development and control of a three DOF spherical induction motor. Karlsruhe, Germany, May 2013. (Cited on pages 8 and 25)
- [23] J. Wang, K. Mitchell, G.W. Jewell, and D. Howe. Multi-degree-of-freedom spherical permanent magnet motors. In *Robotics and Automation, 2001. Proceedings 2001 ICRA. IEEE International Conference on*, volume 2, pages 1798–1805 vol.2, 2001. ISBN 1050-4729. doi:10.1109/ROBOT.2001.932870. (Cited on pages 9 and 25)
- [24] R.S. Wallace. Miniature direct drive rotary actuators. II. eye, finger and leg. In *Robotics and Automation, 1994. Proceedings., 1994 IEEE International Conference on*, pages 1496–1501 vol.2, 1994. doi:10.1109/ROBOT.1994.351279. (Cited on pages 9 and 25)
- [25] B.B. Bederson, R.S. Wallace, and E.L. Schwartz. A miniature pan-tilt actuator: the spherical pointing motor. *IEEE Transactions on Robotics and Automation*, 10(3):298–308, June 1994. ISSN 1042296X. doi:10.1109/70.294205. (Cited on pages 9 and 25)
- [26] Minoru Kuribayashi Kurosawa. State-of-the-art surface acoustic wave linear motor and its future applications. *Ultrasonics*, 38(1–8):15–19, March 2000. ISSN 0041-624X. doi:10.1016/S0041-624X(99)00087-6. (Cited on pages 11 and 21)
- [27] G. H. Kim, J. W. Park, and S. H. Jeong. Analysis of dynamic characteristics for vibration of flexural beam in ultrasonic transport system. *Journal of Mechanical Science and Technology*, 23(5):1428–1434, May 2009. ISSN 1738-494X, 1976-3824. doi:10.1007/s12206-008-1219-6. (Cited on page 12)
- [28] M. Takano, M. Takimoto, and K. Nakamura. Electrode design of multilayered piezoelectric transducers for longitudinal-bending ultrasonic actuators. *Acoustical Science and Technology*, 32(3):100–108, 2011. ISSN 1346-3969. doi:10.1250/ast.32.100. (Cited on pages 12, 59, 101 and 112)
- [29] M. Kurosawa and S. Ueha. Hybrid transducer type ultrasonic motor. *IEEE Transactions on Ultrasonics, Ferroelectrics and Frequency Control*, 38(2):89–92, 1991. ISSN 0885-3010. doi:10.1109/58.68464. (Cited on page 12)
- [30] O. Vyshnevsky, Sergej Kovalev, and Wladimir Wischnewskiy. A novel, single-mode piezoceramic plate actuator for ultrasonic linear motors. *Ultrasonics, Ferroelectrics and Frequency Control, IEEE Transactions on*, 52(11):2047–2053, 2005. doi:10.1109/TUFFC.2005.1561674. (Cited on pages 12 and 22)
- [31] Masahiro Takano, Kenichi Hirosaki, Mikio Takimoto, Satoru Ichimura, and Kentaro Nakamura. Improvements in controllability of ultrasonic linear motors by longitudinal-bending multilayered transducers with independent electrodes. *Japanese Journal of Applied Physics*, 50(7):07HE25, 2011. doi:10.1143/JJAP.50.07HE25. (Cited on pages 13, 53 and 77)
- [32] K. Takemura and T. Maeno. Design and control of an ultrasonic motor capable of generating multi-DOF motion. *Mechatronics, IEEE/ASME Transactions on*, 6(4):499–506, 2001. ISSN 1083-4435. doi:10.1109/3516.974864. (Cited on pages 14 and 25)
- [33] T. Amano, T. Ishii, K. Nakamura, and S. Ueha. An ultrasonic actuator with multidegree of freedom using bending and longitudinal vibrations of a single stator. In *Ultrasonics Symposium, 1998. Proceedings., 1998 IEEE*, volume 1, pages 667–670 vol.1, 1998. ISBN 1051-0117. doi:10.1109/ULTSYM.1998.762236. (Cited on pages 13, 14 and 25)

BIBLIOGRAPHY

- [34] K. Takemura and T. Maeno. Characteristics of an ultrasonic motor capable of generating a multi-degrees of freedom motion. In *IEEE International Conference on Robotics and Automation, 2000. Proceedings. ICRA '00*, volume 4, pages 3660–3665 vol.4, 2000. doi:10.1109/ROBOT.2000.845302. (Cited on page 14)
- [35] Zhirong Li, Chunsheng Zhao, Weiqing Huang, and Zhao-Liang Li. Several key issues in developing of cylinder type 3-DOF ultrasonic motor. *Sensors and Actuators A: Physical*, 136(2):704–709, May 2007. ISSN 0924-4247. doi:10.1016/j.sna.2007.01.016. (Cited on pages 14 and 25)
- [36] Yasuyuki Gouda, Kentaro Nakamura, and Sadayuki Ueha. A miniaturization of the multi-degree-of-freedom ultrasonic actuator using a small cylinder fixed on a substrate. *Ultrasonics*, 44, Supplement:e617–e620, December 2006. ISSN 0041-624X. doi:10.1016/j.ultras.2006.05.015. (Cited on pages 14 and 25)
- [37] Cheol-Ho Yun, Leslie Y. Yeo, James R. Friend, and Bernard Yan. Multi-degree-of-freedom ultrasonic micromotor for guidewire and catheter navigation: The NeuroGlide actuator. *Applied Physics Letters*, 100(16):164101, 2012. ISSN 00036951. doi:10.1063/1.3702579. (Cited on page 15)
- [38] Yasuhiro Sasaki, Sadayuki Takahashi, and Mitsuru Yamamoto. Mechanical quality factor of multilayer piezoelectric ceramic transducers. *Japanese Journal of Applied Physics*, 40(Part 1, No. 5B):3549–3551, 2001. doi:10.1143/JJAP.40.3549. (Cited on page 17)
- [39] Ter Fong Khoo, Dinh Huy Dang, J. Friend, D. Oetomo, and L. Yeo. Triple degree-of-freedom piezoelectric ultrasonic micromotor via flexural-axial. *IEEE Transactions on Ultrasonics, Ferroelectrics and Frequency Control*, 56(8):1716–1724, August 2009. ISSN 0885-3010. doi:10.1109/TUFFC.2009.1236. (Cited on pages 17, 18 and 25)
- [40] Min Hu, Hejun Du, Shih-Fu Ling, and Jin-Kai Teo. A piezoelectric spherical motor with two degree-of-freedom. *Sensors and Actuators A: Physical*, 94(1–2):113–116, October 2001. ISSN 0924-4247. doi:10.1016/S0924-4247(01)00671-9. (Cited on page 18)
- [41] Bo Lu, Manabu Aoyagi, Takehiro Takano, and Hideki Tamura. Examination of sandwich-type multidegree-of-freedom spherical ultrasonic motor. *Japanese Journal of Applied Physics*, 49(7):07HE24, July 2010. ISSN 0021-4922, 1347-4065. doi:10.1143/JJAP.49.07HE24. (Cited on pages 18 and 25)
- [42] M. Aoyagi, S.P. Beeby, and N.M. White. A novel multi-degree-of-freedom thick-film ultrasonic motor. *Ultrasonics, Ferroelectrics and Frequency Control, IEEE Transactions on*, 49(2):151–158, 2002. ISSN 0885-3010. doi:10.1109/58.985699. (Cited on pages 18 and 25)
- [43] Bo Lu and M. Aoyagi. Examination of an outer-rotor-type multidegree-of-freedom spherical ultrasonic motor. In *2012 15th International Conference on Electrical Machines and Systems (ICEMS)*, pages 1–5, 2012. (Cited on page 19)
- [44] Bo Lu, M. Aoyagi, H. Tamura, and T. Takano. Development of a novel rotor-embedded-type multidegree-of-freedom spherical ultrasonic motor. In *2011 International Conference on Mechatronics and Automation (ICMA)*, pages 795–800. IEEE, August 2011. ISBN 978-1-4244-8113-2. doi:10.1109/ICMA.2011.5985763. (Cited on pages 19 and 25)
- [45] K. Takemura, Y. Ohno, and T. Maeno. Design of a plate type multi-DOF ultrasonic

- motor and its self-oscillation driving circuit. *Mechatronics, IEEE/ASME Transactions on*, 9(3):474–480, 2004. ISSN 1083-4435. doi:10.1109/TMECH.2004.834643. (Cited on pages 19 and 25)
- [46] Yasuyuki Goda, Daisuke Koyama, and Kentaro Nakamura. Design of multi-degree-of-freedom ultrasonic micromotors. *Japanese Journal of Applied Physics*, 48(7):07GM06, July 2009. ISSN 0021-4922, 1347-4065. doi:10.1143/JJAP.48.07GM06. (Cited on pages 19 and 25)
- [47] P. Vasiljev, D. Mazeika, and G. Kulvietis. Modelling and analysis of omni-directional piezoelectric actuator. *Journal of Sound and Vibration*, 308(3-5):867–878, 2007. ISSN 0022-460X. doi:10.1016/j.jsv.2007.03.074. (Cited on page 20)
- [48] Manabu Aoyagi, Toshinori Nakajima, Yoshiro Tomikawa, and Takehiro Takano. Examination of disk-type multidegree-of-freedom ultrasonic motor. *Japanese Journal of Applied Physics*, 43(No. 5B):2884–2890, May 2004. ISSN 0021-4922. doi:10.1143/JJAP.43.2884. (Cited on pages 20 and 25)
- [49] Yung Ting, Yu-Ren Tsai, Bing-Kuan Hou, Shuo-Chun Lin, and Cheng-Chin Lu. Stator design of a new type of spherical piezoelectric motor. *Ultrasonics, Ferroelectrics and Frequency Control, IEEE Transactions on*, 57(10):2334–2342, 2010. ISSN 0885-3010. doi:10.1109/TUFFC.2010.1694. (Cited on pages 20 and 25)
- [50] Yung Ting, Yu-Ren Tsai, Bing-Kuan Hou, Shuo-Chun Lin, and Cheng-Chin Lu. Stator analysis and design of a spherical piezoelectric motor. In *Robotics and Biomimetics (ROBIO), 2009 IEEE International Conference on*, pages 1160–1165, 2009. doi:10.1109/ROBIO.2009.5420754. (Cited on page 20)
- [51] Yoseph Bar-Cohen, Xiaoqi Bao, Anthony Hull, and John Wright. Improved multiple-DOF SAW piezoelectric motors, 2003. URL <http://www.techbriefs.com/Briefs/Feb03/NPO20859.html>. (Cited on page 20)
- [52] Kentaro Nakamura, Minoru Kurosawa, Hisayuki Kurebayashi, and Sadayuki Ueha. An estimation of load characteristics of an ultrasonic motor by measuring transient responses. *Ultrasonics, Ferroelectrics and Frequency Control, IEEE Transactions on*, 38(5):481–485, 1991. doi:10.1109/58.84293. (Cited on pages 21 and 133)
- [53] Kayo Otokawa and Takashi Maeno. Development of an arrayed-type multi-degree-of-freedom ultrasonic motor based on a selection of reciprocating vibration modes. In *Ultrasonics Symposium, 2004 IEEE*, volume 2, page 1181–1184, 2004. doi:10.1109/ULTSYM.2004.1417995. (Cited on pages 22 and 25)
- [54] Toshiiku Sashida. Motor device utilizing ultrasonic oscillation. Patent number US4562374. (Cited on page 22)
- [55] Shigeki Toyama and Shigeki Hatae. Multi-degree of freedom spherical ultrasonic motor. In *RoManSy 9*, page 243–252. Springer, 1993. (Cited on page 22)
- [56] Shigeki Toyama, Shigeru Sugitani, Zhang Guoqiang, Yasutaro Miyatani, and Kazuto Nakamura. Multi degree of freedom spherical ultrasonic motor. In *Robotics and Automation, 1995. Proceedings., 1995 IEEE International Conference on*, volume 3, page 2935–2940, 1995. doi:10.1109/ROBOT.1995.525700. (Cited on page 22)
- [57] M. Hoshina, T. Mashimo, and S. Toyama. Development of pipe inspection robot;

BIBLIOGRAPHY

- driving system and control of outer-rotor-typed spherical ultrasonic motor. In *Advanced Robotics, 2009. ICAR 2009. International Conference on*, pages 1–6, 2009. (Cited on page 22)
- [58] L. Howald, H. Rudin, and H.-J. Güntherodt. Piezoelectric inertial stepping motor with spherical rotor. *Review of Scientific Instruments*, 63(8):3909, 1992. ISSN 00346748. doi:10.1063/1.1143290. (Cited on page 23)
- [59] S. Fatikow, J. Seyfried, St Fahlbusch, A. Buerkle, and F. Schmoeckel. A flexible microrobot-based microassembly station. *Journal of Intelligent and Robotic Systems*, 27(1-2):135–169, January 2000. ISSN 0921-0296, 1573-0409. doi:10.1023/A:1008106331459. (Cited on page 23)
- [60] J. Wang, G.W. Jewell, and D. Howe. Analysis, design and control of a novel spherical permanent-magnet actuator. *Electric Power Applications, IEE Proceedings -*, 145(1):61–71, 1998. ISSN 1350-2352. doi:10.1049/ip-epa:19981635. (Cited on page 25)
- [61] C. Livermore, A.R. Forte, T. Lyszczarz, S.D. Umans, A.A. Ayon, and Jeffrey H. Lang. A high-power MEMS electric induction motor. *Journal of Microelectromechanical Systems*, 13(3):465–471, 2004. ISSN 1057-7157. doi:10.1109/JMEMS.2004.828736. (Cited on page 27)
- [62] J. M Smoliga. *Kinematic And Electromyographic Analysis Of The Legs, Torso, And Arms During An Exhaustive Run*. PhD thesis, 2007. (Cited on page 29)
- [63] G. A. Cavagna, P. Franzetti, N. C. Heglund, and P. Willems. The determinants of the step frequency in running, trotting and hopping in man and other vertebrates. *The Journal of Physiology*, 399(1):81, 1988. (Cited on page 29)
- [64] K. Spanner and B. Koc. An overview of piezoelectric motors. In *Actuator 2010 : 12th International Conference on New Actuators & 6th International Exhibition on Smart Actuators and Drive Systems, 14-16 June 2010, Bremen, Germany : conference proceedings*, pages 167–176, Bremen, 2010. ISBN 9783933339126. (Cited on page 31)
- [65] Cunyue Lu, Tian Xie, Tieying Zhou, and Yu Chen. Study of a new type linear ultrasonic motor with double-driving feet. *Ultrasonics*, 44, Supplement:e585–e589, December 2006. ISSN 0041-624X. doi:10.1016/j.ultras.2006.05.191. (Cited on page 31)
- [66] Long Li and Chang-Hong Liang. Analysis of resonance and quality factor of antenna and scattering systems using complex frequency method combined with model-based parameter estimation. *Progress In Electromagnetics Research*, 46:165–188, 2004. (Cited on page 43)
- [67] R. J. Allemang. The modal assurance criterion—twenty years of use and abuse. *Sound and Vibration*, 37(8):14–23, 2003. (Cited on page 46)
- [68] A. Krushynska, V. Meleshko, Chien-Ching Ma, and Yu-Hsi Huang. Mode excitation efficiency for contour vibrations of piezoelectric resonators. *IEEE Transactions on Ultrasonics, Ferroelectrics and Frequency Control*, 58(10):2222–2238, October 2011. ISSN 0885-3010. doi:10.1109/TUFFC.2011.2072. (Cited on page 49)
- [69] Yunlai Shi and Chunsheng Zhao. A new standing-wave-type linear ultrasonic motor based on in-plane modes. *Ultrasonics*, 51(4):397–404, May 2011. ISSN 0041-624X. doi:10.1016/j.ultras.2010.11.006. (Cited on pages 59 and 125)

- [70] Akira Endo and Nobutoshi Sasaki. Investigation of frictional material for ultrasonic motor. *Japanese Journal of Applied Physics*, 26S1(Supplement 26-1):197–199, 1987. doi:10.1143/JJAPS.26S1.197. (Cited on page 64)
- [71] Chunsheng Zhao. *Ultrasonic Motors: Technologies and Applications*. Springer-Verlag Berlin and Heidelberg GmbH & Co. K, 1 edition, March 2011. ISBN 3642153046. (Cited on pages 64, 75, 128 and 135)
- [72] Jifeng Guo, Shujuan Gong, Haixuu Guo, Xiao Liu, and Kehui Ji. Force transfer model and characteristics of hybrid transducer type ultrasonic motors. *IEEE Transactions on Ultrasonics, Ferroelectrics and Frequency Control*, 51(4):387–395, 2004. ISSN 0885-3010. doi:10.1109/TUFFC.2004.1295424. (Cited on pages 68, 70 and 73)
- [73] C. Makkar, W.E. Dixon, W. G. Sawyer, and G. Hu. A new continuously differentiable friction model for control systems design. In *Proceedings, 2005 IEEE/ASME International Conference on Advanced Intelligent Mechatronics*, pages 600–605, 2005. doi:10.1109/AIM.2005.1511048. (Cited on page 69)
- [74] C. Canuda De Wit, H. Olsson, K.J. Astrom, and P. Lischinsky. A new model for control of systems with friction. *IEEE Transactions on Automatic Control*, 40(3):419–425, 1995. ISSN 0018-9286. doi:10.1109/9.376053. (Cited on page 69)
- [75] Jean-Marc Breguet. *Actionneurs” stick and slip” pour micro-manipulateurs*. PhD thesis, Ecole Polytechnique Fédérale de Lausanne, 1998. (Cited on page 69)
- [76] Lauric Garbuio. *Etude du phénomène de lubrification électroactive à l’aide d’actionneurs piézoélectriques. Application à la réduction des forces de frottement sec dans un moteur à combustion interne*. THESE, Institut National Polytechnique de Toulouse - INPT, June 2006. (Cited on page 70)
- [77] J. Wallaschek. Contact mechanics of piezoelectric ultrasonic motors. *Smart materials and structures*, 7:369, 1998. doi:10.1088/0964-1726/7/3/011. (Cited on page 70)
- [78] Kenji Uchino. Piezoelectric ultrasonic motors: overview. *Smart Materials and Structures*, 7(3):273, 1998. doi:10.1088/0964-1726/7/3/002. (Cited on page 75)
- [79] T. Ishii, S. Maeno, K. Nakamura, and S. Ueha. Efficiency improvement of the friction drive in the ultrasonic motor using lubricant. In *2001 IEEE Ultrasonics Symposium*, volume 1, pages 521–524 vol.1, 2001. doi:10.1109/ULTSYM.2001.991676. (Cited on page 75)
- [80] W. Qiu, Y. Mizuno, and K. Nakamura. Experimental verification and modeling of high-efficiency operation in lubricated ultrasonic motors. Dresden, Germany, July 2012. doi:10.1109/ULTSYM.2012.0678. (Cited on page 75)
- [81] Hyun-Phill Ko, Sangsig Kim, Jin-Sang Kim, Hyun-Jai Kim, and Seok-Jin Yoon. Wear and dynamic properties of piezoelectric ultrasonic motor with frictional materials coated stator. *Materials Chemistry and Physics*, 90(2–3):391–395, April 2005. ISSN 0254-0584. doi:10.1016/j.matchemphys.2004.09.037. (Cited on page 76)
- [82] Marc Budinger. *Contribution à la conception et à la modélisation d’actionneurs piézoélectriques cylindriques à deux degrés de liberté de type rotation et translation*. THESE, Institut National Polytechnique de Toulouse - INPT, May 2003. (Cited on page 97)

BIBLIOGRAPHY

- [83] IEEE standard definitions and methods of measurement for piezoelectric vibrators. *IEEE Std No.177*, pages 1–, 1966. doi:10.1109/IEEESTD.1966.120168. (Cited on page 100)
- [84] G. G Yaralioglu, A. S Ergun, B. Bayram, E. Haeggstrom, and B. T Khuri-Yakub. Calculation and measurement of electromechanical coupling coefficient of capacitive micromachined ultrasonic transducers. *IEEE Transactions on Ultrasonics, Ferroelectrics and Frequency Control*, 50(4):449–456, April 2003. ISSN 0885-3010. doi:10.1109/TUFFC.2003.1197968. (Cited on page 101)
- [85] IRE. IRE standards on piezoelectric crystals: Determination of the elastic, piezoelectric, and dielectric constants-the electromechanical coupling factor, 1958. *Proceedings of the IRE*, 46(4):764–778, 1958. ISSN 0096-8390. doi:10.1109/JRPROC.1958.286778. (Cited on pages 101 and 102)
- [86] K. Uchino and S. Hirose. Loss mechanisms in piezoelectrics: how to measure different losses separately. *IEEE Transactions on Ultrasonics, Ferroelectrics and Frequency Control*, 48(1):307–321, January 2001. ISSN 0885-3010. doi:10.1109/58.896144. (Cited on pages 109, 135 and 168)
- [87] Shinjiro Tashiro, Masahiko Ikehiro, and Hideji Igarashi. Influence of temperature rise and vibration level on electromechanical properties of high-power piezoelectric ceramics. *Japanese Journal of Applied Physics*, 36(Part 1, No. 5B):3004–3009, 1997. doi:10.1143/JJAP.36.3004. (Cited on page 109)
- [88] Z. Chen, X. Li, J. Chen, and S. Dong. A square-plate ultrasonic linear motor operating in two orthogonal first bending modes. *IEEE Transactions on Ultrasonics, Ferroelectrics and Frequency Control*, 60(1):115 –120, January 2013. ISSN 0885-3010. doi:10.1109/TUFFC.2013.2543. (Cited on page 125)
- [89] Tomoki Funakubo and Yoshiro Tomikawa. Characteristics of 10 mm multilayer $l_1 - f_2$ mode vibrator and application to a linear motor. *Japanese Journal of Applied Physics*, 42(Part 1, No. 5B):3002–3006, May 2003. ISSN 0021-4922. doi:10.1143/JJAP.42.3002. (Cited on page 126)
- [90] Tobias Hensel and Jörg Wallaschek. Survey of the present state of the art of piezoelectric linear motors. *Ultrasonics*, 38(1–8):37–40, March 2000. ISSN 0041-624X. doi:10.1016/S0041-624X(99)00143-2. (Cited on page 126)
- [91] Cheol-Ho Yun, Takaaki Ishii, Kentaro Nakamura, Sadayuki Ueha, and Koji Akashi. Holding mechanism using a resonance system for a high-power ultrasonic linear motor. *Japanese Journal of Applied Physics*, 41(Part 1, No. 5B):3261–3266, 2002. doi:10.1143/JJAP.41.3261. (Cited on page 126)
- [92] Martin Hildebrand and Ismo Vessonen. Experimental data on damping of adhesively bonded single lap joints. 1997. (Cited on page 129)
- [93] Antoine Ferreira and Patrice Minotti. High-performance load-adaptive speed control for ultrasonic motors. *Control Engineering Practice*, 6(1):1–13, January 1998. ISSN 0967-0661. doi:10.1016/S0967-0661(97)10057-0. (Cited on page 136)
- [94] F.J Arnold and S.S Mühlen. The resonance frequencies on mechanically pre-stressed ultrasonic piezotransducers. *Ultrasonics*, 39(1):1–5, January 2001. ISSN 0041-624X. doi:10.1016/S0041-624X(00)00047-0. (Cited on page 142)

- [95] Académie des sciences. *Histoire de l'Académie royale des sciences ... avec les mémoires de mathématique & de physique... tirez des registres de cette Académie*. Imprimerie de Du Pont (Paris), 1702. (Cited on page 163)
- [96] Gabriel Lippmann. *Principe de la conservation de l'électricité*, volume 24 of *Annales de chimie et de physique*. V. Masson (Paris), 1881. (Cited on page 163)
- [97] Warren P. Mason. Piezoelectricity, its history and applications. *The Journal of the Acoustical Society of America*, 70:1561, 1981. doi:10.1121/1.387221. (Cited on page 163)
- [98] David Zimmerman. Paul Langevin and the discovery of active sonar or asdic. *Northern Mariner*, 12(1):39–52, 2002. (Cited on page 163)
- [99] N. Setter, D. Damjanovic, L. Eng, G. Fox, S. Gevorgian, S. Hong, A. Kingon, H. Kohlstedt, N. Y. Park, G. B. Stephenson, I. Stolitchnov, A. K. TagansteV, D. V. Taylor, T. Yamada, and S. Streiffer. Ferroelectric thin films: Review of materials, properties, and applications. *Journal of Applied Physics*, 100(5):051606–051606–46, September 2006. ISSN 00218979. doi:doi:10.1063/1.2336999. (Cited on page 166)
- [100] American piezo. American piezo ceramics | piezoelectric ceramics | APCI. URL <http://www.americanpiezo.com/piezo-theory/ceramics.html>. (Cited on page 169)
- [101] M. Pereira, A. G. Peixoto, and M. J. M. Gomes. Effect of Nb doping on the microstructural and electrical properties of the PZT ceramics. *Journal of the European Ceramic Society*, 21(10):1353–1356, 2001. doi:10.1016/S0955-2219(01)00017-6. (Cited on page 168)
- [102] eFunda. eFunda: properties of piezo material quartz. URL http://www.efunda.com/materials/piezo/material_data/matdata_output.cfm?Material_ID=Quartz. (Cited on page 169)
- [103] Chandra Shekhar Pandey, Sven Jodlauk, and Jürgen Schreuer. Correlation between dielectric properties and chemical composition of the tourmaline single crystals. *Applied Physics Letters*, 99(14):142906, 2011. ISSN 00036951. doi:10.1063/1.3646912. (Cited on page 169)
- [104] H. Jaffe and D. A. Berlincourt. Piezoelectric transducer materials. *Proceedings of the IEEE*, 53(10):1372–1386, 1965. doi:10.1109/PROC.1965.4253. (Cited on page 169)
- [105] Chandra Shekhar Pandey and Jürgen Schreuer. Elastic and piezoelectric constants of tourmaline single crystals at non-ambient temperatures determined by resonant ultrasound spectroscopy. *Journal of Applied Physics*, 111(1):013516, 2012. ISSN 00218979. doi:10.1063/1.3673820. (Cited on page 169)
- [106] R. Bechmann. The linear piezoelectric equations of state. *British Journal of Applied Physics*, 4:210, 1953. doi:10.1088/0508-3443/4/7/305. (Cited on page 171)
- [107] IEEE standard on piezoelectricity. *ANSI/IEEE Std 176-1987*, 1988. doi:10.1109/IEEESTD.1988.79638. (Cited on page 171)

Résumé

Les moteurs à plusieurs degrés de liberté angulaire sont des systèmes utilisés dans de nombreuses applications avec par exemple la réalisation d'articulation de robots, de roues omnidirectionnelles ou la stabilisation de composants optiques. La méthode classiquement utilisée pour réaliser ce type de plateformes limite cependant la capacité de ces systèmes à être miniaturisés. Une solution facilitant la réalisation de systèmes compacts à plusieurs degrés de liberté angulaire est l'utilisation d'un unique rotor sphérique. Nous proposons dans ce travail, un actionneur ultrasonique piézoélectrique adapté à la fabrication de moteurs sphériques compacts. L'innovation de l'actionneur développé tient dans l'adaptation de sa surface de contact au rotor, ce qui permet d'obtenir une surface étendue de contact et un guidage total du rotor sphérique. L'état de l'art des différents systèmes d'actionnement sphérique à un seul rotor est proposé ainsi que l'ensemble des considérations théoriques utiles à la modélisation et la réalisation de moteurs ultrasoniques. Un modèle complet pour la conception d'actionneurs ultrasoniques est proposé, il décrit l'étude de la géométrie et de ses modes de vibration, l'analyse du contact par l'application d'un modèle de transfert de force et la conversion électromécanique par méthodes semi-analytiques. Un prototype expérimental est proposé ainsi qu'une caractérisation de ses performances. Les données obtenues sont comparées au modèle théorique et permettent de valider les méthodes de conception proposées. L'effet de l'amplitude de stimulation, de la précontrainte et de l'étendue du contact y sont notamment analysés. Bien qu'appliqué au cas particulier d'un actionneur multimode incurvé, la démarche employée est générale et peut-être adaptée à la réalisation d'autres systèmes ultrasoniques.

Abstract

Multi-degree-of-freedom angular motors are used in numerous applications, such as robot articulations, omnidirectional wheels or the stabilization of optical components. Nevertheless, the classical method used to build such platforms limits the miniaturization of these devices. The use of a single spherical rotor is a solution which facilitates the realization of compact multi-degree-of-freedom angular systems. In this work, we propose a piezoelectric ultrasonic actuator adapted to the fabrication of compact spherical motors. The novelty of the developed actuator is the adapted contact surface that allows for an extended contact area and thus the complete guidance of a spherical rotor. The state of the art of single rotor spherical systems is presented along with a presentation of the theoretical considerations useful for the modeling and construction of ultrasonic motors. A complete model for the design of ultrasonic motors is also proposed, which describes the geometry of the actuator and its vibration modes, the analysis of the contact using a force transfer model and the electromechanical conversion using semi-analytical methods. An experimental prototype is proposed along with a characterization of the actuator performance. Experimental data is compared to the theoretical model and validates the proposed design method. Parameters such as electrical amplitude, preloading force and the extent of the contact area are analyzed. Although in this case we demonstrate the application of our design methodology to the specific case of a curved multi-mode actuator, the proposed methodology is general and can be adapted to the design of other ultrasonic systems.

